University of Nevada, Reno

Characteristics of Dynamic Triaxial Testing of Asphalt Mixtures

A thesis submitted in partial fulfillment of the
requirements for the degree of Master of Science in
Civil Engineering

by

Alvaro Ulloa Calderon

Elie Y. Hajj, Ph.D

Thesis Advisor

December, 2009

University of Nevada, Reno
Statewide • Worldwide

THE GRADUATE SCHOOL

We recommend that the thesis
prepared under our supervision by

ALVARO ULLOA CALDERON

entitled

Characteristics Of Dynamic Triaxial Testing Of Asphalt Mixtures

be accepted in partial fulfillment of the
requirements for the degree of

MASTER OF SCIENCE

Elie Y. Hajj, Ph.D., Advisor

Peter E. Sebaaly, Ph.D., Committee Member

Raj V. Siddharthan, Ph.D., Committee Member

George C. Fernandez, Ph.D., Graduate School Representative

Marsha H. Read, Ph. D., Associate Dean, Graduate School

December, 2009

ABSTRACT

Due to the increasing traffic loads and tire pressures, a serious detrimental impact has occurred on flexible pavements in the form of excessive permanent deformation once the critical combination of loading and environmental conditions are reached. This distress, also known as rutting, leads to an increase in road roughness and ultimately jeopardizes the road users' safety.

The flow number (FN) simple performance test for asphalt mixtures was one of the final three tests selected for further evaluation from the twenty-four test/material properties initially examined under the NCHRP 9-19 project. Currently, no standard triaxial testing conditions in terms of the magnitude of the deviator and confining stresses have been specified. In addition, a repeated haversine axial compressive load pulse of 0.1 second and a rest period of 0.9 second are commonly used as part of the triaxial testing conditions. The overall objective of this research was to define the loading conditions that created by a moving truck load in the hot mixed asphalt (HMA) layer. The loading conditions were defined in terms of the triaxial stress levels and the corresponding loading time.

Dynamic mechanistic analysis with circular stress distribution was used to closely simulate field loading conditions. Extensive mechanistic analyses of three different asphalt pavement structures subjected to moving traffic loads at various speeds and under braking and non-braking conditions were conducted using the 3D-Move model. Prediction equations for estimating the anticipated deviator and confining stresses along

with the equivalent deviator stress pulse duration as a function of pavement temperature, vehicle speed, and asphalt mixture's stiffness have been developed.

The magnitude of deviator stress, σ_d and confining stress, σ_c, were determined by converting the stress tensor computed in the HMA layer at 2" below pavement surface under a moving 18-wheel truck using the octahedral normal and shear stresses. In addition, the characteristics of the loading pulse were determined by best-fitting a haversine wave shape for the equivalent triaxial deviator stress pulse.

The tandem axle was proven to generate the most critical combination of deviator and confining stresses for braking and non-braking conditions at 2 inches below the pavement surface. Thus, this study is focused on developing the stress state and pulse characteristics required to determine the critical conditions on HMA mixtures under the loading of the tandem axle.

An increase of 40% was observed in the deviator stress when braking conditions are incorporated. A preliminary validation of the recommended magnitudes for the deviator and confining stresses on a field mixture from WesTrack showed consistent results between the flow number test results and field performance.

Based on laboratory experiments, the critical conditions of different field mixtures from the WesTrack project and also lab produced samples at different air-voids levels were determined. The results indicate that the tertiary stage will occur under the FN test when a combination of a critical temperature and a given loading conditions for specific air voids content occurs.

DEDICATION

The Author dedicates this thesis to God almighty for whom all things are possible now and forever, and to my loving parents, my sisters, and Doris. Thank you for all your love and support.

ACKNOWLEDGMENTS

The Author would like to acknowledge Dr. Elie Hajj for all his guidance, support, and assistance during the preparation of this thesis.

The Author would like to express his gratitude for Dr. Peter Sebaaly for his support, advice, and assistance during the course of this study.

The Author is heartily thankful to Dr. Raj Siddharthan for all his assistance, support, and invaluable efforts in guiding the Author throughout this thesis.

The Author also acknowledges all my colleagues who helped me along the way: Luis, Wendy, Ed, Jose, Andrew, Thusha, Shiva, Thileepan, K. Pratheepan, Nathan, M. Pratheepan, and Corina.

The Author would like to acknowledge Dr. George Fernandez, for his valuable input and assistance in this research.

I owe my deepest gratitude to my parents, for their never-ending love and support in all my efforts, and for giving me the foundation to be who I am. Thank you, Mom and Dad you are the best parents in the world.

Doris, my soul mate and confidant, for always being there for me. Thank you for your love, support, and patience as I went through this journey.

TABLE OF CONTENTS

LIST OF TABLES

LIST OF FIGURES

CHAPTER 1 – INTRODUCTION

As hot mix asphalt (HMA) pavements are subjected to traffic loading in the field, their behavior are highly dependent on the combination of state of stresses, rate of loading, and in-situ temperature of the pavement. When the critical combination of the aforementioned factors is reached, the H MA mix experiences tertiary or plastic flow. The rutting performance of HMA mixtures is the most significantly impacted by these parameters.

Even under moderate traffic loading conditions, HMA pavements will experience significant increases in rutting once their temperature reaches a critical level. Therefore, determining the stress state in a pavement section under a traffic load is an essential step in any rut-depth predictive methodology that utilizes mathematical modeling along with laboratory determined material properties. To achieve the greatest consistency in the modeling process, the traffic-induced stress state and loading pulse duration in the pavement needs to be appropriately duplicated in the laboratory testing of the HMA mixtures.

The past several years have seen considerable progress in developing a test method that could fully characterize the hot mix asphalt behavior in such a way that it would help to predict, with an acceptable confidence, its field performance. As part of the Superpave research program, the National Cooperative Highway Research Program (NCHRP) Project 9-19 proposed a Simple Performance Test (SPT) to evaluate the HMA materials performance related to fatigue cracking and permanent deformation (1).

Due to the increasing traffic loads and tire pressures, a serious detrimental impact has occurred in the form of excessive permanent deformation once the critical loading and environmental conditions are reached. This distress, also known as rutting, leads to an increase in road roughness and ultimately jeopardizes the road users' safety. In response to the need to evaluate permanent deformation behavior of pavement materials under a given set of loads and environmental conditions, the NCHRP Project 9-19 recommended the use of the tertiary flow parameter, also known as flow number (FN), by means of a SPT called Repeated Load Triaxial test (RLT).

The flow number test for asphalt mixtures was one of the final three tests selected for further evaluation from the twenty-four test/material properties initially examined under the NCHRP 9-19 project. The selection of the FN test as one of the final candidates was based on an extensive study of the laboratory measured FN and observed rutting at three field studies: Westrack, MnRoad, and the FHWA ALF test facility. In all three test sites it was found that the FN was highly correlated to field rut depth (within the asphalt layer) at any particular traffic level (2).

The newly proposed provisional AASHTO standard test method for determining the flow number of HMA mixtures does not specify the magnitude of the deviator and confining stresses to be used for testing. The applied deviator and confining stresses in the FN test are intended to duplicate the state of stresses generated in the pavement under given environmental and loading conditions. In other words, the FN test is intended to simulate the actual field conditions by subjecting the HMA specimen to deviator and confining stresses similar to the ones encountered in the HMA layer. Therefore, in order to determine the equivalent loading pulse duration and the equivalent deviator and

confining stresses to be applied in the laboratory, a mechanistic analysis of HMA pavements as subjected to moving loads at various speeds is required.

1.1 OBJECTIVE

The first objective of this study was to define the critical loading conditions created by a moving truck load in the HMA layer. The second objective of this research was to evaluate the combination of traffic-induced loads characteristics and pavement effective temperature, defined as critical conditions, in the laboratory under the RLT test. The third objective was to develop recommendations for the selection of the equivalent deviator pulse characteristics and the magnitudes of the deviator and confining stresses applied in the FN test that best simulate the stress conditions encountered in the pavement under traffic loads.

CHAPTER 2 – BACKGROUND

The performance of a HMA pavement is significantly impacted by the properties of the HMA mixture, and the imposed environmental and loading conditions. Once the combination of these factors reaches a critical level the HMA resistance to a specific distress is compromised contributing to a premature failure.

Permanent deformations in the lateral and longitudinal directions due to differential consolidation create major functional problems. In the transverse direction, rutting along the wheel path modifies drainage characteristics and forces water to collect in the ruts and create a condition of hydroplaning which reduces the skid resistance of the surface course. Also, in colder environments, snow and ice removal is impeded because the surface is not level. In the longitudinal direction, differential permanent deformations due to variability of materials and/or construction increase roughness and reduce the overall serviceability of the road (3).

During the past years there have been dramatic increment in traffic volume, along with the significant increase in the allowable maximum load and tire pressure, which in turn exuberates the extend and severity of permanent deformation of HMA pavements. In light of this continuously growing distress in pavements, considerable effort has been devoted to the selection of an appropriate laboratory test procedure that could be used to predict rutting potential of HMA pavements.

The FN Simple Performance Test for asphalt mixtures was one of the final three tests selected for further evaluation of permanent deformation from the twenty-four test/material properties initially examined under the NCHRP 9-19 project. Research

towards the development of a SPT to be used with the Superpave volumetric mix design methodology (NCHRP 9-19 Project) has indicated that the FN test, under repeated loads show promise as HMA rutting performance indicator **(**4**).**

The resistance of the HMA mixtures to permanent deformation can be evaluated under two types of testing: empirical and fundamental. The empirical tests provide index measures that can be used to relatively compare the rutting resistance of the various HMA mixtures. In the category the most widely used is the Asphalt Pavement Analyzer (APA). On this other hand, fundamental tests provide engineering properties of the mixtures that can be used in the mechanistic-empirical analyses of HMA pavements. In the category of fundamental tests the repeated load triaxial test, or also called FN test, is the most widely used.

In order to determine the HMA critical conditions under moving traffic loads, it is mandatory to understand the fundamental principles of the FN testing conditions. In addition, it is highly important to fully identify the theory used to predict the permanent deformation, as well as the evaluation of the material properties applicable to this test. And finally, the determination of the relationship between the magnitude of the parameter in question to the performance in the field are also desirable.

2.1 PERMANENT DEFORMATION EVALUATION

The mechanistic-empirical method of pavement design is based on the principle of mechanics of materials that relates an input, such as a traffic-induced loading, to an

output or pavement response, such as permanent deformation. The response values are used to predict distress based on laboratory test and field performance data.

Permanent deformation, usually referred to as rutting, is a major load-related distress in flexible pavements. This type of distress is an unrecoverable deformation characterized by longitudinal depressions in the wheel path of the roadway which accumulates under repeated loading (5). It is a progressive movement of materials under static or cyclic loads either in the top asphalt layer or the underlying layers. It develops gradually in the longitudinal direction under the channelized wheel loadings associated with high pavement temperatures. HMA can also exhibit shoving, a form of permanent deformation, which is characterized by zones of upheaval in regions of the roadway where traffic turns, stops, or starts.

2.1.1 Permanent deformation mechanism

Rutting of HMA pavements can result from different mechanisms: consolidation, surface wear, plastic flow, and mechanical deformation (6). One or a combination of factors ranging from mixture design, selection of materials, to inadequate compaction of the pavement or underlying layers during construction may also cause rutting.

Consolidation can occur when there is insufficient compaction during the construction of the pavement. An asphalt mixture with insufficient density is prone to further compaction under traffic, especially in hot weather and at intersections where the loads are slow moving or static. HMA pavements are usually constructed at initial air void content of 7 to 8%. It is anticipated that further compaction of the pavement will

occur under traffic until the pavement has approximately 4% air voids, after which conditions may stabilize.

Consolidation, in general, is not a problem if the asphalt surface is uniformly compacted by traffic. However, with canalized traffic flow, most of the consolidation occurs in the wheel path, creating longitudinal ruts. With consolidation, a depression occurs in the wheel path with no humps on either side of that depression. In addition, it is important to note that the base or subbase may undergo further compaction resulting in rutting of the pavement surface when there is inadequate compaction of these layers during construction or when the pavement surface is under-designed or when there is poor subsurface drainage. The subgrade may also undergo compaction resulting in rutting when an inadequate pavement structure is placed above it.

Surface wear takes place because of the surface abrasion under chains and studded tires used in the winter season. The subsequent depression on the surface is similar to that caused by consolidation, but with the appearance of abrasion. Surface wear rutting of HMA pavements is no longer a significant problem as the use of studded tires is controlled or banned by most state Department of Transportation (DOT).

Plastic flow can result when HMA mixtures exhibit insufficient stability. Some of the more common reasons for mixture instability are: excessive amount of asphalt binder and insufficient air voids, too much rounded aggregate, or too high of the minus #200 material. Plastic flow will normally appear as longitudinal ruts in the pavement near the center of the wheel path with humps of material on either side of the rut. The humps are created as the material is squeezed out from under the heavy loads.

Finally, mechanical deformation results from insufficient structural capacity of the pavement system and can occur when the strength and/or thickness of the pavement layers are insufficient to withstand the designed traffic-induce loads on the existing subgrade. A rut resulting from this type of action will generally be accompanied by longitudinal and/or alligator cracking. It is important to state that this research is mainly focused on the development of permanent deformation that occurred due to instability and imposed shear stresses within the HMA layer.

2.1.2 Prediction models

In the Mechanical Empirical Pavement Design Guide (MEPDG), a predictive rutting system was developed to evaluate the permanent deformation within all rut susceptible layers (HMA and all unbound material layers) in the pavement within the analysis period. Individual rut depths are predicted for each layer as a function of time and traffic repetition. This also allows for the prediction of the total pavement rut depth, with time and traffic repetitions (3).

Permanent deformation characterization models typically use the relationship between the accumulated permanent strain and the number of load repetitions, and are generally expressed in the form:

$$\varepsilon_p = aN^b \tag{2.1}$$

where ε_p is the accumulated permanent strain due to dynamic vertical loading, N is the number of load applications that produced εp and, a and b are regression constants that

depend on the material and stress state conditions. This model is commonly referred to as the "Power Model".

The total rut depth within the HMA layer is calculated by multiplying the permanent strain times the thickness of the HMA layer. The empirical rutting model suggested by the MEPDG is developed using the data from the repeated load triaxial test (FN test) to predict rutting in the HMA layer as shown in Equation 2.2 and 2.3.

$$\frac{\varepsilon_p}{\varepsilon_r} = k_1 \times a \times N^b \times T^c \quad (2.2)$$

$$RD_{HMA} = \varepsilon_p \times h_{AC} \quad (2.3)$$

where, ε_p = Permanent strain within the HMA layer (in/in)
ε_r = Elastic vertical strain within the HMA layer (in/in)
N = Number of load repetitions
T = Temperature of the HMA layer (°F)
a, b, and c = Experimentally determined coefficients from FN test
k_1 = Depth correction function
RD_{HMA} = Total rutting generated in the HMA layer (in)
H_{AC} = Thickness of the HMA layer (in)

The depth correction function k_1 is an empirical attempt based on engineering judgment and very limited field data to adjust the computed plastic strains for the influence of lateral confining pressure at different depths. Equation 2.4 shows k_1 as a function of the total asphalt layer thickness (h_{AC}, inch) and the depth (depth, inch) to the computational point.

$$k_1 = (C_1 + C_2 \times depth) \times 0.328196^{depth} \quad (2.4)$$

where $C_1 = -0.1039 \times {h_{AC}}^2 + 2.4868 \times h_{AC} - 17.342$
$C_2 = 0.0172 \times {h_{AC}}^2 - 1.7331 \times h_{AC} + 27.428$

2.2 STRESS DISTRIBUTION AND PULSE TIME IN HMA LAYERS

A flexible pavement structure is typically composed of several layers of material. Each layer receives the loads from the layer above it, spreads them out, and then passes on these loads to the next layer below. Thus, the material layers are usually arranged in order of descending load bearing capacity with the highest load bearing capacity material on the top and the lowest load bearing capacity material on the bottom.

When a truck, moves on a pavement, it exerts loads that vary in space and time. Conventional pavement analysis models assume the loads as static and stationary completely ignoring the moving nature of the load. In general, there are two main factors that should be considered in any dynamic pavement analysis. First the variation of the interaction between load, time and space. Second the dependency of the material properties on the applied stress and the loading frequency (7).

Traffic moving over a pavement structure results in a large number of rapidly applied stress pluses being applied to the material comprising each layer. Typically, these stress pulses last for only a short period of time. The magnitude and duration of the pulse vary with the type of vehicle and its speed, the geometry of the pavement structure, the material properties at the given environmental conditions, and the position of the element of material under consideration.

When considering the compressive vertical stress at a given point within the pavement system, as the traffic wheel moves along the pavement at a considerable distance from that point, the wheel load will have no significant effect and the compressive stress at that point is considered to be zero. Nonetheless, as the traffic wheel

approaches that point the vertical compressive stress gradually increases until it reaches its maximum value when the wheel load is directly above that location. An opposite trend occurs as the wheel load moves away from that point of interest.

Dynamic response of asphalt pavement under moving traffic-induced loads is a major component for accurate prediction of rutting performance of HMA pavements. Due to the viscoelastic behavior of the HMA layer, advanced material characterization and mechanistic theories must be used in order to simulate, as close as possible, the actual field conditions. In other words, the temperature and load rate dependency of the HMA layer must be considered in mechanistic response models. However, the pulse obtained with the current layered elastic theory models is symmetrical and does not predict residual stresses occurring during the unloading phase.

During the unloading stage of a traffic-induced load, the shape of the wave is asymmetric with the loading portion, contrary to the linear elastic theory, mainly due to the energy dissipation sources inherent in the viscoelastic nature of HMA (8). This behavior was proven in the measurements of the vertical compressive stresses made at Virginia Smart Road (8) at different speeds and pavements depths as shown in Figure 1. Therefore, in order to determine the pulse time to be applied in the laboratory, a more realistic mechanistic analysis of HMA pavements as subjected to moving loads at various speeds and temperatures is required.

The impact of loading pulse duration on HMA behavior has been recognized by numerous researchers. Models currently used to predict the loading time on a pavement are limited in their ability to ensure that the assumed duration of loading is accurate and most importantly, representative of field conditions. This lack of agreement is still an

issue nationwide and the selection of reasonable loading pulse duration is not well established.

In 1971, Barksdale investigated the vertical compressive stress pulses at different points in flexible pavements as a function of speed and depth (9). Using finite element modelling and elastic theory, Barksdale reported that the pulse shape varies from a sinusoidal waveform at the surface to a more triangular shape at greater depths. Additionally, he developed a chart relating the pulse duration to the vehicle speed and the depth beneath the pavement surface, as shown in Figure 2. Later, in order to select the appropriate axial compressive stress pulse time to use in the dynamic testing in the laboratory, the calculated pulse times were empirically corrected to account for viscoelastic behavior and inertia forces based on the vertical stress pulses measured in the AASHO Road Test. More recently, Al-Qadi et al. (10) compared the pulse durations from the Virginia Smart Road project with those obtained using the Barksdale chart. They found that Barksdale's duration times are similar to the ones measured in the Virginia Smart Road project for 1.5 inch (40 mm) and 7.5 inch (190 mm) depths beneath the pavement surface. However, at greater depths, Barksdale's duration times are almost half of those measured in the field.

In 1973, Brown derived an equation to calculate the loading time as a function of both vehicle speed and depth beneath the pavement surface (11). An average of the pulse times of the stresses in three directions obtained from the elastic layered theory was defined as the loading time. Equation 2.5 shows the logarithmic relationship between the loading time, the vehicle speed and the depth from the pavement surface.

$$\log(t) = 0.5d - 0.2 - 0.94\log(S) \quad (2.5)$$

where t is the loading time in seconds, d is the depth from the pavement surface in meters, and S is the vehicle velocity in km/h.

In 1974, McLean presented a chart to estimate the pulse loading time of an applied square wave taking into account the depth from the pavement surface and vehicle speed (12). In addition, the author recognized that the pulse time of the square wave is shorter than that of the sinusoidal or triangular pulse, as shown in Figure 3.

The Mechanistic-Empirical Design Guide recommends using a procedure based on stress distributions to estimate the traffic-induced loading time. In order to calculate the effective duration at the depth of interest, the MEPDG uses Odemark's method of equivalent thickness to transform the pavement structure into a single subgrade layer system, assuming that the stress distribution is developed at a 45º in the equivalent layer system as illustrated in Figure 4. As presented in the MEPDG (3), the time of loading of a haversine waveform in HMA due to moving traffic load is estimated from Equation 2.6.

$$T = \frac{L_{eff}}{17.6\,S} \quad (2.6)$$

where t is the loading time in seconds, L_{eff} is the effective length of stress pulse in inches, and S is the velocity of the moving load in mph.

Concerns were raised that the current MEPDG methodology may be overestimating the pulse duration, which would result in unrealistic distress prediction.

Al-Qadi et al. (13) investigated the accuracy of this methodology and found that with the Odemark's approach adopted in the MEPDG, the far-field effect of an approaching-leaving rolling wheel cannot be incorporated. In other words, the pulse duration considered in the current method only reflects the stresses when the load is on top of the point of interest and does not account for the stresses induced at that point resulting from the moving nature of the traffic-induced load. In addition, the elastic solution does not account for the time dependent response of HMA, and the 45º stress distribution angle is not representative of actual field conditions.

Hu et al. (14) developed equations to estimate the loading pulse time for different waveforms as a function of the vehicle speed, depth beneath the pavement surface, thickness of the HMA layer, and also the moduli ratio between the layer of interest and the immediate succeeding layer below. Their proposed equations were verified with field measured data from the Virginia Smart Road project. They found that for shallow depths (i.e. 2 inch), the moduli ratio (R) hardly influences the compressive stress pulse time, but when the depth is deeper (i.e. 6 inch) the influence of R becomes important. In addition, when the point of interest is near the surface (i.e. 0.5 inch) the best fit of the pulse load is a square wave, and when the depth is less than 3 inch, a haversine wave shape reasonably matched the measured pulse load. Finally, when the depth is greater than 6 inch a triangular wave shape was more accurate.

Garcia et al. (15) studied the horizontal and transverse tensile strain pulse durations measured in four extended-life hot-mix asphalt pavements sections tested at speeds of 2, 6, and 10 mph with the accelerated pavement testing machine (ATLAS). They found that the strain pulse time history is not perfectly symmetrical and it consisted

of both tension and compression. The authors used a haversine waveform to calculate the strain pulse duration by considering only the tensile part of the strain history. The resulting average strain pulse durations for the particular test conditions ranged from 0.130 sec for a vehicle speed of 10 mph and a 6 inch pavement thickness to 1.080 sec for a vehicle speed of 2 mph and a 16.5 inch pavement thickness. However, at speeds of 20 to 60 mph or more, inertial forces and viscous effects would be expected to significantly influence the strain pulse durations.

Yin et al. (16) investigated the effect of loading time on flexible pavements using finite element analysis. They concluded that the vertical stress pulse duration under a circular uniform load is not dependent only on vehicle speed and depth from the pavement surface, but also on the effective pavement temperature. In addition they calculated different pulse time durations of moving loads at different depths and speeds using a haversine function. As an example at a depth of 2.1 inch (55 mm) for speeds of 20, 40 and 60 mph the calculated pulse time durations are 0.058, 0.027, and 0.018 seconds, respectively, which in turn are smaller than the duration of 0.1 seconds commonly used in the FN test. It is important to state that 0.1 seconds was selected to represent a haversine wave pulse obtained from a truck speed of 25 km/h (15.5 mph) at a depth of 190 mm (7.5 inches).

2.3 FLOW NUMBER TEST

Prediction of asphalt concrete mixture performance in the laboratory during design is a necessary step for the production of quality mixtures. Nowadays, the focus is

shifting gradually to cover also the establishment of performance-based laboratory test methods and models to accurately predict mixture performance in advance. Thus, as it was aforementioned, the flow number test was developed to supply a rational engineering-based test and provide the necessary mechanistic input to accurately predict the permanent deformation that occurs in the field.

The flow number test consists of subjecting a HMA specimen at a specified temperature to a repeated haversine axial compressive load pulse (deviator stress) of 0.1 second loading and 0.9 second of rest time. Even though the FN test can be run without a confining pressure, it is recommended that the test be conducted with a static all around confining pressure using compressed air to simulate field conditions. The resulting cumulative permanent axial strain is measured and plotted versus the number of load cycles.

The FN test measures the permanent axial deformation in the HMA mixture as it is subjected to triaxial stress conditions. The test specimen is a 4-inch diameter by 6-inch high cylindrical sample that is cored from the center of a 6-inch by 7-inch Superpave gyratory compacted sample. The test is conducted for a certain amount of cycles, usually 12,000 cycles; axial deformations continuously measured over the middle 4 inches of the sample by two independently monitored linear variable differential transducers (LVDT) placed 180º apart. Also, the permanent vertical strain in the sample is measured as a function of load cycles using the RLT equipment as shown in Figure 5. The resulting cumulative permanent strain can be characterized by the primary, secondary, and tertiary zones, as shown in Figure 6 and discussed next.

- Primary stage – Permanent strain increases rapidly producing a high initial level of rutting with a decreasing rate of plastic deformations. This is mainly due to a rearrangement of the structure of the mix with an eventual concentration of stresses in the surface of contact between the loading plate and sample owed to small irregularities (17), predominantly associated with volumetric change. Researchers have shown that densification is unlikely with pavements well compacted during construction and its contribution, if exists, is only at the first working stage of asphalt pavement (18).
- Secondary stage – Permanent strain rate maintains a constant value that is also associated with volumetric changes; however, shear deformations increase at increasing rate the tertiary creep zone is reached. Lower rates of deformation (slope of accumulated strain vs. load repetitions) during the secondary stage of the uniaxial repeated loading test suggest a more stable mix after initial densification has been achieved, and the structure of the mixture has finished its relocation due to initial traffic compaction (17).
- Tertiary stage – High level of permanent axial strain predominantly associated with plastic or shear deformations under no volume change conditions. In other words, this stage is reached when the specimen is beginning to deform significantly and individual aggregates composing the skeleton of the mix are moving past each other. The point at which the tertiary flow starts is called the flow number. In other words, the FN is defined as the number of load cycles corresponding to the minimum rate of change of permanent axial strain.

The MEPDG utilizes an approach that models both the primary and secondary stages with two major simplifications. First, the primary stage is modeled using an extrapolation of the secondary stage trend. The second simplification is that the tertiary stage, although very important, is not taken into account. Permanent deformation tests used to analyze the tertiary stage are extremely time-consuming and difficult to perform; therefore very little research has been devoted to this type of analysis (19).

The outcome of NCHRP Project 9-19 study was the recommendation of the tertiary flow parameter, FN, to account for the characteristics of the mixture behavior through elastic, viscoelastic and viscoplastic properties that fully incorporates the true non-linear behavior of asphalt mixtures. Therefore, the onset of the tertiary stage, at the number of load cycles corresponding to the minimum rate of change of permanent axial strain was defined as FN, as shown in Figure 7. This new parameter is implemented to rationally explain the tertiary deformation flow that accounts for most of the permanent deformation under increased highway loading conditions (20).

2.3.1 Flow number calculation

As the flow number issued to indicate the beginning of the tertiary stage of permanent deformation in asphalt mixes, the development of a repeatable and stable method for its determination becomes necessary. It is needed not only to establish its use as a mix characterization parameter by itself, but also as a potential procedure to unify the way the parameters from the rutting prediction model are determined, and hence make them more practical for mix characterization purposes. The most widely used methods to

determine the flow number from the cumulated permanent deformation versus loading cycle number are discussed in the following sections.

2.3.1.1 Moving average method

The first procedure used for determining the FN consisted of calculating the rate of variation in permanent strain directly from the data (numerical differentiation), and then finding the number of cycles corresponding to the minimum slope value. Some type of smoothing procedure is usually applied to the calculated slopes before determining FN (usually a moving average re-calculation), but there is not a widely accepted standard regarding this procedure (17).

The proposed method to determine FN during the SPT procedure, included in appendix D of NCHRP Report 513 (21), indicates that the strain rate for the current load cycle (Ni) is calculated as the difference between the permanent strain recorded for the adjacent cycles (N_{i+1} and N_{i-1}, respectively), and then divided by twice the sampling interval (ΔN), as shown in Equation 2.7.

$$\frac{\delta(\varepsilon_p)_i}{\delta N} = \frac{\left(\varepsilon_{pN_{i+1}} - \varepsilon_{pN_{i-1}}\right)}{2\Delta N} \tag{2.7}$$

After the strain rate has been calculated for all load repetitions, it is then smoothed by running a five point moving average for each load cycle. FN is then defined as the load cycle at which the minimum value of the smoothed creep rate occurs. It is important to note that if more than one point share the minimum strain rate, the first

minimum is the one reported as FN (21). However, one low data point could result in a misleading flow number value and this problem was discovered by several researchers (17, 20,22), which in turn constitutes the main limitation of this method.

2.3.1.2 Three-stage method

The three-stage permanent deformation method is used to determine the primary, secondary, and tertiary deformation stages in the flow number test (23). The method consists of first determining the initial point of the secondary stage using the power-law model to fit the curve with a deviation (D_e < 3%), as given in Equation 2.8. Then, a linear regression model is used to obtain the flow number by evaluating the absolute ratio (Rd < 1%) of the model's intercept to the current maximum adjusted cumulative permanent deformation, as shown in Equation 2.9. Finally an exponential model is used to characterize the tertiary stage, and thus the FN is defined as the maximum number of cycles of the secondary stage with an Rd less than 1%.

$$D_e = \frac{|\varepsilon_{p\ Measured} - \varepsilon_{p\ Predicted}|}{\varepsilon_{p\ Measured}} \times 100\% \quad (2.8)$$

$$R_d = \frac{d}{\varepsilon_p} \times 100\% \quad (2.9)$$

where D_e is the deviation of the predicted permanent strain from the power model to the measured data, d is the intercept of the linear regression, and R_d, is the absolute ratio of d to the current maximum ε_p.

Zhou et al. demonstrated the validity of this calculation method through repeated loat test results from seven different field mixes. The field performance matched with the results obtained from the FN test; thus demonstrating the proposed method reliability (23).

2.3.1.3 Stepwise increase approach

The stepwise increase approach consists of obtaining the minimum point of the permanent strain divided by the loading cycle number (ε_p/N) versus the cycle number (N). In addition, Goh et al. (22) suggest minimizing the flow number calculation error by smoothing the cumulative permanent strain curve through a modification of the entire non-uniform discontinuous data points and shifting each point forward along the x-axis (cycle number) and not changing the strain level to provide a stepwise increasing trend, as shown in Figure 8. In other words, the FN is determined as the minimum point of εp/N versus load cycle number using the new modified data points.

Goh et al found that the flow number results from this new, but simple method is consistent compared to other methods for determining the flow number (22). In order to verify the applicability of his method, the researchers compared their results with the Three-stage Method. An R-square of 0.9693 was found from the comparison, validating this method and providing a more practical and easier approach to compute the flow number.

2.3.1.4 Francken method

The Francken method was developed based on triaxial repeated load tests under various temperatures and stress levels and is a combination of a power law function with an added exponential function (24). The model is obtained through a complex regression mathematical model as shown in Equation 2.10.

$$\varepsilon_p(N) = AN^B + C(e^{DN} - 1) \tag{2.10}$$

where ε_P is the axial permanent deformation or permanent strain from FN test, N is the number of loading cycles, and A, B, C, D are the regression constants.

Once the regression constants are obtained, the first derivative of Equation 2.10 with respect to N is obtained, as shown in Equation 2.11, to generate the strain rate.

$$\frac{\delta\varepsilon_p(N)}{\delta N} = \left(A \cdot B \cdot N^{(B-1)}\right) + (C \cdot D \cdot e^{DN}) \tag{2.11}$$

Finally, the second derivative of the Francken model is then computed at each cycle to obtain the rate of change of the slope of permanent strain as presented in Equation 2.12. The cycle number at which the tertiary stage is reached, FN, is then computed at the point where the rate of change of slope changes sign (goes from negative to positive). This point indicates the inflection point in the permanent strain versus number of cycle's curve where the tertiary stage begins.

$$\frac{\delta^2 \varepsilon_p(N)}{\delta N^2} = A \cdot B \cdot (B-1) N^{(B-2)} + (C \cdot D^2 \cdot e^{DN}) \quad (2.12)$$

It is important to note that in the Francken model the regression constant C indicates whether tertiary flow has occurred or not. In addition, the Francken model provides a good representation of all three stages of deformation (i.e. flow) including the tertiary stage (20). Figure 9 shows the Francken model fitted to typical repeated load test data.

Dongre et al. (25) validated the Francken model through a series of 1053 FN test on field mixes. It was found that most of the fits produced less than or equal to 0.01% sum of square error (SSE) between the measured and Francken model fitted data. The researcher probed that the Francken method was successfully able to fit all 1053 curves with acceptable SSE.

2.3.2 Stress conditions

The flow number test consists of subjecting an HMA specimen at a specified temperature to a repeated loading and unloading process so that the cumulative permanent deformation is recorded as a function of number of load cycles and numerically differentiated to calculate the FN.

The newly proposed provisional AASHTO standard test method for determining the flow number of HMA mixtures does not specify the magnitude of the deviator and confining stresses to be used for testing. The applied deviator and confining stresses in the FN test are intended to duplicate the state of stresses generated in the pavement under given environmental and loading conditions. In other words, the FN test is intended to

simulate the actual field conditions by subjecting the HMA specimen to deviator and confining stresses similar to the ones encountered in the asphalt pavement layer.

In 2001 the first attempt to provide standard conditions to be used in the FN test was done by Witczak et al *(26)*. In their research, they suggested the use of a test temperature of 100ºF (37.8ºC) or 130ºF (57.4ºC), and a 10 (68.9), 20 (137.9), or 30 (206.8) psi (kPa) deviator stress under unconfined conditions. The lack of confinement limited the applicability of the data to actual field conditions.

Zhou et al, determined the transition points and paramenter of the three-stage permenant deformation model through a series of repeated load test using a compression load in the form of haversine wave with a stress level of 20 psi (138 kPa) at a temperature of 104ºF (40ºC). In addition, the tests were conducted for 20,000 load cycles or until a large deformation caused the linear variable differential transformer to go out of range. The obtained analysis results validated the proposed algorithm for seven different mixes (23).

Biligrini et a, used in their FN tests a range of temperatures from 90 to 130ºF (32.2 to 54.4ºC) under both unconfined and confined state of stresses. The selection of the stresses was done for a wide range of magnitudes so that the assessed conditions would match to the field performance. Thus, for the unconfined testing the deviator stress levels ranged from 10 to 150 psi, whereas for the confined testing the deviator stress levels were from 150 to 450 psi with one confinement stress level. The results obtained throughout the wide range of stress levels were used to recommend a new comprehensive mathematical model to accurately determine the FN (20).

Currently, no standard testing conditions for the magnitude of the deviator and confining stresses have been specified. However, an unconfined test with a deviator stress of 87 psi (600 kPa) has been recommended in the NCHRP 9-33 project for the HMA mix design manual. The recommended deviator stress level is analogous to the load used in the Superpave gyratory compactor. Dongre et al (25) used this stress level in their study to validate the Francken model. They tested 1053 samples at the effective pavement temperature for different field locations and were successfully able to find the FN.

2.3.3 Rut depth prediction

The flow number test for asphalt mixtures was one of the final three tests selected for further evaluation from the twenty-four test/material properties initially examined under the NCHRP 9-19 project. The selection of the FN test as one of the final candidates was based on an extensive study of the laboratory measured FN and observed rutting at three field studies: Westrack, MnRoad, and the FHWA ALF test facility. In all of these three test sites it was found that the FN was highly correlated to field rut depth (within the asphalt layer) at any particular traffic level (2).

NCHRP Report 580 (27) provides based on research conducted by Sullivan in 2002 (28) the guidelines to predict the rut depth of a HMA pavement from the RLT results. The aforementioned three test site samples selected from NCHRP Project 9-19 were used to calibrate and optimize the proposed shifting procedure. FHWA-Accelerated Loading Facility (ALF), WesTrack, and MnRoad mixes were chosen to optimize the

results for both confined and unconfined testing. Sullivan suggested the following seven steps and associated equations to get field rut depth by using results from unconfined repeated load tests:

- Step 1: Determine the effective field temperature (T_{eff} °F).
- Step 2: Determine the flow number (FN) and plastic strain at failure (ε_{pf}) at any temperature (T_t °F) and stress level (σ)
- Step 3: Perform the stress shifting and determine the flow number in reference stress (FN_r) with the Equation 2.13 and Equation 2.14.

$$\delta = \frac{\left(e^{\log(FN)0.289212-0.71385}+1\right)Log(\sigma)-4.34383}{-1.30118+\left(e^{\log(FN)0.289212-0.71385}+1\right)} \quad (2.13)$$

$$log(FN) = \frac{\ln\left(\frac{-1.30118(\delta)+4.34383}{\log(\sigma_1)-\delta}-1\right)+0.71385}{0.289212} \quad (2.14)$$

- Step 4: Perform temperature shifting and determine the reduced flow number at field temperature (FN_R). Using the E* testing results, the polynomial constant of the temperature shift equation are presented in Equation 2.15.

$$(\alpha)T = aT^2 + bT + c \quad (2.15)$$

Since the mixture was tested at T_t in °F, the E* shift factors, which were determined at a reference temperature of 70°F, need to be further shifted to the reference temperature. The flow number shift factor is determined from the E* shift factor using Equation 2.16.

$$(\alpha)T_{FN} = 0.0423((\alpha(T))^2) + 0.8367\alpha(T) \quad (2.16)$$

Then the FN is converted to the reduced flow number at the effective field pavement temperature (FN_R) by using Equation 2.17.

$$\log(FN_R) = \log(FN) - \log(\alpha(T)) \quad (2.17)$$

Step 5: Determine the ε_{pf}-reduced flow number (FNε) by Equation 2.18:

$$\log(FN_\varepsilon) = \log(FN) - 2.29\log(\varepsilon_{pf}) \quad (2.18)$$

Step 6: Determine the rut depth at 1 million ESALs (corresponding to the εpf-reduced flow number) using Equation 2.19:

$$\log(Rut_{1,000,000}) = -0.6523\log(FN_\varepsilon) + 3.9426 \quad (2.19)$$

Step 7: Determine the rut depth at any desired Equivalent Single Axle Loads (ESALs) using Equation 2.20:

$$\log(Rut) = \log(Rut_{1,000,000}) - 0.002\,(\log(\text{ESAL}))^2 + 0.2815(\log(ESAL)) - 1.6079 \quad (2.19)$$

As it is presented in the NCHRP Report 580, the flow number not only is useful to indicate the start of the tertiary stage of permanent deformation in asphalt mixes, but also provides the required parameters to accurately predict the field rut depth based on mechanistic and fundamental laboratory test and regression data. Thus, the validity and enormous potential of this performance test is once again demonstrated.

To calculate the effective pavement temperature required in step 1, El-Basyouny et al (29) developed an new model to determine a single test temperature at which permanent deformation within a given pavement system, would be equivalent to that which occur from the seasonal temperature fluctuation throughout the annual temperature cycle. The newly revised model is presented in Equation 2.20. In addition, the researchers compared the results obtained using the model with various environmental locations across the nation showing the reasonableness and soundness of the developed T_{eff} model.

$$T_{eff} = 14.62 - 3.361Ln(Freq) - 10.940(z) + 1.121(MAAT) + 1.718(\sigma MAAT) - 0.431(Wind) + 0.333(Sunshine) + 0.08(Rain) \quad (2.20)$$

where Freq is the traffic-induced loading frequency in Hz, z is the critical depth in inches, MAAT is the Mean Annual Air Temperature of the location under study, in ºF, σMAAT is the deviation of the mean monthly air temperature, Wind is the Mean Annual Wind Speed in mph, Sunshine is the Mean Annual Percentage Sunshine.

CHAPTER 3 – STRESS STATE FOR MATERIAL CHARACTERIZATION

The proposed research approach requires a reliable determination of the stress state for material characterization as part of the computation of pavement responses due to traffic-induced loads and imposed environmental conditions. This is essential for a successful mechanistic pavement analysis and for the development of realistic performance-based material specifications. In particular, it is highly important that the effect of temperature and time dependency of viscoelastic materials such as HMA must be considered in any modeling process.

The mechanistic-empirical design method is based on the principle of mechanics of materials that relates an input, such as a traffic-induced loading, to an output or pavement response, such as deformations. The response values are used to predict distress based on laboratory test and field performance data. On the other hand, in order to determine the combination of critical conditions imposed by traffic and the environment to the pavements, it is mandatory to investigate the best approach to characterize materials behavior.

3.1 STRESS INVARIANTS IN PAVEMENTS

Computation of the stress state in a pavement section under a traffic load is an essential step in any rut-depth predictive methodology. The use of a suitable mathematical model of the pavement system and realistic material properties are

required. In order to achieve the greatest consistency in the modeling process, the computed stress state in the pavement needs to be appropriately duplicated in the laboratory testing of the HMA mixtures.

Brown and Bell (30) suggested the use of stress invariants as the most appropriate method of comparing the stress states that affect material behavior and characterization. In addition, they state that the use of stress invariants is particularly advantageous when considering the tension zone in the bottom of bituminous layers and for predicting rutting away from the axis of symmetry of loading.

As indicated by their names, the stress invariant values are the same regardless of the orientation of the coordinate system chosen. For example, the first invariant of stress tensor ($\bar{I}_1$) is the sum of the normal stresses and the second invariant of deviatoric stress tensor ($\bar{I}_{2D}$) is related to shear stress. The octahedral normal and shear stresses (i.e. σ_{oct} and τ_{oct}) at any point within the pavement structure are related to the stress invariants as shown in Equations 3.1 and 3.2, and therefore they are also invariants. These octahedral stress components in terms of principal stresses are:

$$\sigma_{oct} = \frac{1}{3}(\sigma_1 + \sigma_2 + \sigma_3) = \frac{1}{3}\bar{I}_1 \tag{3.1}$$

$$|\tau_{oct}| = \frac{1}{3}\sqrt{(\sigma_1 - \sigma_2)^2 + (\sigma_2 - \sigma_3)^2 + (\sigma_3 - \sigma_1)^2} = \sqrt{\frac{2}{3}\bar{I}_{2D}} \tag{3.2}$$

where σ_1, σ_2, and σ_3 are the principal stresses existing at the point of interest in the HMA layer. Equations 3.1 and 3.2 show that the same $\bar{I}_1$ and $\bar{I}_{2D}$ can be achieved with different combinations of principal stresses.

The octahedral normal and shear stresses are used to convert the stress tensor observed in the HMA layer under moving dynamic loads to deviator and confining stresses in a repeated load triaxial testing set-up (i.e. flow number test (FN)). In the laboratory, the triaxial condition is achieved by applying a static all around confining stress using compressed air and a repeated deviator vertical stress using an axial actuator to a 4-inch diameter by 6-inch high cylindrical HMA sample. The deviator stress, σ_d, and the confining stress, i.e., $\sigma_c = \sigma_2 = \sigma_3$, under triaxial conditions can be written as a function of the octahedral stress components as presented in Equation 3.3 and 3.4, as follows:

$$\sigma_d = \frac{3}{\sqrt{2}}|\tau_{oct}| \tag{3.3}$$

$$\sigma_c = \sigma_3 = \sigma_2 = \sigma_{oct} - \frac{\sigma_d}{3} \tag{3.4}$$

Equations 3.3 and 3.4 show that the magnitude of the deviator and confining stresses in the triaxial test can be evaluated from the octahedral stresses generated in the HMA layer under a moving traffic load. Therefore, in order to define the magnitude of the deviator and confining stresses in the triaxial test for FN, a comprehensive database of traffic-induced pavement stresses was generated to represent the magnitude of the octahedral stresses in HMA layers.

3.2 DATABASE OF PAVEMENT STRESSES TIME-HISTORY

The pavement stresses time history database was generated by conducting a mechanistic analysis of three HMA pavement structures subjected to moving traffic-

induced loads at various speeds and under braking and non-braking conditions using the 3D-Move model (7). The pavement responses from the 3D-Move model were analyzed to identify the magnitude of the octahedral stresses throughout the HMA layer. The following presents the conditions and evaluation steps used in the response computations:

- Pavement geometry:
  - 4" HMA over 6" base
  - 6" HMA over 8" base
  - 8" HMA over 10" base
- Vehicle speeds:
  - 60 mph without braking
  - 40 mph without braking
  - 20 mph with and without braking
  - 2 mph with braking
  -
- Loaded area and pressure distribution:
  - Circular uniform
- HMA mixtures:
  - One aggregate source: Lockwood (andesite)
  - Intermediate Superpave gradation with 12.5 mm nominal max size
  - Three asphalt binder grades: PG52-22, PG58-22, PG64-22
- HMA layer temperatures:
  - 40°C, 50°C, 60°C, and 70°C
- Conduct Superpave mix designs for the three mixtures for 6 millions ESALs.
- Measure the dynamic modulus (|E*|) Master Curves for all three mixtures.
- Use the measured properties of the HMA mixtures in the 3D-Moving Load analyses (3D-Move).

- Use a modulus of 35,000 psi and 15,000 psi for the base and subgrade, respectively.
- Use the 18-wheeler truck configuration with 125 psi tire inflation pressure.
- Evaluate the stress time-histories within the HMA layer at a depth of 2" from the surface in the HMA layer.
- Analyze the computed pavement response data to identify the magnitude of the deviator and confining stresses.

3.3 DESCRIPTION OF THE 3D-MOVE MODEL

The computer code 3D-Moving Load Analysis (3D-Move) utilizes a continuum-based "finite-layer" approach to evaluate the response of a layered medium subjected to a moving surface load (7). The pavement system is characterized through a combination of viscoelastic (for the HMA layer) and elastic (for the base and subgrade) horizontal layers with each layer characterized using a set of uniform properties that rest on a rigid impermeable layer.

The finite-layer approach treats each pavement layer as a continuum and uses the Fourier transform technique to handle complex surface loadings in all three directions (vertical, longitudinal, and transverse). The 3D-Move model incorporates important pavement response factors such as the moving traffic-induced complex 3D contact stress distributions (normal and shear) of any shape, vehicle speed, viscoelastic material characterization for the pavement layers, and non-uniform interface shear stresses caused by braking and turning forces. In addition, rate-dependent material properties (viscoelastic) can be accommodated, thus pavement response as a function of vehicle speed can be studied.

Since Fourier transform technique along with frequency-domain solutions are adopted, the approach allows for the direct use of the frequency sweep test data of HMA mixture in the analysis. In addition, many attempts that included field calibrations (e.g. Penn State University test track, MnRoad, and University of Nevada-Reno UNR Off-road Vehicle study) that compared a variety of independently-measured pavement responses (stresses, strains, and displacements) with those computed have been reported in the literature (7, 31, and 32). These verification studies have validated the applicability and versatility of the approach.

A verification of this model using existing analytical solutions (ELSYM5) and laboratory test results has shown that the 3D-Move program is capable of simulating correctly the static circular loads applied to a layered system (7). In other studies, Siddharthan at al. evaluated strain histories from two different pavements, representing a thin and a thick structure as subjected to loading from a moving tandem axle (7,33).

The 3D-Move analysis was used in conjunction with the dynamic modulus (|E*|) and internal damping (ζ_{AC}), that were measured in the laboratory on the various mixes. The analysis was undertaken to calculate the responses of the various mixes in the pavements as a function of vehicle speed and pavement temperature. The analysis considers a three layers pavement consisting of an HMA layer on top of a crushed aggregate base and the natural subgrade

3.4 LOAD DISTRIBUTION OF AN EIGHTEEN-WHEEL TRUCK

The first step of the mechanistic pavement response analysis is to estimate the load distributions on various tires of the 18-wheel tractor-semitrailer during normal

highway traffic and during braking. Braking causes the vehicle to decelerate and the loads to transfer to the front of the vehicle. In comparison with a two-axle vehicle, the braking characteristics of a tractor-semitrailer are significantly more complex. For a given two-axle vehicle, the load transfer is only a function of the deceleration rate, whereas for a tractor-semitrailer, the load transfer during braking is dependent not only on the deceleration rate, but also on the braking force of the semitrailer.

Braking causes the vehicle to decelerate, which causes load to transfer to the front of the vehicle. The resulting axle load can be higher or lower than the initial static load, depending on the location of the axle. Figure 10 shows the major forces acting on an eighteen-wheel tractor-semitrailer during braking on a downward sloping pavement. Since braking are the primary source of deceleration, the aerodynamic drag and rolling resistance are neglected in this study. In addition, since the typical highway slope is around 4%, the resulting truck tire loads doesn't significantly change, thus the effect of the truck going upwards or downwards is also neglected in this study.

The various axles include; the tractor steering axle, the tractor tandem axle (i.e. driving axle), and the semitrailer tandem axle (i.e. trailer axle). In this study, the tandem axles of the tractor and the semitrailer are considered without equalization, implying that an interaxle load transfer will take place between the rear and the front axle of the tandem group during the braking period of the truck (34).

In order to calculate the normal load on each axle, the tractor and the semitrailer unit are considered as free bodies separately and combined. All the braking conditions equations presented in this study are based on Hajj (35) with a road slope angle equal to zero. In addition, the dimensional parameters used to describe the vehicle in this analysis

are summarized in. Axle and group spacing are chosen according to ASTM E 1572-93 standard (36).

The vertical, horizontal, and moment equilibrium equations for the tractor, semitrailer unit, and tractor-semitrailer combination are written as a function of truck loads and truck geometry resulting in a total of eleven equilibrium equations, three characteristic equations, and fourteen unknowns.

For the tractor, the vertical and horizontal equilibrium are given by Equations 3.5 and 3.6, respectively. The moment equilibrium around the rear and front tandem axle are given by Equations 3.7 and 3.8, respectively.

$$W_s + W_{d_1} + W_{d_2} = W_1 + W_{h_2} \tag{3.5}$$

$$F_s + F_{d_1} + F_{d_2} = \frac{a}{g} W_1 + F_{h_2} \tag{3.6}$$

$$W_s \left(L_1 + \frac{c}{2}\right) + W_{d_1} c = \frac{a}{g} W_1 h_1 + W_1 \left(L_1 + \frac{c}{2} - l_1\right) + F_{h_1} h_3 + W_{h_1} \left(\frac{c}{2} + d_1\right) \tag{3.7}$$

$$W_s \left(L_1 - \frac{c}{2}\right) + W_{h_1} \left(\frac{c}{2} - d_1\right) = \frac{a}{g} W_1 h_1 + W_1 \left(L_1 + \frac{c}{2} - l_1\right) + F_{h_1} h_3 + W_{d_2} \tag{3.8}$$

For the semitrailer unit, the vertical and horizontal equilibrium are given by Equations 3.9 and 3.10, respectively. The moment equilibrium around the front support point of the semitrailer and the trailer rear axle are given by Equations 3.11 and 3.12, respectively.

$$W_{t_1} + W_{t_2} + W_{h_1} = W_2 \tag{3.9}$$

$$F_{t_1} + F_{t_2} + F_{h_1} = \frac{a}{g} W_2 \tag{3.9}$$

$$W_2 + d_2 + F_{h_1} h_3 = \frac{a}{g} W_2 h_2 + W_{t_1} \left(L_2 - \frac{c'}{2} + d_1 \right) + W_{t_2} \left(L_2 + \frac{c'}{2} + d_1 \right) \tag{3.10}$$

$$W_{h_1} \left(L_2 + \frac{c'}{2} + d_1 \right) + F_{h_1} h_3 + W_{t_1} c' = \frac{a}{g} W_2 h_2 + W_2 \left(d_1 + L_2 + \frac{c'}{2} - d_2 \right) \tag{3.11}$$

For the tractor-semitrailer combination, the vertical and horizontal equilibrium are given by Equations 3.12 and 3.13, respectively. The moment equilibrium around the steering axle is given by Equation 3.14.

$$W_s + W_{d_1} + W_{d_2} + W_{t_1} + W_{t_2} = W_1 + W_2 \tag{3.12}$$

$$F_s + F_{d_1} + F_{d_2} + F_{t_1} + F_{t_2} = \frac{a}{g} (W_1 + W_2) \tag{3.13}$$

$$W_1 l_1 + (L_1 + d_2 - d_1) = \frac{a}{g} W_1 h_1 + \frac{a}{g} W_2 W_1 + W_{d_1} \left(L_1 - \frac{c}{2} \right) + W_{d_2} \left(L_1 + \frac{c}{2} \right) + W_{t_1} \left(L_1 + L_2 - \frac{c'}{2} \right) + W_{t_2} \left(L_1 + L_2 + \frac{c'}{2} \right) \tag{3.14}$$

W_{h_i} and F_{h_i} are the vertical and horizontal load respectively at the tractor-semitrailer articulation, "a" is the linear deceleration of the truck along the longitudinal axis, g is the deceleration due to gravity, W_1 and W_2 are the tractor and semitrailer total weights, respectively. W_s, W_{d1}, W_{d2}, W_{t1} and W_{t2}, are the normal tires loads. F_s, F_{d1}, F_{d2}, F_{t1} and F_{t2}, are the braking forces that originate from the brake system and develop on the tire-road interface.

From the above equations, the normal loads on the various axles can be expressed as follows:

Tractor front axle (steering axle):

$$W_s = W_2 \frac{\left[\frac{a}{g}(h_2 d_1 + h_3 L_2) + d_1(L_2 + d_1 - d_2)\right]}{L_1(L_2 + d_1)} + W_1 \frac{\left[\frac{a}{g} h_1 + (L_1 - l_1)\right]}{L_1} - \left(F_{t_1} + F_{t_2}\right) \frac{h_3 L_2}{L_1(L_2 + d_1)} - \left(W_{t_1} - W_{t_2}\right) \frac{c\prime d_1}{2L_1(L_2 + d_1)} - \left(W_{d_1} - W_{d_2}\right) \frac{c}{2L_1} \quad (3.15)$$

Tractor rear axles (driving axles) are shown in Equation 3.16, 317 and 3.18.

$$W_d = W_{d_1} + W_{d_2} = W_2 \frac{\left[\frac{a}{g}\left((h_2 d_1 - h_2 L_1) + h_3(L_1 + L_2)\right) + (d_1 - L_1)(L_2 + d_1 - d_2)\right]}{L_1(L_2 + d_1)} - W_1 \frac{\left[\frac{a}{g} h_1 - l_1\right]}{L_1} + \left(F_{t_1} + F_{t_2}\right) \frac{h_3(L_1 + L_2)}{L_1(L_2 + d_1)} \left(W_{t_1} - W_{t_2}\right) \frac{c\prime(L_1 - d_1)}{2L_1(L_2 + d_1)} \left(W_{d_1} - W_{d_2}\right) \frac{c}{2L_1} \quad (3.16)$$

$$W_{d_1} = W_1 \frac{\left[-\frac{a}{g}(h_3 - h_1) + (L_1 + l_1 - d_1)\right]}{c} + \left(F_s + F_{d_1} + F_{d_2}\right) \frac{h_3}{c} - W_s \frac{(L_1 - d_1)}{c} + W_d \frac{\left(d_1 + \frac{c}{2}\right)}{c} \quad (3.17)$$

$$W_{d_2} = W_1 \frac{\left[\frac{a}{g}(h_3 - h_1) - (L_1 - l_1 - d_1)\right]}{c} + \left(F_s + F_{d_1} + F_{d_2}\right) \frac{h_3}{c} + W_s \frac{(L_1 - d_1)}{c} + W_d \frac{\left(\frac{c}{2} - d_1\right)}{c} \quad (3.18)$$

Semitrailer axles (trailer axles) are presented in Equations 3.19, 3.20 and 3.21.

$$W_t = W_{t_1} + W_{t_2} = W_2 \frac{\left[-\frac{a}{g}(h_2 - h_3) + d_2\right]}{(L_2 + d_1)} - \left(F_{t_1} + F_{t_2}\right) \frac{h_3}{(L_2 + d_1)} + \left(W_{t_1} - W_{t_2}\right) \frac{c\prime d_1}{2(L_2 + d_1)} \quad (3.19)$$

$$W_{t_1} = W_2 \frac{\left[\frac{a}{g}(h_2 - h_3) - d_2\right]}{c\prime} + W_t \frac{\left(L_2 + d_1 + \frac{c\prime}{2}\right)}{c\prime} + \left(F_{t_1} + F_{t_2}\right) \frac{h_3}{c\prime} \quad (3.20)$$

$$W_{t_2} = W_2 \frac{\left[-\frac{a}{g}(h_2 - h_3) + d_2\right]}{c\prime} - W_t \frac{\left(L_2 + d_1 - \frac{c\prime}{2}\right)}{c\prime} - \left(F_{t_1} + F_{t_2}\right)\frac{h_3}{c\prime} \quad (3.21)$$

The calculation of the normal loads on the various axles of the downward braking eighteen-wheel truck requires the following characteristic properties be specified (35):

- Application (treadle) versus actuation (chamber) pressure at each axle: the application pressure is defined as the pressure produced at the output of the treadle valve, whereas the actuation pressure is the pressure experienced at the brake chamber. In the case where some sort of proportioning valve is used, these two pressures will differ significantly (37, 38).

- Brake force versus actuation pressure for the brakes on each axle: the braking force developed at the tire-road interface is determined by the actuation pressure applied to each brake and the gain of each (37, 38).

The braking force on individual wheels can be described by the following equation:

$$F_b = \frac{T_b}{r} = G\frac{P_{ac}}{r} \quad (3.22)$$

where F_b = Brake force (lb)
T_b = Brake torque (in-lb)
r = Tire rolling radius (inch)
G = Brake gain (in-lb/psi)
P_{ac} = Actuation pressure (psi)

The braking system properties of a standard United States (U.S.) eighteen-wheel truck used in this study are taken from a National Highway Traffic Safety Administration (NHTSA) report that was conducted by T. D. Gillespie et al. (38). The NHTSA study considered a linear brake system (i.e. linear relationship between the application and the actuation pressure). Table 2 summarizes the brake system properties of the U.S. eighteen-wheel.

The extent to which vertical load is transferred during braking from the rear tandem tires to the front tandem tires is called the dynamic load transfer coefficient (α) as shown in Equation 3.23. In addition, the load transfer coefficient has a value of 0.0 when the loads on the front and rear tandem tires are equal (i.e. $W_{t_1} = W_{t_2}$; $W_{d_1} = W_{d_2}$).

$$\alpha = \frac{W_{t_1} - W_{t_2}}{2(F_{t_1} + F_{t_2})} = \frac{W_{d_1} - W_{d_2}}{2(F_{d_1} + F_{d_2})} \tag{3.23}$$

Hajj (35) verified that the aforementioned equations against NHSTA data for the case of a level road. Based on this comparison, the author concluded that the equations of force presented in this study can be accurately used to predict the load distributions of an eighteen-wheel tractor-semitrailer vehicle on sloped and level roads.

A constant deceleration of 0.54g was used in this study. This deceleration is the rate that is required for a truck running at 40 mph to come to a complete stop in a distance of 100 feet. This deceleration rate is achieved for a treadle pressure of 80 psi (35).

The load distributions on the various axles of the fully loaded 18-wheel tractor-trailer combination are needed under the non-braking and braking conditions. Table 3 summarizes the load distributions on the various axles of the 18-wheel tractor-trailer combination with and without braking. Braking forces at each tire were included as interface shear stresses with their distribution estimated by multiplying the vertical stress by a coefficient of friction, which is the ratio between the horizontal and vertical loads.

The braking phenomenon resulted in a vertical load on the steering axle (8,489 lb/tire) exceeding the tire load for the non-braking condition (6,000 lb/tire) by about 40 percent. The vertical load on the rear tire (2,161 lb/tire) of the trailer-tandem axle configuration was 33 percent lower than the corresponding tire load for the non-braking condition (4,250 lb/tire).

3.5 MATERIAL PROPERTIES CHARACTERIZATIONS

Pavement performance is highly affected by the material properties and how the imposed loading and environmental conditions influence its behavior. Dynamic response of HMA pavements under moving traffic-induced loads is a major component for accurate prediction of rutting performance on flexible pavements. Due to the frequency-dependent properties of the HMA layer, advanced material characterization and mechanistic theories must be used in order to closely simulate the actual field conditions.

Extensive mechanistic analyses of three different asphalt pavement structures subjected to moving traffic loads at various speeds and under braking and non-braking conditions were conducted. Therefore, a comprehensive material characterization for the HMA layer was necessary. All mixtures were designed following the Superpave volumetric mix design method with a medium traffic level that is equivalent to 3–10 millions equivalent single axle loads (ESAL). In addition, the aggregates for this study were sampled from the Lockwood quarry located approximately 10 miles east of Reno. Figure 11 shows the gradation used in this analysis. The same aggregate source and

gradation were used for all mixtures. The asphalt binders were supplied by Paramount Petroleum Corporation, Fernley, Nevada.

Three different HMA mixtures were analyzed in this research consisted of an intermediate Superpave gradation with a nominal maximum aggregate size of ½ inch. Optimum binder contents of 5.85, 5.46, and 5.61 percent were determined for the PG64-22, PG58-22, and the PG52-22 mixtures, respectively. In addition, the three mixture's design properties are shown in Table 4, Table 5, and Table 6.

The dynamic modulus (|E*|) is the primary material property of HMA mixes that is used in structural pavement design and analysis. Due to the viscoelastic behavior of the HMA pavement, this property varies with temperature and frequency of loading. The dynamic modulus test (AASHTO TP62, 2008) was used to develop the dynamic modulus master curve of the various HMA mixes. A sinusoidal (Haversine) axial compressive stress is applied to a specimen at a given temperature and loading frequency. The applied stress and the resulting recoverable axial strain response of the specimen at different temperatures and frequencies are measured and used to calculate the complex dynamic modulus. The dynamic modulus (|E*|) is the absolute value of the complex modulus (E*) which is actually the summation of two components as seen in Equation 3.24: (1) the storage or elastic modulus component (E') and (2) the loss or viscous modulus (E"). The angle φ in Equation 3.24 is defined as the phase angle which is experimentally determined from the lag between the peak strain and the peak stress.

$$E^* = \frac{\sigma}{\varepsilon} = \frac{\sigma_0 sin\omega t}{\varepsilon_0 (sin\omega t - \emptyset)} = |E^*|\cos\varphi + i|E^*|\sin\varphi = E' + iE'' \quad (3.24)$$

where, E* is the complex dynamic modulus, E' is the storage modulus, E" the loss modulus, σ_0 = peak (amplitude) stress, ε_0 = peak (amplitude) strain, ϕ = phase lag, in degrees, ω = angular velocity in radian per second, and t is the time, seconds.

Mathematically, the absolute value of the complex dynamic modulus is defined as the maximum (peak) dynamic stress (σ_o) divided by the recoverable axial strain (ε_o) as shown in Equation 3.25.

$$|E^*| = \frac{\sigma_0}{\varepsilon_0} \tag{3.25}$$

The dynamic modulus master curves are represented by the sigmoidal function presented in Equation 3.25. The sigmoidal function describes the time dependency of the modulus at the reference temperature. In addition, the shift factors are required to shift the reduced frequency from the reference temperature to any temperature of interest. Also the shift factors describe the temperature dependency of the modulus, as presented in Equations 3.26 and 3.27.

$$\log(E^*) = \delta + \frac{\alpha}{1+e^{\beta+\gamma\log(t_r)}} \tag{3.26}$$

$$t_r = \frac{t}{a(T)} \tag{3.27}$$

$$log(t_r) = \log(t) - log[a(T)] \tag{3.28}$$

where, t_r = time of loading at the reference temperature, α, δ = fitting parameters for a given set of data, δ represents the minimum value of E*, and α + δ represents the

maximum value of E*, β + γ = parameters describing the shape of the sigmoidal function, a(T) = shift factor as a function of temperatures, T = temperature of interest, and t = time of loading at a given temperature of interest.

Prior to shifting the mixture data, the relationship between asphalt binder viscosity and temperature must be established. This is done by first converting the binder stiffness data at each temperature to viscosity using Equation 3.29. The binder complex modulus and phase angle data are determined over a range of temperature for a loading of 1.59 Hz. (10 rad/sec) using the dynamic shear rheometer (DSR). The parameters of the ASTM VTS equation are found by linear regression of the Equation 3.30 after loglog transformation to the viscosity data and log transformation of the temperature data.

The regression parameters from Equation 3.30 are used to calculate the viscosity for any temperature. In addition, it is important to state that Equation 3.30 is not applicable at low temperatures and high rate of loading where the asphalt binder viscosity exceeds 2.7×10^{10} Poises. Figures 12 through 14 show the resulting A and VTS parameters for the binders used in this research.

$$\eta = \frac{G^*}{10}\left(\frac{1}{sin\delta}\right)^{4.8628} \tag{3.29}$$

$$loglog(\eta) = A + VTS\log(T_R) \tag{3.30}$$

where, η = viscosity, CPoise, G* = binder complex shear modulus, Pa, δ = binder phase angle, º, A = regression intercept, VTS = regression slope of viscosity temperature susceptibility, and T_R = temperature in Rankine at which the viscosity was determined.

The laboratory measured dynamic modulus test results are presented in Table 7, Table 8, and Table 9 for the PG64-22, PG58-22, and PG52-22 mix, respectively. The master curves is constructed using the principle of time temperature superposition of the material, selecting a reference temperature of 70 ºF (21 ºC) and then shifting data at various temperature with respect to time until the curves merges into a single smooth function. Figures 15-16 show the dynamic modulus master curves |E*| and the phase angle for the evaluated mixtures at the reference temperature of 21°C (70°F), respectively. A higher |E*| value was found for the PG64-22 mix, followed by the PG58-22 mix followed by the PG52-22 mix. In addition, the determined E' and E" at the appropriate HMA layer temperature are then used in the 3D-Move analysis.

The internal damping for the HMA layer was measured as a function of the loading frequency in the laboratory and it was included in the 3D-Move by writing the dynamic modulus (|E*|) in its complex form (39) as shown in Equation 3.31:

$$E^* = E\left(1 + 2i\zeta_{AC}\right) = E' + iE'' \tag{3.31}$$

in which, ζ_{AC} is the internal damping of the HMA, and |E*|, E', and E" are experimentally determined by the dynamic modulus test as a function of loading frequency, and are subsequently used to calculate ζ_{AC} using Equation 3.32.

$$\zeta_{AC} = \frac{E''}{2E'} = \frac{\tan(\varphi)}{2} \tag{3.32}$$

The 3D-Move model requires as an input the complex dynamic shear modulus, G*, either as an input or as part of the master curve. Therefore, it is necessary to express G* in terms of the complex dynamic modulus, (|E*|), as shown in Equations 3.33.

$$G^* = \frac{E^*}{2(1+\upsilon)} \tag{3.33}$$

In this research the base course and subgrade layers are treated as linear elastic materials with an elastic modulus of 35,000 psi and 15,000 psi, respectively. The internal damping of the unbound layers is assumed to be 5%. The Poisson's ratio was assumed to be 0.4 for all three layers.

3.6 STRUCTURAL ANALYSIS

Extensive mechanistic analyses of three different asphalt pavement structures subjected to moving traffic loads at various speeds and under braking and non-braking conditions were conducted using the 3D-Move model. The research analyzed three pavement structures: 4 inch HMA over 6 inch crushed aggregate base (CAB), 6 inch HMA over 8 inch CAB, and 8 inch HMA over 10 inch CAB subjected to a tractor-semitrailer combination (presented in Figure 10) moving on a leveled road with and without braking. Table 10 shows the physical properties of each pavement layer as well as the main characteristics of the pavement structures under analysis.

The traffic-induced load is modeled for a fully loaded 18-wheel truck having a steering axle, a driving and a trailer axle. The steering axle consists of a single axle

configuration with single tire, whereas the driving and trailer axles consist of a tandem axle configuration with dual tires. Table 3 shows the axle loads used in the analysis.

The analysis' axes are given as follows: the longitudinal direction X represents the traffic travel direction, Y is the transverse direction, and Z the vertical direction measured from the surface of the pavement. Because of the symmetry about the longitudinal centerline of the truck, only one-half of the 18-wheel truck is modeled. Figure 17 shows a pavement layer system (infinite in the horizontal direction but finite in the vertical direction) subjected to loads from a tractor-semitrailer.

The locations to compute pavement responses are inputted to the program 3D-Move. A total of 56, 70, and 84 output locations were included in the cases of steering axle loading for the 4, 6 and 8 inch HMA layer, respectively. In the case of driving and trailer axles loading a total of 48, 60, and 72 output locations were analyzed for the 4, 6 and 8 inch HMA layer, respectively. These locations were distributed within and outside the loaded areas, forming a grid in the plane parallel to the transverse Y-Z plane. Since this study is only interested in the rutting developed in the HMA layer, only the responses within the HMA layer were evaluated.

Pavement responses such as stresses, strains, and displacements were computed by the 3D-Move model as a function of time. The resulting pavement responses were analyzed to identify the time-history of the octahedral stresses throughout the HMA layer. Since rutting in the HMA layer is generally confined to the top 4 inches only, the responses at 2-inch below the pavement surface under the steering, driving tandem and trailer tandem axles were further evaluated in the analysis. This location was recommended by Epps et al. (40) based on WesTrack field tests. In addition, Chen et al.

(41) concluded that the top 2 inches of the HMA layer were critical for permanent deformation in their forensic evaluation of premature pavement failures in Texas.

The stress distribution at the tire-pavement interface is significantly affected by tire type, inflation pressure, and load. Previous studies showed that the stress distribution at the tire-pavement interface is not uniform, and it influences the HMA pavement resistance to rutting and fatigue failures (42, 43, 44, 45). Both the uniform and non-uniform stress distributions are currently under investigation at the University of Nevada, Reno, however, only the analyses for the uniform stress distributions with circular loaded areas are presented in this thesis

3.7 EQUIVALENT DEVIATOR AND CONFINIG STRESSES TIME-HISTORIES

For each mixture type (i.e. PG64-22, PG58-22 and PG52-22), the pavement normal stresses (σ_x, σ_y. σ_z., τ_{xy}, τ_{xz} and τ_{yz}) were calculated under the steering, driving and trailer tandem axles by the 3D-Move model at many points along a transverse line located at a depth of 2-inch below the pavement surface. The analysis were performed using the material properties described in Section 3.5 for all the combinations of truck speed, pavement effective temperature, pavement structure, mixture type, and braking and non-braking conditions. A total of 180 3D-Move runs were conducted for each axle type.

For the non-braking scenario, the driving and the trailer tandem axles imposed the same load onto the pavement (Table 3); hence the same analysis was used for both axles. It was found that the tandem axle of the analyzed truck generated a more critical stress

condition than the steering axle when the 3D state of stresses is analyzed. It is believed that the critical axle for rutting in the HMA layer is the one that generates high deviator stress coupled with low confining stress. It may be noted that when only the vertical compressive stress, σ_z, is taken into consideration, misleading conclusions may be drawn, this is mainly due to the fact that σ_z is higher in all cases for the steering axle loading. However when the 3D state of stresses is evaluated, it becomes clear that the more critical conditions are imposed by the tandem axles.

The maximum deviator and confining stresses along with the maximum vertical compressive stress are presented in Table 11-13 for the non-braking conditions and in Table 14-16 for the braking conditions. In addition, the differences between the stresses imposed by steering axle and the tandem axle are presented in the aforementioned tables.

For example for the PG64-22 mix, 6" HMA layer, 50ºC, and 40 mph the deviator stress under the tandem axle was only lower than that under the steering axle by 4 psi; while the confinement stress under the tandem axle was lower than that of the steering axle by 9 psi (more than double). Nonetheless, the vertical compressive stress for the steering axle is 4 psi higher than that for the tandem axle, which in turn could mislead the selection of the most critical axle for rutting analysis if the full 3D state of stresses is not evaluated. The aforementioned example is illustrated in Figures 18 and 19 for the non-braking and braking conditions, respectively. In the case of braking, it is clear that the deviator stress under the tandem axle was higher coupled with a lower confinement, as shown in Figure 19.

The principal stresses in the HMA layer were calculated under the driving tandem axles for braking and no braking conditions. In the case of braking, the driving tandem

axle was selected over the trailer axle due to the fact that the combination of front and rear axles is 1,210 lb higher than for the trailer axle. In addition, the imposed horizontal load per tire in the driving axle is 407 lb greater than in the trailer axle, as shown in Table 3.

By using Equations 3.1 and 3.2 the octahedral stress components were evaluated at the aforementioned locations. The octahedral normal and shear stresses are used to convert the stress tensor observed in the HMA layer under moving dynamic loads to deviator and confining stresses in a repeated load triaxial testing set-up in the laboratory (i.e. flow number test). Subsequently, the corresponding deviator and confining stresses were determined using Equations 3.3 and 3.4. The location where the maximum σ_d occurred was considered as the critical location for further calculations.

Figure 20 through 28 show the calculated time-histories for the non-braking condition of the deviator and confining stresses for all combinations of pavement structures, pavement effective temperatures, truck speeds, and HMA mixture types under the driving tandem axles. Figure 29 through 37 show the calculated time-histories for the braking condition. It is important to state that the resulting loading pulse waves are, as expected, not symmetrical. This result shows the 3D-Move capability to model the viscoelastic behavior of the HMA layer and the time-dependency of the responses.

It should be noted that even-though both deviator and confining stresses are dynamic (i.e. time dependant), the conventional flow number tests are conducted with a static cell pressure and a dynamic deviator stress. A static all around air pressure is applied in the laboratory due to testing and equipment limitations.

3.7.1 Maximum equivalent deviator and confining stresses

Based on the mechanistic analysis performed under the conditions presented above, the maximum deviator and confining stresses for each critical location were evaluated under braking and non-braking conditions. The maximum equivalent deviator and confining stresses created by traffic load at 2 inches below the pavement surface are presented in Table 17-19 for both braking and non-braking conditions. Additionally, Figures 38 to 40, and Figures 41-43 show the calculated maximum deviator and confining stresses in the PG64-22, PG58-22 and PG52-22 HMA layers under the tandem driving axle without braking and with braking, respectively.

In the case of the PG64-22 mix under the no braking condition, the maximum deviator stress and confining stress varied from 69 to 102 psi and 27 to 47 psi, respectively. The total vertical stress varied from 109 to 129 psi. In the case of the PG58-22 mix under the no braking condition, the maximum deviator stress and confining stress varied from 72 to 96 psi and 29 to 43 psi, respectively. The total vertical stress varied from 109 to 125 psi. In the case of the PG52-22 mix under the no braking condition, the maximum deviator stress and confining stress varied from 74 to 94 psi and 28 to 39 psi, respectively. The total vertical stress varied from 109 to 124 psi.

Except in the case of the 4-inch HMA layer, an increase in the deviator stress and a decrease in the confining stress were observed with the increase in temperature. The impact of speed on the maximum deviator stress was more significant in the case of 4" HMA layer at 40 and 50°C, while the impact of speed on the maximum confining stress was more significant in the case of 6 and 8" HMA layers.

For the PG64-22 mix with braking, the maximum deviator stress and confining stress varied from 111 to 132 psi and 31 to 40 psi, respectively. The total vertical stress varied from 142 to 162 psi. In the case of the PG58-22 mix under the braking condition, the maximum deviator stress and confining stress varied from 109 to 127 psi and 31 to 44 psi, respectively. The total vertical stress varied from 142 to 159 psi. In the case of the PG52-22 mix under the braking condition, the maximum deviator stress and confining stress varied from 111 to 125 psi and 30 to 39 psi, respectively. The total vertical stress varied from 141 to 158 psi.

In general, due to the imposed additional shear stresses generated by the deceleration (i.e. braking) of the vehicle at intersections and stopping areas, an average increase of 40% and 5% are anticipated in the deviator and confining stresses, respectively.

In order to explain the relationship between deviator and confining stresses and pavement effective temperature showed in Figures 20-37, the principal stresses components of Equation 3.1 and 3.2 were examined separately. For example, Figure 44 shows the principal stress for the PG64-22 mix for the three analyzed pavement structures and a vehicle speed of 20 mph without braking. From the figure, it is clear that for a HMA layer of 4 inches and temperatures between 40 and 50ºC, tension stresses (i.e. negative) are developed at 2 inches below the pavement surface. This behavior could be explained due to the high depth ratio in this particular structure (ratio between depths of point of interest and HMA layer thickness) coupled with bending that occurs when the HMA is stiff. However, at higher temperatures the HMA tends to deform when the loading occurs, resulting in pure compression. In addition, the decreasing trend for the

squared difference between first and third principal stresses (i.e. $(\sigma_1-\sigma_3)^2$) explains the decreasing trend for the deviator stress as a function of temperature. The confining stress increasing trend is explained with the increase in the bulk stress as a function of temperatures.

For the 6 and 8 inches HMA layers only compression stresses are developed at 2 inch below pavement surface. This behavior is explained due to the lower depth ratio and the similar magnitudes of the second and third principal stresses. In addition, there is an increasing trend in the squared difference between first and third principal stresses as a function of temperature. This explains why the deviator stress for thick pavements increases when the temperature increases too. On the other hand, the bulk stress remains almost constant and the deviator stress tends to increase as a function of temperature. Thus, the confining stresses decrease as the pavement temperatures increases. The same behavior for deviator and confining stresses is observed for vehicle speeds of 40 and 60 mph for all the HMA mixtures evaluated in this study.

Similar trends for deviator and confining stresses as a function of pavement temperature are observed when the pavement structure is subjected to breaking forces. In addition, the principal stresses magnitudes are higher for the braking conditions than when no braking is applied to the pavement. This behavior is illustrated in Figure 45 for the case of an 18-wheeler truck travelling at 20 mph with braking forces. Appendix A shows the principal stresses, principal stresses differences, and principal stresses squared differences for braking and non-braking conditions for the three different mixtures evaluated in this study.

As part of the process of finding the mixtures critical conditions, this study have develop recommendations for the selection of the equivalent deviator and confining stresses to be used in the flow number test that best simulate the stress conditions encountered in the pavement under traffic loads. A statistical analysis is necessary in order to provide prediction equation with variables that are statistical significant to ensure the best regression possible. This is fully detailed in Chapter 4.

3.8 EQUIVALENT DEVIATOR PULSE DURATION

The results of the comprehensive mechanistic analyses describe in the previous sections were used to evaluate and characterize the loading pulse generated by the critical axle of the 18-wheel truck under both the braking and non braking conditions.

The deviator stress pulse duration was calculated for all the mixes under both non-braking and braking conditions. The pulse time was determined by best-fitting a haversine wave shape for the deviator stress pulse that was calculated from the octahedral shear stress (τ_{oct}) at 2-inch below pavement surface under a moving 18-wheel truck at different speeds and temperatures. The haversine pulse was represented by equation 3.34 where t_p is the duration of the pulse in seconds.

$$y(t) = \sin^2\left(\frac{\pi}{2} + \pi\frac{t}{t_p}\right) \tag{3.34}$$

A nonlinear optimization procedure was formulated to zero-in on the best-fit haversine pulse. Figure 46 shows an example of the calculated deviator stress and its best-fit haversine pulses for the PG64-22 mix at 70°C under non-braking conditions.

From the figure, it can be seen that the haversine pulse is a good approximation of the deviator stress pulse.

The influence if the moduli ratio of the pavement layers on the stress pulse was neglected in the study. This parameter won't affect the results mainly due to the fact that when the depth is shallow (i.e 2 inches below the pavement surface), the moduli ratio hardly influences the compressive stress pulse duration. However, when the depth is deeper (greater than 6 inches), the influence of the moduli ratio on the compressive stress pulse duration becomes more significant (14).

Table 20 shows the haversine pulse duration (t_p) for the deviator stress at 2-inch below the pavement surface for the different pavement structures, pavement temperatures, and vehicle speeds. The data show that the haversine pulse duration of the deviator stress is a function of the vehicle speed and pavement temperature. In all the evaluated cases, the pavement thickness and mixture type did not have a significant impact on the deviator stress pulse time at 2 inches below the pavement surface.

For a speed of 2 mph with braking, the pulse duration was significantly higher than all other cases with an average pulse duration of 0.43 seconds. Furthermore, the pulse duration for 20 mph in the case of braking was found to be lower than that for the non-braking condition. For example, in the case of 6-inch HMA layer at 50°C, a loading pulse time range of 0.051 to 0.058 second was found for the non-braking condition while loading pulse duration of 0.043 second was found for the braking condition. In other words, on the average the pulse duration decreased under braking by as much as 21%.

Consequently, since HMA is a viscoelastic material and its properties are highly affected by the applied loading time, the non-braking condition seems to result in a more

critical condition than the non-braking condition where in fact, the opposite performance was expected.

Figures 47 to 49, and Figures 50 to 52 show the haversine fitted for deviator stresses pulse durations in the PG64-22, PG58-22 and PG52-22 HMA layers under the tandem driving axle without braking and with braking, respectively. From the aforementioned figures, a clear trend is observed for the non-braking case, where the pulse duration decreases for all cases as the effective pavement temperature increases.

This behavior is explained by the fact that since HMA is a viscoelastic material it will exhibit, at higher temperatures, lower dynamic modulus, |E*|, which in turn will produce a narrower deviator stress time-history distribution, as seen in Figure 20 through 28 for non-braking conditions. In addition, for thin pavements at higher temperatures the HMA becomes soft leading to higher strains; which in turn reflects the reduction in the deviator stress and thus the narrower distribution. On the other hand, in the case of thick pavements, even though the magnitude of the deviator stress increases as temperature increases, as explained in Section 3.7.1, the time-history distribution remains narrow compared with the wave shape at lower temperatures. This phenomenon leads to smaller pulse durations with a smoother pulse shape. In the case of braking conditions, a more constant pulse time is obtained with a clear difference between the pulse duration of 2 mph versus 20 mph. In addition, it is clear that the presence of interface shear stresses overcome the HMA stiffness. These results probe the impact on the vehicle traveling speed to the deviator stress pulse time.

CHAPTER 4 – STATISTICAL ANALYSIS

As part of the process of finding the HMA mixtures critical conditions, recommendations for the selection of the deviator and confining stresses along with the deviator stress pulse duration to be used in the FN test that best simulate the stress conditions encountered in the pavement under traffic loads are developed. A statistical analysis is necessary in order to provide prediction equation with variables that are statistically significant to ensure the best regression possible.

4.1 STATISTICAL ANALYSIS TECHNIQUES ON MODEL SELECTION

Computation of the stress state in a pavement section under traffic loads is an essential step in any rut-depth predictive methodology. The use of a suitable mathematical model of the pavement system and realistic material properties is also essential. In order to achieve the greatest consistency in the modeling process, the computed stress state in the pavement needs to be appropriately duplicated in the laboratory testing of the HMA mixtures.

Multiple Linear Regression (MLR) analysis technique is used to analyze the database of pavement responses based on the computational model 3D-Move. The statistical analysis is performed for braking and non-braking conditions relating the following variables: effective pavement temperature, vehicle traveling speed, HMA layer modulus and pavement structure. The resulting models are developed to predict the magnitude of deviator and confining stress along with the corresponding deviator stress

pulse duration based on the aforementioned variables. The SAS macro REGDIAG, developed by Dr. Fernandez, was used in this analysis (46).

The MLR shows the relationship between two sets of variables, described by a linear equation that predicts the response variable from a function of predictor variable. The estimated MLR model contains regression parameters that are estimated by least squares criterion in such a way that prediction is optimized. The statistical significance of the overall fit is determined by an F test by comparing the regression model variance to the error variance. The MLR modeling is considered to be most widely used technique by many disciplines.

The R^2 is defined as the proportion of variance of the response that is predictable from the predictor variables. The R^2 estimate is an indicator of how well the model fits the data (e.g., an R^2 close to 1.0 indicates that the model has accounted for almost all of the variability with the variables specified in the model). The concept of R^2 is visually examined in an overlay plot of ordered and centered response variables (describing the total variation) and the corresponding residuals (describing the residual variation) versus the ascending observation sequence. Whether a given R^2 value is considered to be large or small depends on the context of the particular study. It should be noted that the R^2 is not recommended for selecting the best model because it does not account for the presence of redundant predictor variables; however, the $R^2_{(adjusted)}$ is recommended for model selection because the sample size and number of predictor variables are used in adjusting the R^2 estimate.

In addition to R^2 and $R^2_{(adjusted)}$, model selection is also be based on the Akaike's Information Criterion (AIC), the Root-Mean-Square Error (RMSE), and the Mallows Cp

statistics generated with each model. RMSE is the measure of MLR model error standard deviation, whereas AIC is the MLR model variance statistically adjusted for the sample size and number of parameters. The approach of selecting the best model is described in Section 4.2.

4.2 PREDICTION MODEL SELECTION

A minimum RMSE and AIC values and a maximum R^2 and $R^2_{(adjusted)}$ estimates are the characteristics of an optimum subset for a given number of variables. For a subset with p parameters, including the intercept, the Cp statistic is a measure of total squared error that is estimated by adding the model error variance and the bias component introduced by not including important variables. Mallows recommends selecting the model where the ratio Cp/p approaches the value of 1, when Cp/p is plotted against p (47). In addition, the statistically significant variables are selected based on a 5 percent significance level.

Figure 53 shows an example plot of Cp/p against p used to develop the equivalent deviator stress prediction model for a 6-inch HMA layer over 8-inch crushed aggregate base. It is clear that the only combination of variables that leads to a Cp/p equal to 1 is by using 5 predictor variables. Figure 54 shows all the parameters that were taken into account in order to select the best model. In addition, it is clear that the model number 5 has the minimum RMSE and AIC along with the maximum R^2 and $R^2_{(adjusted)}$. The complete statistical analysis output is presented in Appendix B.

As with any MLR analysis, correspondent assumptions were checked and verified by the actual data to avoid any incorrect or misleading conclusions. The assumptions for a valid MLR are:

1. Model parameters are correctly specified – the augmented partial residual plot is used to detect the need of any quadratic term, and the "interaction test" plot is used to detect the need of an interaction term between any two predictor variables.

2. Residuals from the regression are independent and have zero mean, constant variance, and normal distribution – the normal probability plot (normal quartile-quartile plot) along with the D'Agostino-Pearson Omnibus normality test are used to verify the normality distribution of the residuals. The residual plot against predicted value is checked for the constant variance assumption.

3. Influential outliers are absent. A cutoff value of 1.5 is used for influential observation detection. Also a cutoff value of 2.5 is used for the absolute value of the student residuals.

4.2 DEVIATOR STRESS PULSE DURATION PREDICTION MODELS

Based on the computed deviator stresses time-histories, a MLR was conducted in order to determine the prediction models that relate the statistically significant variables such as pavement effective temperature, vehicle traveling speed, and HMA modulus with the deviator stress pulse time. Equations 4.1 and 4.2 show the predictive equations for the deviator stress haversine fitted pulse duration at 2-inch below the pavement surface for braking and non-braking conditions, respectively. Fitting parameters (R^2) of 0.984 and 0.999, and ($R^2_{adjusted}$) of 0.983 and 0.999 were found for the non-braking and braking conditions, respectively.

Non-braking condition:

$$\log(t_p) = -0.00353(T) - 0.0236(S) + 0.00015(S)^2 - 0.6654 \quad (4.1)$$

($R^2 = 0.984$, $R^2_{adj} = 0.983$)

Braking condition:

$$\log(t_p) = -0.000387(T) - 0.05531(S) - 0.23603 \quad (4.2)$$

($R^2 = 0.999$, $R^2_{adj} = 0.999$)

where, t_p is the deviator stress pulse duration at 2-inch below pavement surface in seconds, T is the asphalt layer temperature in ºC, and S is the vehicle travelling speed in mph. Figures 55 and 56 show the relationship between the predicted deviator stress pulse duration using Equations 4.1 and 4.2 and the computed values presented in Table 20. Since the mechanistic analysis under braking conditions was undertaken for two speeds of 2 and 20 mph, there is a noticeable gap in the results presented in Figure 56.

It should be noted that the above regression equations are based on data that were determined under a range of temperatures between 40 and 70°C and vehicle speeds of 20 to 60 mph for non-braking condition and 2 to 20 mph for braking condition. It is recommended that these equations not be used outside the specified ranges for temperature and speed.

4.3 DEVIATOR AND CONFINING STRESSES PREDICTION MODELS

In order to simplify the applicability of the proposed work, generalized equations for estimating the triaxial deviator and confining stresses for a given pavement structure and temperature and under a given vehicle speed have been developed. The effect of the

mixture type on the predicted stresses was indirectly accounted for by the use of the corresponding asphalt mixture's modulus at the effective pavement temperature and loading frequency at 2 inch below the pavement surface. The following shows the prediction equations obtained through MLR for the deviator and confining stresses at 2 inch below the pavement surface.

- 4 inch HMA layer

a) Non-braking:

$$\sigma_d = -0.0844(T) + 0.06|E^*| + 83.708 \quad (4.3)$$
($R^2 = 0.958$, $R^2_{adj} = 0.956$)

$$\sigma_c = 0.0232(T) - 0.0169|E^*| + 32.495 \quad (4.4)$$
($R^2 = 0.977$, $R^2_{adj} = 0.975$)

b) Braking:

$$log(\sigma_d) = -0.000179(T) + 0.000319|E^*| - 2.9 \times 10^{-7}|E^*|^2 + 2.06 \quad (4.5)$$
($R^2 = 0.981$, $R^2_{adj} = 0.978$)

$$\sigma_c = -0.034|E^*| + 0.00029(S)(|E^*|) + 37.50 \quad (4.6)$$
($R^2 = 0.970$, $R^2_{adj} = 0.967$)

- 6 inch HMA layer (without braking):

a) Non-braking:

$$\sigma_d = -0.804(T) + 0.0066(T^2) + 0.076(S) - 0.000922(T)(S) - 7.045 \times log(|E^*|) + 114.37 \quad (4.7)$$
($R^2 = 0.928$, $R^2_{adj} = 0.915$)

$$\sigma_c = -0.000967(T^2) - 0.1107(S) + 0.00171(T)(S) + 0.00139(T)(|E^*|) + 31.41 \quad (4.8)$$
($R^2 = 0.990$, $R^2_{adj} = 0.989$)

b) Braking:

$$log(\sigma_d) = 0.000204|E^*| - 3.21 \times 10^{+7}|E^*|^2 + 2.98 \times 10^{-6}(S)(|E^*|) - 4.19 \times 10^{-6}(T)(|E^*|) + 2.05 \quad (R^2 = 0.789, R^2_{adj} = 0.745) \quad (4.9)$$

$$\sigma_c = 0.335(T)+0.0334|E^*| -0.0033(T^2)-0.0014\cdot(S)(|E^*|)+0.00132(T)(|E^*|)+22.12 \quad (R^2 = 0.993, R^2_{adj} = 0.991) \quad (4.10)$$

- 8 inch HMA layer (without braking):

a) Non-braking:

$$\sigma_d = 0.000576(T^2) + 0.000316(S^2) + 0.0463(|E^*|) - 0.00199(T)(|E^*|) + 79.01 \quad (R^2 = 0.982, R^2_{adj} = 0.980) \quad (4.11)$$

$$\sigma_c = -0.000826(T^2) - 0.11284(S) + 0.00168(T)(S) + 0.00139(T)(|E^*|) + 30.26 \quad (R^2 = 0.990, R^2_{adj} = 0.988) \quad (4.12)$$

b) Braking:

$$log(\sigma_d) = 9.17\times10^{-5}|E^*| - 2.32\times10^{-7}|E^-|^2 + 2.61\times10^{-6}(S)(|E^*|) - 3.17\times10^{-6}(T)(|E^*|)+2.046 \quad (R^2 = 0.956, R^2_{adj} = 0.950) \quad (4.13)$$

$$\sigma_c = 5.94\times10^{-5}|E^*|^2 + 0.0196(S^2) - 0.0027(S)(|E^*|)+0.00214(T)(|E^*|) - 0.00641(S)(T)+30.12 \quad (R^2 = 0.992, R^2_{adj} = 0.989) \quad (4.14)$$

where σ_d and σ_c are the deviator and confining stresses in psi, respectively, T is the effective asphalt layer temperature in ºC, S is the vehicle speed in mph, and |E*| is the mixture's dynamic modulus at 2 inches and at the effective pavement temperature and for a given vehicle speed in ksi. In addition, there is no highly significant covariance between the variables (i.e. temperature, speed and stiffness), thus the variables are independent. In addition, the appropriate $|E^*|$ is based on the pulse time (t_p) obtained from

the prediction models for the deviator stress pulse duration using either Equation 4.1, for non-braking condition, or Equation 4.2, for braking.

There have been several recent studies that looked into the conversion of the loading time into the testing frequency (48, 49, and 50). One of the approaches that is used in the Mechanistic-Empirical Pavement Design Guide (MEPDG) is to convert the loading time (t_p) to cyclic frequency (f, in hertz) using $1/t_p$ (51). An alternative approach that is used in the field of rheology is to convert the loading time to cyclic frequency using the angular frequency (in rads per second) as $f = 1/(2\pi t_p)$. As this study was not designed to identify the most appropriate approach, the $|E^*|$ was determined at a loading frequency that is consistent with the MEPDG methodology.

Figure 57 shows the relationship between the predicted deviator and confining stress to the computed values presented in Tables 11-13 for the non-braking conditions, whereas Figure 58 shows the relationship between the predicted equivalent deviator and confining stress to the computed values presented in Tables 14-16 for the braking conditions.

The prediction equations are presented in terms of the statistically significant variables at the 5 percent significance level. Overall, the models' accuracies were above 95%, which indicate that good correlations exist between the calculated and predicted values.

It may be noted that the direct influence of speed on the magnitude of the maximum deviator and confining stresses with and without braking was only statistically significant in the case of the 6" and 8" HMA layers. In the case of the 4" HMA layer, the speed was indirectly incorporated through the asphalt layer dynamic modulus. In other

words, the |E*| input for Equations 4.3 through Equation 4.14 will vary depending on the vehicle speed resulting in different predicted stresses. This finding was mainly because the change in speed in the case of the 4" HMA layer did not result in a consistent impact on the maximum deviator and confining stresses (i.e. the change in stresses as a function of speed was more significant at 40 and 50°C when compared to the 60 and 70°C)

As it was mentioned in the previous section, the above regression equations are based on data that were determined under a range of temperatures of 40 to 70°C and vehicle speeds of 20 to 60 mph for non-braking condition and 2 to 20 mph for braking condition. It is recommended that these equations not be used outside the specified ranges for temperature and speed.

CHAPTER 5 – LABORATORY EXPERIMENTS

Extensive mechanistic analyses of three different asphalt pavement structures subjected to moving traffic loads at various speeds and under braking and non-braking conditions were conducted using the 3D-Move model. Prediction equations for estimating the anticipated deviator and confining stresses along with the equivalent deviator stress pulse duration as a function of pavement temperature, vehicle speed, and asphalt mixture's modulus have been developed. Based on these findings, a series of laboratory experiments were conducted in order to identify the HMA critical conditions to be implemented in the mix design process.

The critical conditions of HMA mixtures are defined as the critical combination of effective pavement temperature and traffic-induced loading. The selected test to evaluate these conditions is the FN or also referred to as Repeated Load Triaxial (RLT). The applied deviator and confining stresses in the FN test are intended to duplicate the state of stresses generated in the pavement under given environmental and loading conditions. In other words, the FN test is intended to simulate the actual field conditions by subjecting the HMA specimen to deviator and confining stresses similar to the ones encountered in the asphalt pavement layer.

The proposed models to simulate the equivalent deviator and confining stresses along with the deviator stress pulse duration are used to identify the critical conditions of two different field HMA mixtures from the WesTrack Project, and one of the laboratory produced mixtures at three different air voids levels.

5.1 CASE OF STUDY: WESTRACK

A preliminary investigation was carried out in an attempt to identify the critical conditions of the field HMA mixtures and to assess the applicability of the recommended predictive equations for deviator and confining stresses along with pulse duration. The WesTrack Project was selected to validate the aforementioned conditions, mainly due to the availability of recorded data during the two year period; and also due to the accessibility of field mixtures that were used in the project.

Prior to fully explain the laboratory test conditions and HMA mixtures analyzed, it is highly important to provide an overview and a brief description of the WesTrack Project in order to be able to explain the reasons why these field mixtures showed their particular performance.

5.1.1 The WesTrack Project

WesTrack is an accelerated pavement test facility constructed in Nevada approximately 60 miles southeast of Reno. The pavement test facility was designed, constructed, and operated by a team of private companies and universities. The contract, entitled "Accelerated Field Test of Performance-Related Specifications for Hot-Mix Asphalt Construction" (Contract No. DTFH61-94-C-00004), was sponsored by the Federal Highway Administration (FHWA).

The test track included 26 HMA pavement test sections. In addition, it was designed and constructed between October 1994 and October 1995. Traffic was initiated

in March 1996 and was completed in February 1999. Five million equivalent single-axle loads (ESALs) were placed on the track during the trafficking period (52).

The objective of WesTrack experiment was to evaluate the effect of variations in materials and construction quality of HMA mixtures, such as asphalt content, in-place air voids, and aggregate gradation, on pavement performance under constant traffic and environmental conditions. One performance-graded asphalt binder was used for all the sections, PG 64-22 from *Westcoast Refinery*. Optimum asphalt binder content was determined using the Superpave volumetric mix design procedure. The asphalt content was then varied plus and minus 0.7% from the optimum asphalt binder content to have three levels of asphalt binder content designated as low, medium, and high. Three levels of in-place air voids were selected which were 4%, 8%, and 12%. Three gradations having a nominal maximum size of 19 mm were used for the sections. The aggregate source was from a quarry near Dayton, Nevada.

Four driverless trucks were used to traffic the pavement sections and were capable of applying 350,000 ESALs per month of operation. A scheme of the truck configuration is presented in Figure 59. A total of 10 of the original 26 sections were rehabilitated due to excessive rutting (over 1 inch) after 1.5 million ESALs. Table 21 shows the experimental design of the 26 original sections as well as 8 of the ten rehabilitated sections. Figure 60 shows track configuration and the mixture types along with the level of asphalt content and air void content used in the WesTrack Project (53).

The pavement structure consists of a six inch HMA layer laid in two three inch lifts, 12 inches of dense-graded crushed aggregate base course, 12 inches of engineered fill, and 6 inches of scarified and mixed subgrade soil. In addition, an LTPP weather

station was located at the track, along with two LTPP seasonal monitoring devices to monitor pavement temperature with depth, and to measure moisture contents in the base, fill, and subgrade soil. Data were collected from the start of the loading cycles in April 1996 to April 1999. Hourly temperatures for the HMA layer at 5 depths for four sections (sections 12, 19, 25, and 55) were recorded.

Several original sections failed early in rutting; they were replaced with a mix that followed the coarse gradation, but changed from the crushed gravel used in the original sections to a more angular, quarried andesite aggregate. The total experiment yielded significantly different levels of permanent deformation among the various test sections.

Rut depth was measured with the Dipstick, the Arizona DOT transverse profile device, and the laser transverse profile device developed by Nevada Automotive Test Center NATC (40). The frequency of testing was biweekly when the track was subjected to traffic. During periods of rapid rutting or fatigue cracking, testing frequency was increased. After 1.5 million ESALs, 5 sections failed in rutting and by the end of the trafficking period (5 million ESALs), only 15 of the original sections survived.

The “fine plus” mixtures showed a slight increase in rut depth as the initial in-place air-voids were increased (52). A large increase in rut depth was noted at the high binder content. The high binder content mixtures at both the medium and low air-void contents were removed after 1.5 million ESALs due to excessive rutting. The rutting behavior of the “fine plus” graded mixture was sensitive to changes in asphalt binder content at levels above the optimum asphalt binder content.

The “coarse” mixtures showed an increase in rut depth as the initial in-place air-voids were increased (52). The rut depth of this mixture at all asphalt binder contents was

large. The high binder content mixtures at both the medium and low air-void contents were removed after 1.5 million ESALs due to excessive rutting.

The “coarse” graded mixtures experienced the highest rut depth. As the initial air-voids were decreased, the differences among the rutting of the “fine plus” and the “coarse” graded mixtures decrease. In general, higher rut depths were observed for the “coarse” graded mixtures as compared to the “fine” graded mixtures under all conditions available for comparisons (52).

Due to the exhibited performance presented above, two sections or cells were selected for laboratory evaluation: Cell 55, reconstructed section, and Cell 19, original section. The selection of these two cells was done primarily because the temperature sensors were place right on those sections and field HMA mixtures were available. Table 22 summarizes the main properties of these two cells.

5.1.2 WesTrack Cell 55

Repeated load flow number testing was performed for the WesTrack Cell 55 HMA mix. The Cell 55 HMA mix is a coarse-graded mixture that was manufactured with an unmodified PG64-22 asphalt binder and has an optimum binder content of 6.4% and in-place air voids of 4%. The aggregate gradation used is shown in Figure 61. The pavement section consisted of a 6-inch HMA layer on top of a 12-inch aggregate base, overlying the subgrade. The pavement was subjected to four driverless tractor/triple-trailers with three single-axle semi-trailer followed by two trailers, each with two singles dual axles travelling at a speed of 40 mph.

Based on temperature records and rut depth measurements (53), the maximum and minimum recorded temperatures at a depth of 1.5 inch from the pavement surface coupled with the right and left wheel path rut depths as a function of applied Equivalent Single Axle Load (ESAL) were analyzed. The resulting relationship between ESAL level and pavement temperature and rut depths are presented in Figure 62.

A strong correlation between pavement temperature and rate of rutting is observed at ESALs range between 140,000 and 215,000. The rut depth increased from 0.45 inch to 0.60 inch (a 33% increase) when the maximum pavement temperature increased during seven consecutive days from a 40°C to a maximum of 46°C. It appears that the combination of elevated temperature for extended period of time and the applied ESAL level contributed to a significant increase in rutting. This correlation indicates that, even under constant loading conditions and for a given number of loading repetitions, HMA pavements will experience significant increases in rutting once their temperature reaches a critical level.

For this WesTrack section, the critical temperature is expected to be between 40 and 46°C. Consequently, flow number tests were carried out at four different temperatures: 40, 45, 50, and 55°C. At each temperature, the corresponding deviator and confining stresses were determined using equations 4.7 and 4.8. The equations require the knowledge of the modulus of the mix at 2 inches below the pavement surface. Hence, a series of dynamic modulus (|E*|) tests were conducted on the WesTrack Cell 55 HMA mixture and the variations of |E*| were estimated at each of these temperatures using the master curve and shift factors. Tables 23-24 show the dynamic modulus testing results for Cell 55 and Cell 19. In order to develop the dynamic modulus master curve, the A-

VTS parameter of the binder is required which was measured and shown in Figure 63. Figures 64 and 65 show the |E*| master curve and the phase angle for cells 55 and 19.

The loading rate was calculated from the analysis of the deviator stress pulse time using Equation 4.1 at the corresponding temperature and vehicle speed. In addition, the rest period is assumed to be the truck traveling time over the distance separating the truck tandem axles. For this particular case an axle separation of 5.2 m was used in the WesTrack Project and a truck traveling speed of 40 mph, resulting in a rest period of 0.3 seconds. Using the determined |E*| along with the corresponding temperature and the vehicle speed (40 mph), deviator and confining stresses were determined. A deviator stress of 77 psi was found at all temperatures. The confining stress was found to decrease with the increase in temperature.

The FN test was conducted using the determined stress conditions at the four temperatures for 20,000 cycles or until the specimen reaches 5% strain, whichever occurs first. Two replicates were conducted at each temperature. The flow number was calculated using the stepwise increase method (22), the three stage permanent deformation method (23) and the Francken method (24). Table 25 summarizes the testing conditions and results obtained with three different calculation methods.

Figure 66 summarizes the FN test results. The FN was found to be sensitive to the analysis method. In general, comparable results for the FN were found between the three-stage and the stepwise analysis methods. However, a smaller FN was found for all temperatures when the Francken method is used. No flow number was found at 40°C when the test results were analyzed using the three-stage method and the Francken approach. On the other hand the stepwise method showed an average FN of 19,250 at

40°C. A closer look at the data shows no initiation for the tertiary stage at 40°C after 20,000 cycles which indicates that the stepwise method leads to different results.

For temperatures greater than 40°C, the mixture exhibited a tertiary stage regardless of the FN calculation method. A decrease in the FN was observed at temperatures greater than 40°C. The data indicate that the 45°C temperature is the mixture specific critical temperature under the applied loading conditions. This critical temperature is consistent with the analysis of the WesTrack field observations presented earlier (Figure 62) indicating the general applicability of the procedures and generalized equations presented in this study. Although this is a promising result, additional investigations with different mixes from the WesTrack Project and other similar projects are needed for further validation. Additionally, the FN at the critical temperature and under the determined testing conditions needs to be further investigated for possible correlation with the applied ESALs in the field.

5.1.3 WesTrack Cell 19

The Cell 19 HMA mix is original section designated as a "fine plus" mixture that was manufactured with an unmodified PG64-22 asphalt binder and has an optimum binder content of 5.4% and in-place air voids of 8%. The aggregate gradation is shown in Figure 61. It is similar to the fine gradation plus approximately 2 percent bag house fines. The pavement section consisted of a 6-inch HMA layer on top of a 12-inch aggregate base, overlying the subgrade. The pavement was subjected to the same loading conditions as the Cell 55.

Based on the temperature records and the rut depth measurements (53), the maximum and minimum recorded temperatures at a depth of 1.5 inch from the pavement surface coupled with the right and left wheel path rut depths as a function of applied Equivalent Single Axle Load (ESAL) were analyzed. The resulting relationship between ESAL level and pavement temperature and rut depths are presented in Figure 68.

A rapid increase in permanent deformation is observed during the first 234,000 ESAL applications. Later the rut depth continued increasing with a smaller rate up to almost 1,500,000 ESALs. After these loading applications the rut depth becomes stable in time with almost no increase for the following 4,500,000 ESALs. This behavior may be explain due to the fact that an 8% in-place air void level was placed in the cell leading the HMA mixture to a consolidation process when the first loads are applied. In addition, there is no correlation between the effective pavement temperature and the rut depth measurements. Nonetheless, it is clear that during the first million ESALs the high temperature varied from 30 to 55ºC.

Consequently, flow number tests were carried out at six different temperatures: 30, 35, 40, 45, 50, and 55°C. At each temperature, the corresponding deviator and confining stresses were determined using equations 4.7 and 4.8. The equations require the knowledge of the modulus of the mix at 2 inches below the pavement surface. Hence, as it was done on WesTrack Cell 55 the A-VTS parameters were obtained, as shown in Figure 69, along with a series of dynamic modulus (|E*|) tests. The variations of |E*| were estimated at each of these temperatures using the master curve and phase angle shown in Figures 64 and 65.

The loading rate was calculated from the analysis of the deviator stress pulse time using Equation 4.1 at the corresponding temperature and vehicle speed. In addition, the rest period is assumed exactly the same as for the Cell 55. A deviator stress range of 75 to 77 psi was found. The confining stress was found to decrease with the increase in temperature.

The FN test was conducted using the determined stress conditions at the six temperatures for 20,000 cycles or until the specimen reaches 5% strain, whichever occurs first. Due to the fact that only 4 –gallon buckets of field HMA mixture were provided, only one replicate was conducted at each temperature. The flow number was calculated using the stepwise increase method (22), the three stage permanent deformation method (23) and the Francken method (24). Table 26 summarizes the testing conditions and results obtained with three different calculation methods.

Figure 70 summarizes the FN test results. As in the results for WesTrack Cell 55, the FN was found to be sensitive to the FN analysis method. Comparable results for the FN were found between the three-stage and the stepwise analysis methods. Overall the Francken model resulted in lower FN values when compared to the three-stage and stepwise approaches. No flow number was found at 30 and 35°C when the test results were analyzed using the three-stage method and the Francken approach. On the other hand the stepwise method showed a FN of 18,295 at 35°C. Therefore, the critical conditions for this particular mix are a combination of 40ºC with the applied loading characteristics. In addition, it is important to note that even the WesTrack Cell 19 shows higher stiffness than WesTrack Cell 55, as seen in Figure 64, the critical temperature is smaller, which in turn indicates the impact of the air void content on the predicted flow

number. Thus, a series of laboratory experiments for a laboratory produced mix with different air void contents is required to fully describe the effect of in-place HMA density on FN.

5.2 HMA DENSITY IMPACT ON CRITICAL CONDITIONS

The rutting performance of a HMA pavement is significantly impacted by the inherent properties of the HMA mixture. Regardless of how well the mix design and structural design have been developed, the properties of the materials delivered to the job site, such as gradation, binder content, and the in-place density (i.e., air-voids) will ultimately control the behavior of the pavement under the combined action of traffic and environment.

The design and construction of HMA mixtures represent the two most important steps in building HMA pavements. Usually, an HMA mixture is designed in the laboratory and a job mix formula (JMF) is produced for field implementation. Along with the JMF comes specification limits which control the acceptable ranges of the produced mixture. Specification limits are developed to recognize the inherent variability in the production and lay-down process; however, variations within these limits may still impact the performance of the HMA pavement. The impact of these variations on performance can be positive toward one distress mode while negative toward another.

In order to evaluate the impact of density on the determination of the HMA critical conditions, three air void levels were assessed: 7% to represent typical in-place air void content, 4% to represent mix design air void level, and 2% to represent high

compaction effort in the field. The lab produced PG64-22 mix was selected to undertake this analysis. As mentioned in Section 3.5, this HMA mixture consisted of an intermediate Superpave gradation with a nominal maximum aggregate size of ½ inch, as presented in Figure 11. In addition, the optimum binder content is 5.85% as shown in Table 4. The pavement structure selected for this experiment is a 6-inch HMA layer on top of an 8-inch aggregate base, overlying the subgrade. The pavement is assumed to be subjected to a fully loaded 18-wheeler truck, as shown in Figure 10, with a traveling speed of 40 mph without braking.

The FN test was conducted using the determined stress conditions at each testing temperatures for 20,000 cycles or until the specimen reaches 5% strain, whichever occurs first. At each temperature, the corresponding deviator and confining stresses were determined using equations 4.7 and 4.8. The equations require the knowledge of the modulus of the mix at 2 inches below the pavement surface. Hence, a series of dynamic modulus (|E*|) tests were conducted on the PG64-22 mix at the target air void levels (i.e. 7, 4, 2%) and the variations of |E*| were estimated at each of these temperatures using the master curve and shift factors. Tables 27 and 28 show the dynamic modulus testing results for the PG64-22 laboratory produced mixture. In addition, Figures 71 and 72 show the |E*| master curve and the phase angle for the PG64-22 mix at the three air void levels. It is clear that lower the air void level stiffer the mix would be.

The loading rate was calculated from the analysis of the deviator stress pulse time using Equation 4.1 at the corresponding temperature and vehicle speed. In addition, the rest period is assumed to be the truck traveling time over the distance between axles. For this particular case an axle separation of 370.1 in (9.4 m) coupled with a tandem axle

spacing of 47.2 (1.2m) were used, resulting in a rest period of 0.5 seconds. Using the determined |E*| along with the corresponding temperature and the vehicle speed (40 mph), deviator and confining stresses were determined. Overall, the deviator stress varied between 74 and 77 psi as a function of temperature while the confining stress varied between 40 and 59 psi as a function of temperature. At each air void level, the confining stress was found to decrease with the increase in temperature.

The flow number was calculated using the stepwise increase method (22), the three stage permanent deformation method (23) and the Francken method (24). Table 29 summarizes the testing conditions and results for all three air-void level.

Figure 73 shows the FN as a function of temperature for all three air-void levels. The FN sensitivity to the FN analysis method was once again obvious. Overall the Francken method resulted in lower FN values when compared to the three-stage and stepwise methods. Figure 74 shows the FN as a function of air-voids level at the various testing temperatures. The data shows an increase in the FN with the decrease in air voids.

The PG64-22 mix at 7% air voids exhibited a tertiary stage at a temperature greater than 35°C. On the other hand, the PG64-22 mix at 4% and 2% air voids exhibited a tertiary stage at a temperature greater than 40°C. The data indicate the existence of a critical temperature between 35 and 40°C for the PG64-22 mix at 7% air voids and a critical temperature between 40 and 45°C for the PG64-22 mix at both 4% and 2% air voids. However the critical temperature of the PG64-22 mix at 2% air voids was observed at a higher number of load repetitions (i.e. FN) when compared to the critical temperature of the PG64-22 mix at 4% air voids.

The results indicate that the HMA critical conditions determined in the FN test are affected by the density of the samples. In other words, when the critical conditions for a certain mix are stated, it becomes highly important to take into account the air-voids level in the final assessment.

CHAPTER 6 – CONCLUSIONS AND RECOMMENDATIONS

The overall objective of this research was to define the critical loading conditions created by a moving truck load in the HMA layer. In addition the encountered critical conditions of HMA mixtures, defined as the critical combination of testing temperature, deviator and confining stresses, along with the loading rate under the repeated load triaxial (RLT) testing were evaluated. In order to achieve these objectives, a extensive database of computed stress histories of three different asphalt pavement structures subjected to moving traffic loads at various speeds and under braking and non-braking conditions were conducted using the 3D-Move model.

As part of the process of finding the mixtures critical conditions, this study have developed recommendations for the selection of the equivalent deviator pulse characteristics and the deviator and confining stresses to be used in the flow number test that best simulate the stress conditions encountered in the pavement under traffic loads. Prediction equations for estimating the anticipated deviator and confining stresses along with the equivalent deviator stress pulse duration as a function of pavement temperature, vehicle speed, and asphalt mixture's modulus have been developed. Overall, good correlations between the calculated and predicted stresses and pulse duration were found.

It may be concluded that the haversine pulse is a good approximation of the equivalent triaxial deviator stress pulse. It is clear that non-symmetrical shape of the loading pulse from this research matched well with the shape of the field measurements made at the Virginia Smart Road investigation. In addition, it was proven that the haversine pulse duration is a function of the vehicle speed and pavement temperature. In

all of the evaluated cases, neither pavement thickness nor mixture properties significantly impacted the pulse duration at 2 inches below the pavement surface.

The tandem axle was proven to generate the most critical combination of deviator and confining stresses for braking and non-braking conditions at 2 inches below the pavement surface. Thus, this study focused on developing the stress state and pulse characteristics required to determine the critical conditions on HMA mixtures under the loading of the tandem axle.

Prediction equations for estimating the anticipated deviator pulse duration as a function of pavement temperature, and vehicle speed have been developed with fitting parameters (R^2) of 0.984 and 0.999, and ($R^2_{adjusted}$) of 0.983 and 0.999 for the non-braking and braking conditions, respectively. It should be noted that the above regression equations are based on data that were determined under a range of temperatures between 40 and 70°C, and vehicle speeds of 20 to 60 mph for non-braking condition and 2 to 20 mph for braking condition. It is recommended these equations not be used outside the specified ranges for temperature and speed.

The triaxial testing conditions that are representative for vehicle braking also were investigated. The braking conditions, though it generates interface shear stresses, leads to lower deviator pulse duration and higher amplitude. The deviator pulse duration decreased by as much as 21% under braking, while the amplitude increased by 40% when compared with the values computed with non-braking. The impact of these changes are important in FN tests since HMA mixtures exhibit viscoelastic characteristics.

The moduli ratio of the pavement layers was not incorporated in the analysis process. This parameter won't affect the results mainly due to the fact that when the

depth is shallow (i.e. 2 inches below the pavement surface), the moduli ratio hardly influences the compressive stress pulse duration.

The magnitude of deviator stress, σ_d , and confining stress, σ_c, were determined by converting the stress tensor computed in the HMA layer at 2 inch below pavement surface under a moving 18-wheel truck using the octahedral normal and shear stresses. In addition, the characteristics of the loading pulse were developed by best-fitting a haversine wave shape for the equivalent triaxial deviator stress pulse. Based on these findings, a series of laboratory experiments were conducted in order to identify the hot-mixed asphalt (HMA) critical conditions to be implemented in the design process.

The amplitude of the equivalent triaxial deviator and confining stresses are highly affected by the mixture's dynamic modulus, |E*|, the pavement effective temperature and vehicle speed. The equivalent triaxial stresses are independent of the pavement structure. Under no braking conditions, the test results show that the magnitude of the deviator and confining stresses ranged from 69-102 psi and 27-47 psi, respectively. In the case of braking, the magnitude of the deviator and confining stresses ranged from 108-132 psi and 30-47 psi, respectively. On average, the imposed additional shear stresses generated by the braking of the vehicle at stopping areas resulted in a 40% increase in the deviator stress (from 85 to 119 psi) and a slight increase (5%) in the confining stress. Additionally, higher deviator stresses coupled with similar or lower confining stresses were observed in the 4 inch HMA layer when compared to the 8 inch HMA layer. The amplitudes of the deviator and confining stresses range from 69-102 psi to 27-43 psi, respectively.

To achieve the greatest consistency in the modeling process, the traffic-induced stress state and loading pulse duration in the pavement needs to be appropriately duplicated in the laboratory testing of the HMA mixtures. Based on the results of this study, it may be concluded that the equivalent deviator and confining stresses to be applied in the Flow Number (FN) test are highly influenced by the mixture's modulus, the effective pavement temperature, and the vehicle traveling speed. In addition, the standard pulse time loading of 0.1 second applied to the FN does not simulate the actual equivalent traffic-induced deviator stress pulse duration. This was also proven in the Virginia Smart Road study, were haversine loading durations as low as 0.02 seconds were measured for a truck speed close to 40 mph. Thus, it may be concluded that the current standard procedure is not representative of the actual field conditions.

A preliminary investigation was carried out on field mixtures from WesTrack in an attempt to evaluate the critical conditions and the applicability of the recommended predictive equations. Under laboratory conditions, a critical temperature of 45°C was observed for the WesTrack Cell 55 mix above which it became unstable. This laboratory determined critical temperature showed consistency with the rutting field performance of the mix where an increase in rutting was observed at a given ESALs range along with an increase in the maximum pavement temperature during seven consecutive days from 40°C to 46°C.

For the WesTrack Cell 19, a rapid increase in permanent deformation was observed during the first 234,000 ESAL applications. This behavior may be explain due to the fact that an 8% in-place air void level was placed in the section leading the HMA mixture to a consolidation process when the first loads are applied. Therefore, the critical

conditions for this particular mix are a combination of 40ºC and the applied loading characteristics. In addition, it is important to note that even-though the WesTrack Cell 19 shows higher modulus than WesTrack Cell 55, its critical temperature was lower, which in turn indicates the significant impact of the air void content in the flow number test.

In order to evaluate the impact of density on the determination of the HMA critical conditions, three air void levels were assessed. It is clear that for a fixed mixture gradation and binder content, the lower the air void level the stiffer the mix would be. In addition, based on the laboratory experiment a series of conclusions can be drawn. The PG64-22 mix at 7% air voids exhibited a tertiary stage at a temperature greater than 35°C. On the other hand, the PG64-22 mix at 4% and 2% air voids exhibited a tertiary stage at a temperature greater than 40°C. The data indicate the existence of a critical temperature between 35 and 40°C for the PG64-22 mix at 7% air voids and a critical temperature between 40 and 45°C for the PG64-22 mix at both 4% and 2% air voids. However the critical temperature of the PG64-22 mix at 2% air voids was observed at a higher number of load repetitions when compared to the critical temperature of the PG64-22 mix at 4% air voids. Thus, it may be concluded that the HMA critical conditions determined in the FN test are affected by the density of the samples. In other words, when the critical conditions for a certain mix are stated, it becomes highly important to take into account the air-voids level in the final assessment.

For all the analysis made, it was found that the FN is sensitive to the calculation method used. In general, comparable results for the FN were found between the three-stage and the stepwise analysis methods. However, a smaller FN was found for all temperatures when the Francken method is used.

The critical conditions of different field mixtures from the WesTrack Project and also laboratory produced samples at different air-voids levels were determined in the laboratory. It appears that the combination of elevated temperatures for a extended period of time and the traffic-induced loading contributes to the increased rate of rutting. The results indicate that the tertiary stage will occur under the FN test when a combination of a critical temperature and a given loading conditions for a specific air voids content occurs. Though this is a promising result, additional investigations with different mixes from the WesTrack Project and other similar projects are recommended for further validation.

It is recommended to evaluate field mixtures with known rutting performance in the laboratory for permanent deformation characteristics under the repeated load triaxial test to assess not only the critical conditions of the HMA under non-braking, but also to validate the prediction models developed for the braking conditions.

REFERENCES

1.Witczak, M., Kaloush, K., Pellinen, T., El-Basyouny,M., and Von Quintus, H., "Simple Performance Test for Superpave Mix Design", NCHRP Report 465, *Transportation Research Board-National Research Council*, Washington D.C., 2002.

2. Sullivan, B., Quayum, M., Kaloush, K., and Witczak, M. "Evaluation and Challenges of the Flow Number Simple Performance Test", *Proceedings of the Tenth International Conference on Asphalt Pavements*, Quebec, 2006.

3. National Cooperative Highway Research Program, "Guide for Mechanistic-Empirical Design of New and Rehabilitated Pavement Structures", *Transportation Research Board*, National Research Council, February 2004.

4. Carpenter, S., and Vavrik, W., "Repeated Triaxial Testing During Mix Design for Performance Characterization", *Transportation Research Board: Journal of the Tranportation Research Board*, No 1767, TRB, National Research Council, Washington D.C., 2001, pp. 76-84.

5. McGennis, R.B., Anderson, R.M., Kennedy, T.W., and Solamanian, M., "Background of Superpave Asphalt Mixture Design and Analysis", *Report No. FHWA-SA-95-003, Federal Highway Administration*, Washington, D.C., 1994.

6. Marker, V., "Problems with Asphalt Pavements," *Proceeding of the Asphalt State-of-the-Art Conference held at Woodbridge*, NJ, May 11, 1981.

7. Siddharthan, R., Yao, J., and Sebaaly, P., "Pavement Strain from Moving Dynamic 3D Load Distribution", *Journal of Transportation Engineering,* vol. 134, No. 6, November 1998.

8. Al-Qadi, I., Wang, H., Jun Yoo, P., and Dessouky, S., "Dynamic Analysis and In Situ Validation of Perpetual Pavement Response to Vehicular Loading", *Transportation Research Records*, TRB, National Research Council, Washington, D.C., 2008.

9. Barksdale, R.D., "Compressive Stress Pulse Time in Flexible Pavements for Use in Dynamic Testitng", *Highway Research Record 345*, HRB, National Research Council, Washington, D.C., 1971, pp. 32-44.

10. Al-Qadi, I.L., Louizi, A., Elseifi, M., and Lahouar, S., "The Virginia Smart Road: The Impact of Pavement Instrumentation on Understanding Pavement Performacnce", *Journal of the Association of Asphalt Pavement Technologist*, AAPT, Vol 73, 2004.

11. Brown, S.F., "Determination of Young's Modulus for Bituminous Materials in Pavement Design", *Highway Research Record 431*, National Research Council, Washington D.C., 1973, pp. 38-49.

12. McLean, D.B, "Permanent Deformation Characteristics of Asphalt Concrete", Ph.D. dissertation, University of California, Berkeley, 1974.

13. Al-Qadi, L.L., Elsefi, M. A., Yoo, P. J., Dessouky, S., Gibson, N., Harman T., Dangelo, J., and Petros, K., "Accuracy of Current Complex Modulus Selection Procedure from Vehicular Load Pulse", *NCHRP 1-37 A Mechanistic-Empirical Pavement Design Guide*, Transportation Research Record, Washington, D.C., 2008.

14. Hu, X., Zhou, F. L., Walubita, L., and Scullion, T., "Proposed Loading Wave Forms and Loading Time Equations for M-E Pavement Design and Analysis", *Transportation Research Board*, Washington, D.C., 2009.

15. Garcia, G., and Thompson, M., "Strain and Pulse Duration Considerations for Extended-Life Hot-mix Asphalt Pavement Design", *Journal of the Transportation Research Board*, No. 2087, Washington, D.C., 2008.

16. Yin, H., Solaimanian, M., and Kumar, T., "The Effect of Loading Time on Flexible Pavement Dynamic Response: a Finite Element Analysis", *Journal Mechanics of Time-Dependent Materials*, Vol. 11, 2008.

17. Archilla, A., Diaz, L., and Carpenter, S., "Proposed Method to Determine the Flow Number from Laboratory Axial Repetead Loading Tests in Bituminous Mixtures", *Transportation Research Board,* TRB, Washington D.C.,2007.

18. Eisenmann, J. and Hilmer, A., "Influence of Wheel load and Inflation Pressure on the Rutting Effect at Theoretical Investigations*". 6th International Conference on the Structural Design of Asphalt Pavements*, University of Michigan, Ann Arbor, Michigin, 1987, p. 392-403.

19. National Cooperative Highway Research Program, "Specification Criteria for Simple Performance Tests for Rutting",NCHRP Report 580, *Transportation Research Board*, National Research Council, 2007.

20. Biligiri, K., Kaloush, K., Mamlouk, M., and Witczak, M., "Rational Modeling of Tertiary Flow for Asphalt Mixtures", *Transportation Research Board*, TRB, Washington D.C., 2007.

21. Bonaquist, R., Christensen, D. and Stump, W. (2003), "Simple Performance Tester for Superpave Mix Design: First-Article Development and Evaluation*". NCHRP Report 513, Transportation Research Board,* TRB, Washington D.C., 2001.

22. Goh, S. W., and You., Z.,"A Simple Method to Determine the Tertiary Flow in the Repeated Load Test", *Proceedings of the Mid-Continent Transportation Research Forum*, University of Wisconsin-Madison, Madison, Wisconsin, 2008.

23. Zhou, F., Scoullion, T., Pellinen, and Sun, L., "Verification and Modeling of Three-stage Permanent Deformation Behavior of Asphalt Mixes", *Journal of Transportation Engineering*, ASCE, 2004.

24. Francken, L., "Permanent Deformation Law of Bituminous Road Mixes in Repeated Load Triaxial Compression", *Proceeding of Fourth International Conference on the Structural Design of Asphalt Pavements*, University of Michigan, Ann Arbor, MI, 1977.

25. Dongre, R., D'Angelo, J., Copeland, A., "Refinement of Flow Number as Determined by the Asphalt Mixture Performance Tester for Use in routine QC/QZ Practice", Transportation Research Board, TRB, Washington D.C., 2009.

26. Kaloush, K. E., « Simple Performance Test for Permanent Deformation of Asphalt Mixtures », PhD Dissertation, Department of Civil and Environmental Engineering, Arizona State Universtity, Tempe, Arizona., 2001.

27. National Cooperative Highway Research Program, "Specification Criteria for Simple Performance Tests for Rutting", Report 580 – Volume II- Flow Number and Flow Time, *Transportation Research Board*, National Research Council, 2007.

28. Sullivan, B. "Development of Flow Number and Flow Time Candidate Simple Performance Test for Asphalt Mixtures." M.S. thesis, Department of Civil and Environmental Engineering, Arizona State University, Tempe, AZ, 2002.

29. El-Basyouny, M,. and Goo Jeong, M., "Effective Temperature for Permanent Deformation and Fatigue Distress Analysis on Asphalt Mixtures", *Transportation Research Board*, TRB, Washington D.C., 2009.

30. Brown, S. F., and Bell, C.A. The "Validity of Design Procedures for the Permanent Deformation of Asphalt Pavements", *Proceedings of the 4th International Conference on the Structural Design of Asphalt Pavements*, Ann Arbor, Vol. 1, 1977, pp 467-482.

31. Siddharthan, R.V., El-Mously, M., Krishnamenon, N., and Sebaaly, P.E., "Validation of a Pavement Response Model using Full-Scale Field Tests," International Journal in Pavement Engineering, Vol. 3(2), 2002, pp. 85-9.

32. Siddharthan, R., Sebaaly, P.E., El-Desouky, M., Strand, D., and Huft, D. "Heavy Off-road Vehicle Tire-Pavement Interactions and Response," *Journal of Transportation Engineering*, ASCE, Vol. 131(3), March/April 2005, pp. 239-247.

33. Siddharthan, R. V., and P. E. Sebaaly, "Investigation of AC Layer Strains from Wide-base Single Tires," *Transportation Research Board*, National Research Council, Washington, D.C., 1999.

34. Wong, J. Y., "Theory of Ground Vehicles, Second Edition" Textbook, ISBN 0-471-52496-4, 1993. Department of Mechanical and Aerospace Engineering Carleton University, Ottawa, Canada.

35. Hajj, E., "Hot Mix Asphalt Mixtures for Nevada's Intersections", Ph.D. dissertation, University of Nevada-Reno, Nevada, December 2005.

36. Annual Book of ASTM Standards (2001). "Classifying highway vehicles from known axle count and Spacing." *American Society for Testing and Materials*, Method E1572-93, Vol. 04-03.

37. Gillespie, T.D., "Fundamentals of Vehicle Dynamics" Textbook, ISBN 1-56091-199-9, 1992.

38. Gillespie, T.D., and L. Balderas, "An Analytical Comparison of the Dynamic Performance of a European Heavy Vehicle and a Generic U.S. Heavy Vehicle," *The University of Michigan Transportation Research Institute*, Report No. UMTRI-87-17, August 1987, 374 p.

39. Rosset, J. M., "Dynamic and damping coefficients of foundations", *Proceedings of the ASCE National Convention on Dynamic Response of Pile Foundations: Analytical Aspects*, M. W. O'Neal and k. Dobry, eds., ASCE, New York, 1980, p. 1–30.

40. Epps, J.A., Leahy, R. B., Mitchell, T. Ashmore, C., Seeds, S., Alvi, and S., Monismith, C.L., "WesTrack – The Road to Performance-Related Specifications", *Proceedings of the International Conference on Accelerated Pavement Testing,* Reno, Nevada, 1999.

41.Chen, D., Bilyeu, J., Scullion, T., Lin, D., Zhou, F., "Forensic Evaluation of Premature Failures of Texas Specific Pavement Study-1 Sections", *J. Performance Construction Facility,* Texas, 2003, p. 67-74.

42. Sebaaly, P. E., "Dynamic forces on pavements: summary of tire testing data", Report No. FHWA-DTFH 61-90-C-00084, FHWA, U.S. Department of Transportation, 1992.

43. De Beer, M., and Fisher, C., "Contact stresses of pneumatic tires measured with the vehicle-road surface pressure transducer array (VRSPTA) system for the University of California at Berkeley (UCB) and the Nevada Automotive Test Center (NATC)", CSIR Report CR-97/053, Council for Sc. and Ind. Res., Pretoria, South Africa, 1997.

44. Myers, L., Roque, R., Ruth, B., and Drakos, C., "Measurement of contact stresses for different truck tire types to evaluate their influence on near-surface cracking and rutting", *Transportation Research Records*, Vol. 1655, TRB, National Research Council, Washington, D.C., 1999, p. 175–184.

45.Weissman, S. L., "Influence of tire-pavement contact stress distribution on development of distress mechanisms in pavements", *Transportation Research Records*, Vol. 1655, TRB, National Research Council, Washington, D.C., 1999, p. 161–167.

46. Fernandez, G.C.J., "REGDIG.sas Macro for Performing Multiple Linear Regression Analysis". Department of Applied Economics and Statistics, MS204, UNR, Reno NV.

47. Neter, J., Kutner, M.H., Nachtsheim, C.J. and Wasserman, W., "Applied Linear Regression Models", Irwin, Homewood, IL, 1996, chap. 8.

48. Dongre, R. N., Myers, L. A., and D'Angelo, J. A., "Conversion of Testing Frequency to Loading Time: Impact on Performance Predictions Obtained from the Mechanistic–Empirical Pavement Design Guide", *Presented at 85th Annual Meeting of the Transportation Research Board*, Washington, D.C., 2006.

49. Al-Qadi, I. L., Elseifi, M. A., Yoo, P. J., Dessouky, S. H., Gibson, N., Harman, T., D'Angelo, J., and Petros, K., "Accuracy of Current Complex Modulus Selection Procedure from Vehicular Load Pulse: NCHRP Project 1-37A Mechanistic–Empirical Pavement Design Guide", *Transportation Research Records*, Vol. 2087, TRB, National Research Council, Washington, D.C., 2008, pp. 81–90.

50. Al-Qadi, I. L., W. Xie, and Elseifi, M. A., "Frequency Determination from Vehicular Loading Time Pulse to Predict Appropriate Complex Modulus in MEPDG", *Journal of the Association of Asphalt Paving Technologists*, Vol. 77, 2008, pp. 739-772.

51. *Guide for Mechanistic-Empirical Design of New and Rehabilitated Pavement Structures*. NCHRP 1-37A Final Report. ARA, Inc., ERES Consultants Division, Champaign, Ill., 2004. http:/www.trb.org/mepdg/guide.htm.

52. National Cooperative Highway Research Program,"Recommended Performance-Related Specification for Hot-Mix Asphalt Construction: results of the WesTrack Project", *Transportation Research Board*, Washington, D.C., 2002.

53. Nichols Consulting Engineers,"WesTrack Database Beta Version", *Federal Highways Administration*, Nevada, 2002.

TABLES

Table 1. Summary of Tractor and Semitrailer Sizes and Weights.

Tractor Properties	
Center of gravity height, h_1, in. (m)	32.0 (0.82)
Center of gravity to steering axle distance, l_1, in. (m)	84.8 (2.15)
Wheelbase distance, L_1, in. (m)	224.4 (5.70)
Tandem axles spacing, c, in. (m)	47.2 (1.20)
Tractor total weight, W_1,lb (kN)	16,000 (71.0)
Static steering axle load, W_s, lb (kN)	12,000 (54.0)
Static driving axle load, W_d, lb (kN)	34,000 (152.0)
Semitrailer Properties	
Center of gravity height, h_2, in. (m)	76.0 (1.93)
Center of gravity to front articulation distance, d_2, in. (m)	204.7 (5.20)
Wheelbase distance, L_2, in. (m)	370.1 (9.40)
Tandem axles spacing, c′,in. (m)	47.2 (1.20)
Semitrailer total weight (fully loaded), W_2,lb (kN)	64,000 (285.0)
Static trailer axle load, W_t,lb (kN)	34,000 (152.0)
General Properties	
Articulation height, h_3, in. (m)	49.0 (1.25)
articulation offset, d_1, in. (m)	15.3 (0.39)
Vehicle total Weight, W, lb (kN)	80,000 (356.0)

Table 2. Summary of a U.S. Tractor-semitrailer Brake System Properties.

Truck unit	**Axle**	**Torque gain[+] (in-lb/psi)**	**Pushout pressure (psi)**
Tractor	Steering	1322.5	13.5
	Tandem leading driving	3280.0	5.8
	Tandem trailing driving	3280.0	5.8
Semi-trailer	Tandem leading trailer	2818.8	5.5
	Tandem trailing trailer	2818.8	5.5

[+] For a loaded truck-semitrailer

Table 3. Vertical Load on Various Axles of the Fully Loaded 18-Wheel Tractor-Trailer

Braking Action	**Axle**	**Vertical Load per Tire (lb)**	**Horizontal Load per Tire (lb)**
No Braking	Steering	6,000	0
	Front Driving	4,250	0
	Rear Driving	4,250	0
	Front Trailer	4,250	0
	Rear Trailer	4,250	0
Braking (at an average deceleration rate of 17.2 ft/sec^2)	Steering	8,489	2,161
	Front Driving	5,132	2,968
	Rear Driving	3,351	2,968
	Front Trailer	4,405	2,561
	Rear Trailer	2,868	2,561

Table 4. PG64-22 Mix Design and Aggregate Properties

Mix Design		
Nominal Maximum Aggregate Size, mm		12.5
Property	**Value**	**Requirement**
Design ESALs, millions	6	--
N_{inital}	8	--
N_{design}	100	--
N_{max}	160	--
Optimum Binder Content, %	5.85	--
Hydrated Lime, %	None	--
Liquid Antistrip, %	None	--
Max specific gravity, G_{mm}	2.424	--
%Gmm at N_{ini}	88.5	≤ 89.0
%Gmm at N_{des}	96.0	96.0
%Gmm at N_{max}	97.5	≤ 98.0
VMA, %	14.3	14.0% Min.
VFA, %	72.1	65-75
Percent Effective Binder P_{be}, %	4.50	--
Dust Proportion, $P_{0.075}/P_{be}$	1.2	0.6-1.2
Unconditioned Tensile Strength on 6" Gyratory Samples @ 77°F, psi	119	--
Conditioned Tensile Strength on 6" Gyratory Samples @77°F, psi	108	--
Tensile Strength Ratio, %	90	80 Min.

Aggregate Properties			
Aggregate Bulk Specific Gravity, G_{sb}			2.556
Aggregate Effective Specific Gravity, G_{se}			2.651
Sieve Size	**%Passing**	**Control Points**	
		Min	**Max**
19.0 mm (3/4")	100.0	100	--
12.5 mm (1/2")	94.3	90	100
9.5 mm (3/8")	85.9	--	90
4.75 mm (No. 4)	58.4	--	--
2.36 mm (No. 8)	42.1	28	58
2.00 mm (No. 10)	39.8	--	--
1.18 mm (No. 16)	34.2	--	--
0.6 mm (No. 30)	27.0	--	--
0.425 mm (No. 40)	21.6	--	--
0.3 mm (No. 50)	15.6	--	--
0.15 mm (No. 100)	8.2	--	--
0.075 mm (No. 200)	5.26	2	10
Aggregates	**Description**		**Bin %**
Aggr. 1	3/4 inch		10.0%
Aggr. 2	1/2 inch		10.0%
Aggr. 3	3/8 inch		28.0%
Aggr. 4	Rock Dust		30.0%
Aggr. 5	Wade Sand		22.0%

Table 5. PG58-22 Mix Design and Aggregate Properties

Mix Design		
Nominal Maximum Aggregate Size, mm		12.5
Property	**Value**	**Requirement**
Design ESALs, millions	6	--
N_{inital}	8	--
N_{design}	100	--
N_{max}	160	--
Optimum Binder Content, %	5.46	--
Hydrated Lime, %	None	--
Liquid Antistrip, %	None	--
Max specific gravity, G_{mm}	2.420	--
%Gmm at N_{ini}	88.6	≤ 89.0
%Gmm at N_{des}	96.0	96.0
%Gmm at N_{max}	96.9	≤ 98.0
VMA, %	14.1	14.0% Min.
VFA, %	71.6	65-75
Percent Effective Binder P_{be}, %	4.43	--
Dust Proportion, $P_{0.075}/P_{be}$	1.2	0.6-1.2
Unconditioned Tensile Strength on 6" Gyratory Samples @ 77°F, psi	114	--
Conditioned Tensile Strength on 6" Gyratory Samples @77°F, psi	97	--
Tensile Strength Ratio, %	85	80 Min.

Aggregate Properties			
Aggregate Bulk Specific Gravity, G_{sb}			2.556
Aggregate Effective Specific Gravity, G_{se}			2.628
Sieve Size	**%Passing**	**Control Points**	
		Min	**Max**
19.0 mm (3/4")	100.0	100	--
12.5 mm (1/2")	94.3	90	100
9.5 mm (3/8")	85.9	--	90
4.75 mm (No. 4)	58.4	--	--
2.36 mm (No. 8)	42.1	28	58
2.00 mm (No. 10)	39.8	--	--
1.18 mm (No. 16)	34.2	--	--
0.6 mm (No. 30)	27.0	--	--
0.425 mm (No. 40)	21.6	--	--
0.3 mm (No. 50)	15.6	--	--
0.15 mm (No. 100)	8.2	--	--
0.075 mm (No. 200)	5.26	2	10
Aggregates	**Description**		**Bin %**
Aggr. 1	3/4 inch		10.0%
Aggr. 2	1/2 inch		10.0%
Aggr. 3	3/8 inch		28.0%
Aggr. 4	Rock Dust		30.0%
Aggr. 5	Wade Sand		22.0%

Table 6. PG52-22 Mix Design and Aggregate Properties

Mix Design		
Nominal Maximum Aggregate Size, mm		12.5
Property	**Value**	**Requirement**
Design ESALs, millions	6	--
N_{inital}	8	--
N_{design}	100	--
N_{max}	160	--
Optimum Binder Content, %	5.61	--
Hydrated Lime, %	None	--
Liquid Antistrip, %	None	--
Max specific gravity, G_{mm}	2.425	--
%Gmm at N_{ini}	88.2	≤ 89.0
%Gmm at N_{des}	96.0	96.0
%Gmm at N_{max}	97.5	≤ 98.0
VMA, %	14.0	14.0% Min.
VFA, %	71.5	65-75
Percent Effective Binder P_{be}, %	4.35	--
Dust Proportion, $P_{0.075}/P_{be}$	1.2	0.6-1.2
Unconditioned Tensile Strength on 6" Gyratory Samples @ 77°F, psi	76	--
Conditioned Tensile Strength on 6" Gyratory Samples @77°F, psi	62	--
Tensile Strength Ratio, %	82	80 Min.

Aggregate Properties			
Aggregate Bulk Specific Gravity, G_{sb}			2.556
Aggregate Effective Specific Gravity, G_{se}			2.651
Sieve Size	**%Passing**	**Control Points**	
		Min	**Max**
19.0 mm (3/4")	100.0	100	--
12.5 mm (1/2")	94.3	90	100
9.5 mm (3/8")	85.9	--	90
4.75 mm (No. 4)	58.4	--	--
2.36 mm (No. 8)	42.1	28	58
2.00 mm (No. 10)	39.8	--	--
1.18 mm (No. 16)	34.2	--	--
0.6 mm (No. 30)	27.0	--	--
0.425 mm (No. 40)	21.6	--	--
0.3 mm (No. 50)	15.6	--	--
0.15 mm (No. 100)	8.2	--	--
0.075 mm (No. 200)	5.26	2	10
Aggregates	**Description**		**Bin %**
Aggr. 1	3/4 inch		10.0%
Aggr. 2	1/2 inch		10.0%
Aggr. 3	3/8 inch		28.0%
Aggr. 4	Rock Dust		30.0%
Aggr. 5	Wade Sand		22.0%

Table 7. Dynamic Modulus Testing Results – PG64-22 mix 7% Air voids.

Testing Temperature, ºC	Testing Frequency, Hz					
	25 Hz	10 Hz	5 Hz	1 Hz	0.5 Hz	0.1 Hz
Mixture |E*|, psi						
4.4	2,034,333	1,874,333	1,746,333	1,451,667	1,319,667	1,035,267
21.1	1,263,000	1,084,667	956,133	685,067	580,867	365,200
37.8	392,050	294,000	232,950	127,450	97,850	49,250
54.4	103,500	70,667	52,000	25,467	19,100	10,733
Mixture phase angle, º						
4.4	7.8	8.8	9.6	11.7	12.7	15.6
21.1	14.4	16.1	17.6	21.6	23.2	27.7
37.8	29.2	31.2	32.3	34.6	34.4	34.4
54.4	38.8	37.5	36.5	34.2	32.4	28.4

Table 8. Dynamic Modulus Testing Results — PG58-22 Mix.

Testing Temperature, ºC	Testing Frequency, Hz					
	25 Hz	10 Hz	5 Hz	1 Hz	0.5 Hz	0.1 Hz
Mixture |E*|, psi						
4.4	1,776,333	1,610,667	1,481,333	1,175,000	1,044,333	767,000
21.1	833,733	681,533	577,967	365,233	297,033	167,900
37.8	290,267	208,667	160,533	80,767	60,000	29,867
54.4	85,167	56,967	41,600	20,400	15,800	9,667
Mixture phase angle, º						
4.4	9.6	10.8	11.8	14.7	16.2	20.1
21.1	20.4	23.0	24.9	29.4	30.7	33.6
37.8	33.6	34.8	35.1	35.6	35.0	33.5
54.4	39.4	37.3	35.8	32.8	30.7	26.3

Table 9. Dynamic Modulus Testing Results – PG52-22 Mix.

Testing Temperature, ºC	Testing Frequency, Hz					
	25 Hz	10 Hz	5 Hz	1 Hz	0.5 Hz	0.1 Hz
Mixture |E*|, psi						
4.4	2,066,667	1,873,333	1,718,667	1,346,000	1,182,000	813,000
21.1	860,067	671,967	540,100	308,600	225,150	98,700
37.8	182,933	121,750	82,250	26,850	18,400	9,300
54.4	41,767	24,633	16,700	8,267	6,833	5,200
Mixture phase angle, º						
4.4	9.5	11.1	12.4	16.6	18.8	25.0
21.1	25.6	29.1	32.3	38.4	39.7	41.1
37.8	43.6	43.8	43.3	41.2	39.0	32.6
54.4	43.3	39.9	37.4	30.6	27.3	19.8

Table 10. Properties of Pavement Materials.

Layer	**Thickness, inch (m)**	**Unit Weight, pci (kN/m^3)**	**Shear Modulus, psi (kPa)**	**Damping Ratio**	**Poisson's Ratio, ν**
HMA	4, 6 & 8 (0.1, 0.15 & 0.2)	0.0876 (23.8)	Variable	Variable	0.40
Base	6, 8 & 10 (0.15, 0.2 & 0.25)	0.0663 (18.0)	12,500 (8.6×10^4)	5.0%	0.40
Subgrade	400 (10)	0.0626 (17.0)	5,357.1 (3.7×10^4)	5.0%	0.40

Table 11. Maximum Stresses of Steering vs Tandem axle for PG64-22 mix – Non-braking.

HMA layer temperature (°C)	HMA layer thickness (in)	18-wheel traveling speed (mph)	Max deviator stress, σ_d (psi)			Max confining stress, σ_c (psi)			Vertical stress, σ_Z (psi)		
			Single	Tandem	Difference	Single	Tandem	Difference	Single	Tandem	Difference
40	4	20	103	98	5	34	28	6	90	87	3
		40	103	100	2	33	28	5	88	85	3
		60	104	102	2	32	27	5	87	84	3
	6	20	83	77	7	54	44	10	104	101	4
		40	84	77	7	56	46	10	104	100	3
		60	84	77	7	58	47	10	103	100	3
	8	20	73	71	3	52	43	9	110	105	5
		40	73	70	3	55	45	9	109	105	5
		60	73	69	4	56	47	10	109	105	5
50	4	20	93	88	5	39	31	8	102	97	5
		40	98	90	7	38	31	7	99	94	5
		60	100	92	8	37	30	7	97	92	5
	6	20	81	77	4	45	37	9	109	104	5
		40	81	77	4	48	39	9	107	103	4
		60	82	77	5	49	40	9	107	103	4
	8	20	76	74	2	44	36	8	112	106	6
		40	76	73	2	46	38	9	112	106	6
		60	75	72	3	48	39	9	113	106	7
60	4	20	80	80	0	41	33	8	112	107	6
		40	84	82	2	41	33	8	110	104	6
		60	86	82	3	41	33	8	109	103	6
	6	20	80	78	1	41	32	9	112	107	5
		40	80	78	2	41	33	8	112	107	5
		60	80	77	2	42	34	8	111	106	5
	8	20	79	78	1	38	31	7	113	108	6
		40	78	77	1	40	32	8	113	107	6
		60	78	76	2	41	33	8	113	107	6
70	4	20	79	81	-2	42	34	8	119	113	6
		40	79	80	-1	42	34	8	118	112	6
		60	79	80	-1	42	34	8	117	111	6
	6	20	81	81	0	36	29	7	116	110	6
		40	81	80	1	37	30	7	116	109	6
		60	81	80	1	37	30	7	115	109	6
	8	20	81	80	1	35	29	7	115	108	6
		40	80	80	1	36	29	7	114	108	6
		60	80	79	1	37	30	7	114	109	6

Table 12. Maximum Stresses of Steering vs Tandem axle for PG58-22 mix – Non-braking.

HMA layer temperature (°C)	HMA layer thickness (in)	18-wheel traveling speed (mph)	Max deviator stress, σ_d (psi)			Max confining stress, σ_c (psi)			Vertical stress, σ_z (psi)		
			Single	Tandem	Difference	Single	Tandem	Difference	Single	Tandem	Difference
40	4	20	100	91	9	37	30	7	96	92	4
		40	104	94	10	36	29	6	93	89	4
		60	107	96	11	35	29	6	91	88	3
	6	20	84	77	7	47	40	7	108	102	5
		40	83	77	6	51	42	10	106	102	4
		60	83	77	7	53	43	10	105	101	4
	8	20	75	73	3	48	39	9	111	106	5
		40	74	72	3	50	41	9	110	105	5
		60	74	72	2	51	42	9	110	105	5
50	4	20	88	84	4	40	32	8	105	103	2
		40	92	87	5	39	31	8	102	101	1
		60	96	89	7	38	31	7	100	98	2
	6	20	80	77	4	44	35	8	110	106	4
		40	81	77	4	46	37	9	109	106	3
		60	81	77	4	47	38	9	108	104	4
	8	20	77	75	2	43	34	8	112	108	4
		40	76	75	2	44	36	8	111	107	4
		60	76	74	2	46	37	9	111	105	6
60	4	20	81	80	1	41	33	8	111	104	7
		40	84	81	3	41	33	8	109	103	6
		60	86	83	3	41	33	9	107	103	4
	6	20	80	78	2	40	32	8	113	105	8
		40	80	78	2	42	34	8	111	106	5
		60	80	77	3	43	35	8	111	106	5
	8	20	79	77	1	39	31	7	113	107	6
		40	78	76	2	41	33	8	113	105	8
		60	78	76	2	42	34	8	112	106	6
70	4	20	78	79	0	42	34	8	115	110	5
		40	80	79	1	42	33	8	113	110	3
		60	81	80	1	42	33	8	112	110	2
	6	20	80	79	1	38	31	7	114	109	5
		40	80	78	1	39	32	7	114	110	4
		60	80	78	2	40	32	8	113	109	4
	8	20	79	79	1	37	30	7	114	108	6
		40	79	78	1	38	31	7	114	107	7
		60	79	78	1	39	32	7	113	109	4

Table 13. Maximum Stresses of Steering vs Tandem axle for PG52-22 mix – Non-braking.

HMA layer temperature (°C)	HMA layer thickness (in)	18-wheel traveling speed (mph)	Max deviator stress, σ_d (psi)			Max confining stress, σ_c (psi)			Vertical stress, σ_z (psi)		
			Single	Tandem	Difference	Single	Tandem	Difference	Single	Tandem	Difference
40	4	20	94	89	5	39	31	8	103	98	6
		40	99	92	7	38	30	7	99	94	5
		60	103	94	9	37	30	7	96	93	3
	6	20	83	79	4	44	36	8	109	103	6
		40	84	79	5	47	38	9	108	103	4
		60	84	79	5	48	39	9	107	103	4
	8	20	78	76	2	43	35	8	112	106	6
		40	78	75	3	45	36	9	111	106	5
		60	77	74	3	47	38	9	111	107	4
50	4	20	82	81	1	41	33	8	113	109	4
		40	86	83	3	41	32	8	110	108	2
		60	89	86	4	40	32	8	107	104	3
	6	20	81	79	2	39	31	7	113	106	7
		40	82	79	3	41	33	8	112	106	6
		60	82	79	3	42	34	8	111	106	5
	8	20	80	78	2	38	31	7	113	108	5
		40	79	78	2	39	32	8	113	109	4
		60	79	77	2	41	33	8	112	108	4
60	4	20	79	80	-1	42	33	8	118	112	6
		40	79	80	-1	42	33	9	116	113	3
		60	81	80	0	42	33	9	115	112	3
	6	20	81	81	1	36	29	7	116	110	6
		40	81	80	1	37	30	7	115	109	6
		60	81	80	2	38	31	7	114	109	5
	8	20	81	80	1	36	29	7	114	111	3
		40	80	79	1	37	30	7	114	110	4
		60	80	79	1	37	30	7	114	109	5
70	4	20	79	82	-2	42	34	8	121	115	6
		40	79	81	-2	42	33	8	119	114	5
		60	80	81	-1	42	34	8	118	115	3
	6	20	82	82	0	35	29	7	117	112	5
		40	82	81	1	36	29	7	116	110	6
		60	82	81	1	36	30	6	116	110	6
	8	20	81	81	1	35	28	6	115	110	5
		40	81	80	1	35	29	7	115	111	4
		60	81	80	1	36	29	7	115	111	4

Table 14. Maximum Stresses of Steering vs Tandem axle for PG64-22 mix –Braking.

HMA layer temperature (°C)	HMA layer thickness (in)	18-wheel traveling speed (mph)	Max deviator stress, σ_d (psi)			Max confining stress, σ_c (psi)			Vertical stress, σ_Z (psi)		
			Single	Tandem	Difference	Single	Tandem	Difference	Single	Tandem	Difference
40	4	2	115	123	-8	46	33	13	106	100	5
		20	134	132	1	41	30	12	95	91	4
	6	2	101	112	-11	56	41	15	112	108	4
		20	108	113	-5	65	47	18	107	105	2
	8	2	93	109	-17	55	41	14	115	110	5
		20	95	108	-13	64	47	17	113	109	4
50	4	2	95	117	-21	50	36	14	117	111	6
		20	112	122	-10	47	33	13	107	101	6
	6	2	93	112	-19	47	35	12	117	110	7
		20	99	112	-13	54	40	14	113	108	5
	8	2	91	110	-19	46	35	11	118	111	7
		20	93	110	-17	53	40	14	116	112	4
60	4	2	87	113	-26	50	37	13	123	114	9
		20	94	116	-22	50	36	14	118	110	8
	6	2	90	112	-22	43	32	10	121	106	15
		20	93	112	-19	47	35	12	118	112	6
	8	2	90	111	-20	42	32	10	119	112	7
		20	91	110	-19	46	35	11	118	113	5
70	4	2	85	113	-28	49	37	13	126	118	8
		20	87	113	-27	50	37	13	123	118	5
	6	2	90	112	-22	43	31	12	121	117	4
		20	90	112	-22	43	32	10	121	116	5
	8	2	90	111	-20	40	31	10	120	115	5
		20	91	111	-20	42	32	10	119	116	3

Table 15. Maximum Stresses of Steering vs Tandem axle for PG58-22 mix –Braking.

HMA layer temperature (°C)	HMA layer thickness (in)	18-wheel traveling speed (mph)	Max deviator stress, σ_d (psi)			Max confining stress, σ_c (psi)			Vertical stress, σ_z (psi)		
			Single	Tandem	Diference	Single	Tandem	Diference	Single	Tandem	Diference
40	4	2	103	119	-16	48	35	13	112	106	6
		20	123	127	-4	44	32	12	102	97	5
	6	2	97	112	-15	51	38	13	115	110	5
		20	104	113	-9	59	44	15	110	104	6
	8	2	92	110	-18	50	37	13	117	111	6
		20	94	109	-15	58	43	15	114	110	4
50	4	2	92	115	-23	50	37	13	119	111	8
		20	106	120	-14	48	34	14	111	106	5
	6	2	91	112	-21	46	35	11	119	112	7
		20	98	112	-14	52	39	13	114	107	7
	8	2	91	110	-19	45	34	11	118	112	6
		20	92	110	-18	51	38	13	116	109	7
60	4	2	87	113	-26	50	37	13	123	114	9
		20	96	117	-21	49	36	13	116	110	6
	6	2	90	112	-22	43	33	10	121	114	7
		20	94	112	-18	48	36	12	117	110	7
	8	2	90	111	-21	42	32	10	119	112	7
		20	91	111	-20	47	35	12	118	111	7
70	4	2	85	113	-28	50	37	13	125	116	9
		20	90	114	-24	50	37	13	120	116	4
	6	2	89	112	-23	42	31	11	122	115	7
		20	91	112	-21	45	32	13	119	112	7
	8	2	90	111	-21	41	31	10	120	114	6
		20	91	111	-20	44	32	12	118	115	3

Table 16. Maximum Stresses of Steering vs Tandem axle for PG52-22 mix –Braking.

HMA layer temperature (°C)	HMA layer thickness (in)	18-wheel traveling speed (mph)	Max deviator stress, σ_d (psi)			Max confining stress, σ_c (psi)			Vertical stress, σ_Z (psi)		
			Single	Tandem	Difference	Single	Tandem	Difference	Single	Tandem	Difference
40	4	2	92	116	-24	50	36	14	120	115	5
		20	113	125	-12	46	33	13	110	103	6
	6	2	92	113	-21	45	34	11	119	114	5
		20	102	114	-12	52	39	13	114	109	5
	8	2	91	111	-20	44	33	11	118	112	6
		20	95	111	-16	51	38	13	116	110	6
50	4	2	86	113	-27	50	37	13	124	116	8
		20	95	118	-23	49	36	13	118	112	6
	6	2	89	112	-23	42	32	10	121	115	6
		20	94	113	-19	46	35	11	118	113	5
	8	2	90	111	-21	41	31	10	120	113	7
		20	92	111	-19	45	34	11	118	110	8
60	4	2	84	113	-29	49	37	12	126	118	8
		20	88	114	-26	50	37	13	123	114	9
	6	2	89	112	-23	41	31	10	122	116	6
		20	91	112	-21	43	33	10	121	114	7
	8	2	90	111	-21	40	31	9	120	115	5
		20	91	111	-20	42	32	10	119	113	6
70	4	2	84	113	-29	49	37	12	127	119	8
		20	85	113	-28	50	37	13	125	116	9
	6	2	89	112	-23	41	31	10	123	118	5
		20	89	112	-23	42	32	10	122	115	7
	8	2	90	111	-21	40	30	10	120	114	6
		20	90	111	-21	41	31	10	120	112	8

Table 17. Maximum Stresses at 2 inch Below the Pavement Surface of the PG64-22 mix.

HMA layer temperature (ºC)	HMA layer thickness (in)	18-wheel traveling speed (mph)	Max deviator stress, σ_d (psi)	Max confining stress, σ_c (psi)	Total vertical stress, $\sigma_d + \sigma_c$ (psi)
40	4	2 (braking)	123	33	156
		20 (braking)	132	30	162
		20	98	28	126
		40	101	28	128
		60	102	27	129
	6	2 (braking)	112	41	153
		20 (braking)	113	47	160
		20	77	44	120
		40	77	46	123
		60	77	47	124
	8	2 (braking)	109	41	150
		20 (braking)	108	47	155
		20	71	43	114
		40	70	45	115
		60	69	47	116
50	4	2 (braking)	117	36	153
		20 (braking)	122	33	155
		20	88	31	119
		40	90	31	121
		60	92	30	122
	6	2 (braking)	112	35	148
		20 (braking)	112	40	152
		20	77	37	113
		40	77	39	116
		60	77	40	117
	8	2 (braking)	110	35	145
		20 (braking)	110	40	150
		20	74	36	110
		40	73	38	111
		60	73	39	111
60	4	2 (braking)	113	37	150
		20 (braking)	116	36	152
		20	80	33	113
		40	82	33	115
		60	82	33	115
	6	2 (braking)	112	32	144
		20 (braking)	112	35	147
		20	78	32	110
		40	78	33	111
		60	77	34	111
	8	2 (braking)	111	32	142
		20 (braking)	111	35	146
		20	78	31	109
		40	77	32	109
		60	76	33	109
70	4	2 (braking)	113	37	150
		20 (braking)	113	37	150
		20	81	34	115
		40	80	34	114
		60	80	34	114
	6	2 (braking)	112	31	143
		20 (braking)	112	32	144
		20	81	29	110
		40	80	30	110
		60	80	30	110
	8	2 (braking)	111	31	142
		20 (braking)	111	32	143
		20	80	29	109
		40	80	29	109
		60	79	30	109

Table 18. Maximum Stresses at 2 inch Below the Pavement Surface of the PG58-22 mix.

HMA layer temperature (ºC)	HMA layer thickness (in)	18-wheel traveling speed (mph)	Max deviator stress, σ_d (psi)	Max confining stress, σ_c (psi)	Total vertical stress, $\sigma_d + \sigma_c$ (psi)
40	4	2 (braking)	119	35	154
		20 (braking)	127	32	159
		20	91	30	121
		40	94	30	124
		60	96	29	125
	6	2 (braking)	112	38	150
		20 (braking)	113	44	157
		20	77	40	117
		40	77	42	119
		60	77	43	120
	8	2 (braking)	110	37	147
		20 (braking)	109	43	152
		20	73	39	112
		40	72	41	113
		60	72	42	114
50	4	2 (braking)	115	37	152
		20 (braking)	120	34	154
		20	84	32	116
		40	87	31	118
		60	89	31	120
	6	2 (braking)	112	35	146
		20 (braking)	112	39	151
		20	77	35	112
		40	77	37	114
		60	77	38	115
	8	2 (braking)	110	34	144
		20 (braking)	110	38	148
		20	75	34	109
		40	75	36	111
		60	74	37	111
60	4	2 (braking)	113	37	150
		20 (braking)	117	36	153
		20	80	33	113
		40	81	33	114
		60	83	33	116
	6	2 (braking)	112	33	144
		20 (braking)	112	36	148
		20	78	32	110
		40	78	34	112
		60	77	35	112
	8	2 (braking)	111	32	143
		20 (braking)	111	35	146
		20	77	31	108
		40	76	33	109
		60	76	34	110
70	4	2 (braking)	113	37	150
		20 (braking)	114	37	151
		20	79	34	113
		40	79	33	112
		60	80	33	113
	6	2 (braking)	112	31	142
		20 (braking)	112	32	144
		20	79	31	110
		40	78	32	110
		60	78	32	110
	8	2 (braking)	111	31	142
		20 (braking)	111	32	143
		20	79	30	109
		40	78	31	109
		60	78	32	110

Table 19. Maximum Stresses at 2 inch Below the Pavement Surface of the PG52-22 mix.

HMA layer temperature (ºC)	HMA layer thickness (in)	18-wheel traveling speed (mph)	Max deviator stress, σ_d (psi)	Max confining stress, σ_c (psi)	Total vertical stress, $\sigma_d + \sigma_c$ (psi)
40	4	2 (braking)	116	36	152
		20 (braking)	125	33	158
		20	89	31	120
		40	92	30	122
		60	94	30	124
	6	2 (braking)	113	34	147
		20 (braking)	114	39	153
		20	79	36	115
		40	79	38	117
		60	79	39	118
	8	2 (braking)	111	33	144
		20 (braking)	111	38	149
		20	76	35	111
		40	75	37	112
		60	74	38	112
50	4	2 (braking)	113	37	150
		20 (braking)	118	36	154
		20	81	33	114
		40	84	32	116
		60	86	32	118
	6	2 (braking)	112	32	144
		20 (braking)	113	35	148
		20	79	31	110
		40	79	33	112
		60	79	34	113
	8	2 (braking)	111	31	142
		20 (braking)	111	34	145
		20	78	31	109
		40	78	32	110
		60	77	33	110
60	4	2 (braking)	113	37	150
		20 (braking)	114	37	151
		20	80	33	113
		40	80	33	113
		60	80	33	113
	6	2 (braking)	112	31	143
		20 (braking)	112	33	145
		20	81	29	110
		40	80	30	110
		60	80	31	111
	8	2 (braking)	111	31	142
		20 (braking)	111	32	143
		20	80	29	109
		40	79	30	109
		60	79	30	109
70	4	2 (braking)	113	37	150
		20 (braking)	113	37	150
		20	82	34	116
		40	81	34	115
		60	81	34	115
	6	2 (braking)	112	31	143
		20 (braking)	112	32	144
		20	82	29	111
		40	81	29	110
		60	81	30	111
	8	2 (braking)	111	30	141
		20 (braking)	111	31	142
		20	81	28	109
		40	80	29	109
		60	80	29	109

Table 20. Pulse Duration at 2 inch Below the Pavement Surface.

HMA layer temperature (°C)	HMA layer thickness (in)	18-wheel traveling speed (mph)	Deviator stress pulse duration, sec		
			PG 64-22 Mix	PG 58-22 Mix	PG 52-22 Mix
40	4	2 (braking)	0.456	0.436	0.415
		20 (braking)	0.051	0.048	0.043
		20	0.065	0.061	0.055
		40	0.033	0.031	0.029
		60	0.023	0.022	0.020
	6	2 (braking)	0.433	0.433	0.426
		20 (braking)	0.046	0.043	0.043
		20	0.069	0.062	0.056
		40	0.036	0.032	0.030
		60	0.025	0.023	0.021
	8	2 (braking)	0.444	0.424	0.435
		20 (braking)	0.045	0.042	0.044
		20	0.066	0.061	0.056
		40	0.035	0.032	0.029
		60	0.024	0.022	0.020
50	4	2 (braking)	0.416	0.415	0.415
		20 (braking)	0.043	0.043	0.041
		20	0.057	0.057	0.051
		40	0.030	0.028	0.026
		60	0.020	0.020	0.018
	6	2 (braking)	0.432	0.424	0.432
		20 (braking)	0.043	0.043	0.043
		20	0.058	0.056	0.051
		40	0.031	0.029	0.026
		60	0.021	0.020	0.018
	8	2 (braking)	0.432	0.433	0.429
		20 (braking)	0.045	0.043	0.043
		20	0.060	0.055	0.051
		40	0.030	0.028	0.026
		60	0.021	0.020	0.018
60	4	2 (braking)	0.412	0.415	0.432
		20 (braking)	0.042	0.042	0.042
		20	0.051	0.052	0.049
		40	0.027	0.027	0.025
		60	0.018	0.019	0.017
	6	2 (braking)	0.430	0.433	0.429
		20 (braking)	0.043	0.043	0.043
		20	0.051	0.052	0.049
		40	0.027	0.027	0.025
		60	0.018	0.019	0.017
	8	2 (braking)	0.434	0.442	0.426
		20 (braking)	0.043	0.043	0.044
		20	0.051	0.052	0.049
		40	0.026	0.027	0.025
		60	0.018	0.018	0.017
70	4	2 (braking)	0.422	0.424	0.435
		20 (braking)	0.041	0.042	0.042
		20	0.048	0.050	0.047
		40	0.024	0.026	0.024
		60	0.016	0.018	0.016
	6	2 (braking)	0.432	0.424	0.432
		20 (braking)	0.045	0.043	0.042
		20	0.049	0.050	0.049
		40	0.024	0.026	0.024
		60	0.016	0.018	0.016
	8	2 (braking)	0.432	0.424	0.426
		20 (braking)	0.044	0.043	0.042
		20	0.049	0.051	0.049
		40	0.025	0.026	0.024
		60	0.017	0.018	0.016

Table 21. WesTrack Experimental Design.

Original 1995 Construction										1997 Rehabilitation		
Design Air Void Content %	Aggregate Gradation Design											
	Fine			Fine Plus			Coarse			Coarse		
	Design Asphalt Contents (%)											
	4.7	5.4	6.1	4.7	5.4	6.1	5.0	5.7	6.4	5.1	5.8	6.5
4		4	18		12	21/9		23	25		39	55
8	2	1/15	14	22	19/11	13	8	5/24	7	38	35/54	37
12	3/16	17		10	20		26	6		56	36	

Table 22. Properties of WesTrack cells 19 and 55.

Property	**Section 19**	**Section 55**
Binder Grade/ Source	PG 64-22; West Coast	PG 64-22; Idaho
HMA Thickness	6 inches	6 inches
Aggregate Source	Quarry near Dayton, NV (partially crushed fluvial deposit); Sand from Wadsworth, NV	Lockwood
Aggregate Gradation	Fine-Plus	Coarse
Asphalt Content (%)	5.4 (Optimum)	6.5 (Opt +0.7%)
In-place Air Void (%)	8	4

Table 23. Dynamic Modulus Testing Results – WesTrack Cell 55.

Testing Temperature, ºC	Testing Frequency, Hz					
	25 Hz	10 Hz	5 Hz	1 Hz	0.5 Hz	0.1 Hz
Mixture |E*|, psi						
4.4	1,776,333	1,610,667	1,481,333	1,175,000	1,044,333	767,000
21.1	833,733	681,533	577,967	365,233	297,033	167,900
37.8	290,267	208,667	160,533	80,767	60,000	29,867
54.4	85,167	56,967	41,600	20,400	15,800	9,667
Mixture phase angle, º						
4.4	9.6	10.8	11.8	14.7	16.2	20.1
21.1	20.4	23.0	24.9	29.4	30.7	33.6
37.8	33.6	34.8	35.1	35.6	35.0	33.5
54.4	39.4	37.3	35.8	32.8	30.7	26.3

Table 24. Dynamic Modulus Testing Results – WesTrack Cell 19.

Testing Temperature, ºC	Testing Frequency, Hz					
	25 Hz	10 Hz	5 Hz	1 Hz	0.5 Hz	0.1 Hz
Mixture |E*|, psi						
4.4	2,280,000	2,139,000	2,030,500	1,769,500	1,651,000	1,365,000
21.1	1,296,500	1,123,000	993,350	713,550	607,600	383,600
37.8	490,400	366,950	286,550	149,050	109,900	51,000
54.4	137,400	90,700	64,400	28,750	20,850	11,150
Mixture phase angle, º						
4.4	6.1	6.8	7.4	9.1	10.0	12.6
21.1	14.2	16.2	18.0	22.9	24.8	30.1
37.8	29.7	32.2	33.8	36.6	36.7	36.4
54.4	41.0	39.9	38.9	36.5	34.5	29.0

Table 25. Flow Number Test Conditions and Results – WesTrack Cell 55.

Testing Temp (°C)	Dynamic Modulus (psi)	Deviator Stress (psi)	Confining Stress (psi)	Rep	Flow Number Three Stage Method		Flow Number Stepwise Method		Flow Number Francken Method	
					Result	Average	Result	Average	Result	Average
40	258,000	77	42	1	No FN*	No FN*	19,900	19,250	No FN*	No FN*
				2	No FN*		18,600		No FN*	
45	182,000	77	39	1	11,400	11,950	9,700	10,200	4,395	5,345
				2	12,500		10,700		6,295	
50	130,000	77	37	1	7,100	6,900	6,900	6,450	4,095	3,845
				2	6,700		6,000		3,595	
55	95,600	77	35	1	4,000	4,050	3,200	3,100	1,795	1,695
				2	4,100		3,000		1,595	

* A flow number was not found

Table 26. Flow Number Test Conditions and Results – WesTrack Cell 19.

Testing Temperature (°C)	Dynamic Modulus (psi)	Deviator Stress (psi)	Confining Stress (psi)	Rep	Flow Number Three Stage Method	Flow Number Stepwise Method	Flow Number Francken Method
30	868,965	77	64	1	No FN*	20000	No FN*
35	627,812	76	59	1	No FN*	18295	No FN*
40	437,213	76	53	1	4449	4295	2595
45	297,583	75	47	1	3196	2697	1995
50	201,212	75	43	1	946	896	545
55	137,380	76	39	1	195	300	172

* A flow number was not found

Table 27. Dynamic Modulus Testing Results – PG64-22 mix 4% Air voids.

Testing Temperature, ºC	Testing Frequency, Hz					
	25 Hz	10 Hz	5 Hz	1 Hz	0.5 Hz	0.1 Hz
Mixture |E*|, psi						
4.4	2,410,000	2,224,500	2,082,500	1,753,000	1,611,000	1,288,500
21.1	1,282,000	1,086,500	947,750	655,000	550,900	344,850
37.8	477,900	359,200	285,250	154,400	117,900	60,250
54.4	152,200	104,450	76,850	37,300	27,850	15,550
Mixture phase angle, º						
4.4	7.7	8.5	9.2	11.3	12.3	15.2
21.1	16.7	18.7	20.3	24.3	25.6	28.9
37.8	30.0	31.4	32.0	33.2	32.8	32.2
54.4	37.8	35.9	34.6	32.5	30.8	27.1

Table 28. Dynamic Modulus Testing Results – PG64-22 mix 2% Air voids

Testing Temperature, ºC	Testing Frequency, Hz					
	25 Hz	10 Hz	5 Hz	1 Hz	0.5 Hz	0.1 Hz
Mixture |E*|, psi						
4.4	2,754,000	2,560,500	2,412,500	2,058,000	1,901,500	1,543,000
21.1	1,534,500	1,315,000	1,156,000	815,650	691,650	441,250
37.8	603,500	459,000	367,350	203,600	157,050	83,200
54.4	196,900	136,750	101,900	50,800	39,000	22,500
Mixture phase angle, º						
4.4	7.4	8.0	8.6	10.3	11.2	13.6
21.1	15.6	17.6	19.1	23.0	24.3	27.8
37.8	28.9	30.5	31.3	32.8	32.4	31.8
54.4	37.1	35.7	34.7	32.6	31.0	27.2

Table 29. Flow Number Test Conditions and Results – PG64-22 mix.

Testing Temp (°C)	Dynamic Modulus (psi)	Deviator Stress (psi)	Confining Stress (psi)	Rep	Flow Number Three Stage Method		Flow Number Stepwise Method		Flow Number Francken Method	
					Result	Average	Result	Average	Result	Average
PG64-22 Mix at 7% Air Voids										
35	536,355	77	54	1	No FN*	No FN*	No FN*	No FN*	No FN*	No FN*
				2	No FN*		No FN*		No FN*	
40	370,573	76	49	1	10,600	10,300	10,297	9,748	4,795	5,045
				2	9,999		9,198		5,295	
45	250,272	76	44	1	4,499	3,750	4,095	3,995	2,895	2,495
				2	3,000		3,895		2,095	
50	168,416	76	40	1	1,998	1,948	1,999	1,948	1,095	1,045
				2	1,897		1,896		995	
PG64-22 Mix at 4% Air Voids										
40	439,407	76	52	1	No FN*	No FN*	No FN*	No FN*	No FN*	No FN*
				2	No FN*		No FN*		No FN*	
45	314,857	75	48	1	7,999	7,497	7,495	6,947	6,095	5,445
				2	6,995		6,398		4,795	
50	226,523	75	44	1	4,696	4,747	4,895	4,797	4,095	3,845
				2	4,798		4,699		3,595	
PG64-22 Mix at 2% Air Voids										
40	551,586	75	59	1	No FN*	No FN*	No FN*	No FN*	No FN*	No FN*
				2	No FN*		No FN*		No FN*	
45	399,534	75	53	1	13,699	12,097	15,598	13,197	12,820	13,149
				2	10,495		10,796		13,477	
50	290,276	74	48	1	8,796	7,847	9,795	8,695	8,595	7,745
				2	6,897		7,595		6,895	

* A flow number was not found

FIGURES

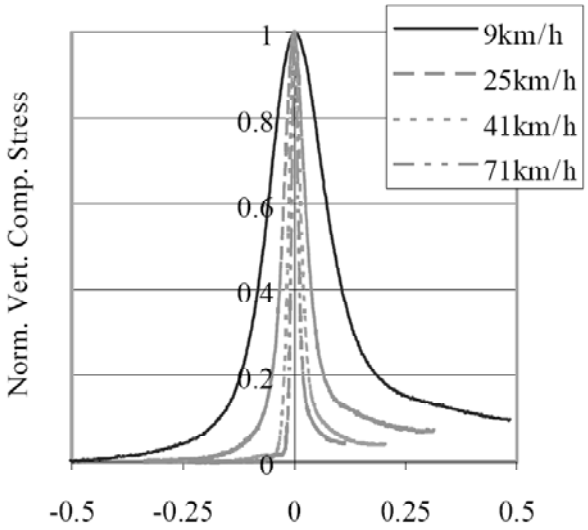

Figure 1 Measured normalized compressive stress pulse at Virginia Smart Road (10).

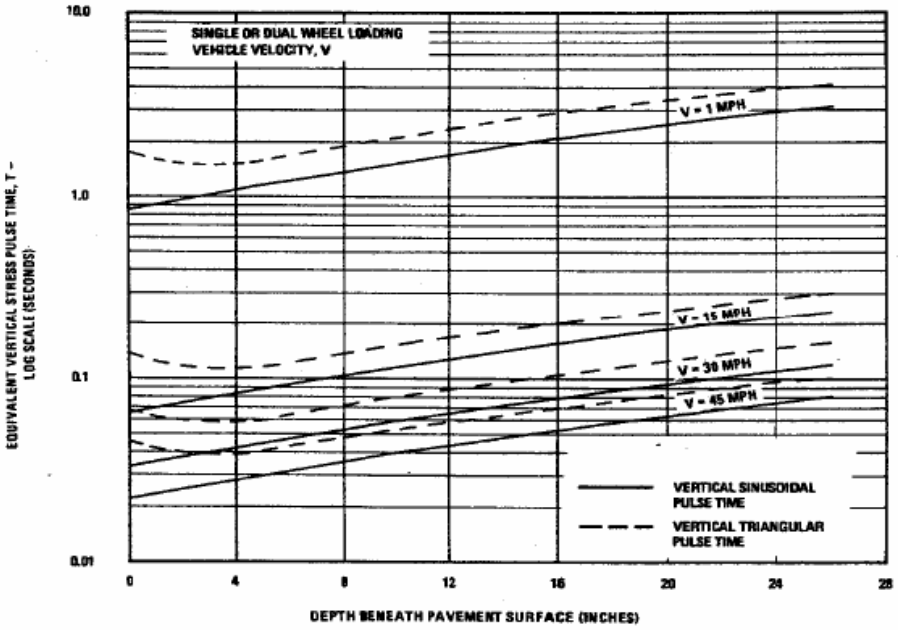

Figure 2 Vertical stress pulse time under haversine or triangular loading (Barksdale).

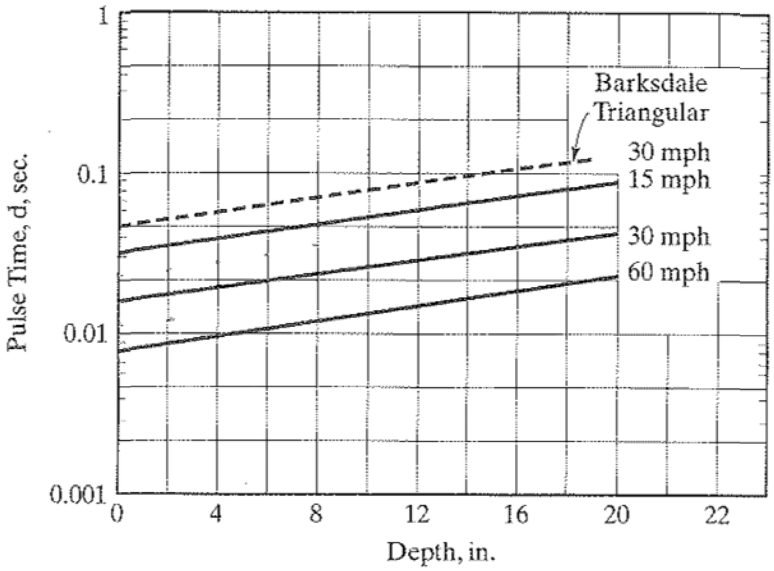

Figure 3 Vertical stress pulse time under square wave form (McLean).

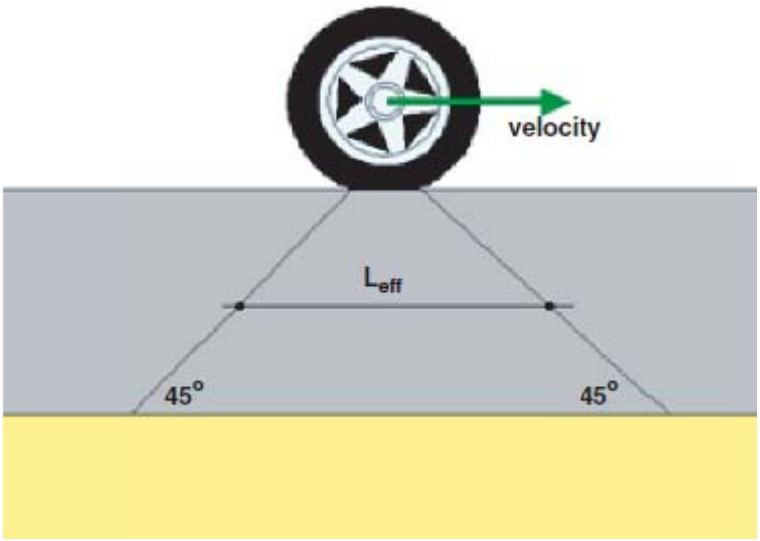

Figure 4 Schematic of load pulse frequency determination by MEPDG.

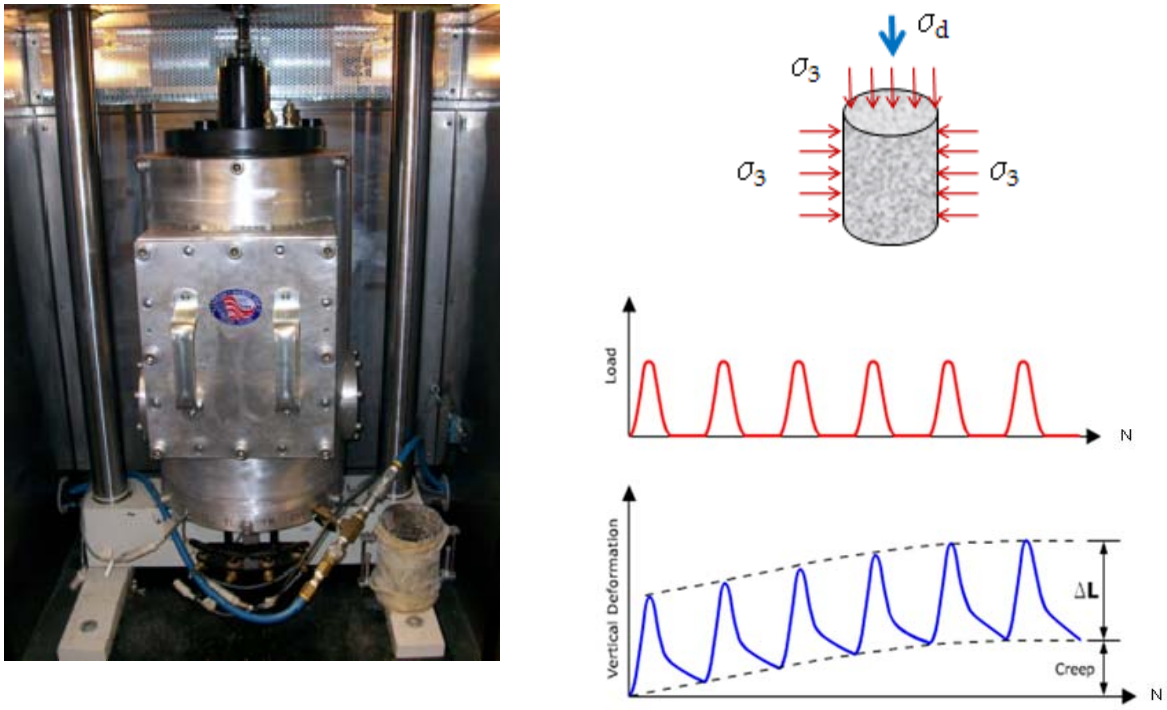

Figure 5 Repeated Load Triaxial (RLT) schematics.

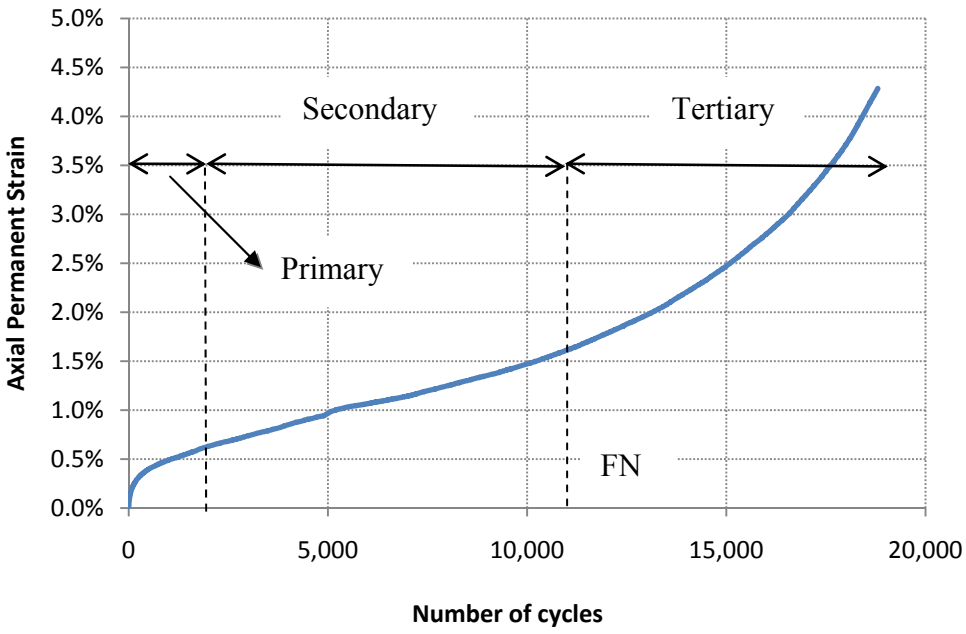

Figure 6 Cumulative permanent axial strain vs number of cycles.

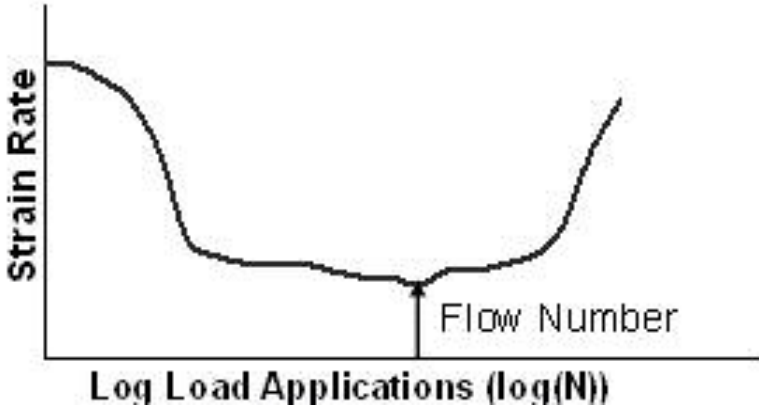

Figure 7 Determination of flow number as the cycle with minimum strain rate (20).

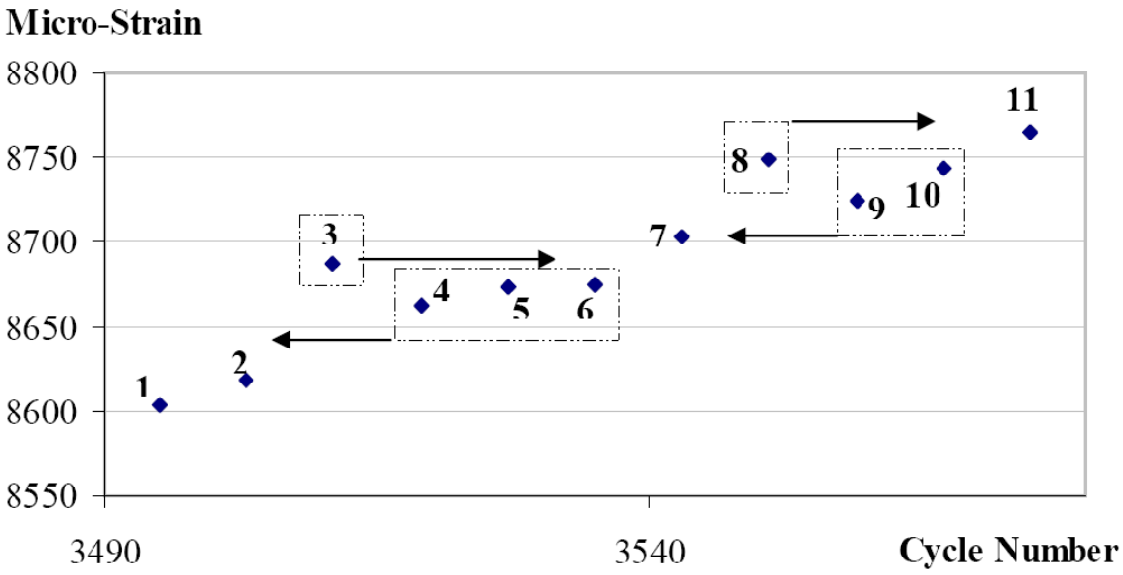

Figure 8 Smoothening process in the Stepwise Increase Approach (22).

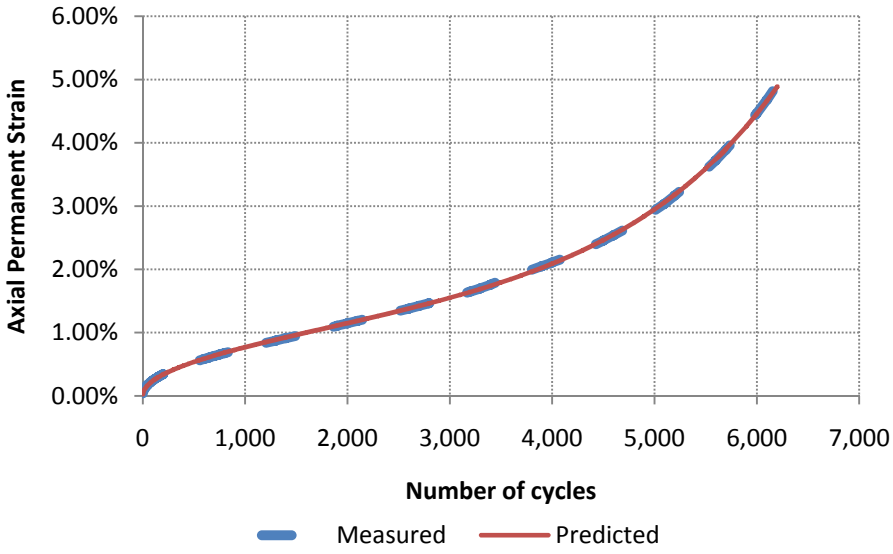

Figure 9 Typical permanent strain vs loading cycle fitted with the Francken Model.

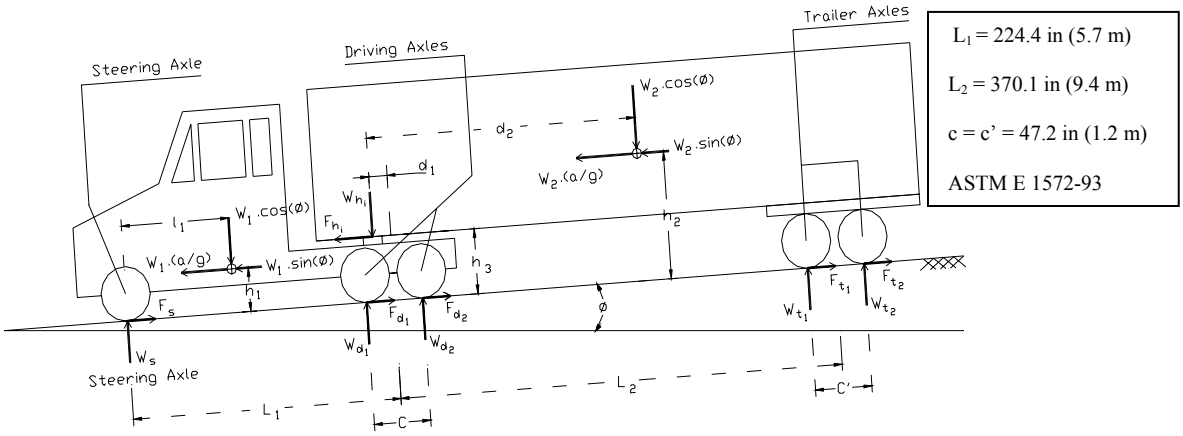

Figure 10 Forces acting on a tractor-semitrailer during braking on a downward slope (35).

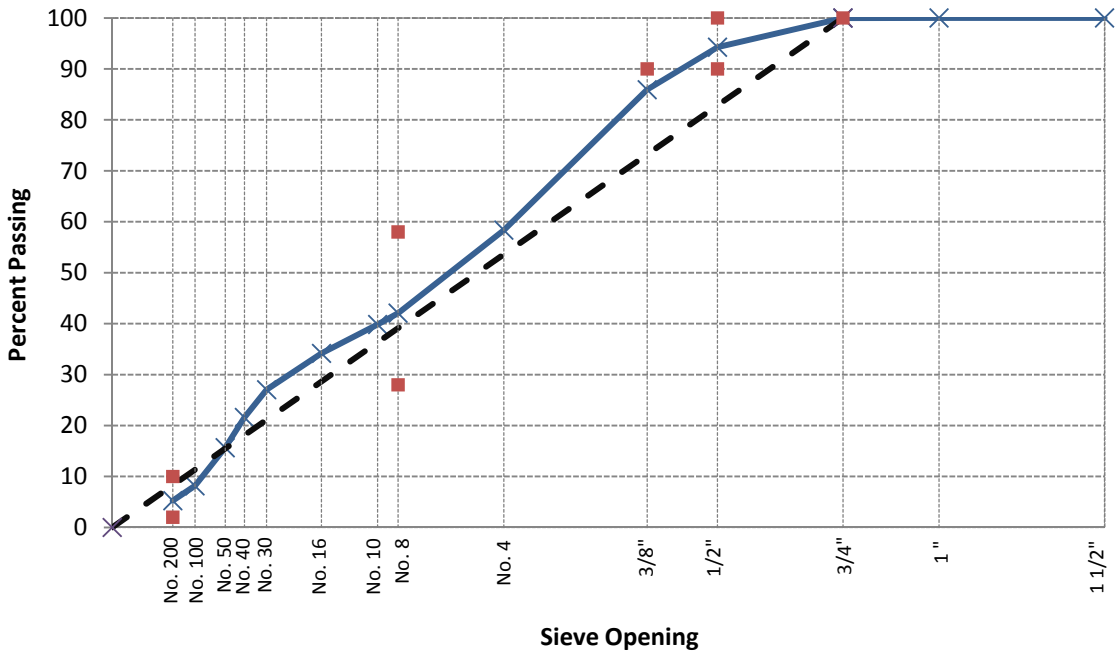

Figure 11 Aggregate gradation used in the analysis.

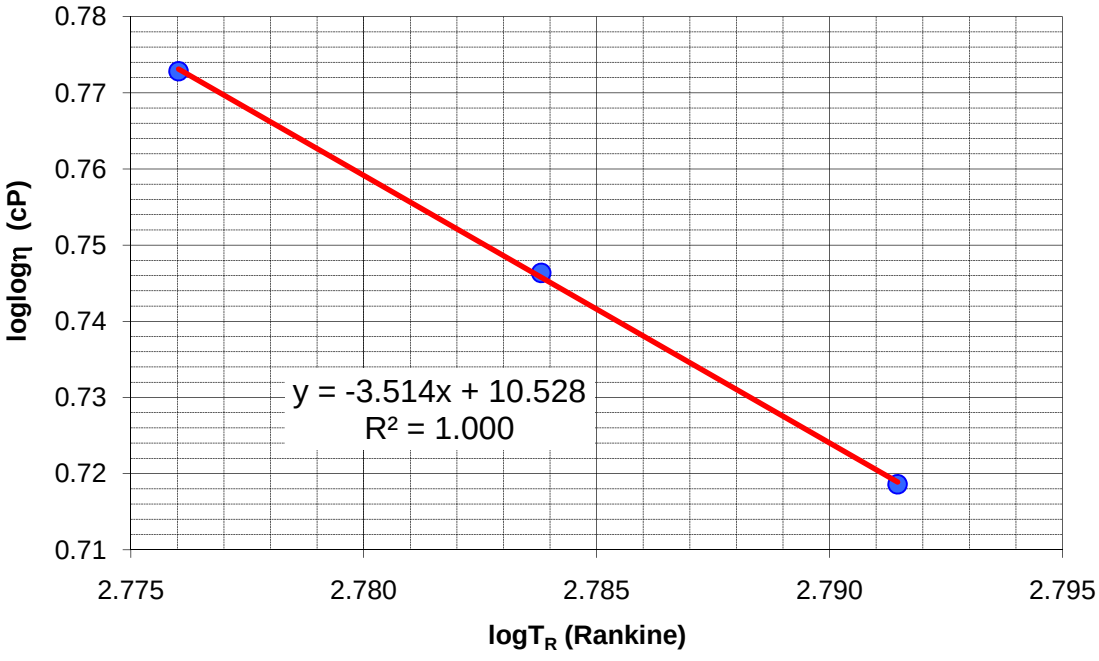

Figure 12 A-VTS determinations for binder PG64-22.

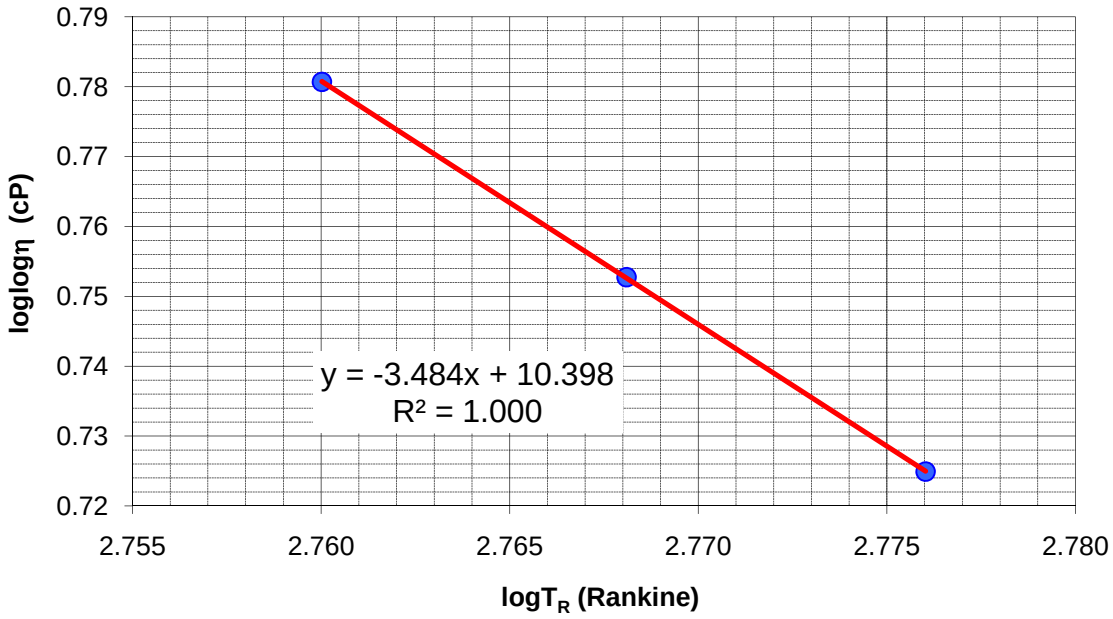

Figure 13 A-VTS determinations for binder PG58-22.

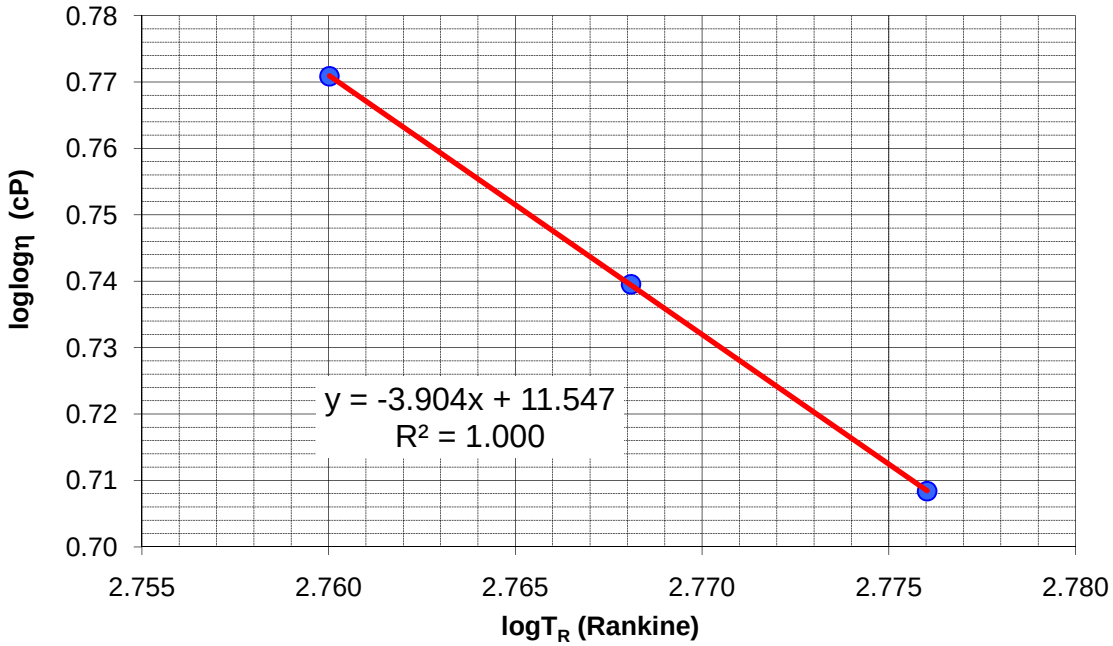

Figure 14 A-VTS determinations for binder PG52-22.

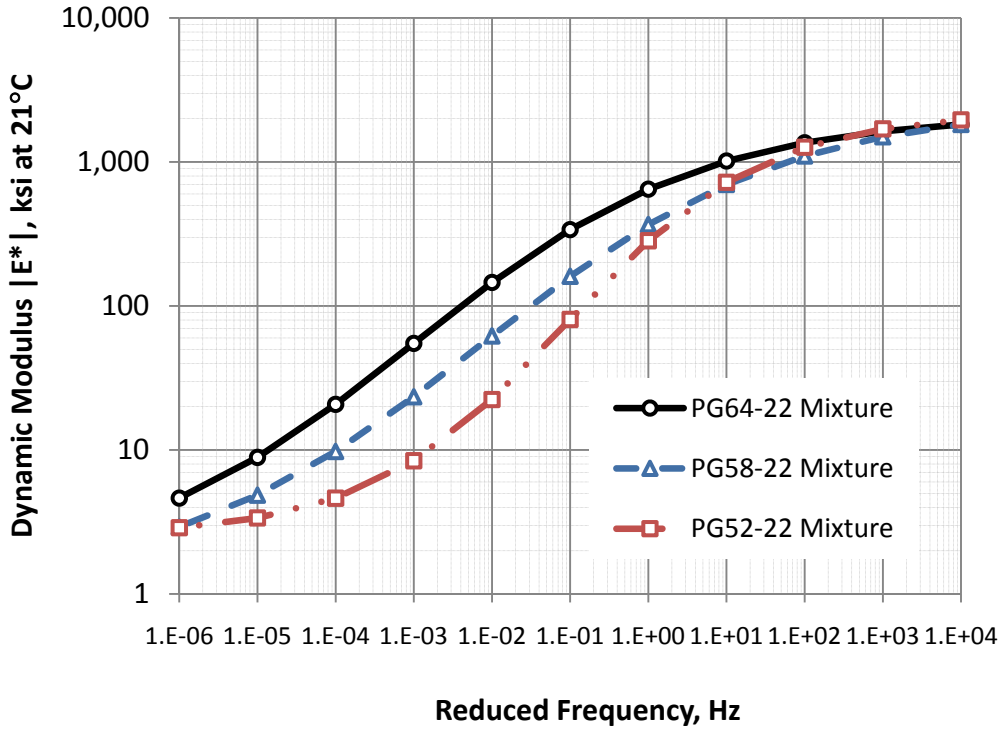

Figure 15 Dynamic modulus master curves at 21°C (70°F).

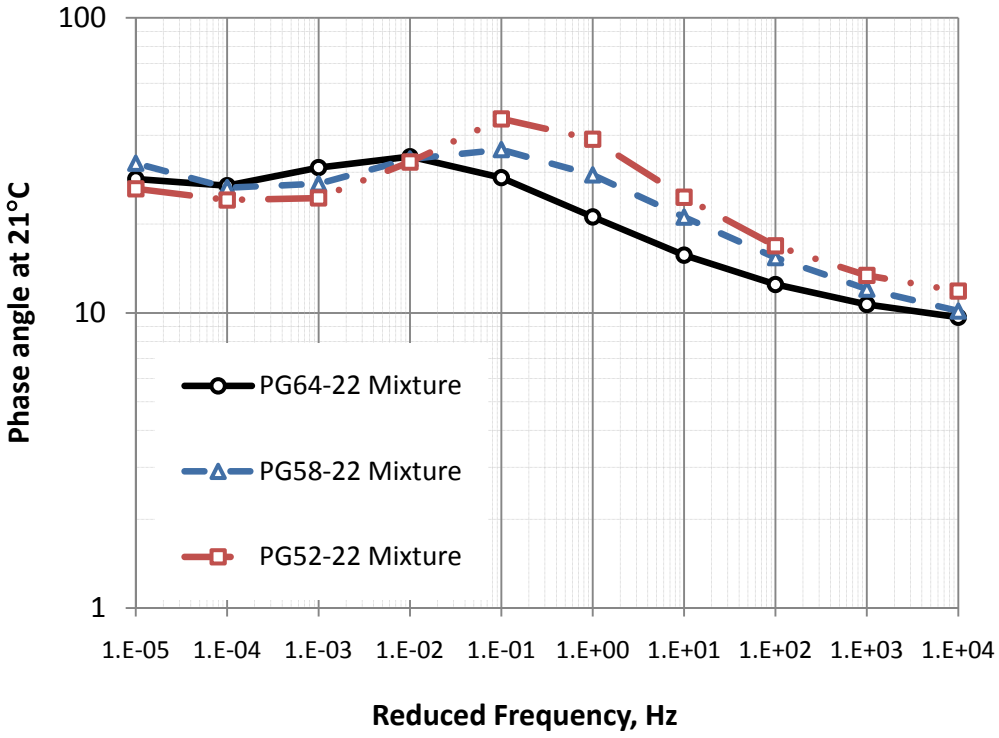

Figure 16 Phase angle at 21°C (70°F)

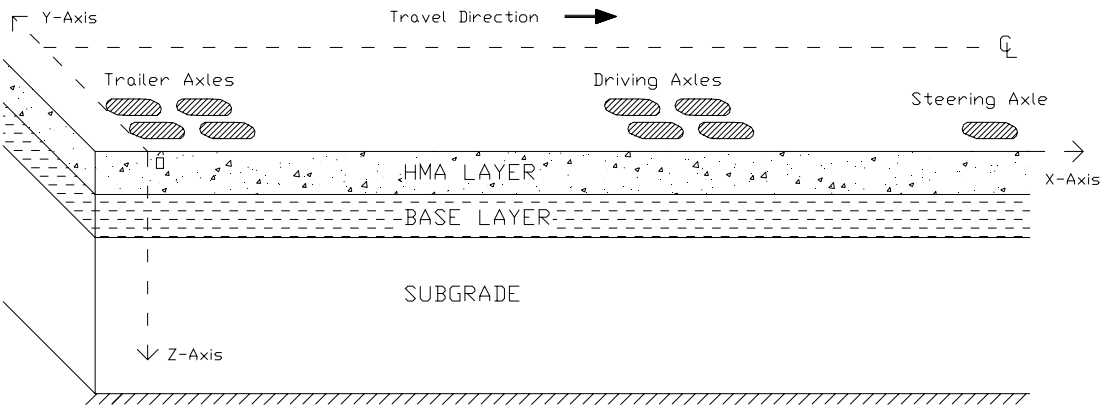

Figure 17. Axle configuration used in the 3D-Move program.

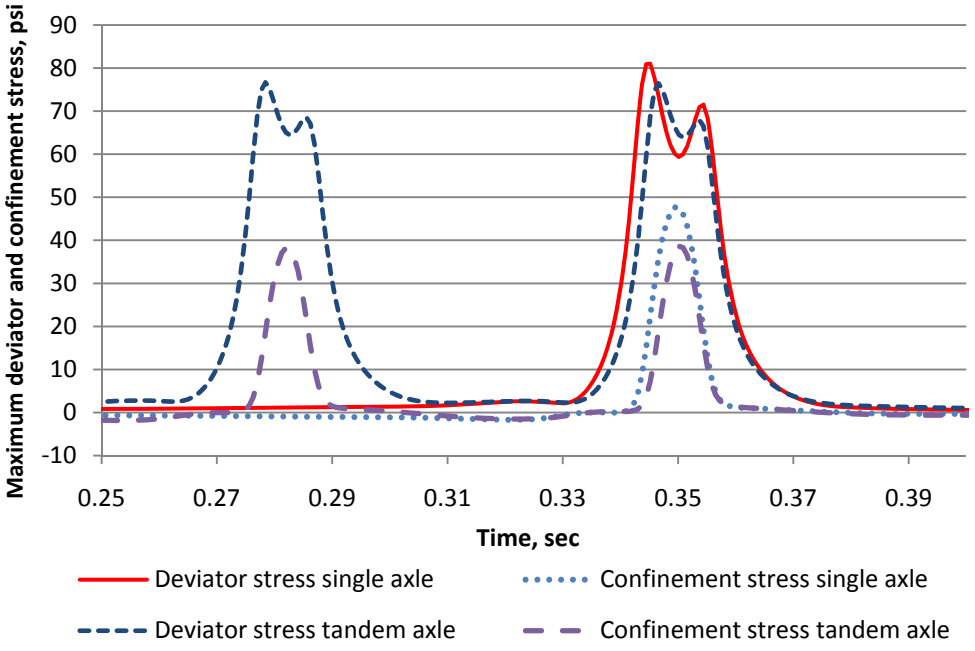

Figure 18. Stress state for single versus tandem axle – Non-braking conditions.

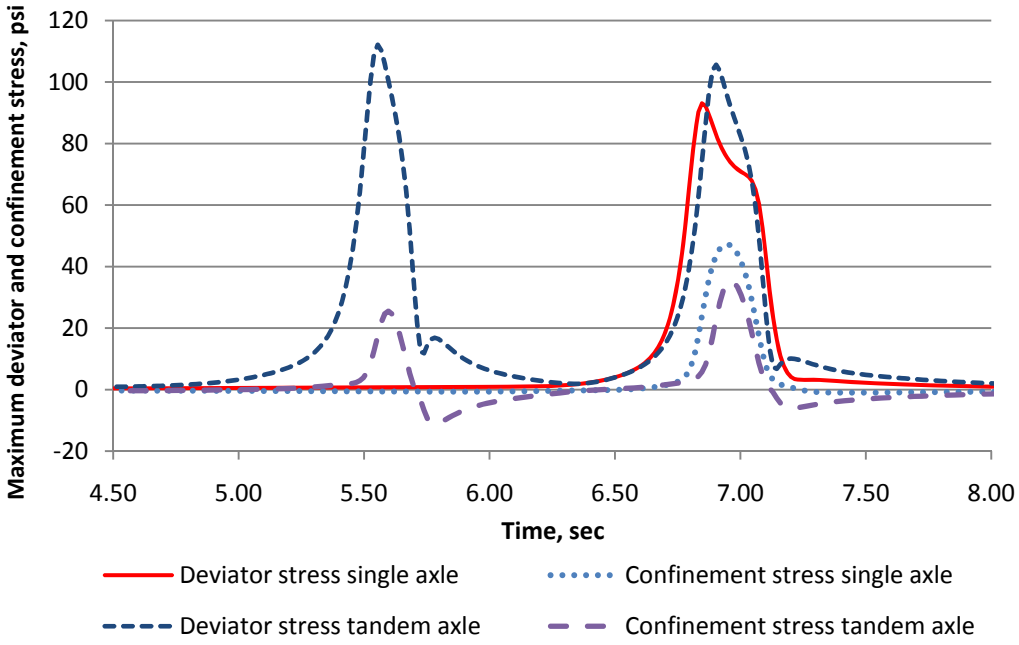

Figure 19. Stress state for single versus tandem axle –Braking conditions.

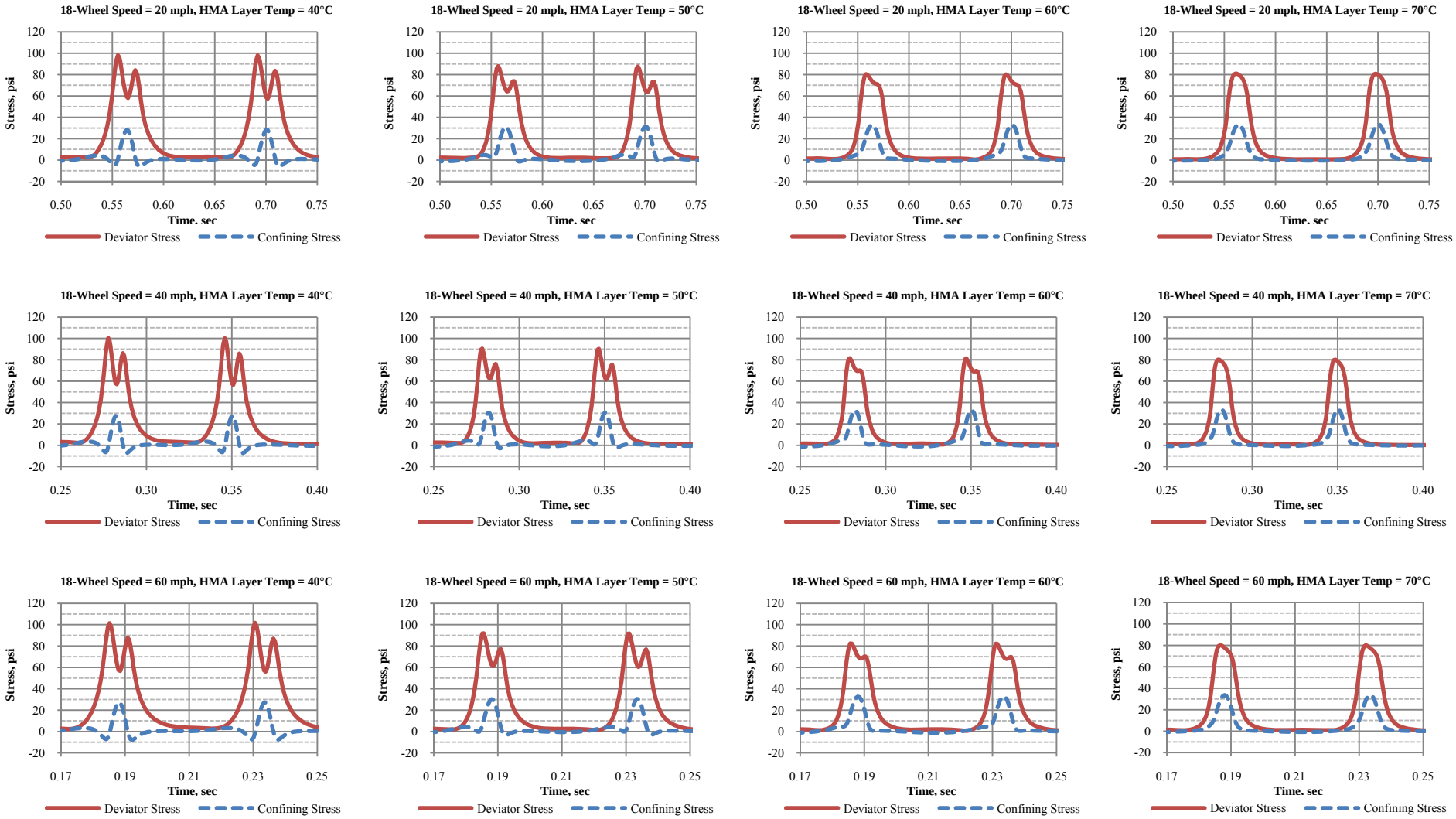

Figure 20. Calculated σ_d and σ_c stress history at 2 inch below the surface of the PG64-22 mix – non-braking - 4" HMA over 6" base.

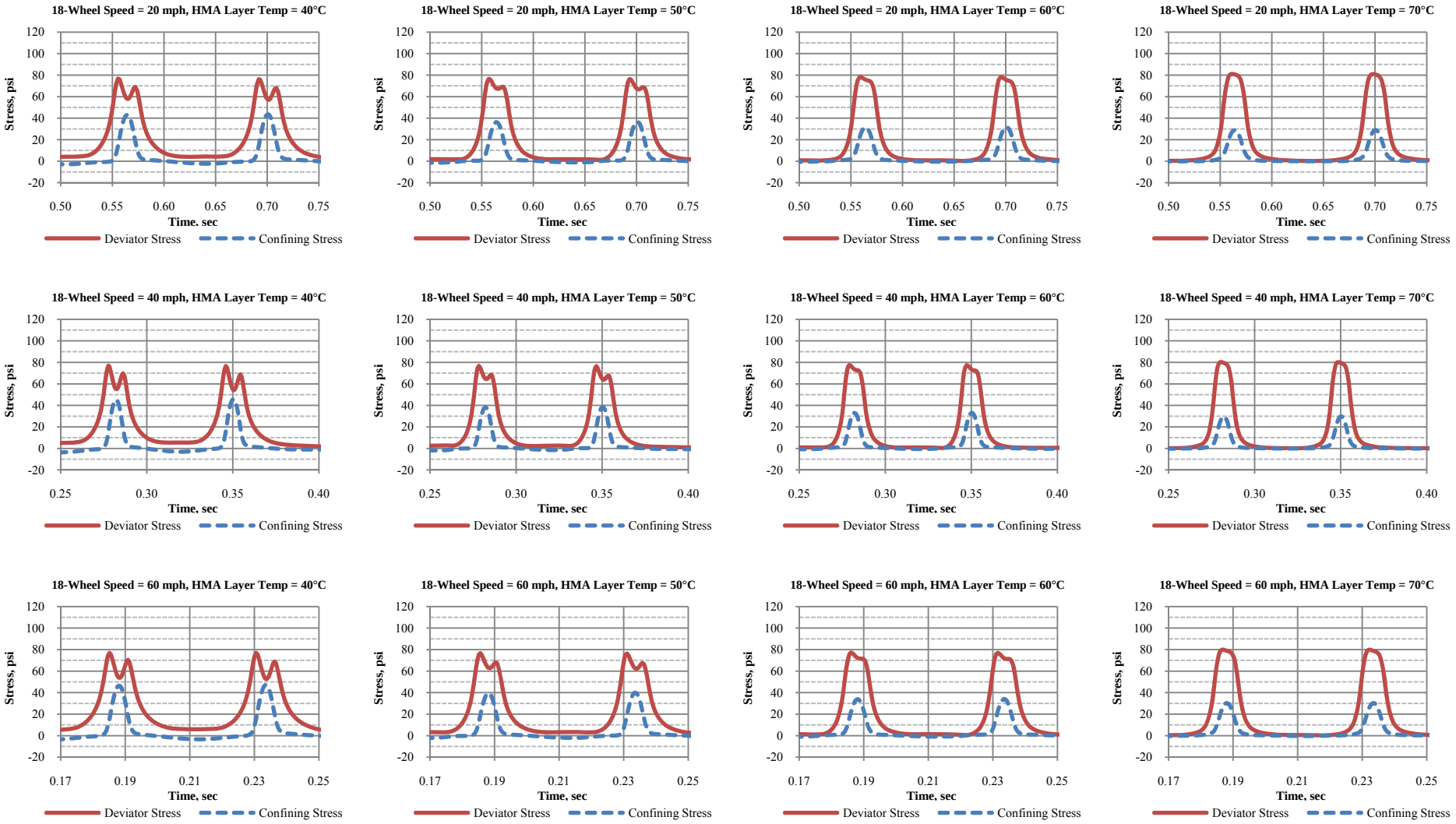

Figure 21. Calculated σ_d and σ_c stress history at 2 inch below the surface of the PG64-22 mix – non-braking – 6" HMA over 8" base.

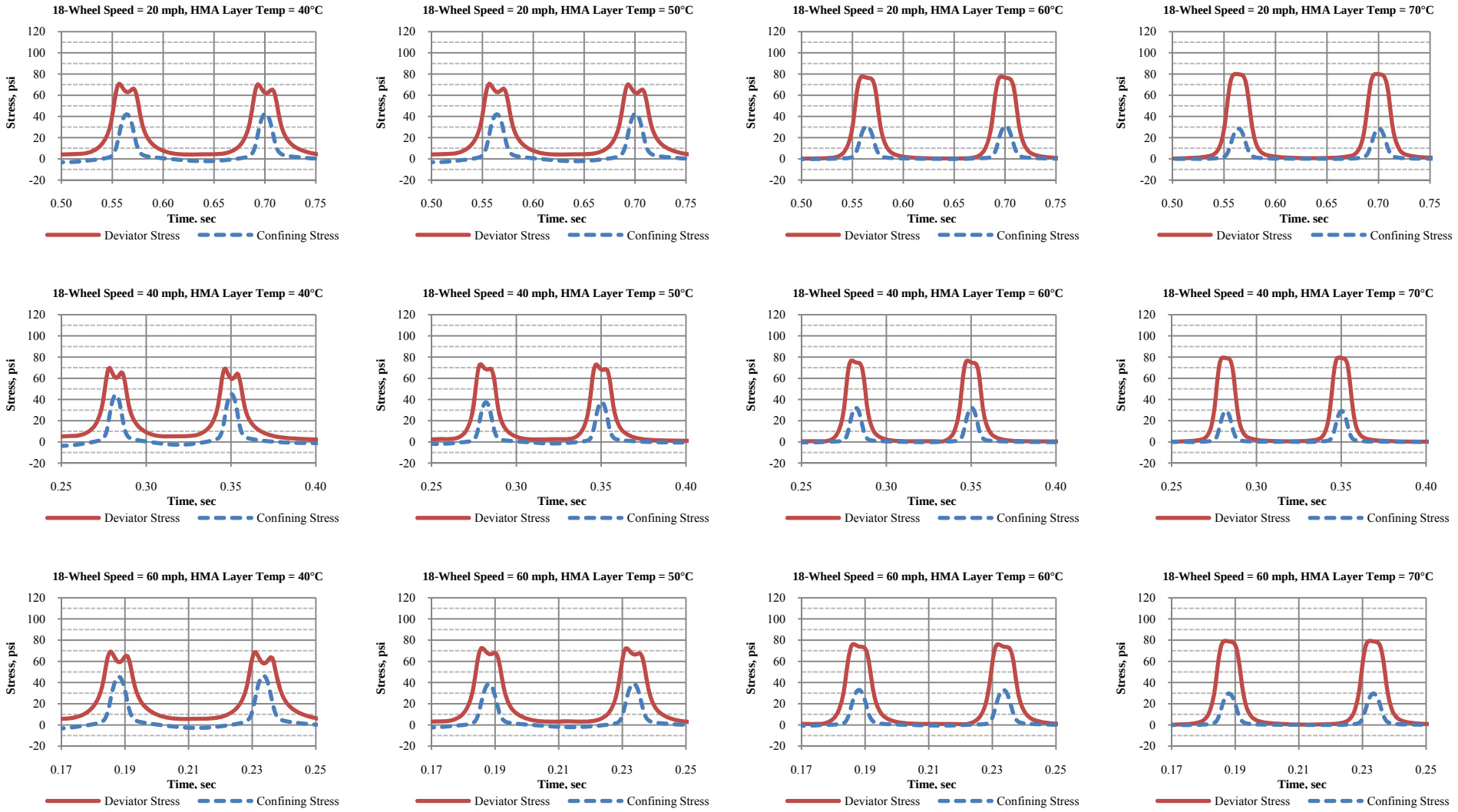

Figure 22. Calculated σ_d and σ_c stress history at 2 inch below the surface of the PG64-22 mix – non-braking – 8" HMA over 10" base.

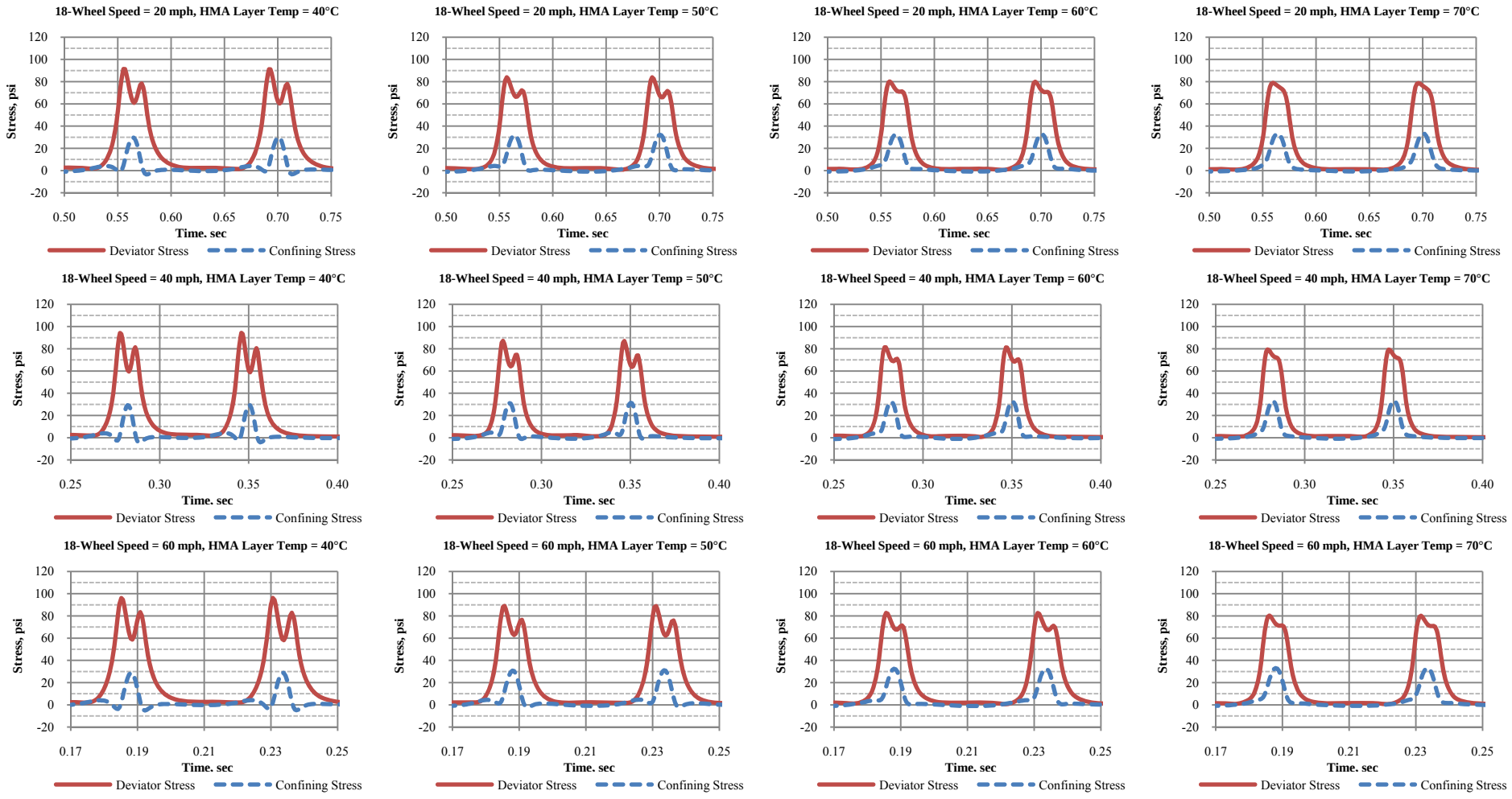

Figure 23. Calculated σ_d and σ_c stress history at 2 inch below the surface of the PG58-22 mix – non-braking – 4" HMA over 6" base.

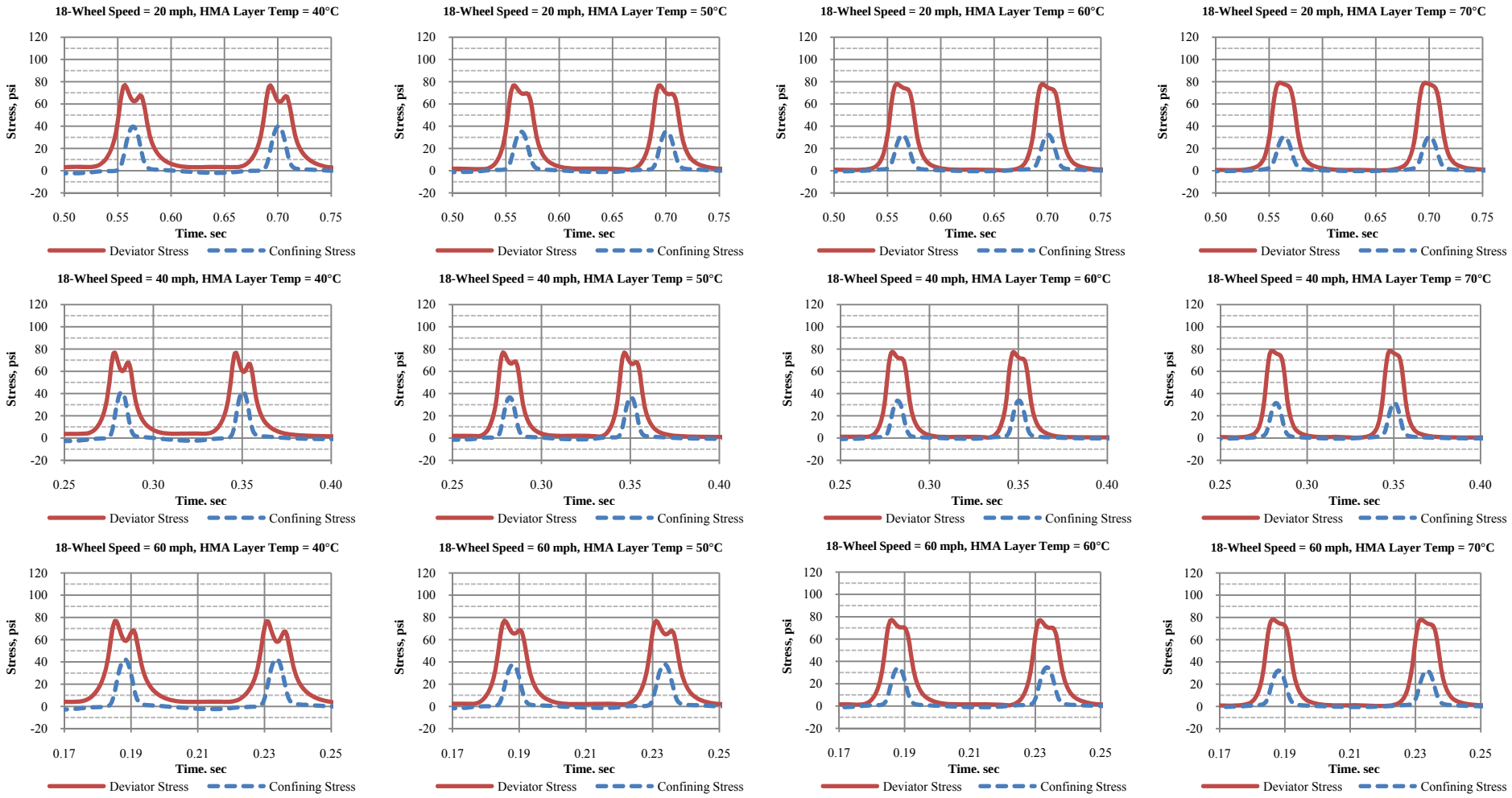

Figure 24. Calculated σ_d and σ_c stress history at 2 inch below the surface of the PG58-22 mix – non-braking – 6" HMA over 8" base.

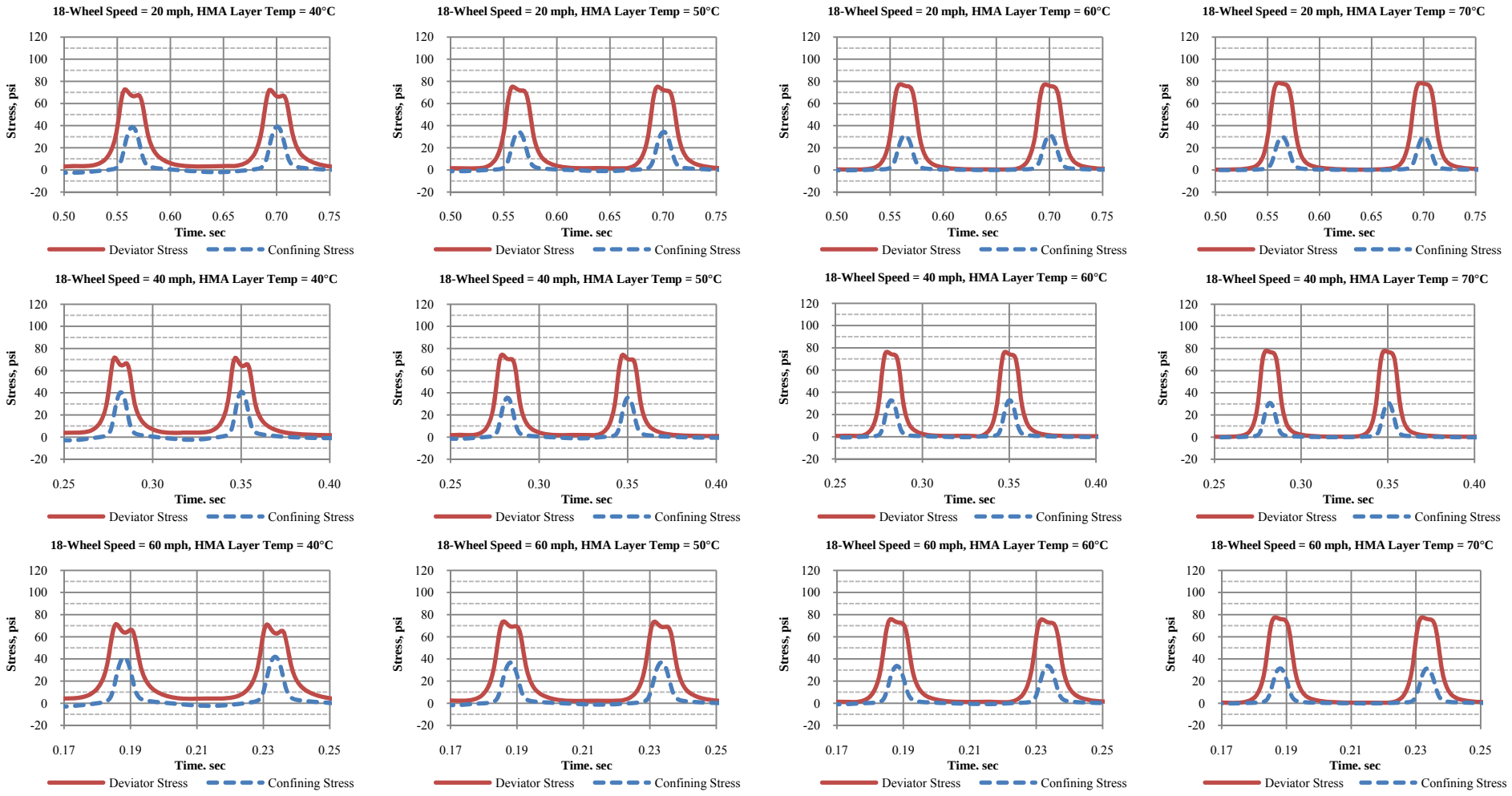

Figure 25. Calculated σ_d and σ_c stress history at 2 inch below the surface of the PG58-22 mix – non-braking – 8" HMA over 10" base.

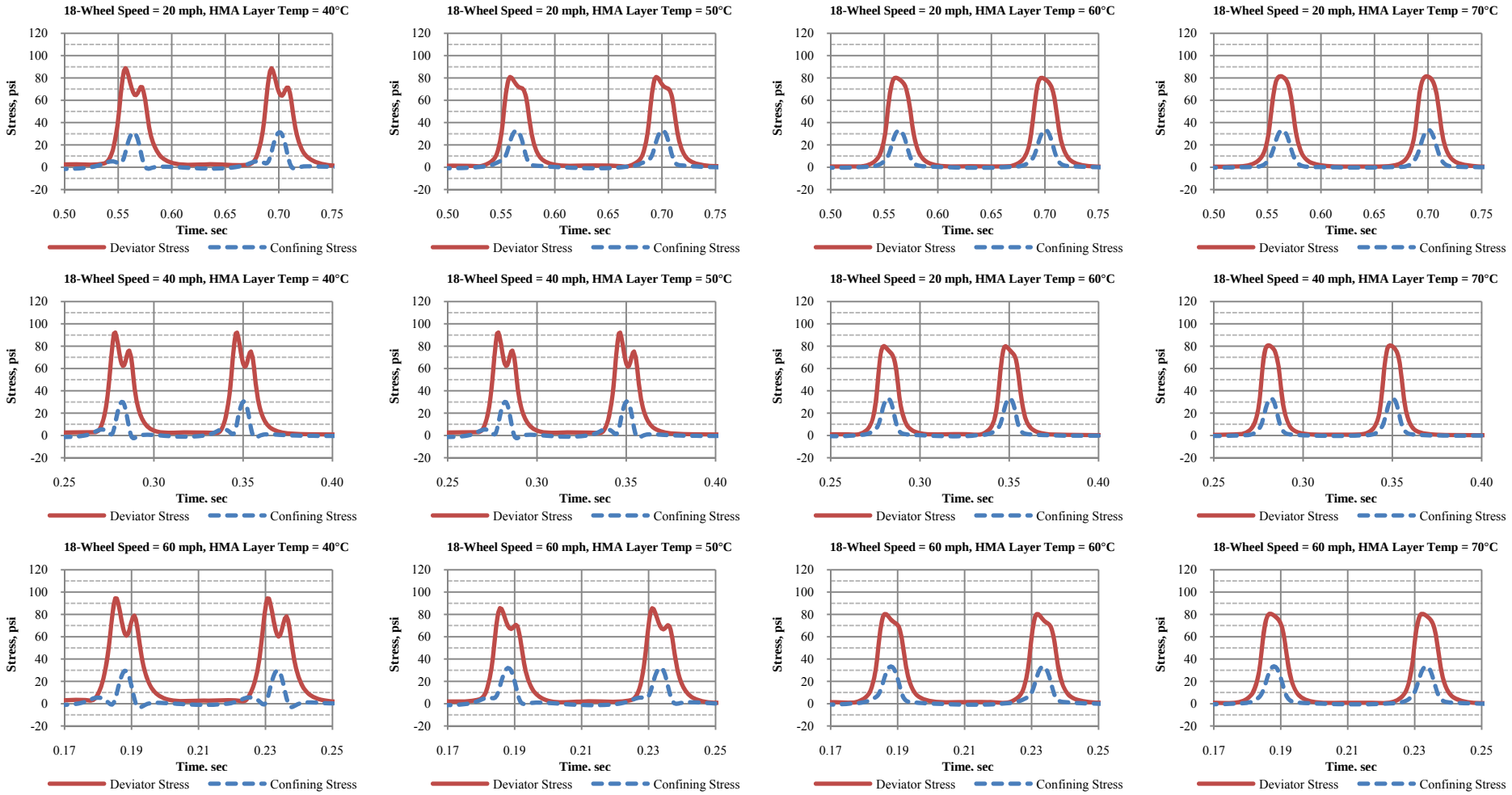

Figure 26. Calculated σ_d and σ_c stress history at 2 inch below the surface of the PG52-22 mix – non-braking – 4" HMA over 6" base.

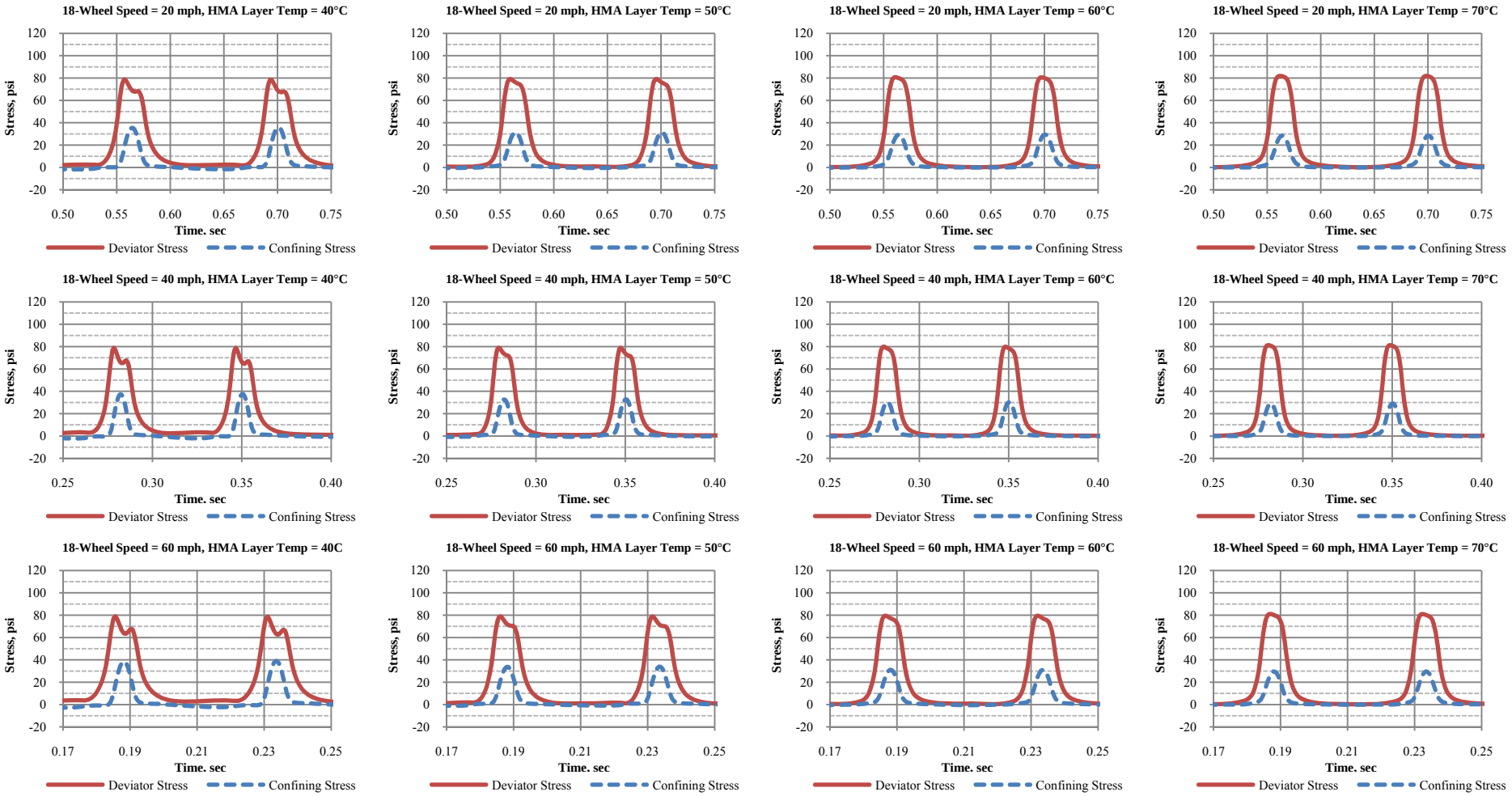

Figure 27. Calculated σ_d and σ_c stress history at 2 inch below the surface of the PG52-22 mix – non-braking – 6" HMA over 6" base.

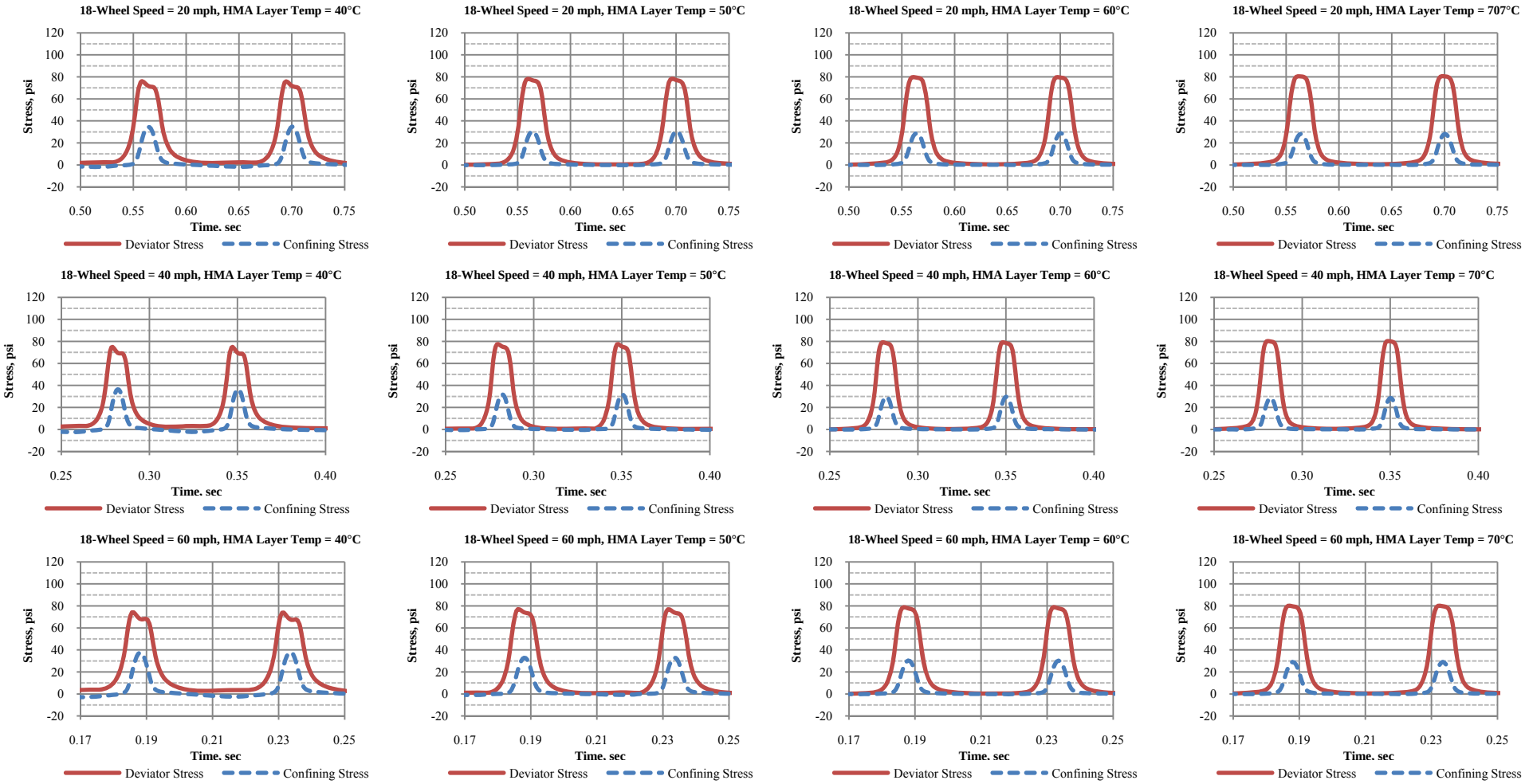

Figure 28. Calculated σ_d and σ_c stress history at 2 inch below the surface of the PG58-22 mix – non-braking – 8" HMA over 10" base.

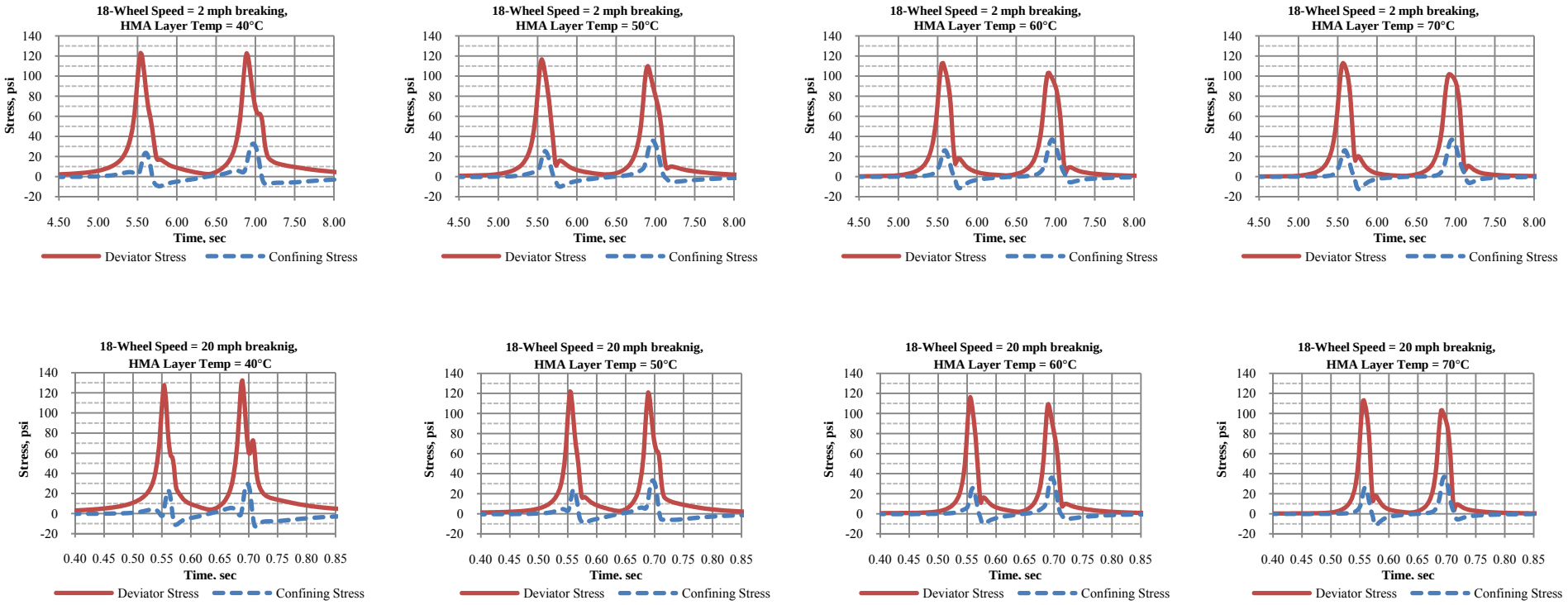

Figure 29. Calculated σ_d and σ_c stress history at 2 inch below the surface of the PG64-22 mix –-braking – 4” HMA over 6” base.

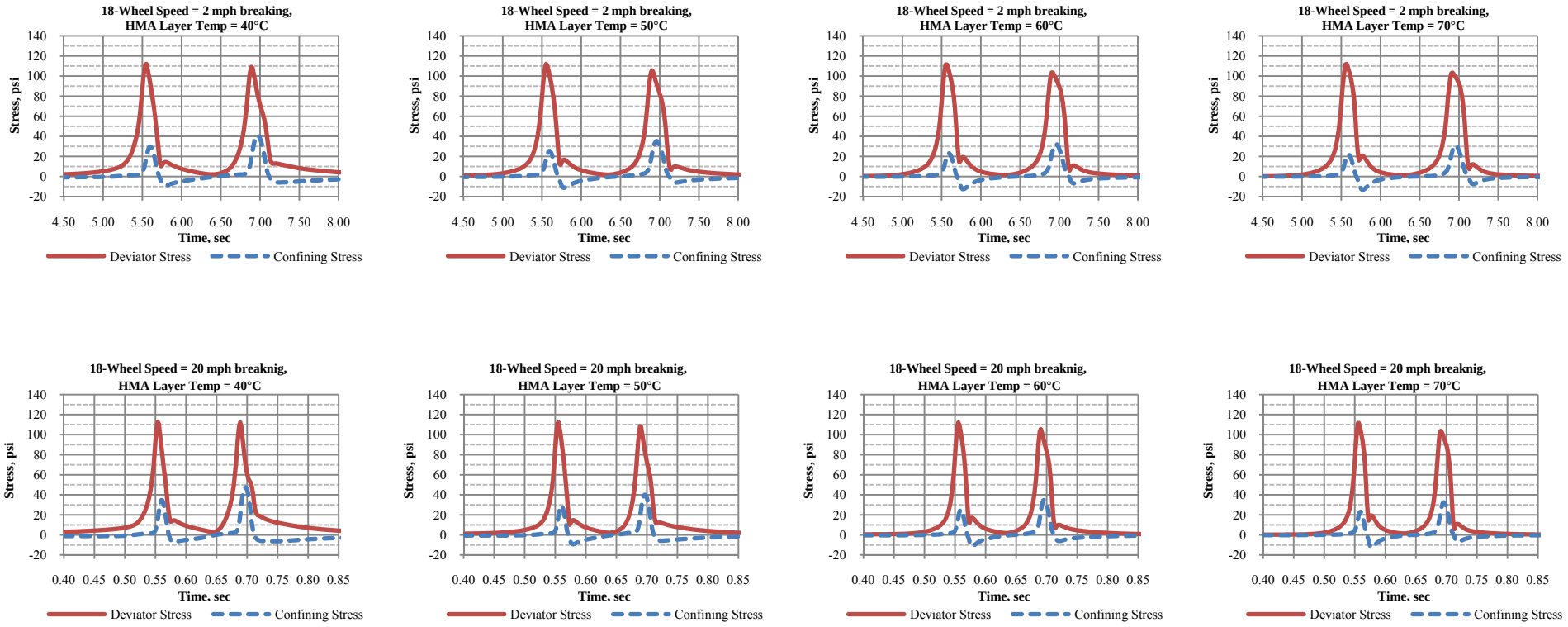

Figure 30. Calculated σ_d and σ_c stress history at 2 inch below the surface of the PG64-22 mix –-braking – 6” HMA over 10” base.

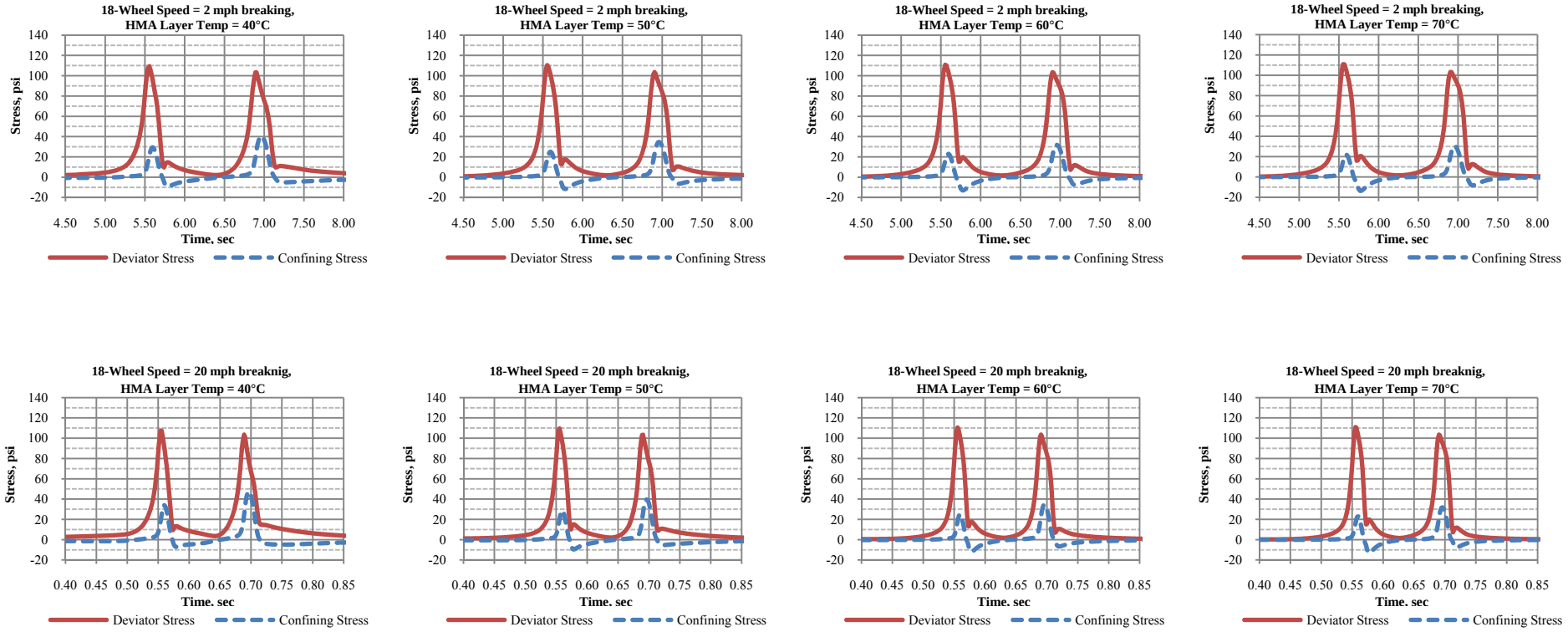

Figure 31. Calculated σ_d and σ_c stress history at 2 inch below the surface of the PG64-22 mix – braking – 8" HMA over 10" base.

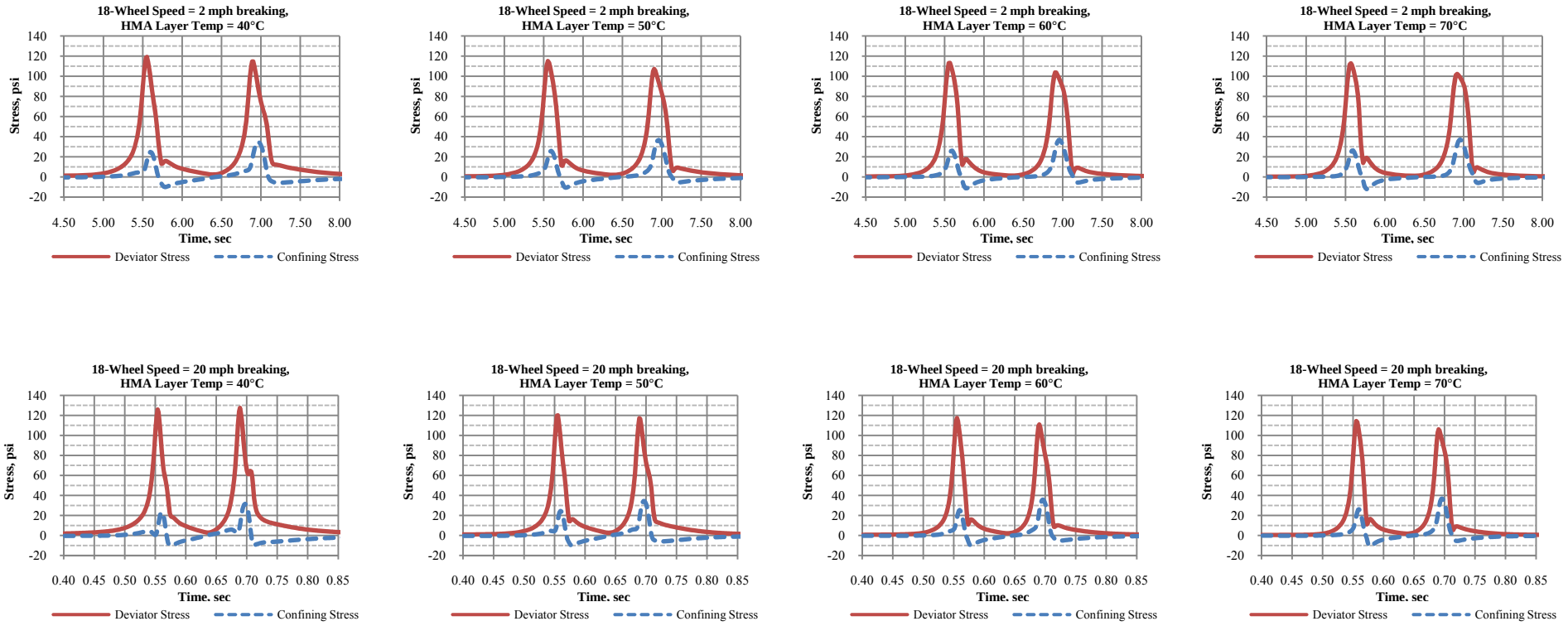

Figure 32. Calculated σ_d and σ_c stress history at 2 inch below the surface of the PG58-22 mix –-braking – 4” HMA over 6” base.

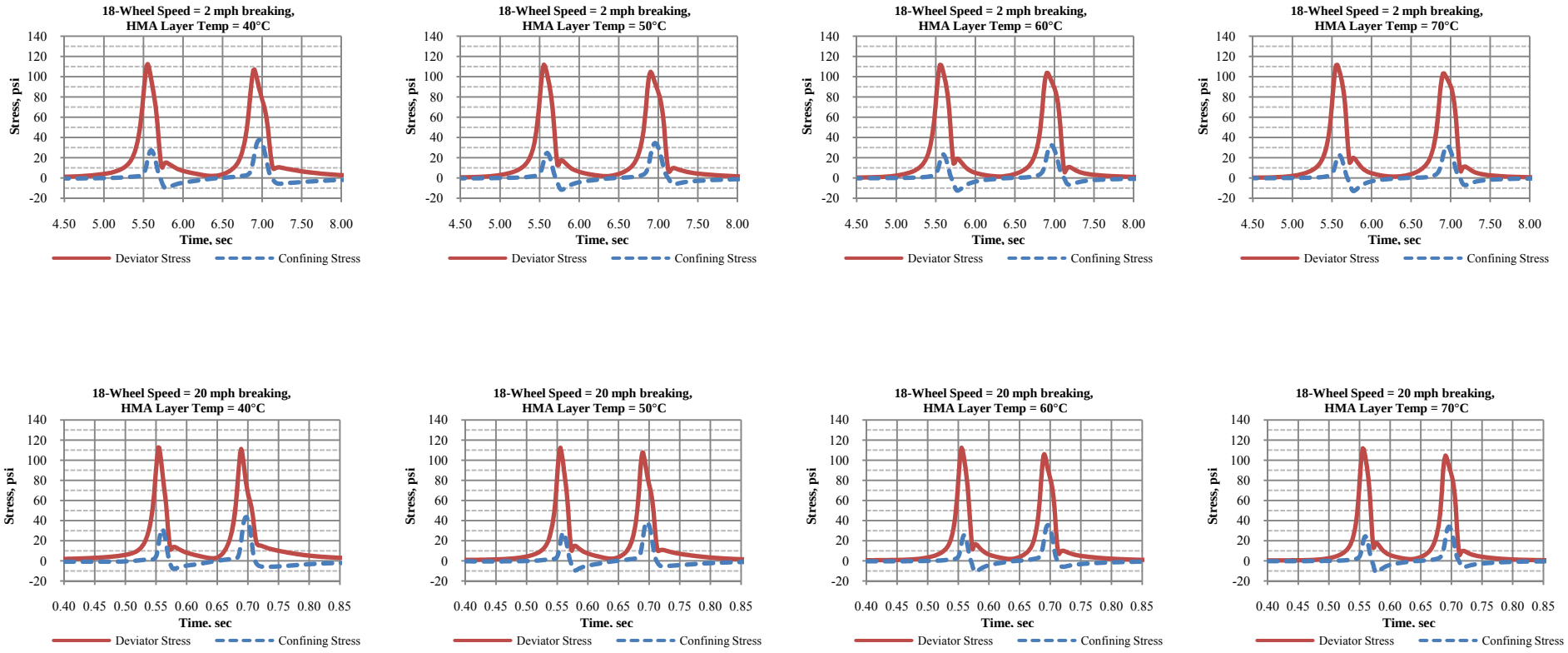

Figure 33. Calculated σ_d and σ_c stress history at 2 inch below the surface of the PG58-22 mix –-braking – 6” HMA over 8” base.

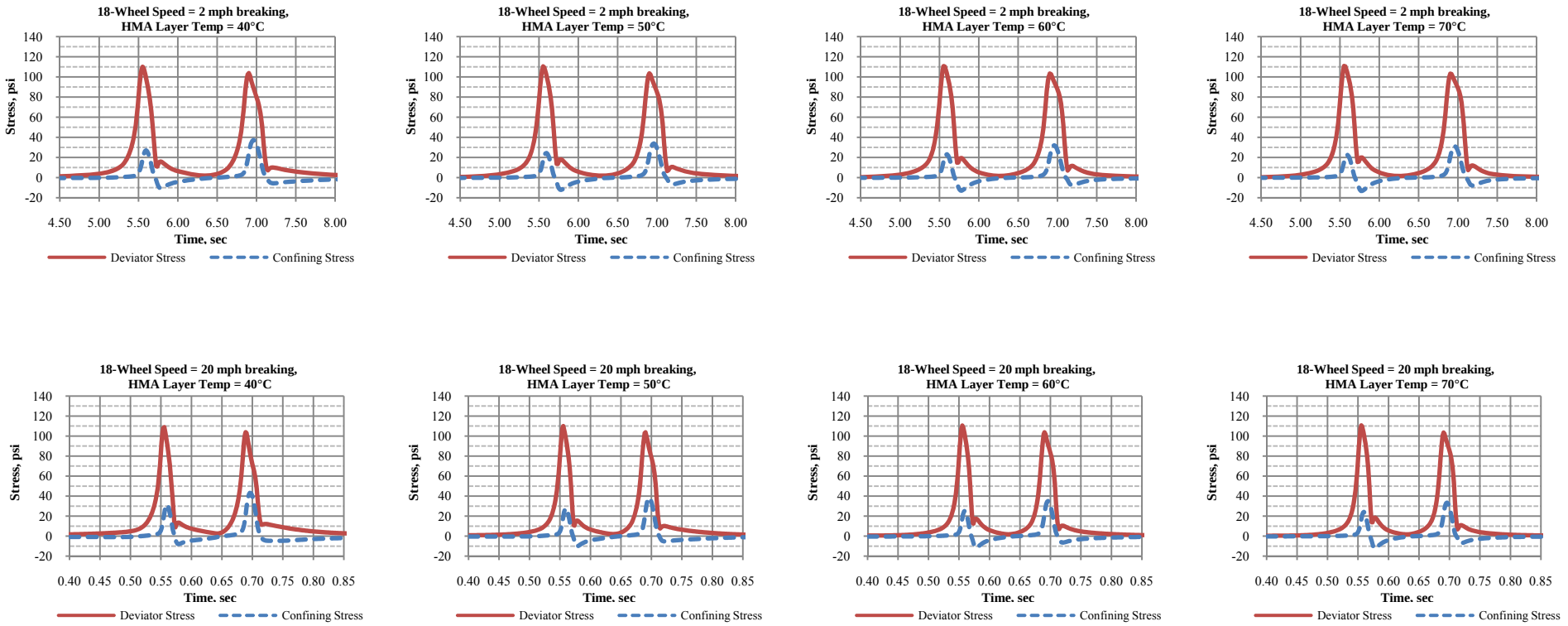

Figure 34. Calculated σ_d and σ_c stress history at 2 inch below the surface of the PG58-22 mix –-braking – 8” HMA over 10” base.

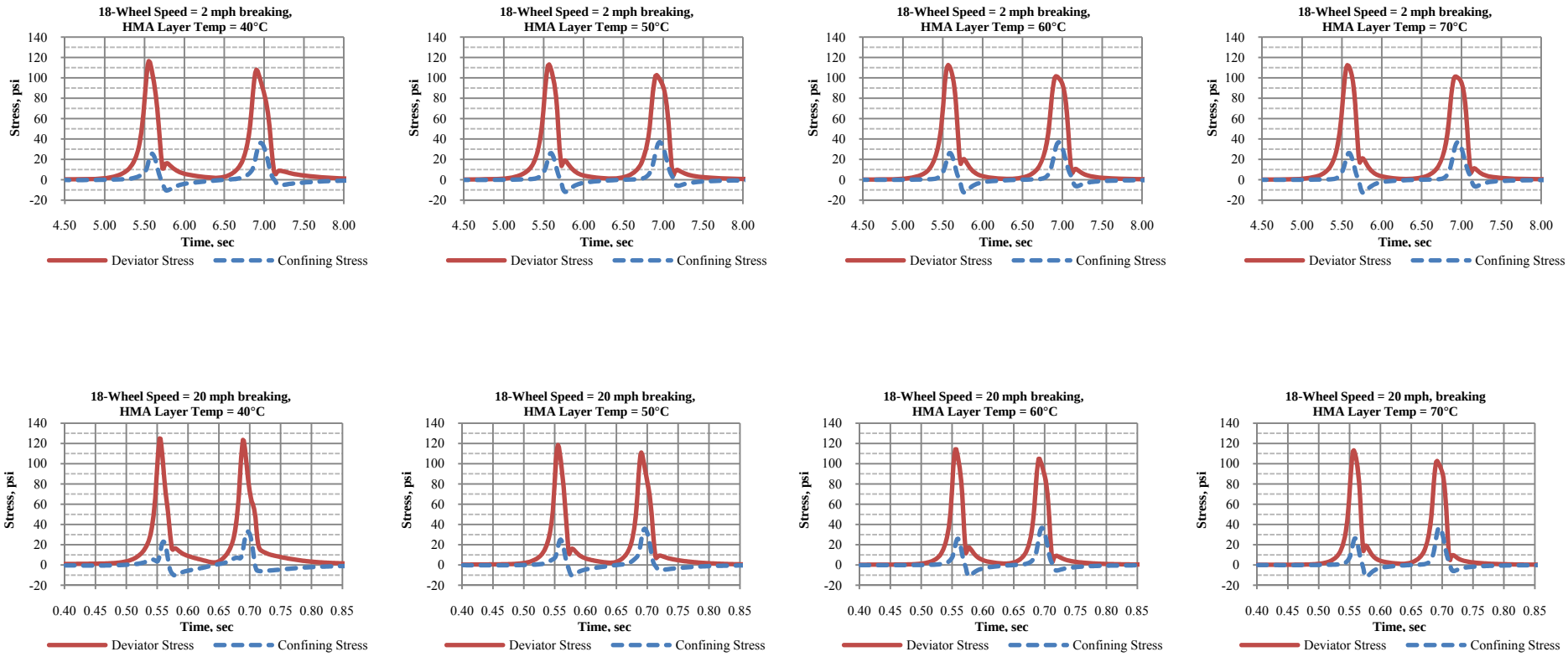

Figure 35. Calculated σ_d and σ_c stress history at 2 inch below the surface of the PG52-22 mix – braking – 4" HMA over 6" base.

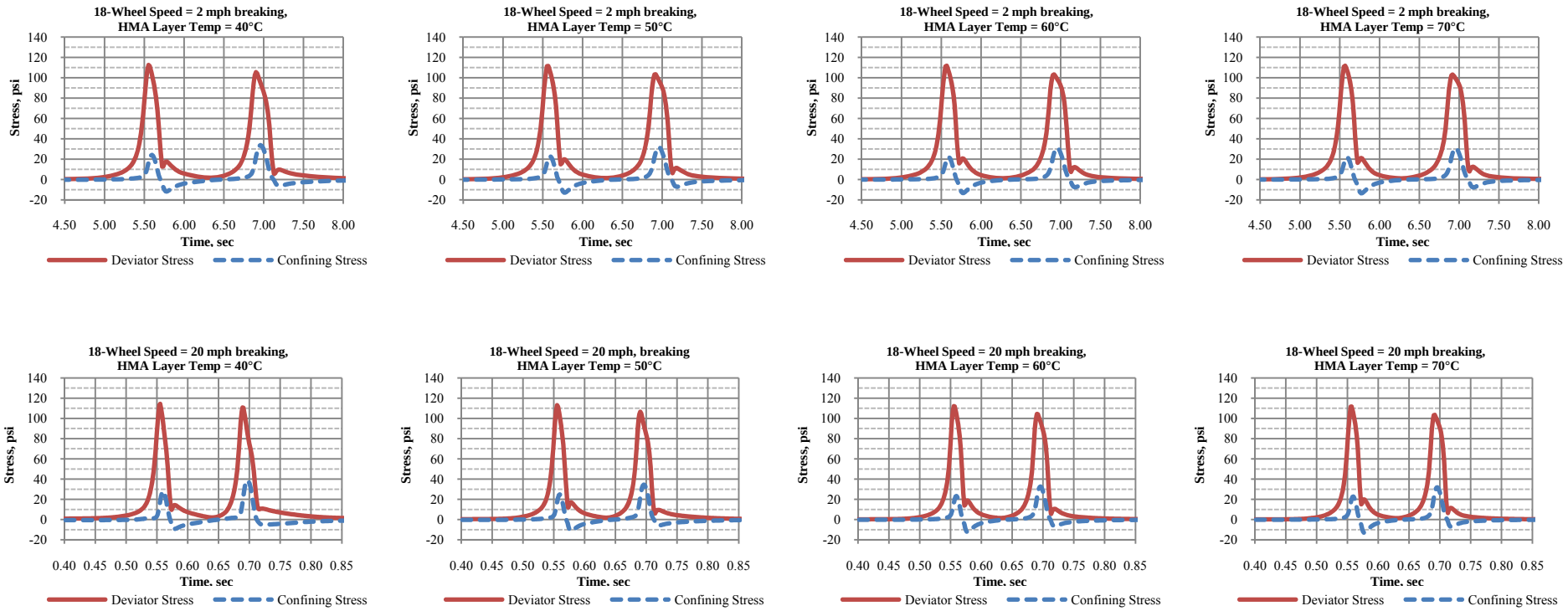

Figure 36. Calculated σ_d and σ_c stress history at 2 inch below the surface of the PG52-22 mix – braking – 6" HMA over 8" base.

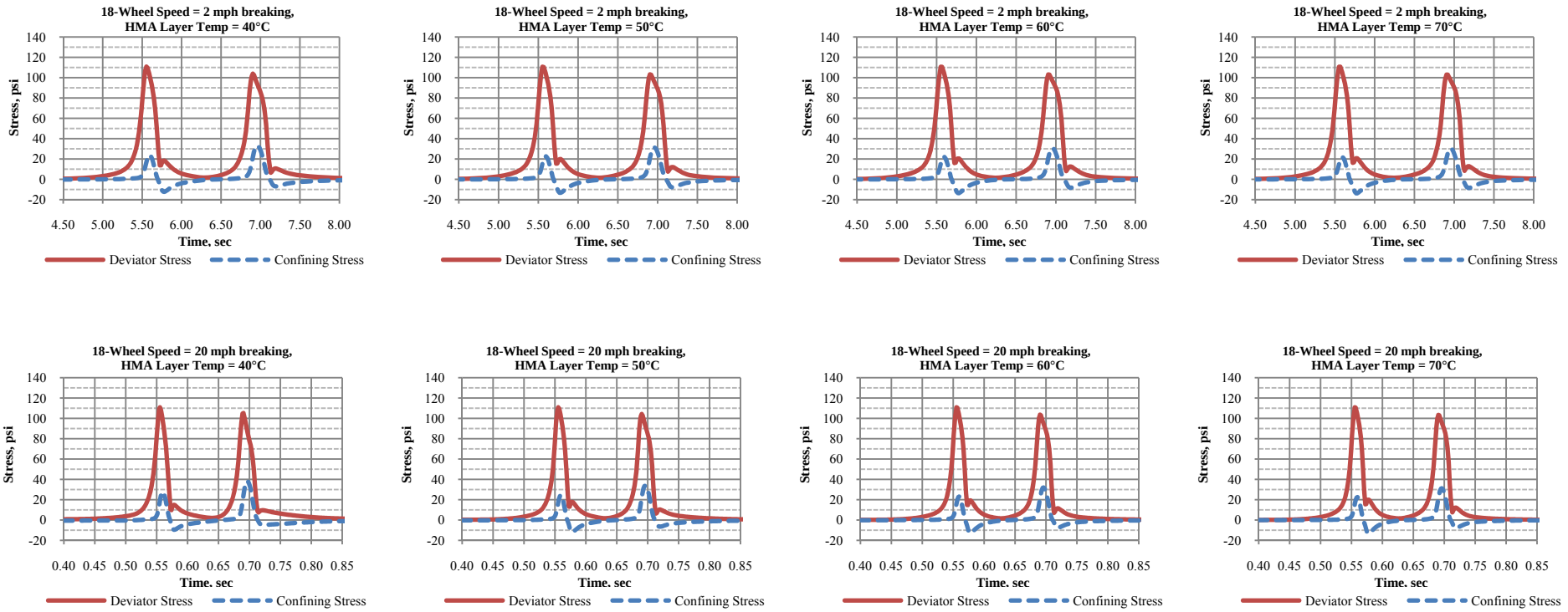

Figure 37. Calculated σ_d and σ_c stress history at 2 inch below the surface of the PG52-22 mix –braking – 8” HMA over 10” base.

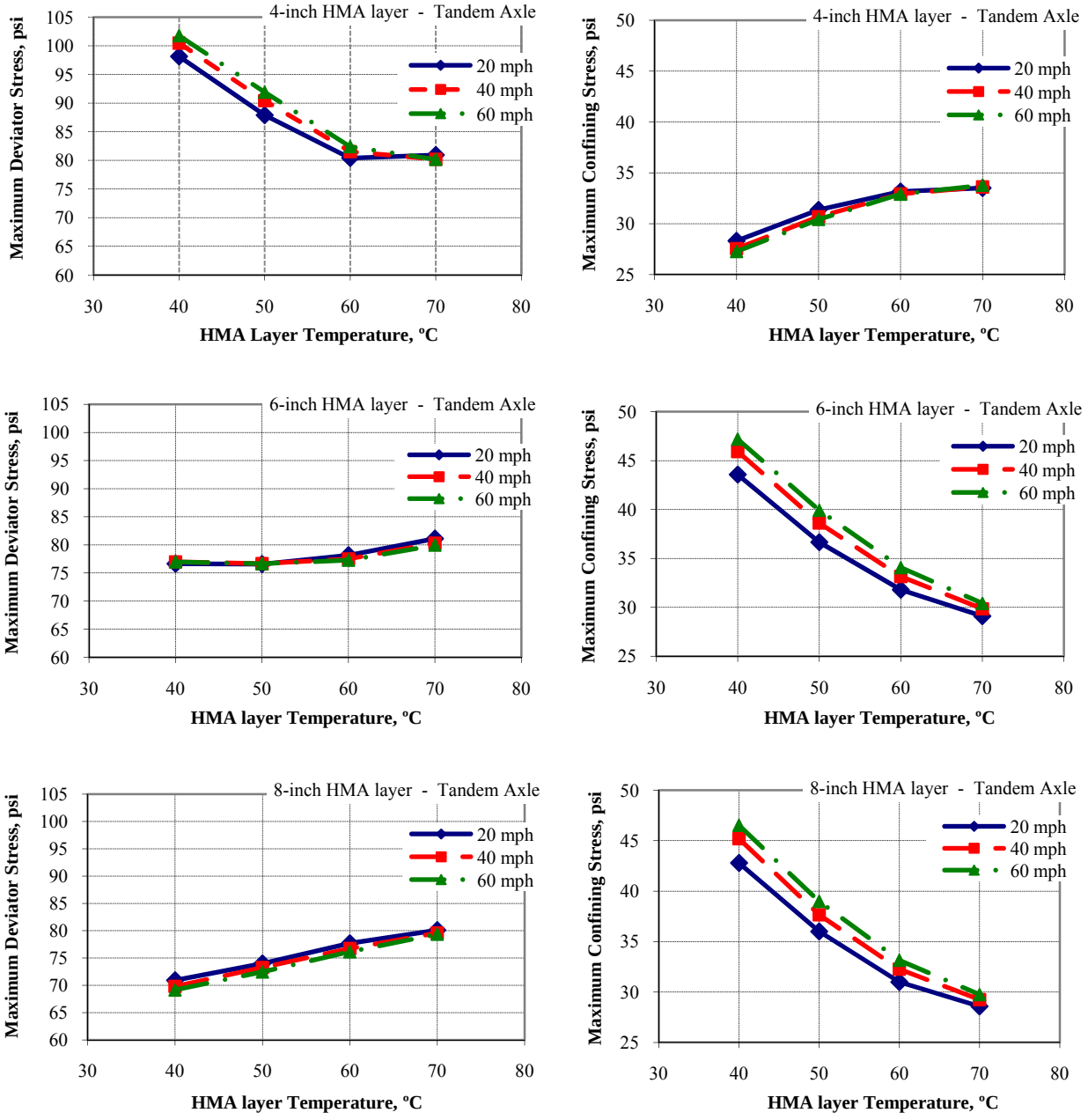

Figure 38. Maximum σ_d and σ_c stresses at 2 inch below the surface of the PG64-22 mix – non-braking.

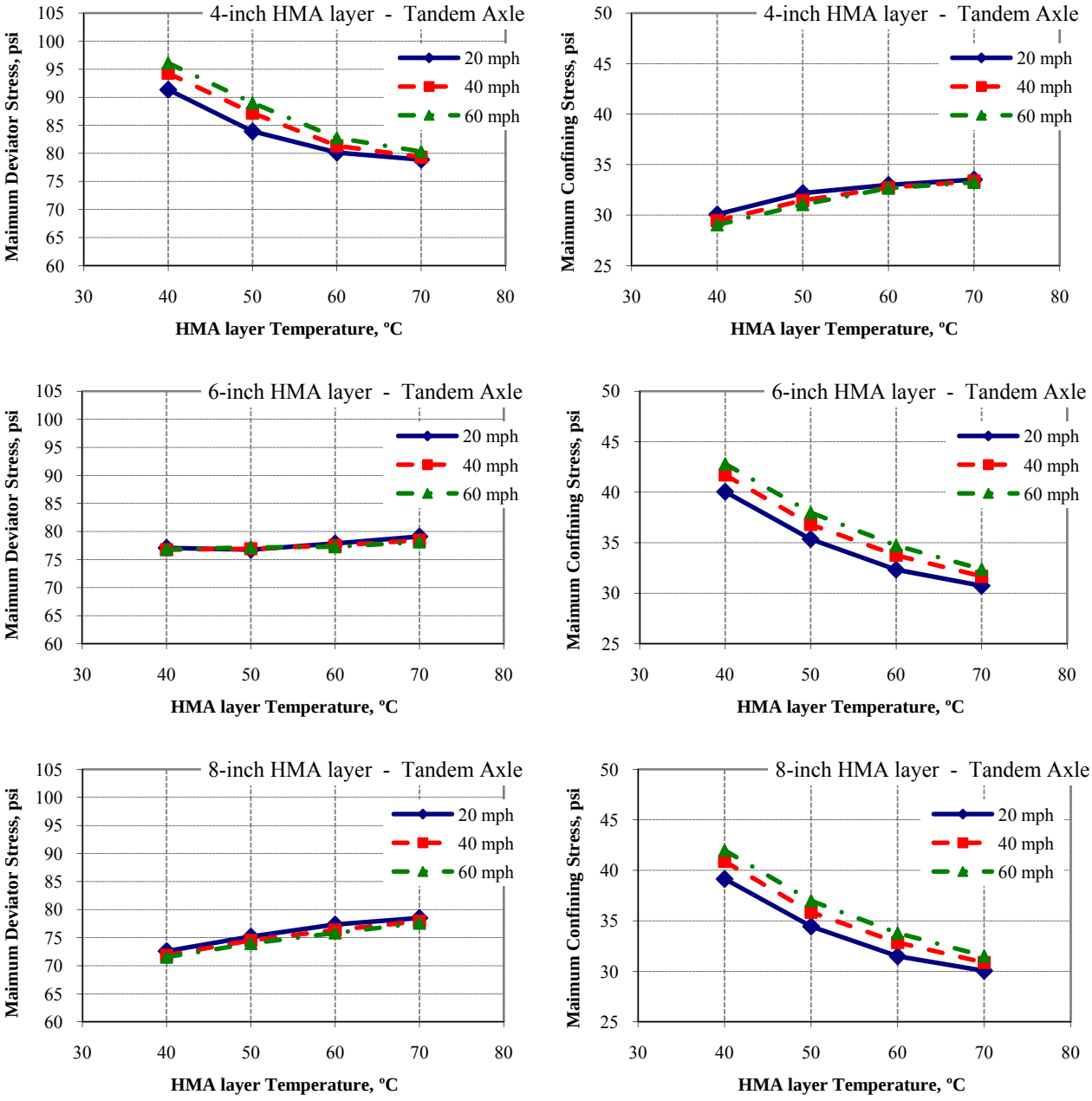

Figure 39. Maximum σ_d and σ_c stresses at 2 inch below the surface of the PG58-22 mix – non-braking.

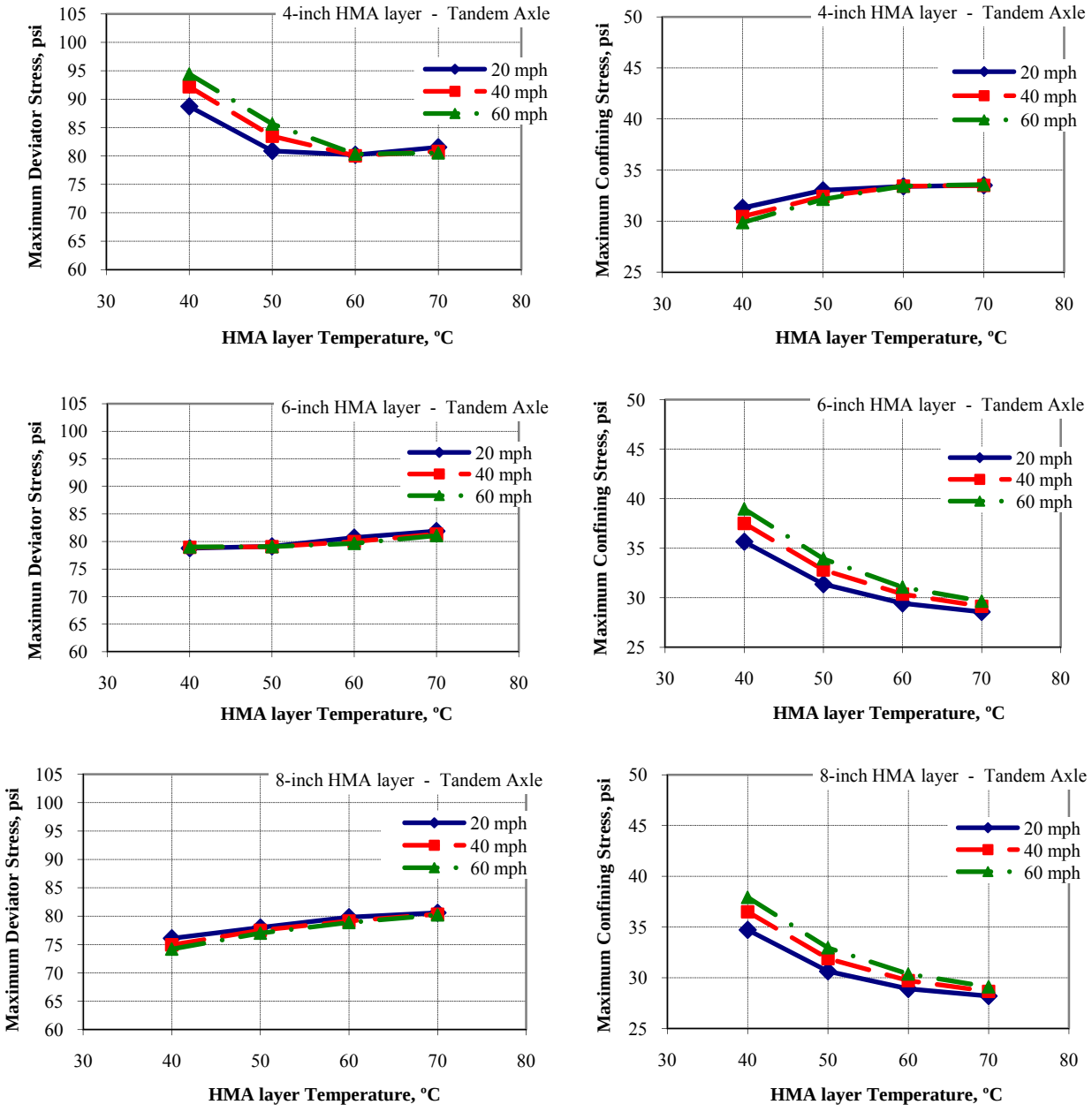

Figure 40. Maximum σ_d and σ_c stresses at 2 inch below the surface of the PG52-22 mix – non-braking.

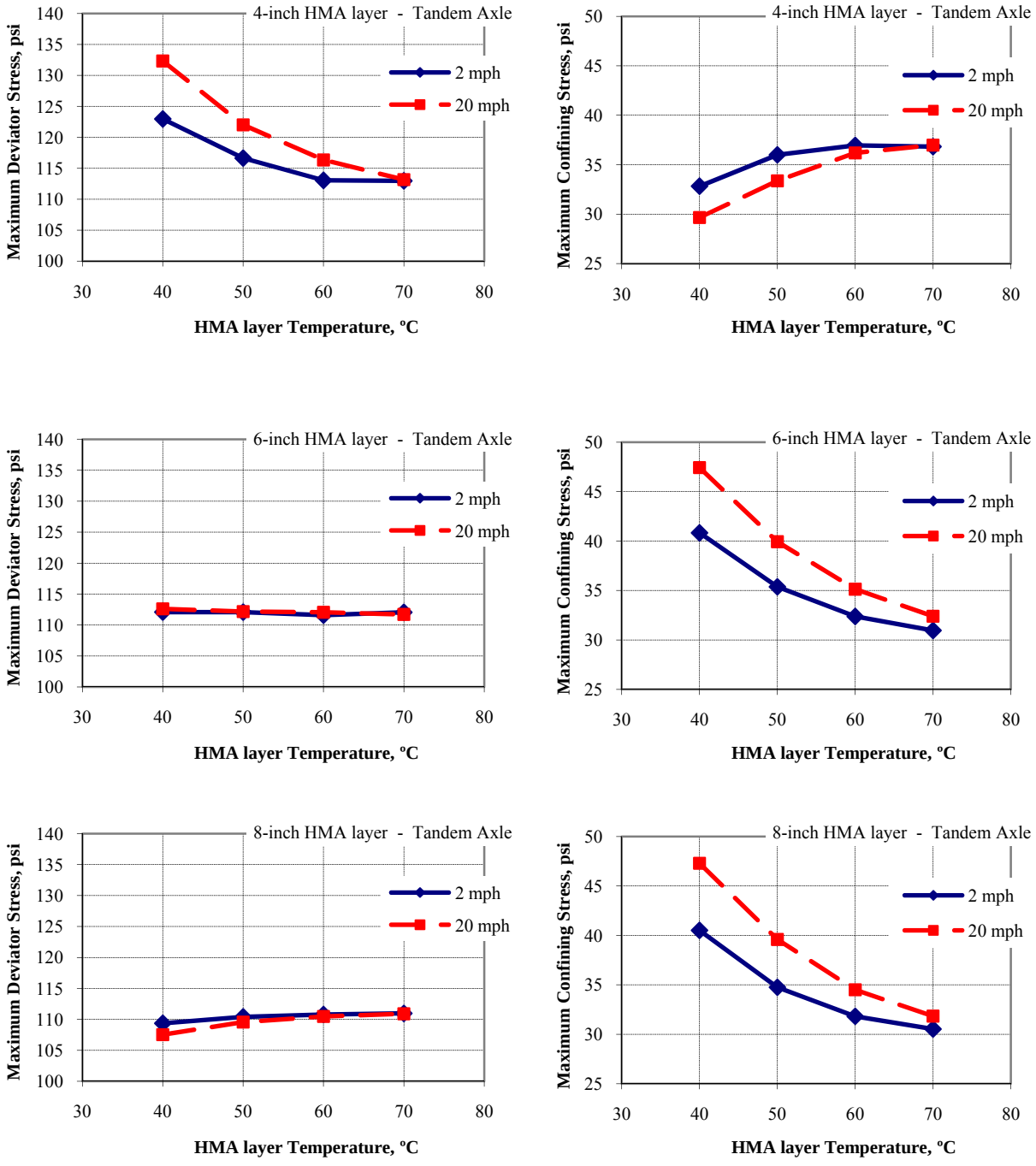

Figure 41. Maximum σ_d and σ_c stresses at 2 inch below the surface of the PG64-22 mix – braking.

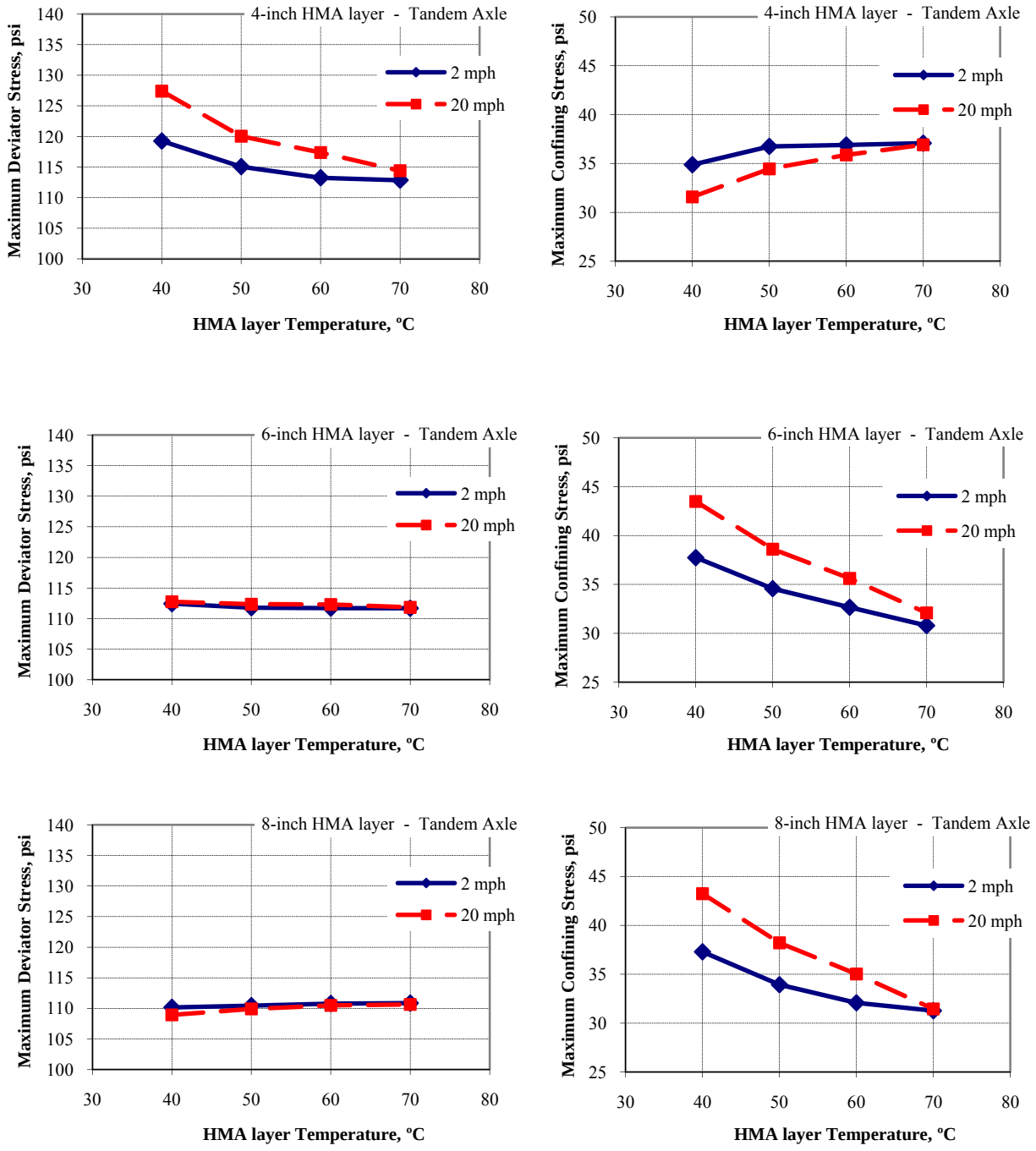

Figure 42. Maximum σ_d and σ_c stresses at 2 inch below the surface of the PG58-22 mix – braking.

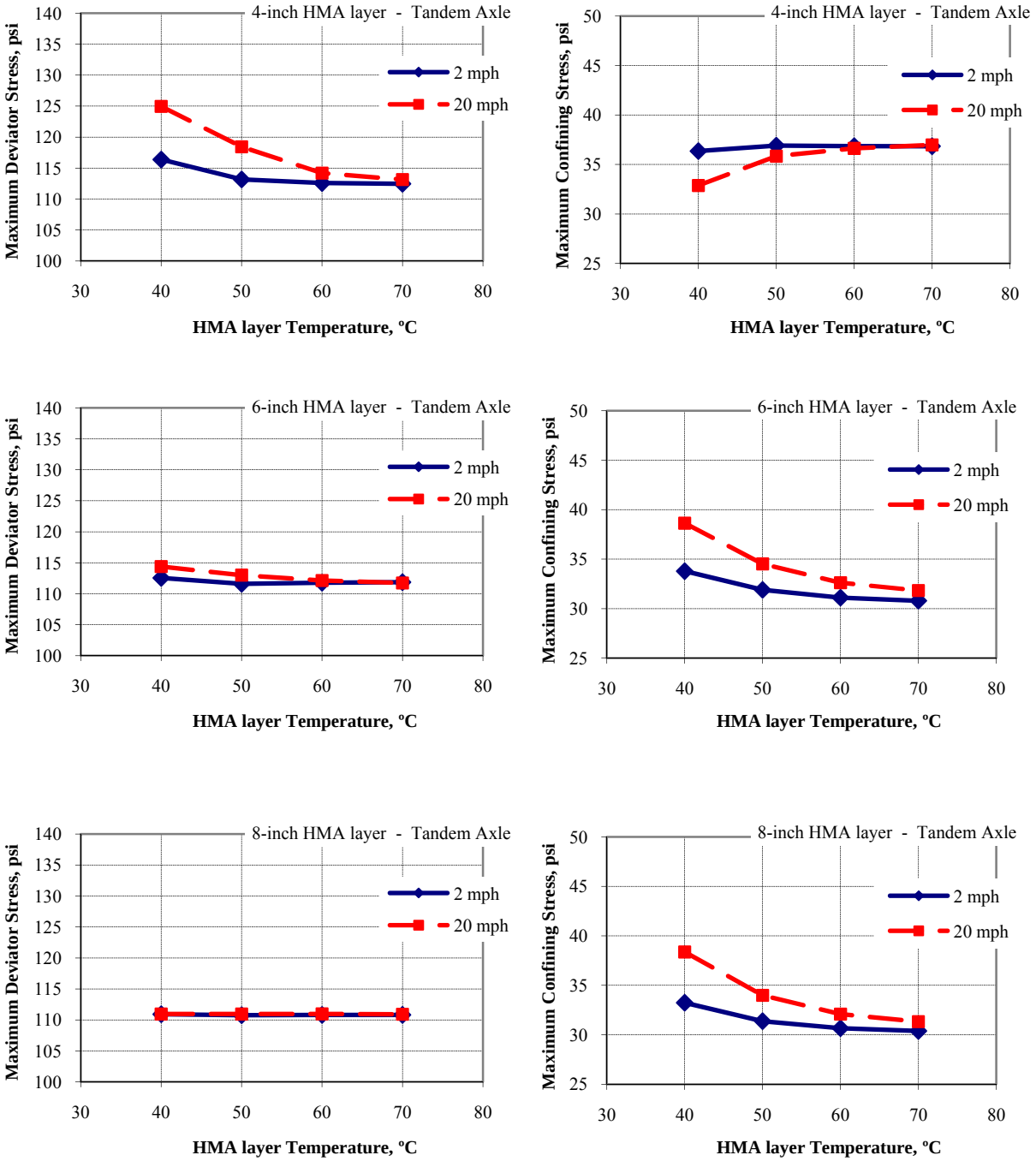

Figure 43. Maximum σ_d and σ_c stresses at 2 inch below the surface of the PG52-22 mix – braking.

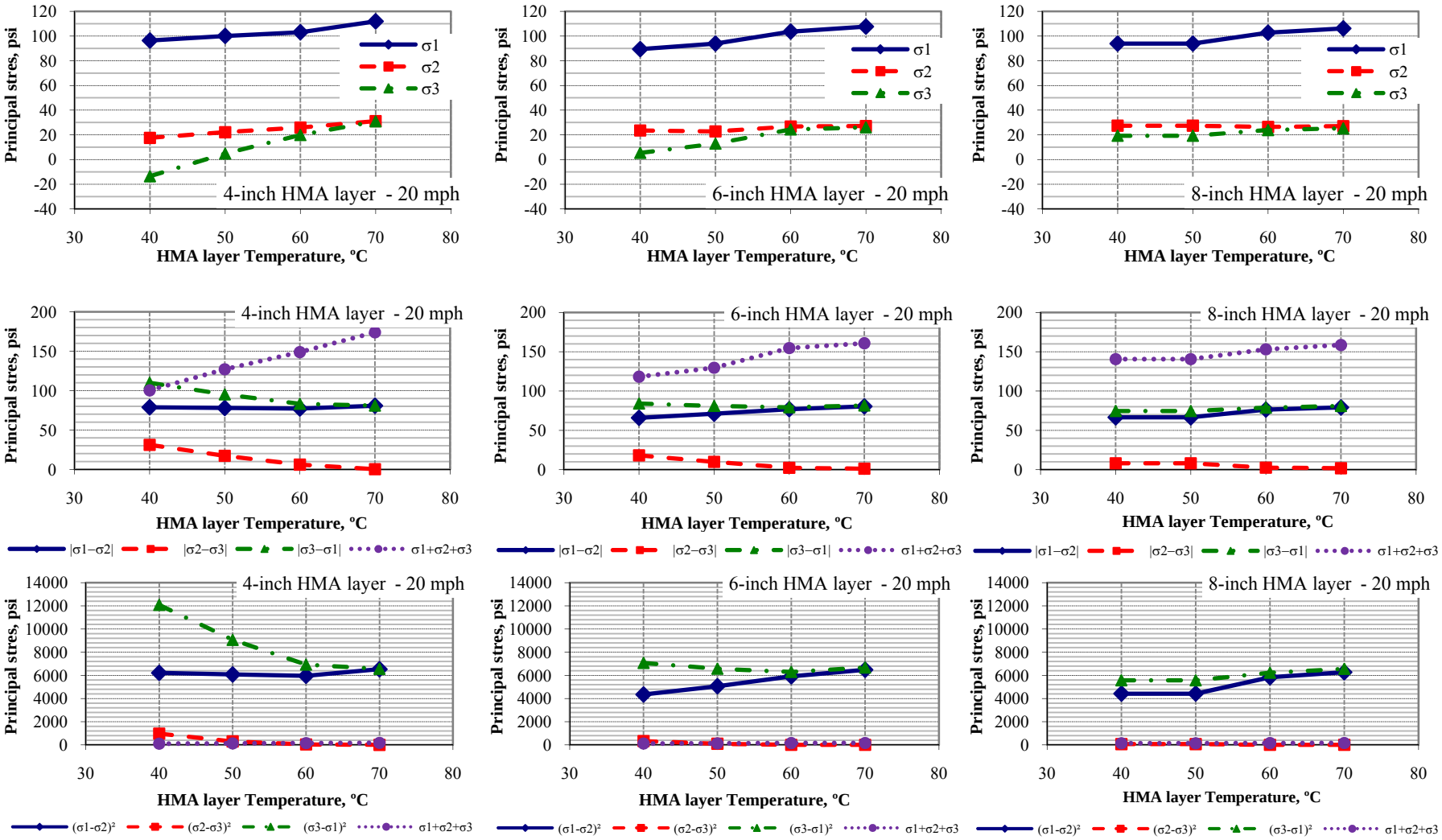

Figure 44. Calculated principal stresses at 2 inch below the surface for the PG64-22 mix – non-braking.

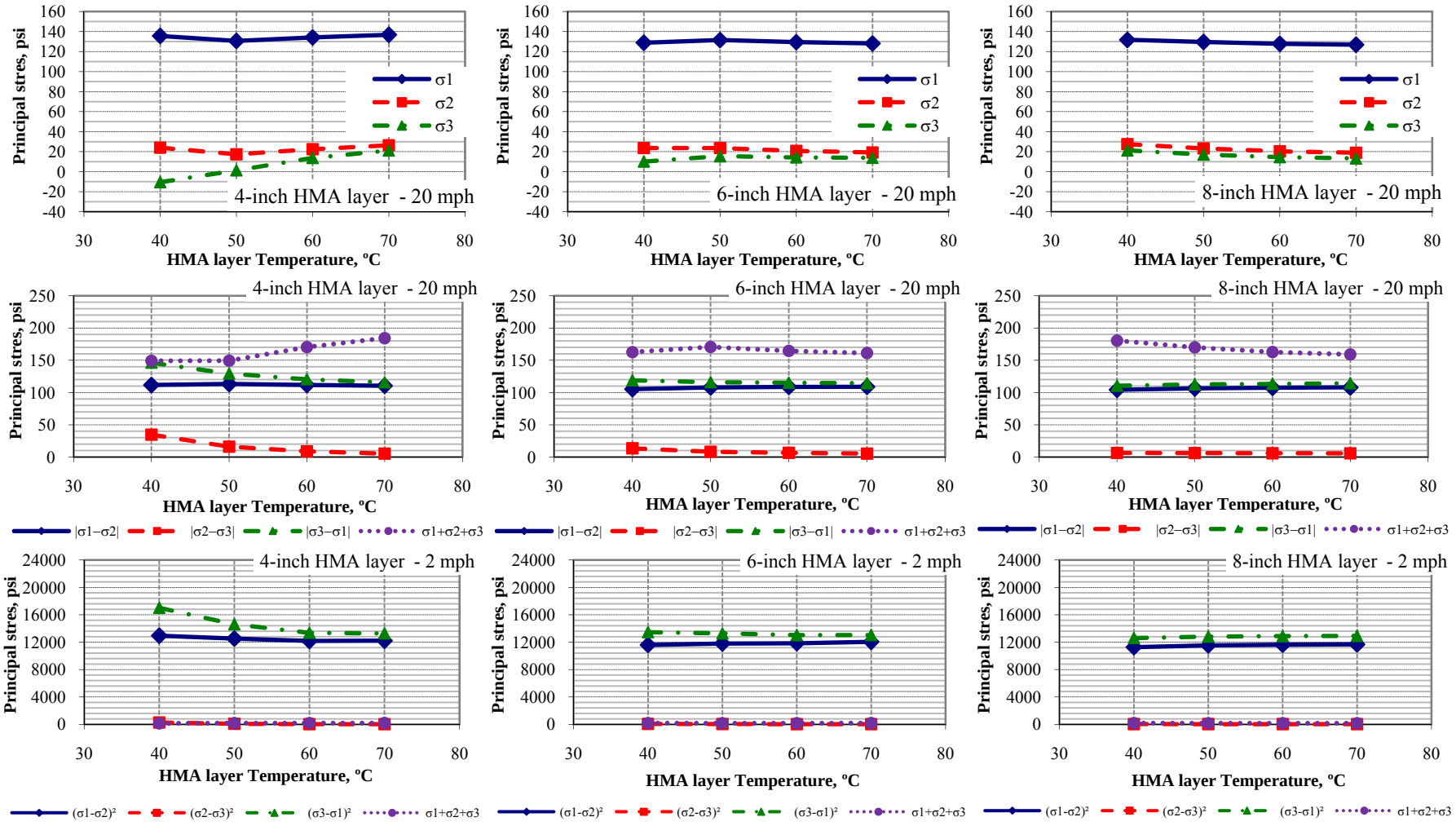

Figure 45. Calculated principal stresses at 2 inch below the surface for the PG64-22 mix –Braking.

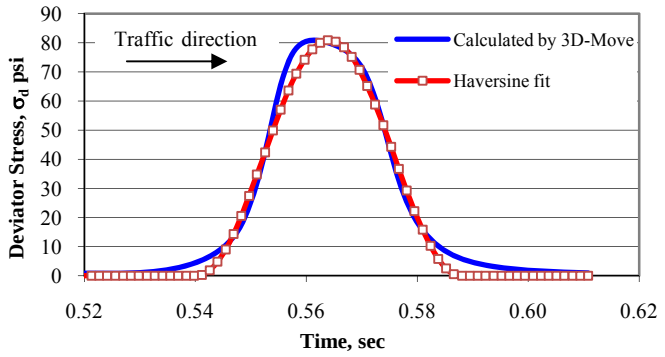

(a) Vehicle speed of 20 mph with non-braking conditions

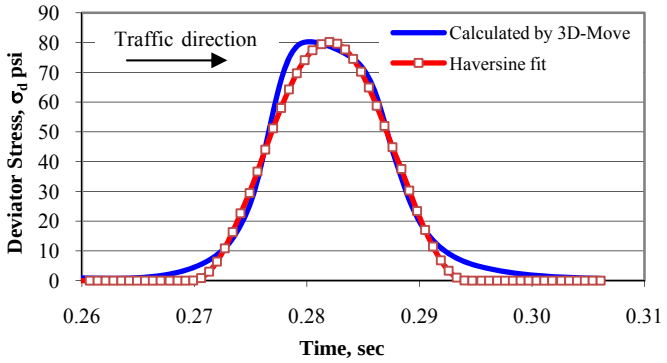

(b) Vehicle speed of 40 mph with non-braking conditions

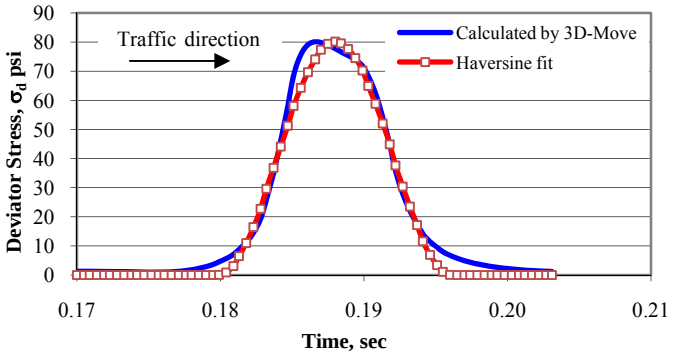

(c) Vehicle speed of 60 mph with non-braking conditions

Figure 46. Example of deviator pulse loading time fitting at 2 inch below the surface – non-braking.

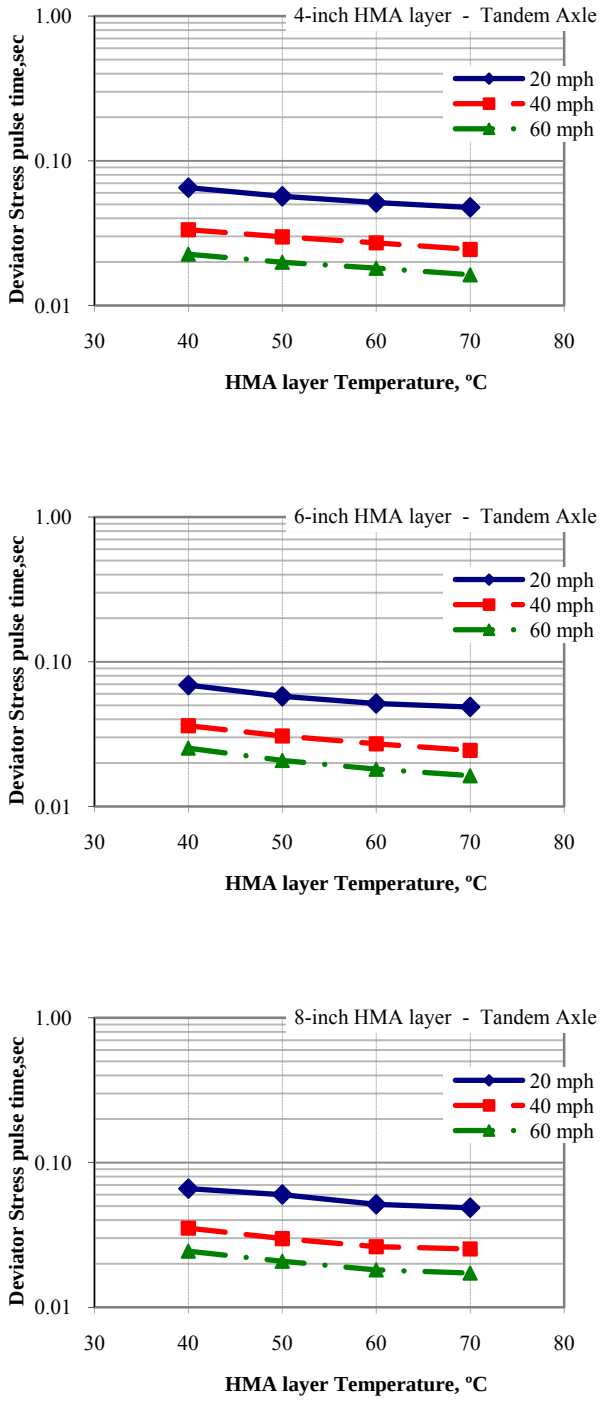

Figure 47. Deviator stress pulse time at 2 inch below the surface of the PG64-22 mix – non-braking.

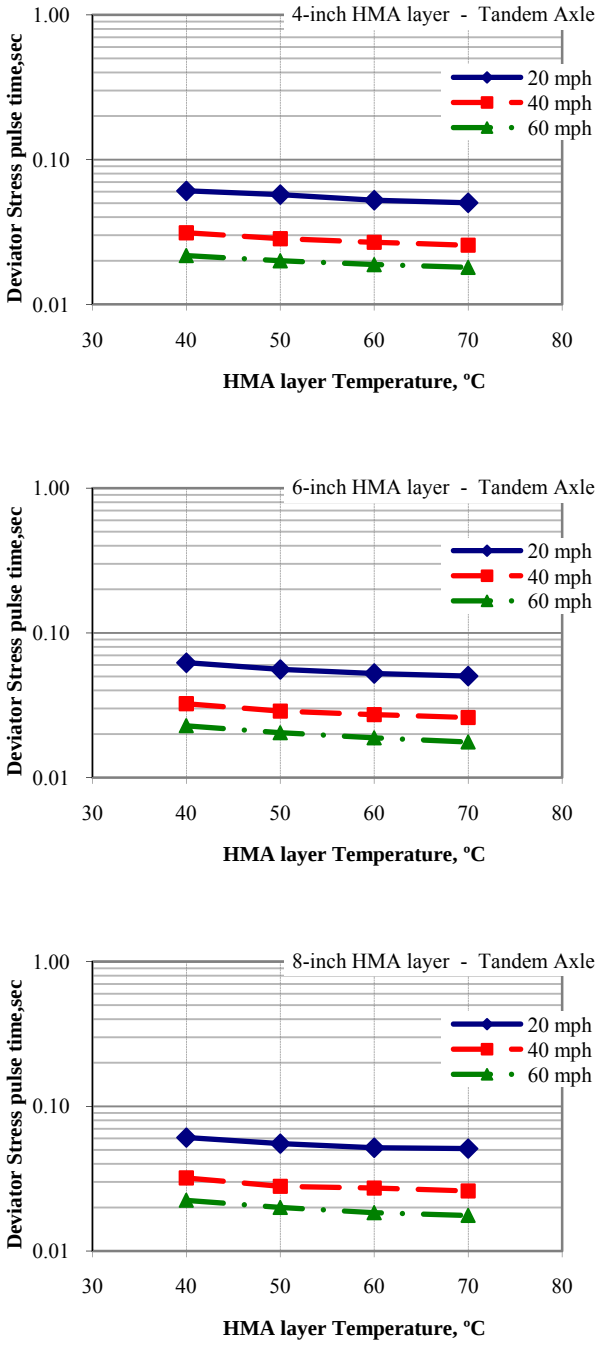

Figure 48. Deviator stress pulse time at 2 inch below the surface of the PG58-22 mix – non-braking.

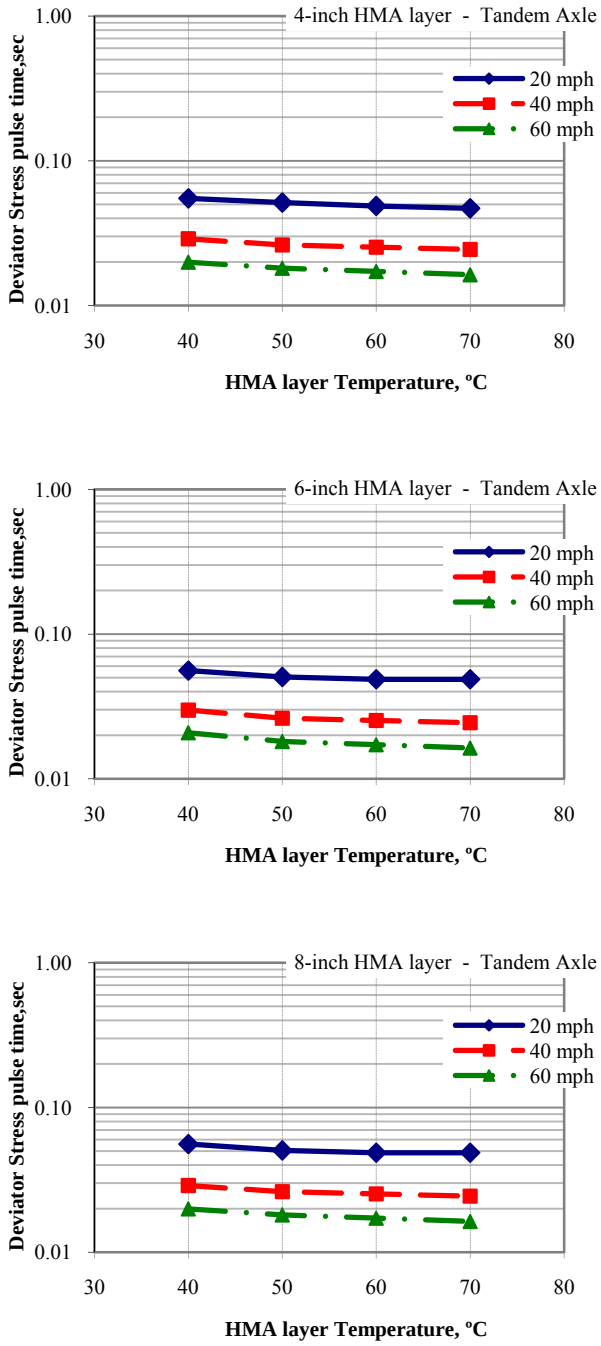

Figure 49. Deviator stress pulse time at 2 inch below the surface of the PG52-22 mix – non-braking.

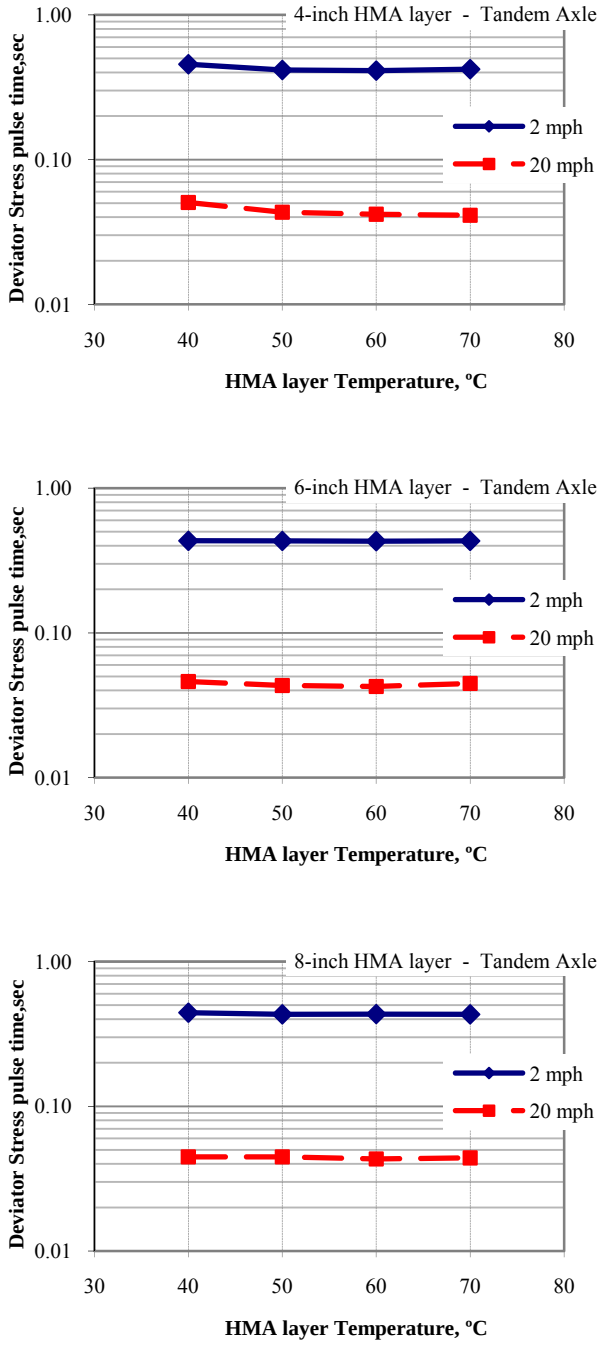

Figure 50. Deviator stress pulse time at 2 inch below the surface of the PG64-22 mix – braking.

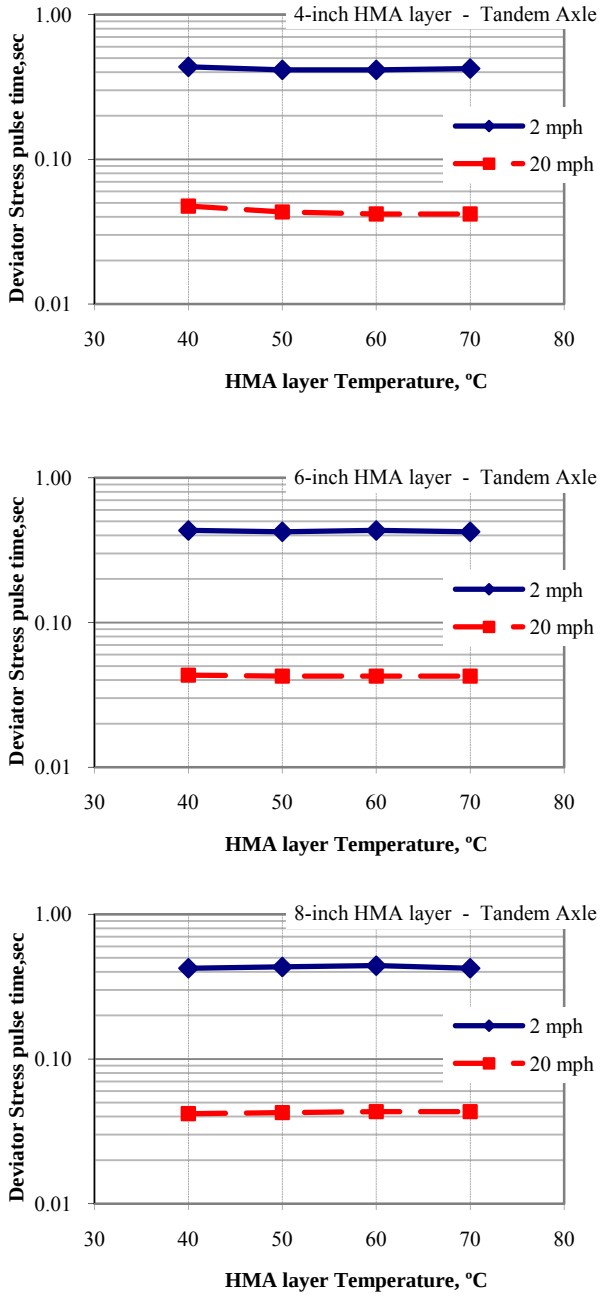

Figure 51. Deviator stress pulse time at 2 inch below the surface of the PG58-22 mix – braking.

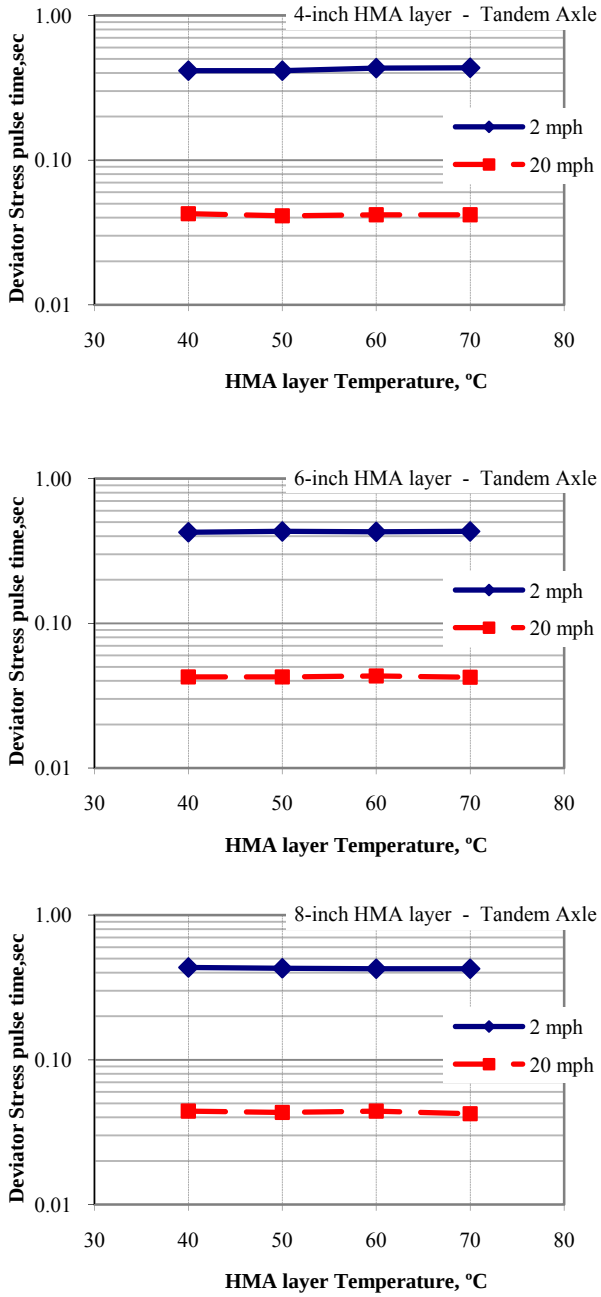

Figure 52. Deviator stress pulse time at 2 inch below the surface of the PG52-22 mix – braking.

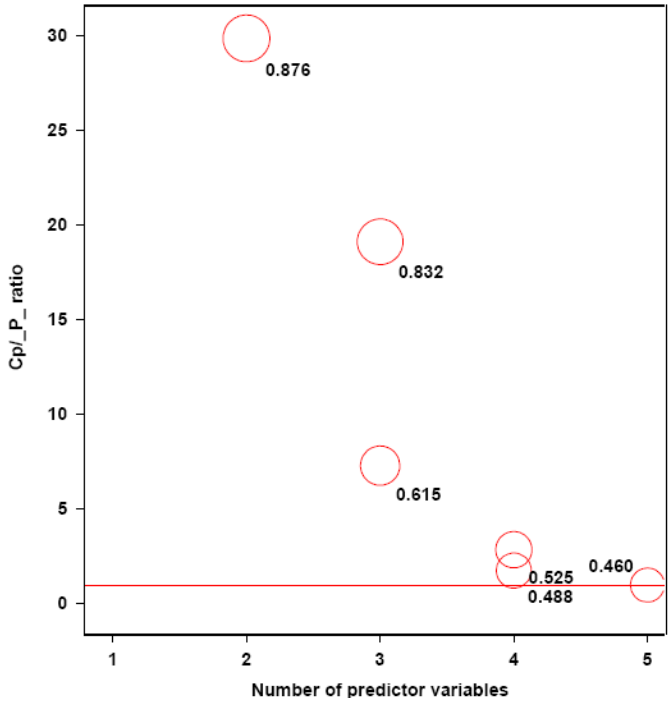

Figure 53. Plot of Cp/p vs p with 5 variable – SAS output.

Number in Model	R-Square	Adjusted R-Square	C(p)	AIC	Root MSE	SBC	Variables in Model
1	0.6632	0.6533	107.3567	-3.1487	0.93173	0.01834	X7
1	0.4125	0.3952	211.0897	16.8815	1.23058	20.04852	X8
2	0.7109	0.6933	89.6320	-6.6429	0.87626	-1.89233	X3 X7
2	0.6859	0.6669	99.9404	-3.6673	0.91324	1.08329	X7 X8
3	0.8617	0.8487	29.2308	-31.1867	0.61547	-24.85260	X3 X7 X8
3	0.7474	0.7237	76.5286	-9.5014	0.83178	-3.16734	X2 X3 X7
4	0.9159	0.9050	8.8132	-47.0821	0.48771	-39.16453	X2 X3 X7 X8
4	0.9026	0.8900	14.3187	-41.7966	0.52486	-33.87905	X3 X4 X7 X8
5	0.9275	0.9154	6.0000	-50.4389	0.46022	-40.93779	X2 X3 X4 X7 X8

Figure 54. Summary table for R^2 model selection – SAS output.

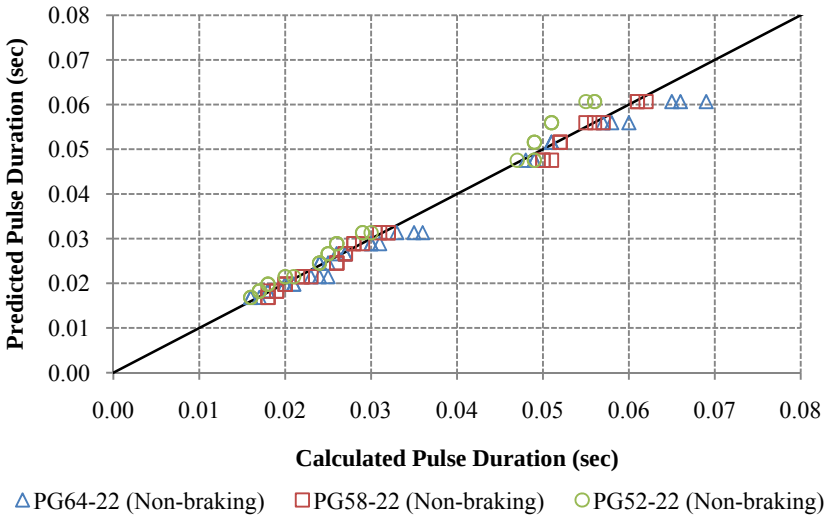

Figure 55. Predicted versus calculated pulse duration – non-braking.

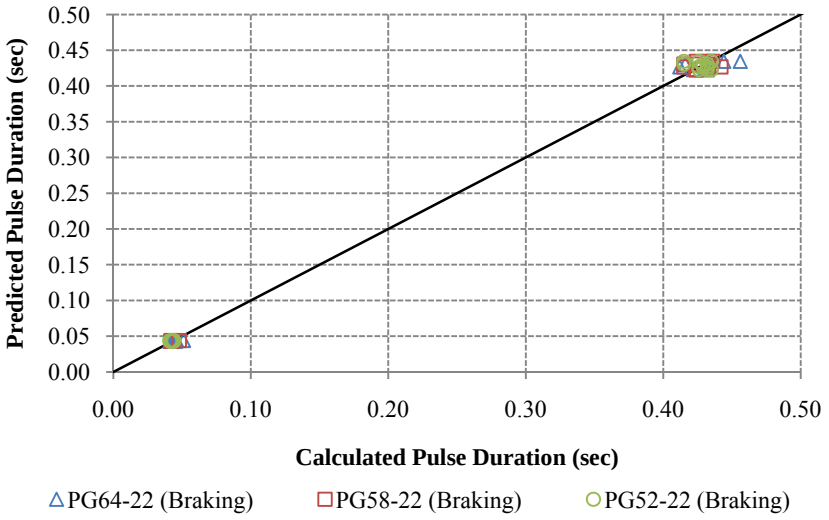

Figure 56. Predicted versus calculated pulse duration –braking.

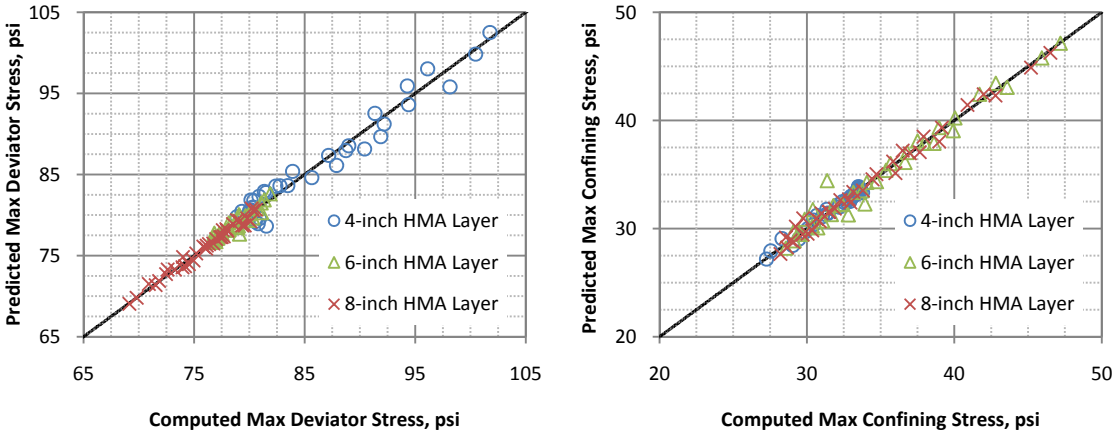

Figure 57. Predicted versus calculated deviator and confining stresses – non-braking.

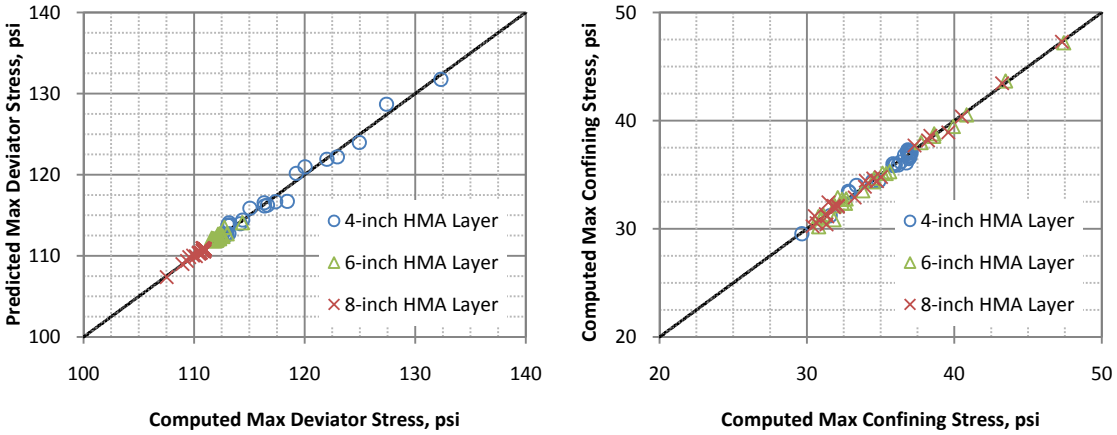

Figure 58. Predicted versus calculated deviator and confining stresses – braking.

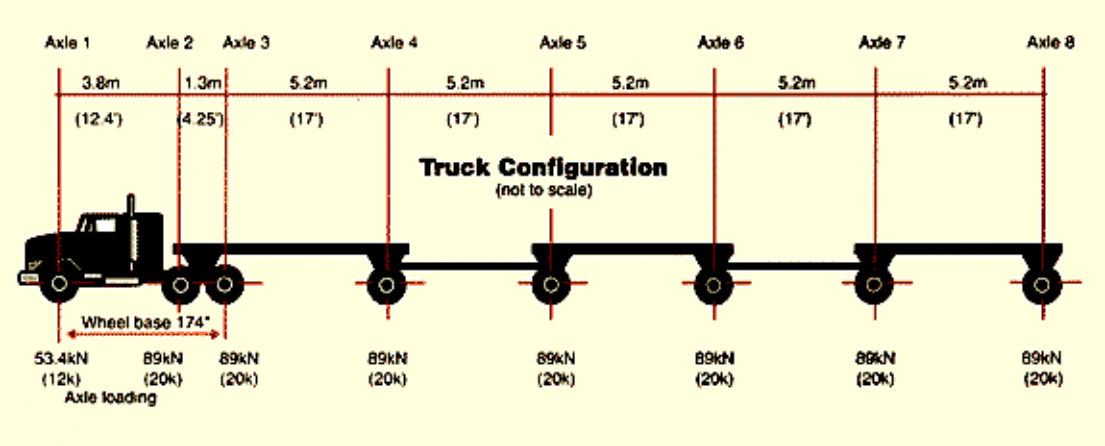

Figure 59. Tractor/trailer configuration used in WesTrack Project (52).

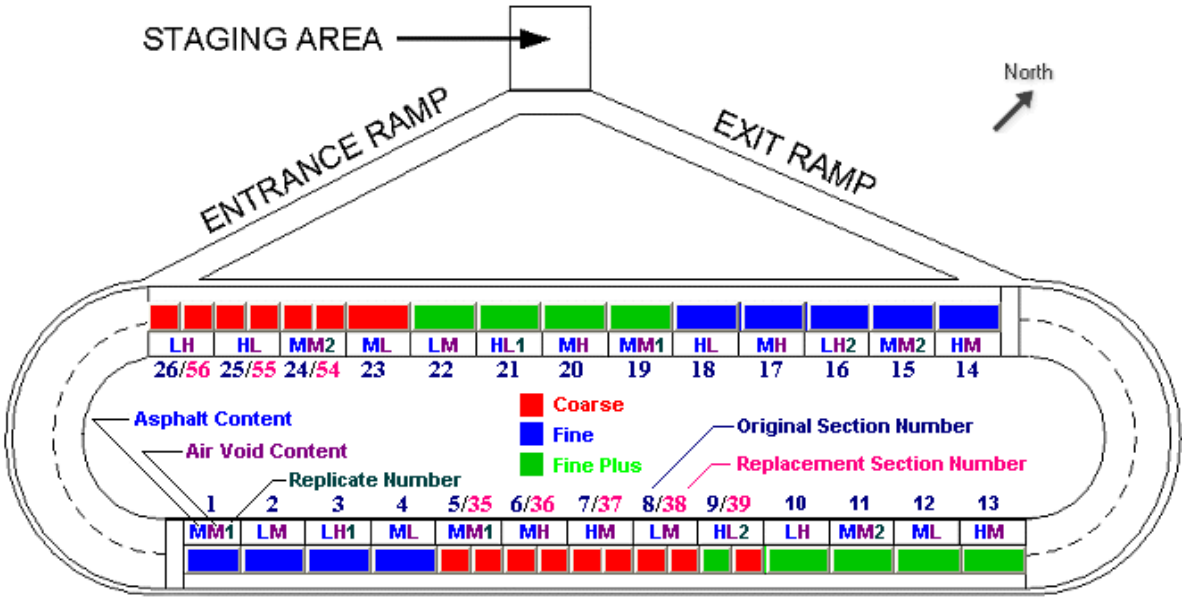

Figure 60. WesTrack Project track configuration (53).

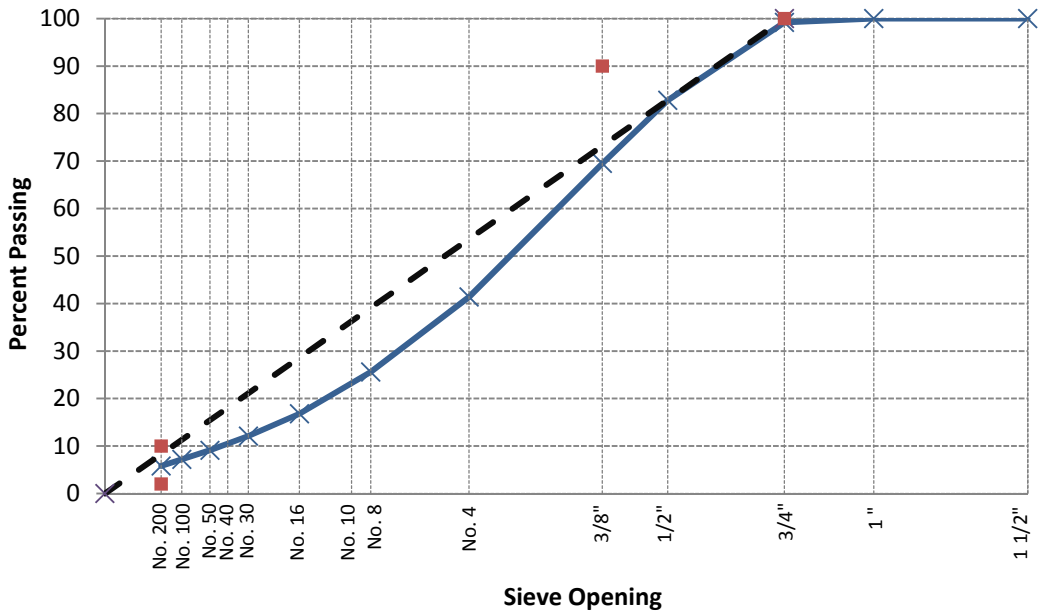

Figure 61. WesTrack Cell 55 aggregate gradation.

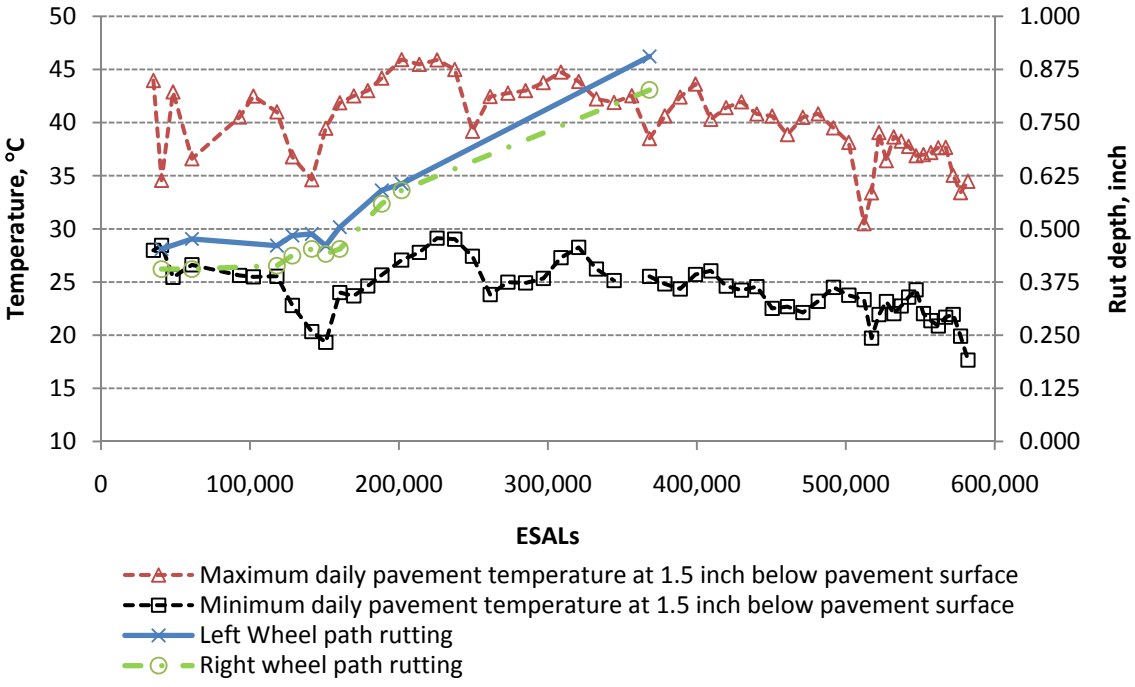

Figure 62. Temperature profile and rut depths in Cell 55 versus applied ESAL.

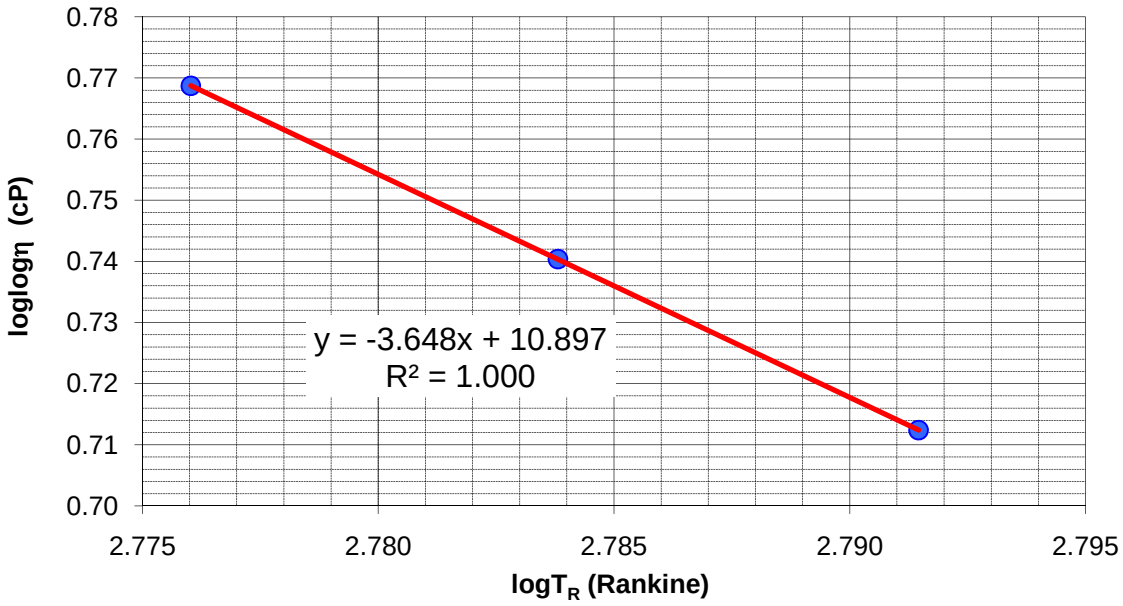

Figure 63. A-VTS determinations for WesTrack Cell 55.

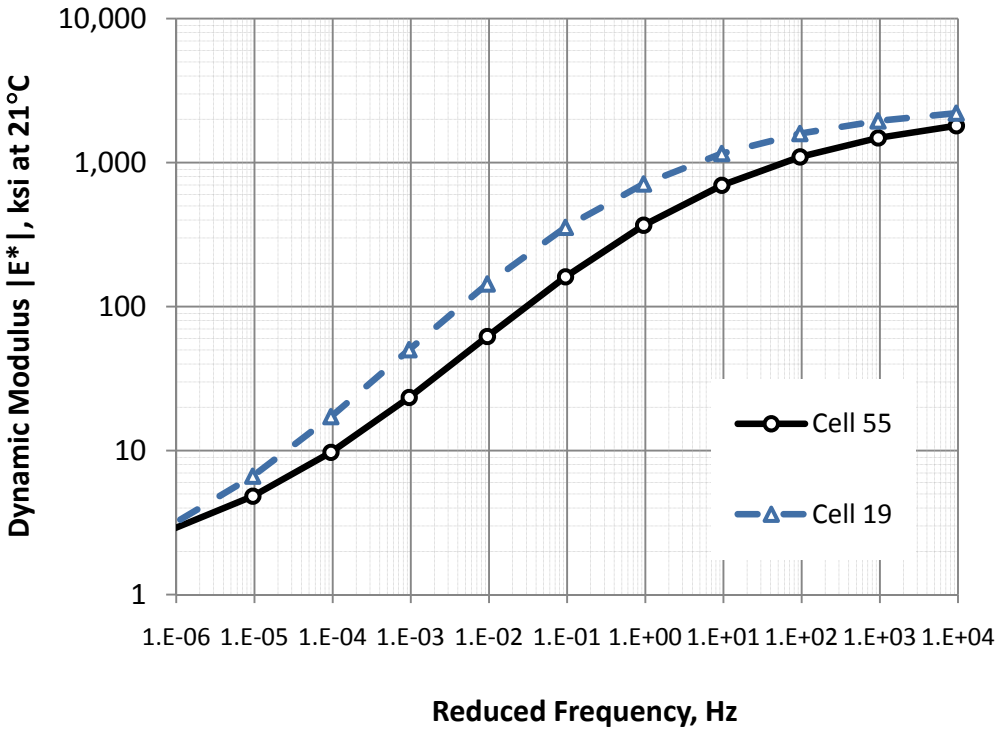

Figure 64. Dynamic modulus master curve for WesTrack Cell 55 & 19 at 21ºC.

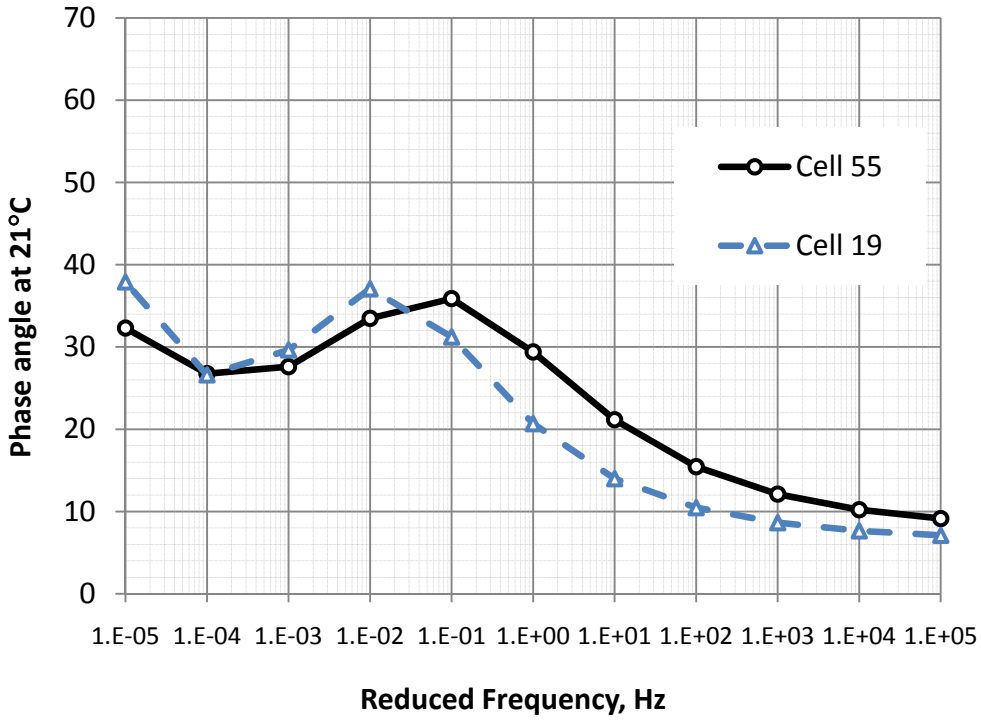

Figure 65. Phase angle for WesTrack Cell 55 and 19.

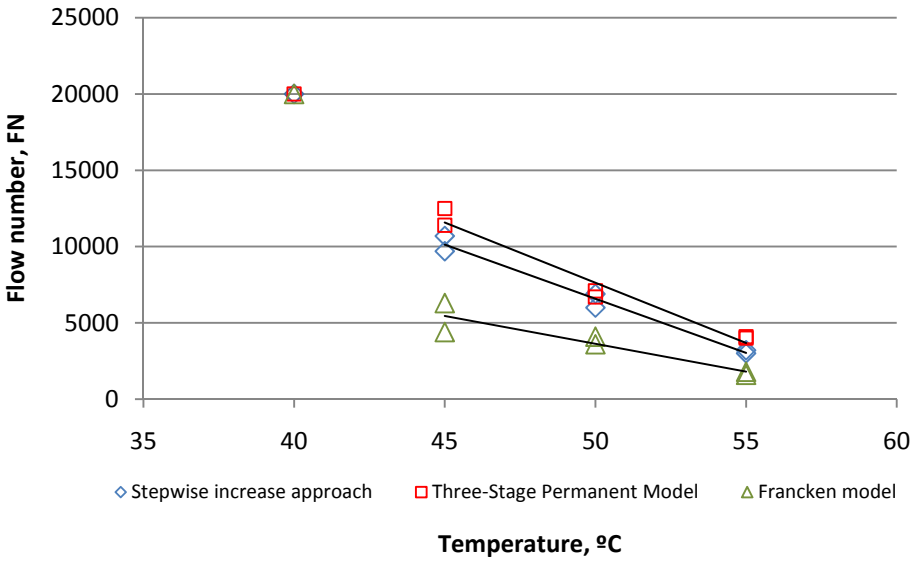

Figure 66. Flow Number test results for Cell 55 mix.

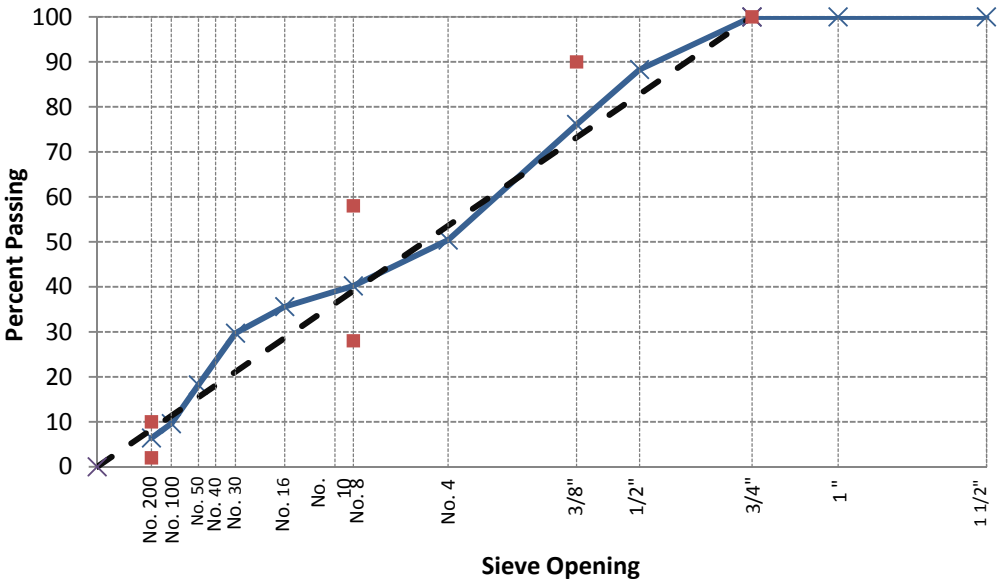

Figure 67. WesTrack Cell 19 aggregate gradation.

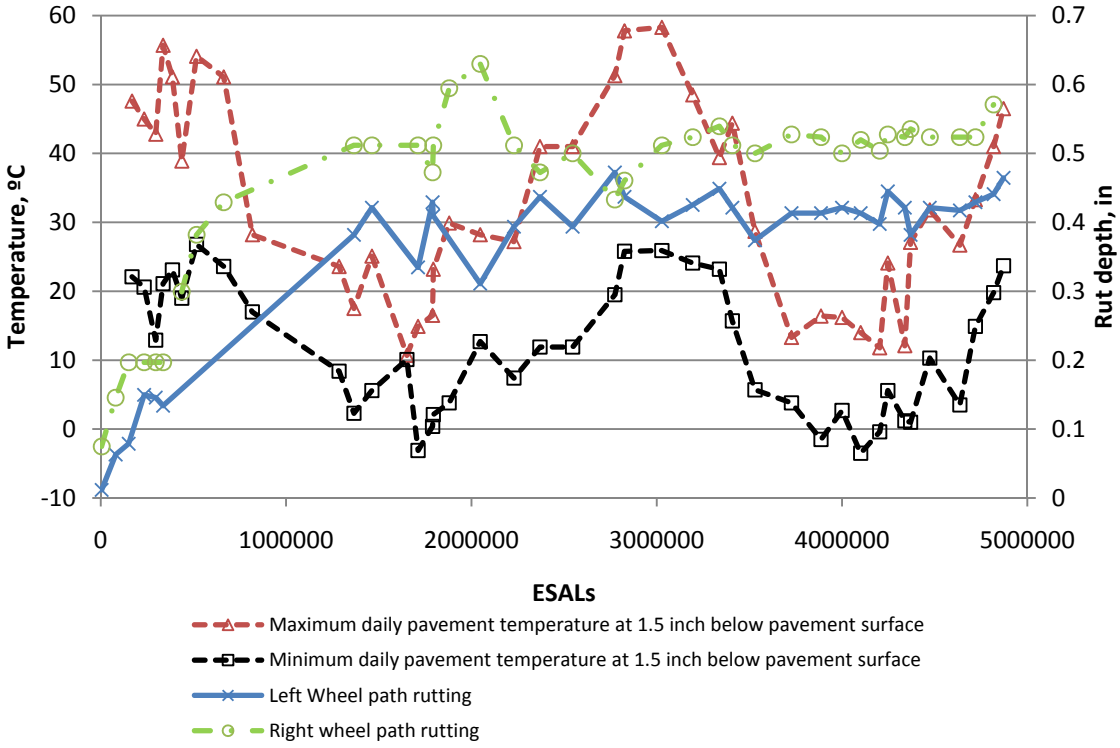

Figure 68. Temperature profile and rut depths in Cell 19 versus applied ESAL.

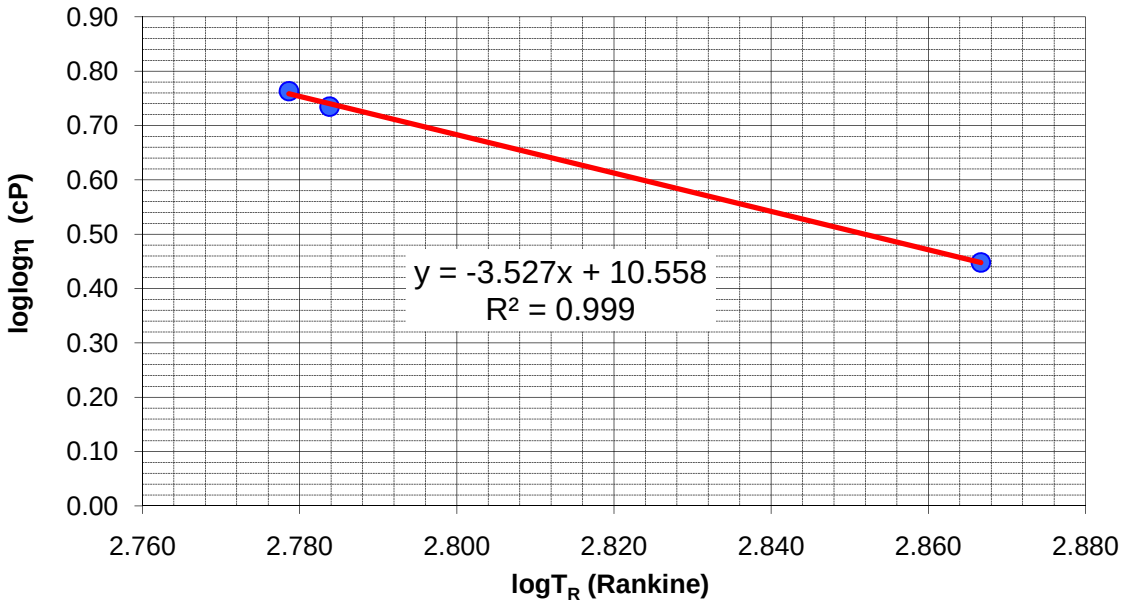

Figure 69. A-VTS determinations for binder WesTrack Cell 19.

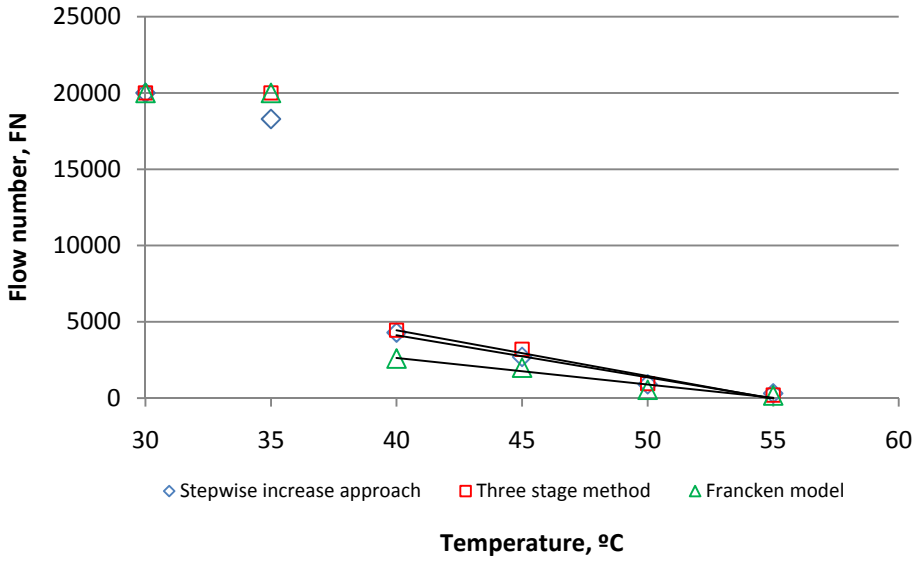

Figure 70. Flow Number test results for Cell 19 mix.

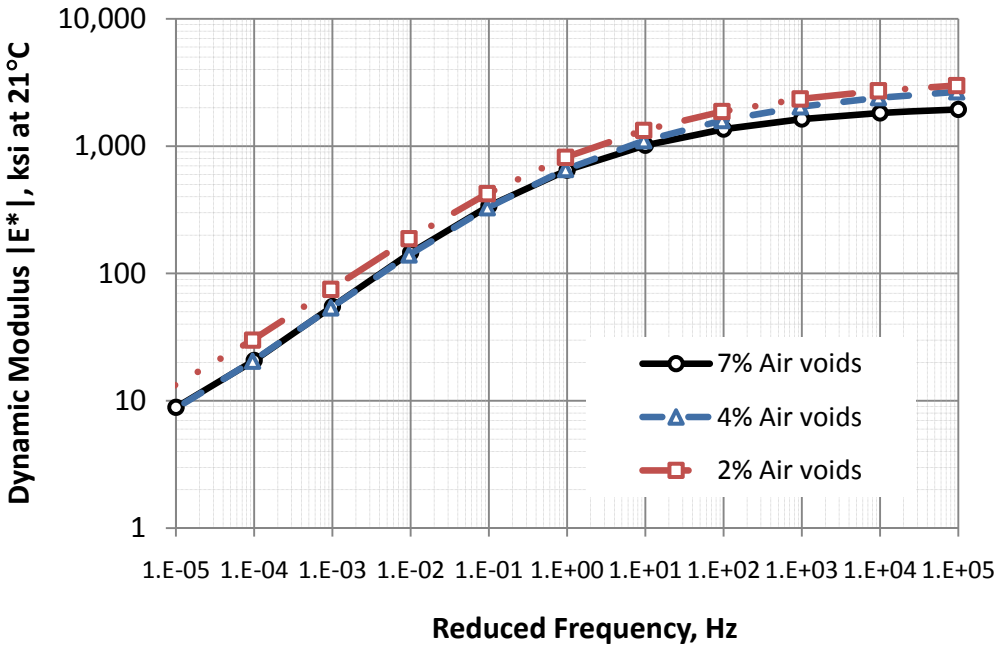

Figure 71. Dynamic modulus master curve for PG64-22 mix at 7, 4, 2% air voids.

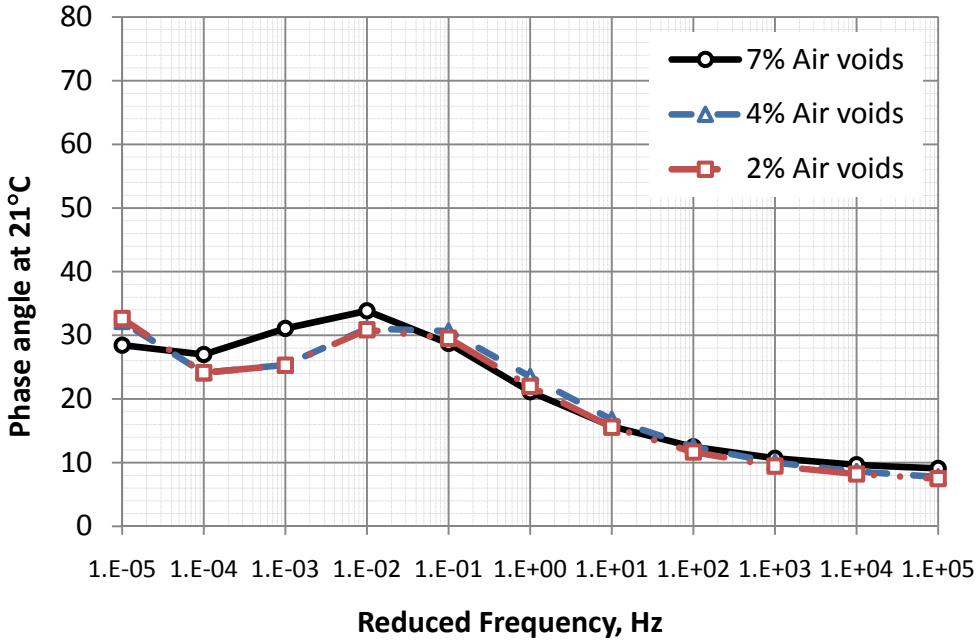

Figure 72. Phase angle for PG64-22 mix at 7, 4, 2% air voids.

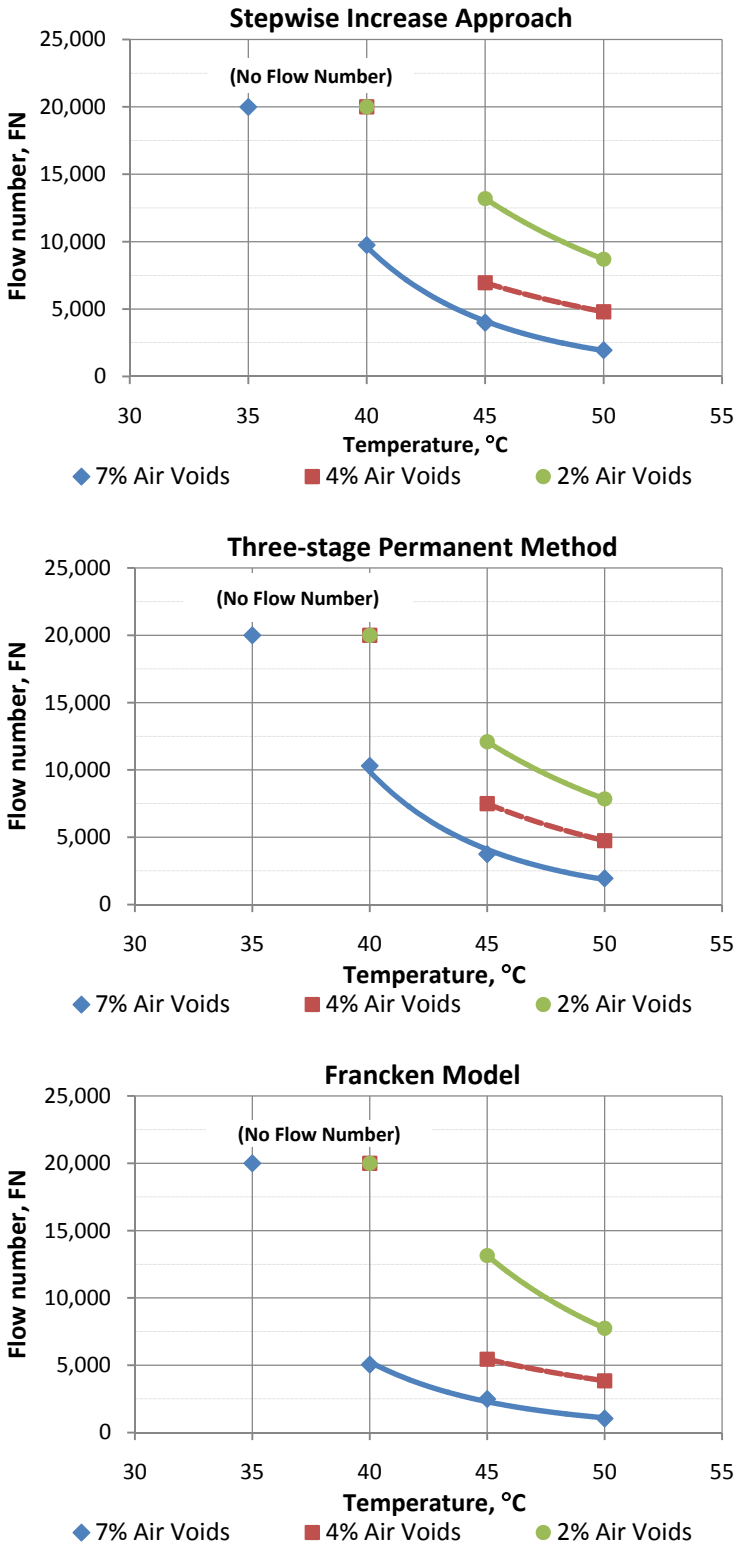

Figure 73. Flow number versus temperature for 7, 4, 2% air voids.

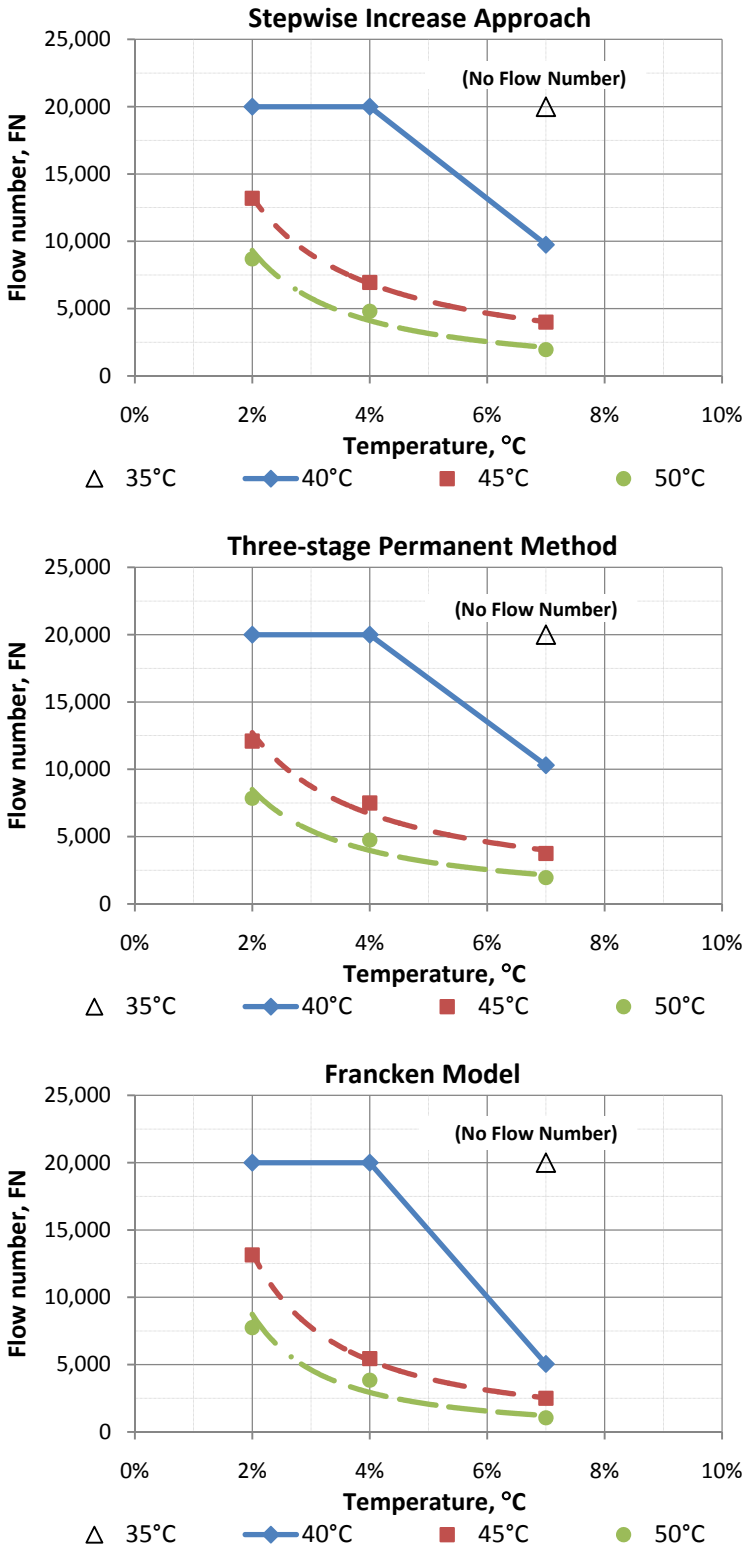

Figure 74. Flow number versus air-void levels for different testing temperatures.

APPENDIX A

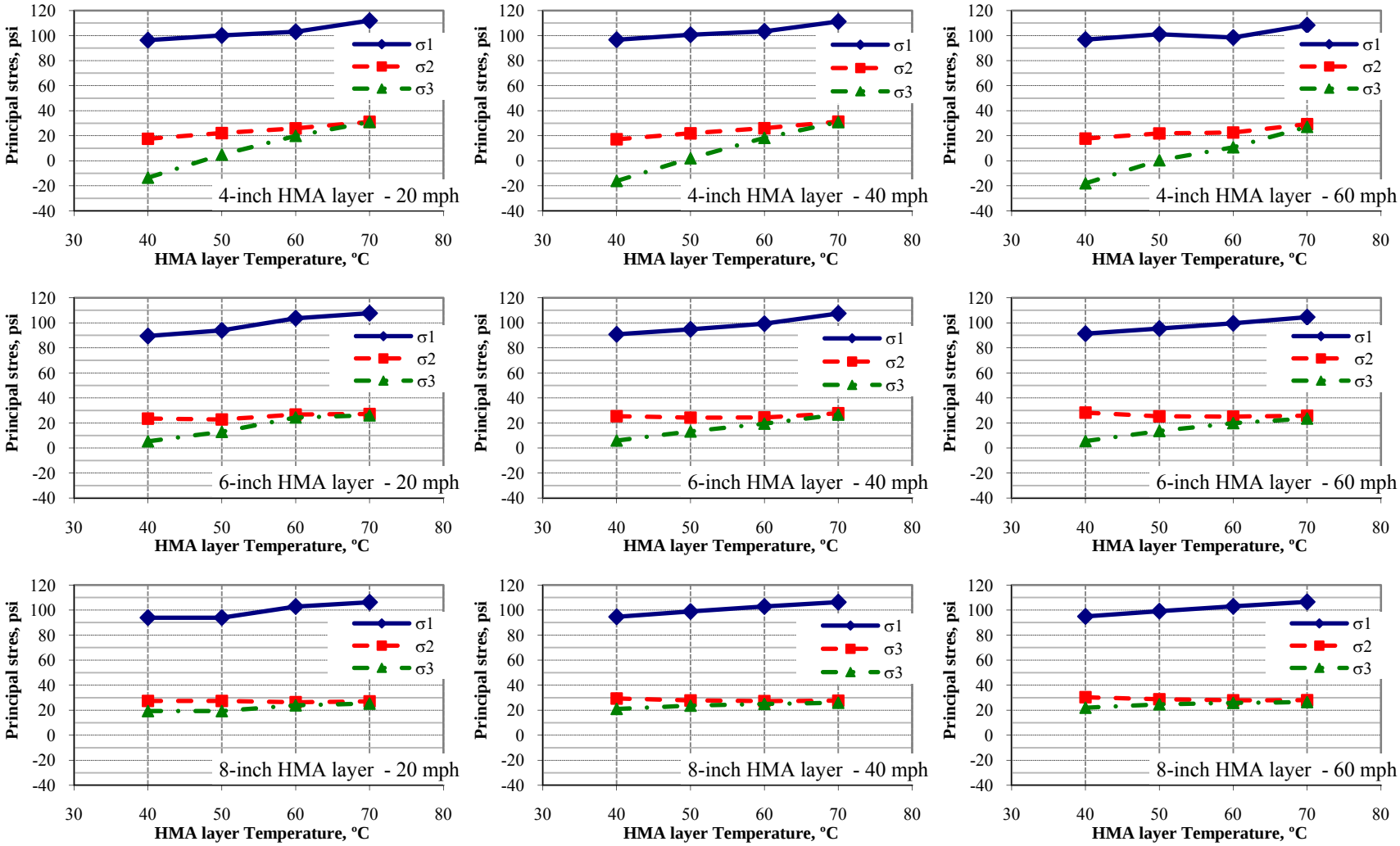

Figure A.1 Calculated principal stresses at 2 inch below the surface for the PG64-22 mix – non-braking.

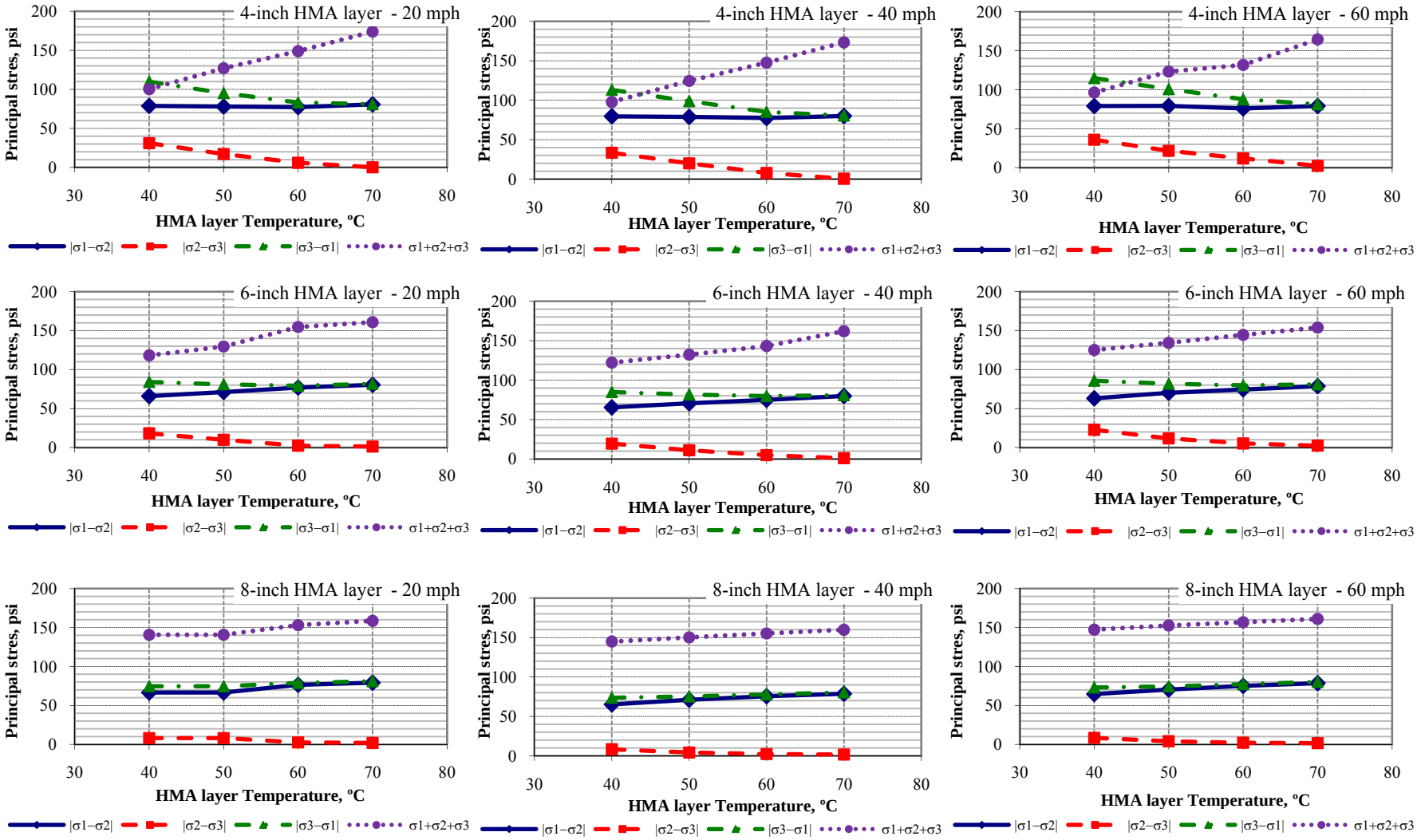

Figure A.2 Calculated principal stresses differences at 2 inch below the surface for the PG64-22 mix – non-braking.

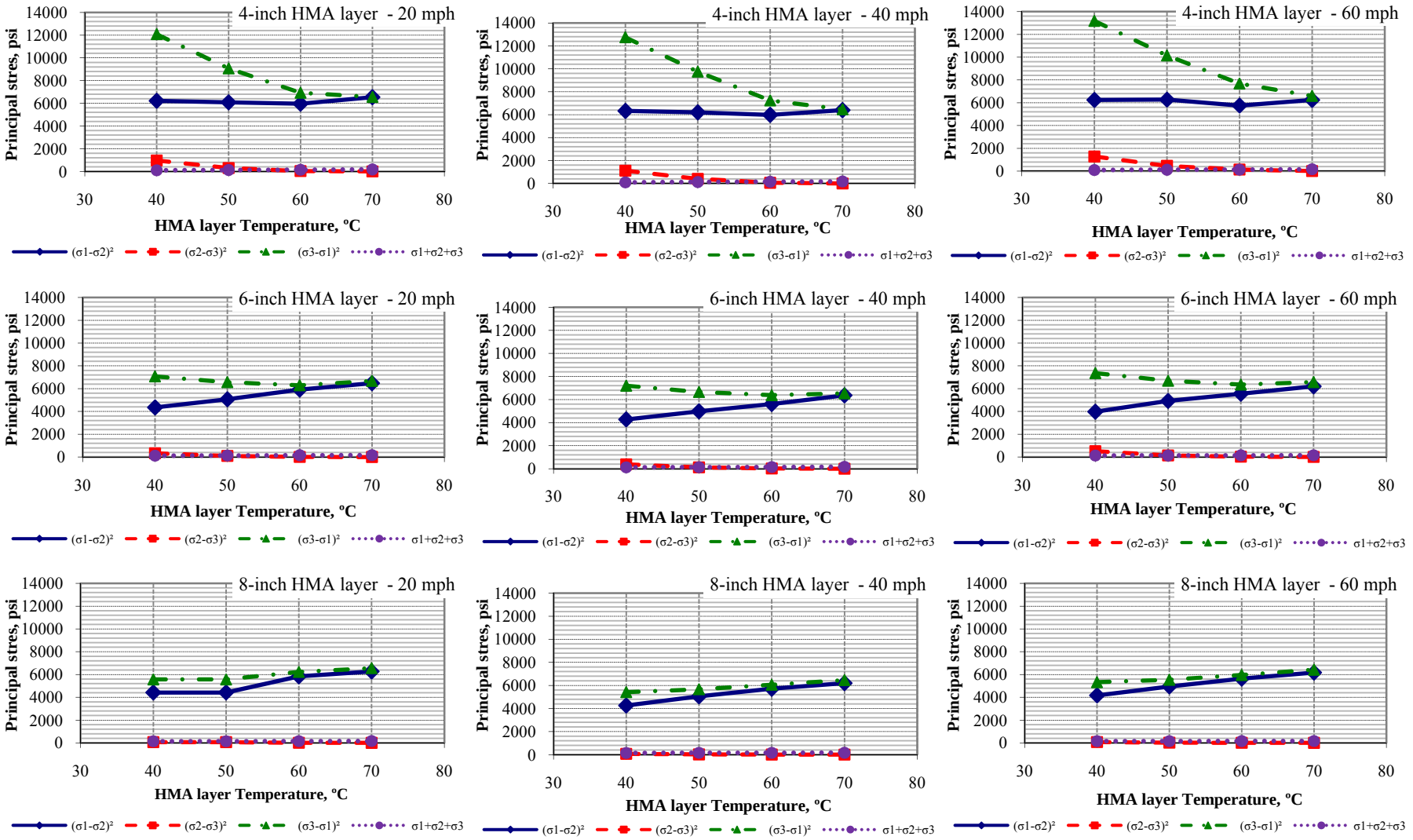

Figure A.3 Calculated principal stresses square differences at 2 inch below the surface for the PG64-22 mix – non-braking.

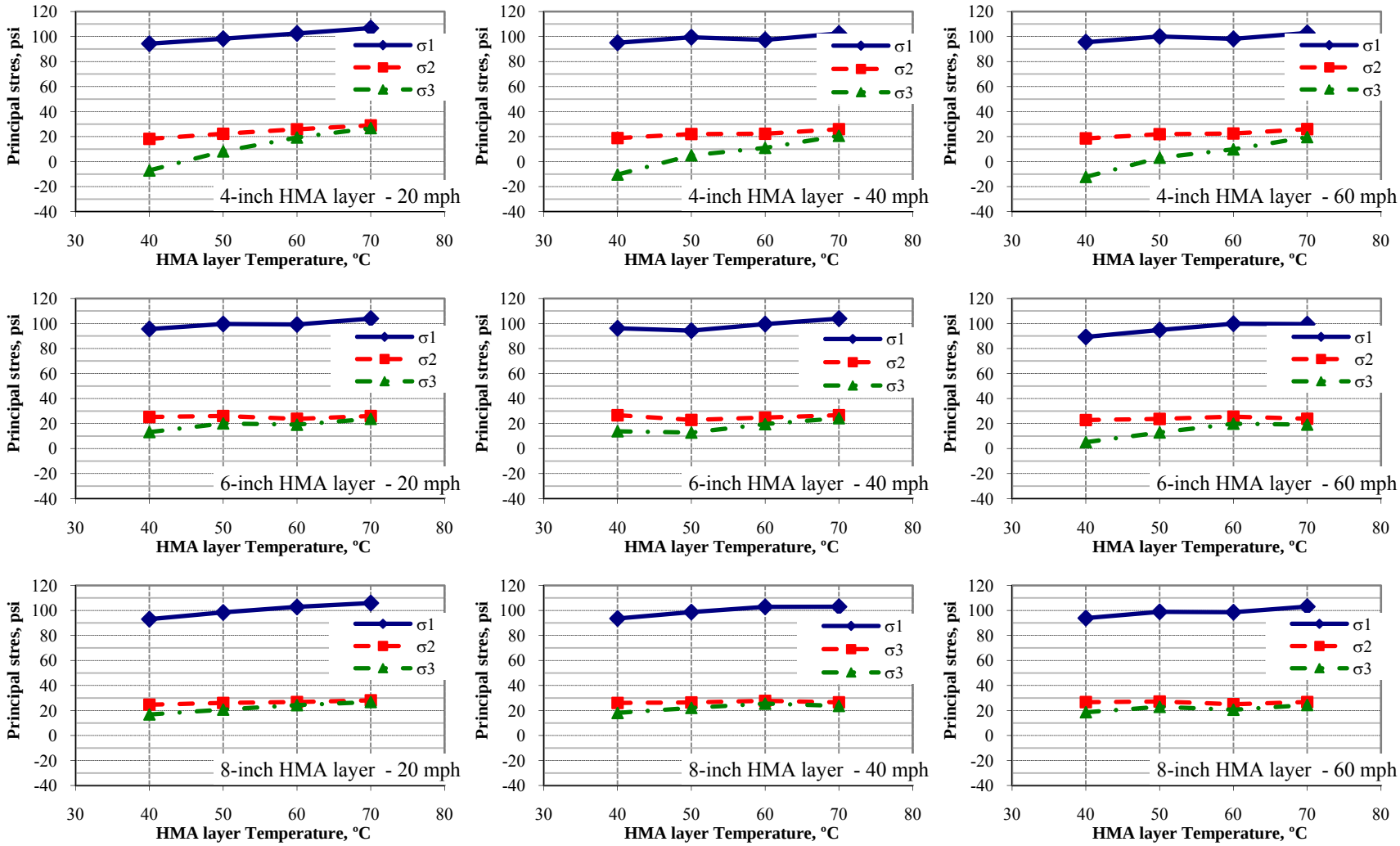

Figure A.4 Calculated principal stresses at 2 inch below the surface for the PG58-22 mix – non-braking.

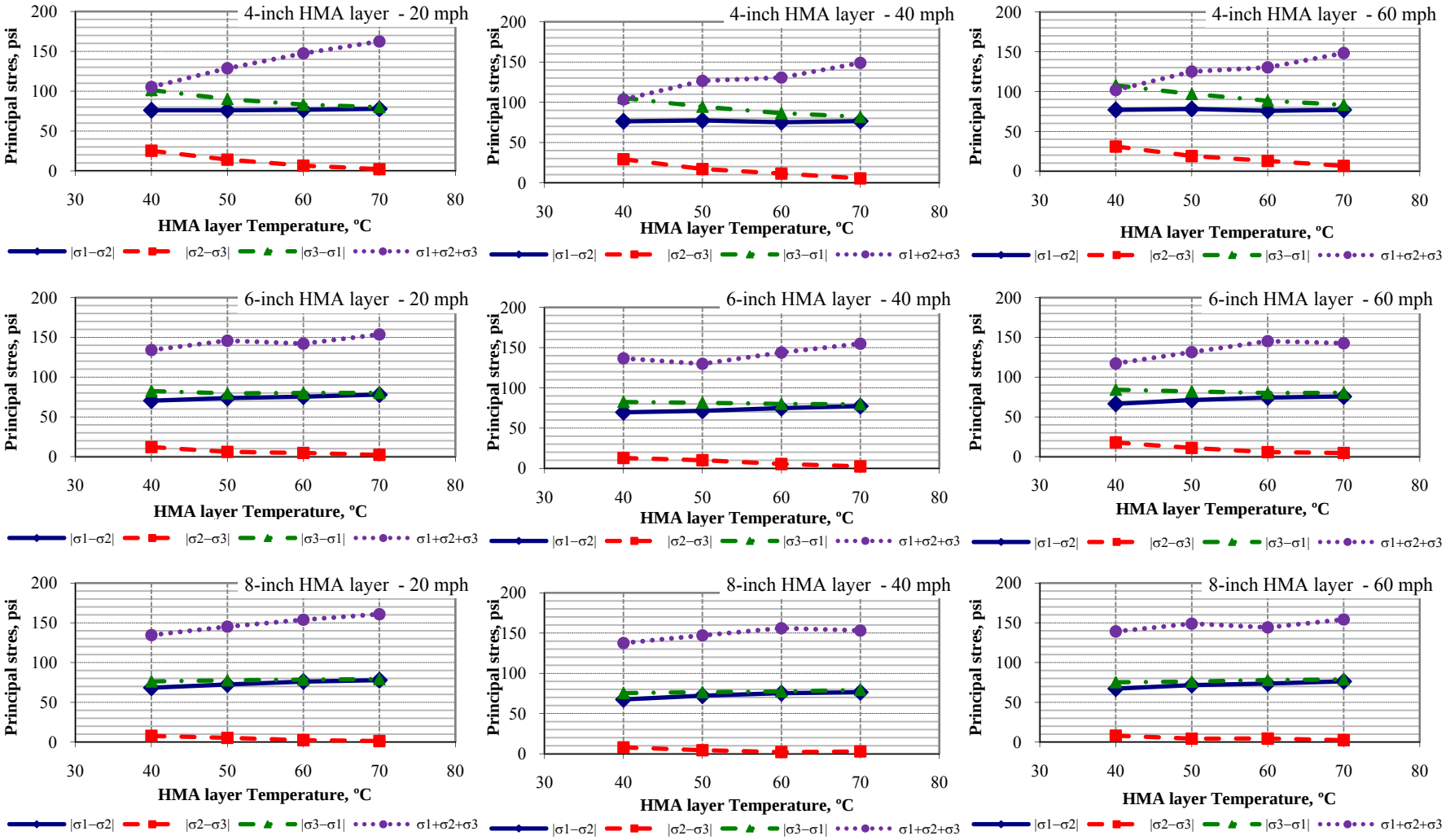

Figure A.5 Calculated principal stresses differences at 2 inch below the surface for the PG58-22 mix – non-braking.

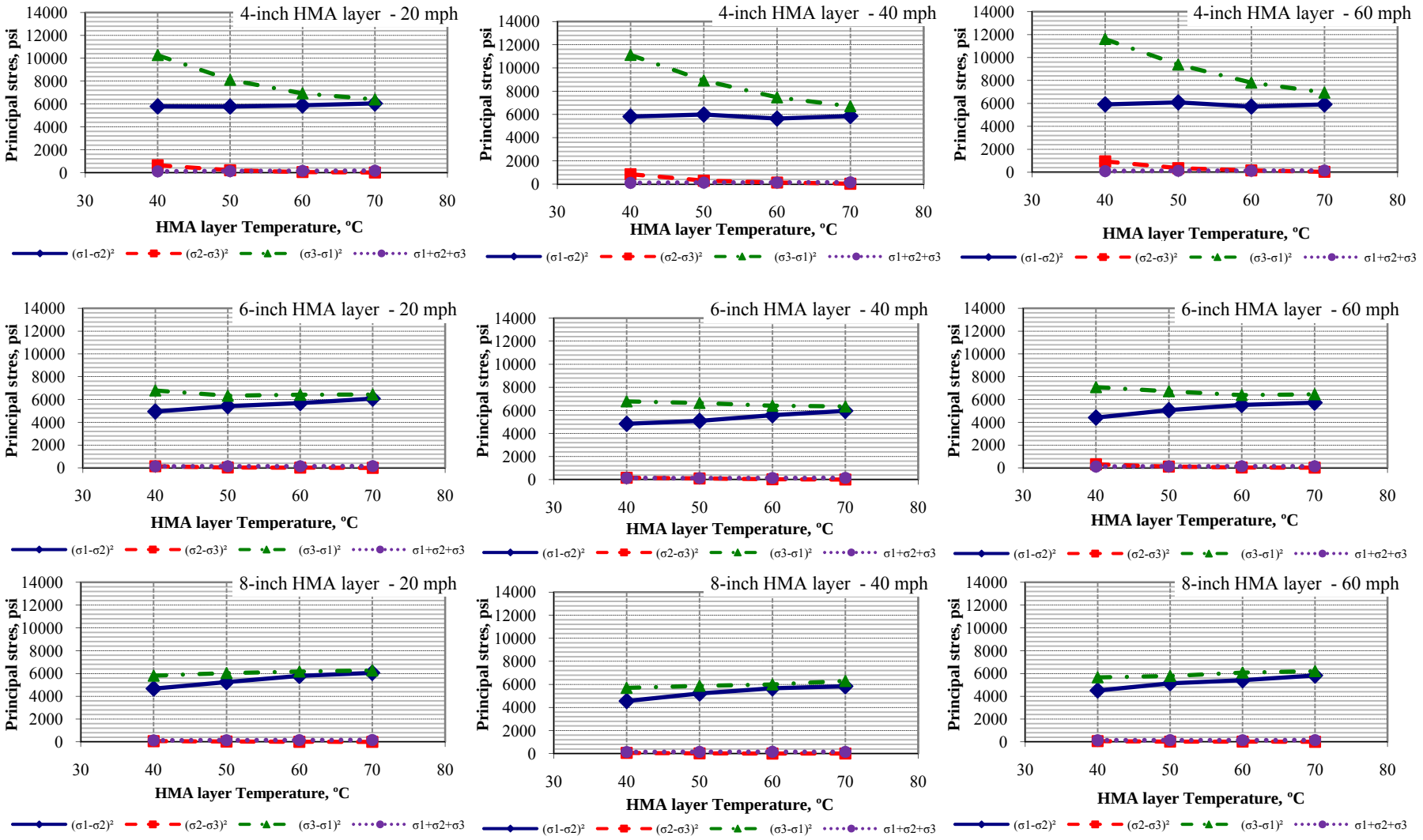

Figure A.6 Calculated principal stresses square differences at 2 inch below the surface for the PG58-22 mix – non-braking.

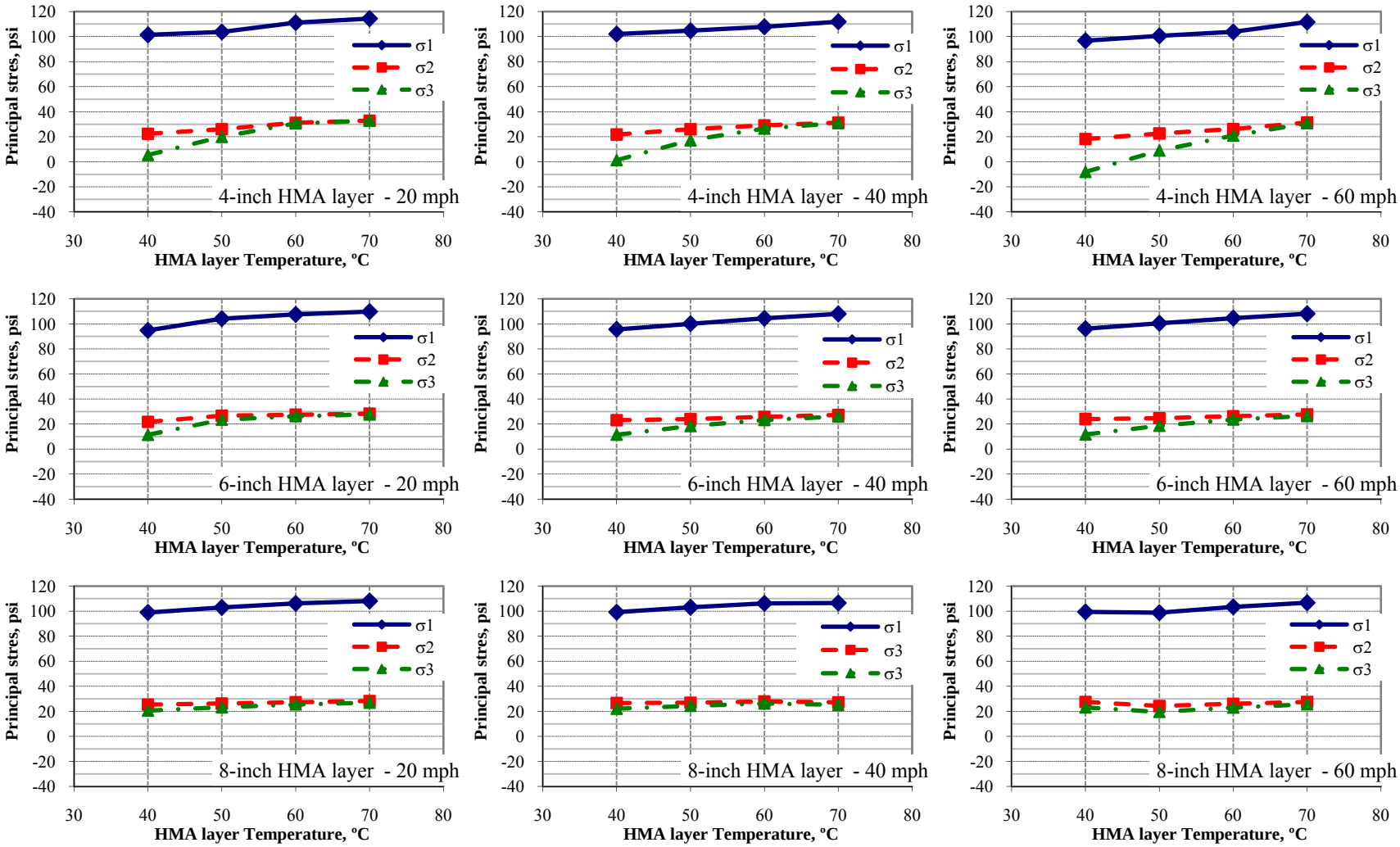

Figure A.7 Calculated principal stresses at 2 inch below the surface for the PG52-22 mix – non-braking.

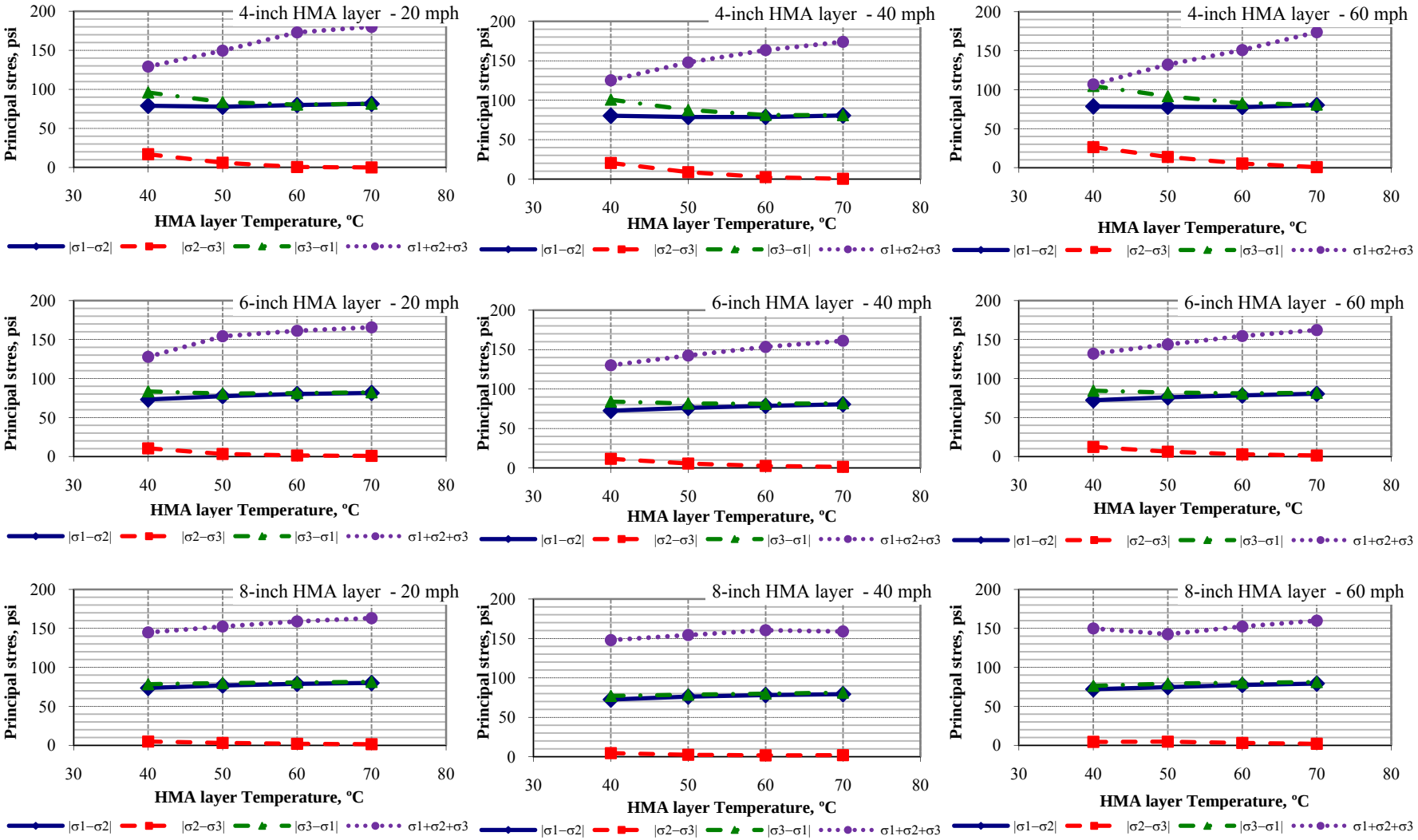

Figure A.8 Calculated principal stresses differences at 2 inch below the surface for the PG52-22 mix – non-braking.

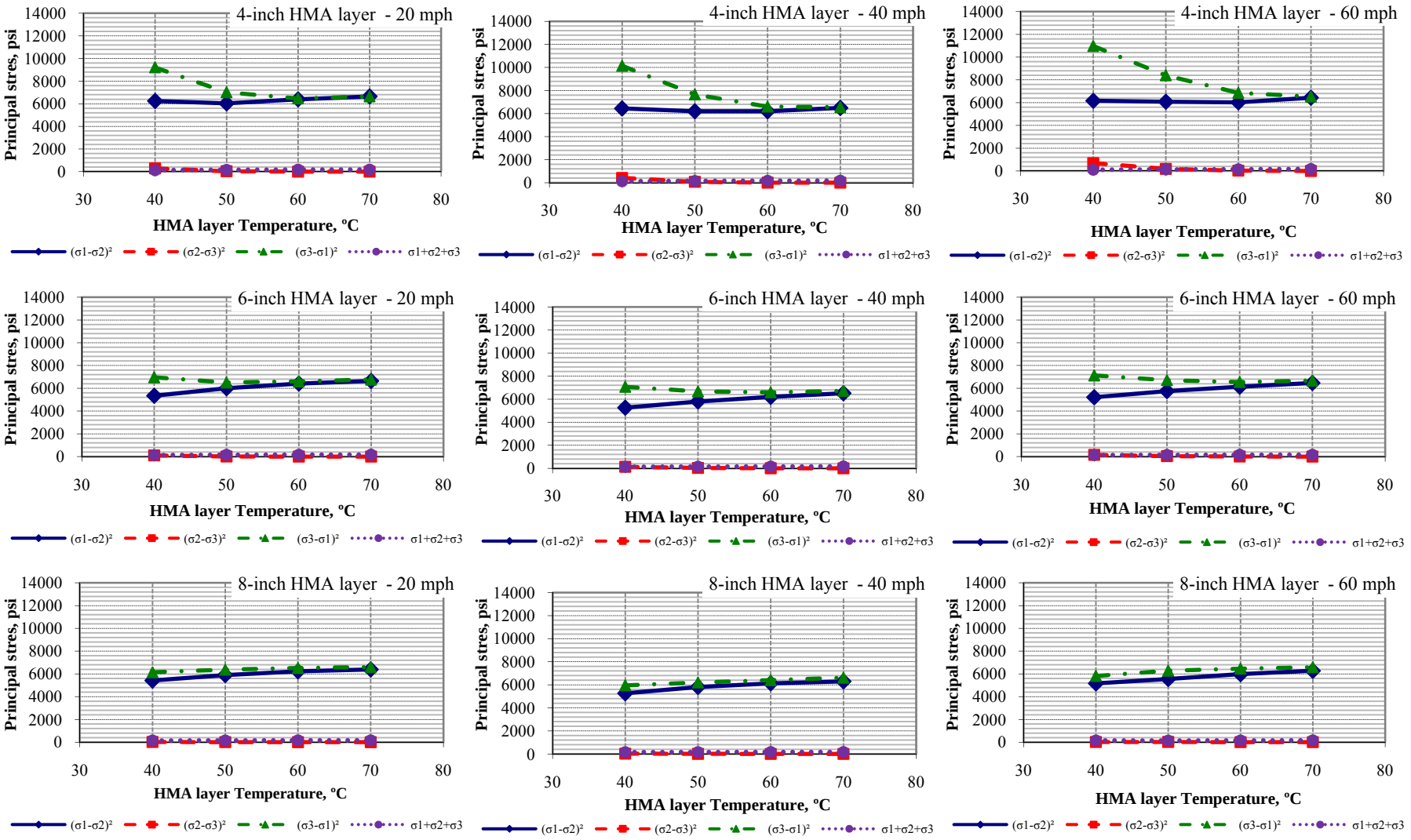

Figure A.9 Calculated principal stresses square differences at 2 inch below the surface for the PG52-22 mix – non-braking.

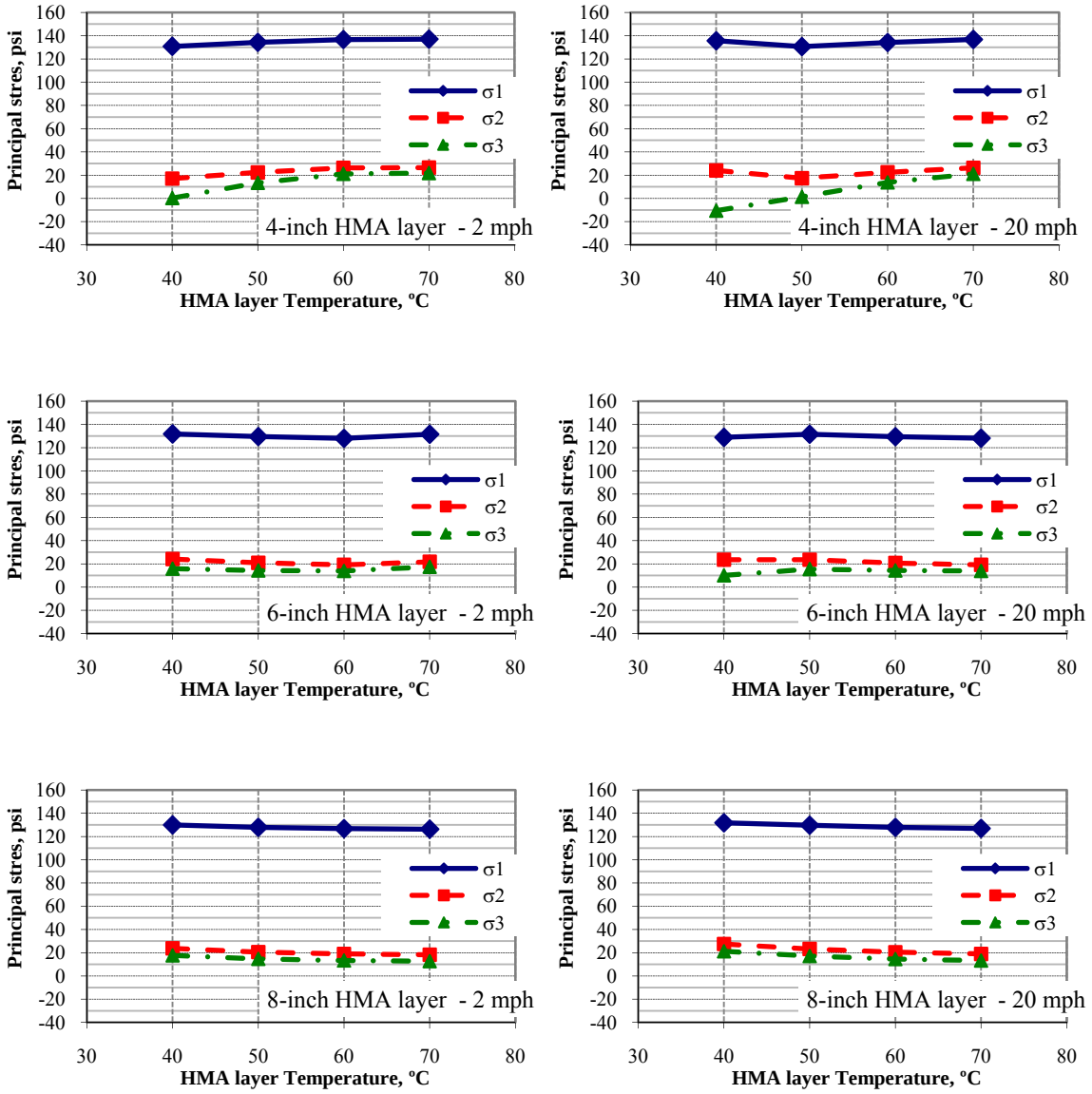

Figure A.10 Calculated principal stresses at 2 inch below the surface for the PG64-22 mix –Braking.

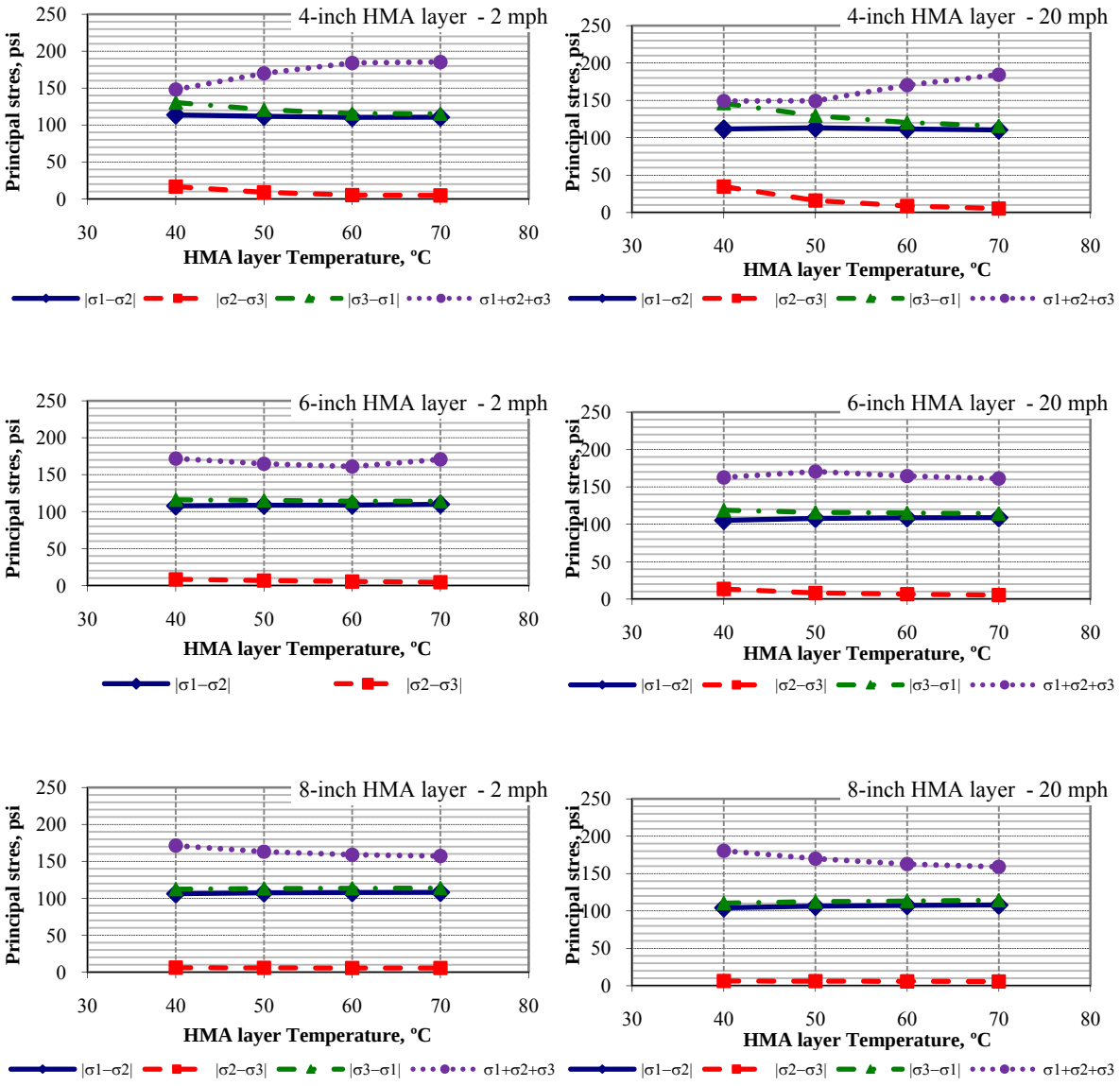

Figure A.11 Calculated principal stresses differences at 2 inch below the surface for the PG64-22 mix –Braking.

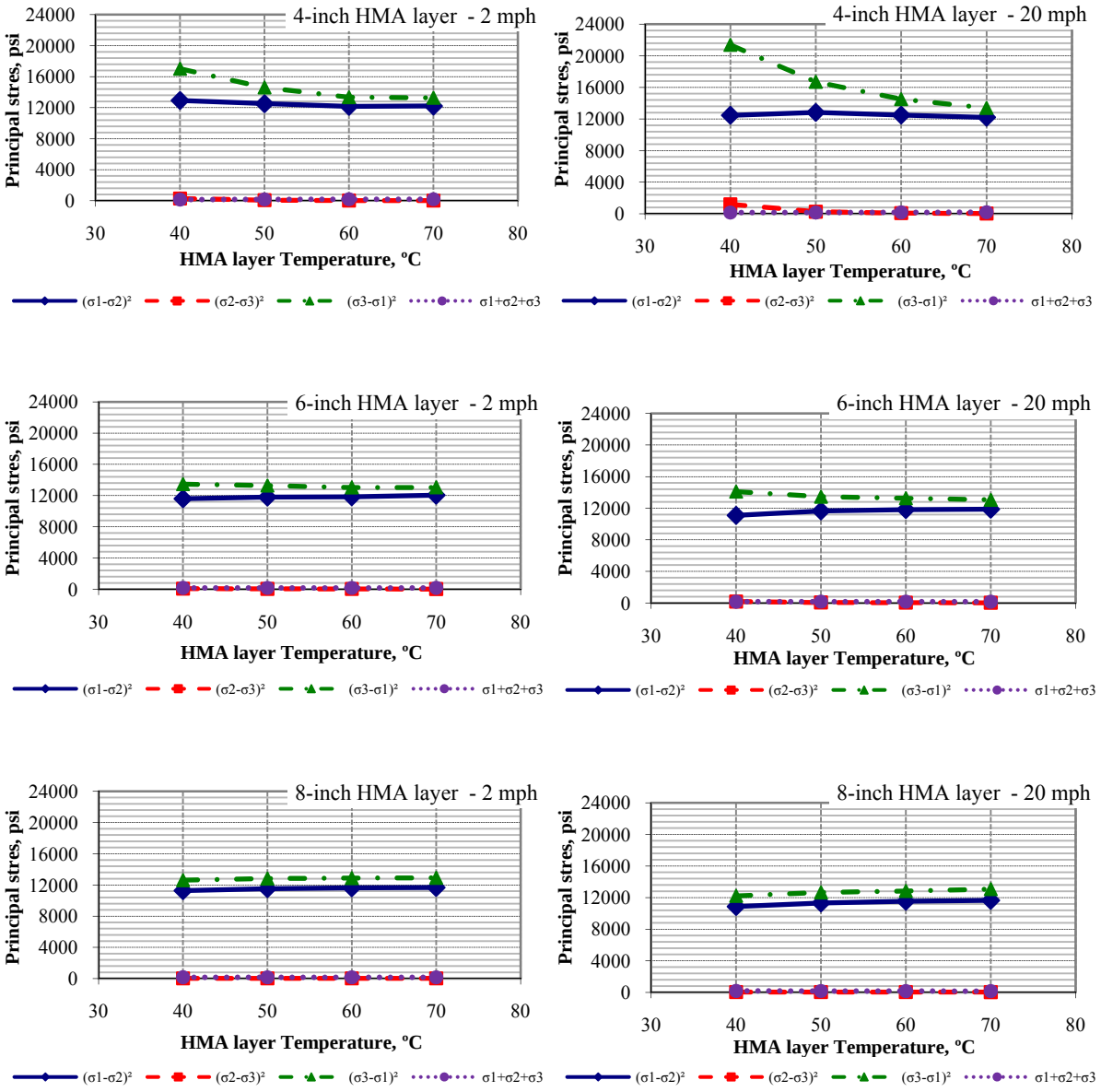

Figure A.12 Calculated principal stresses square differences at 2 inch below the surface for the PG64-22 mix –Braking.

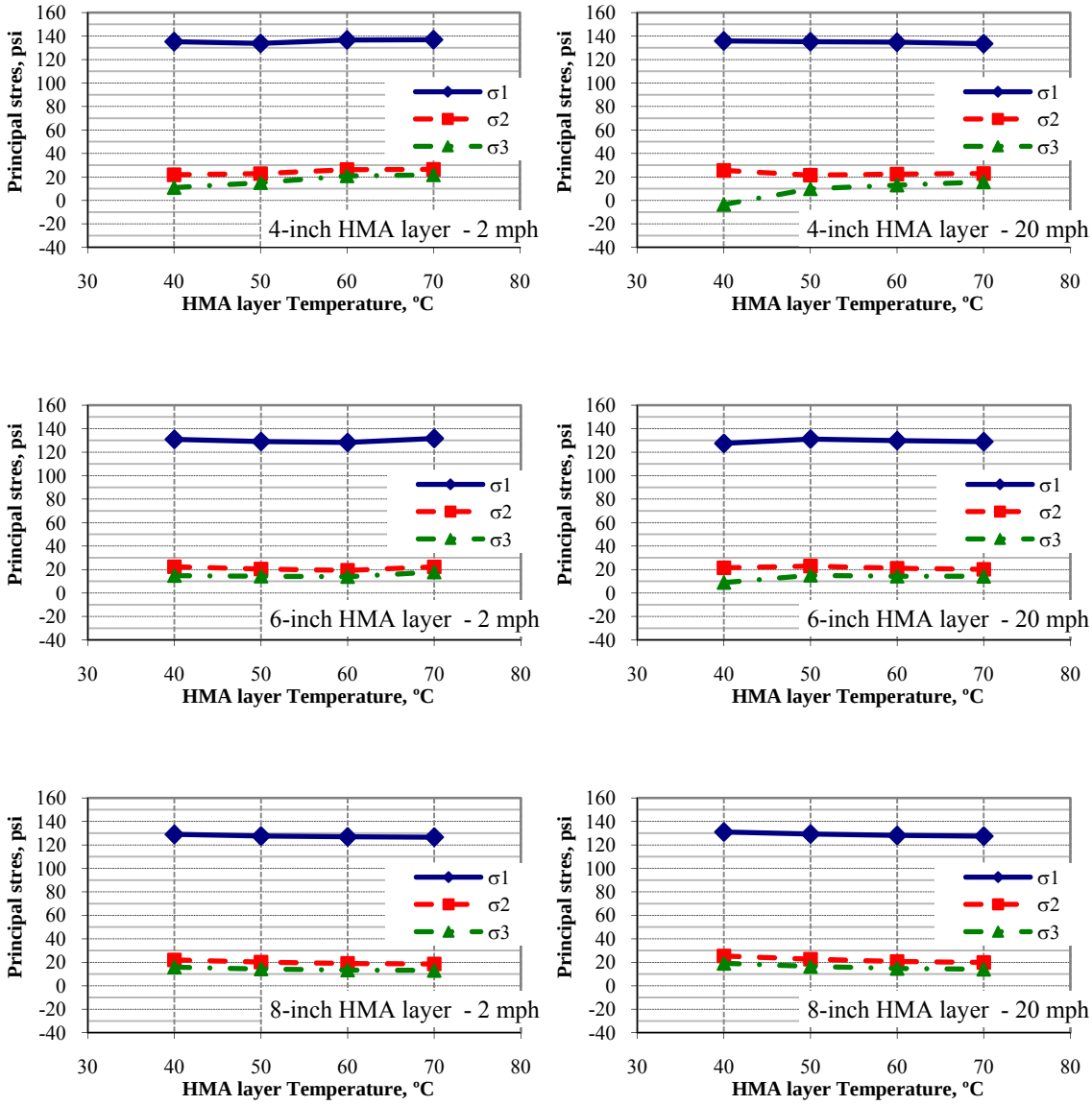

Figure A.13 Calculated principal stresses at 2 inch below the surface for the PG58-22 mix –Braking.

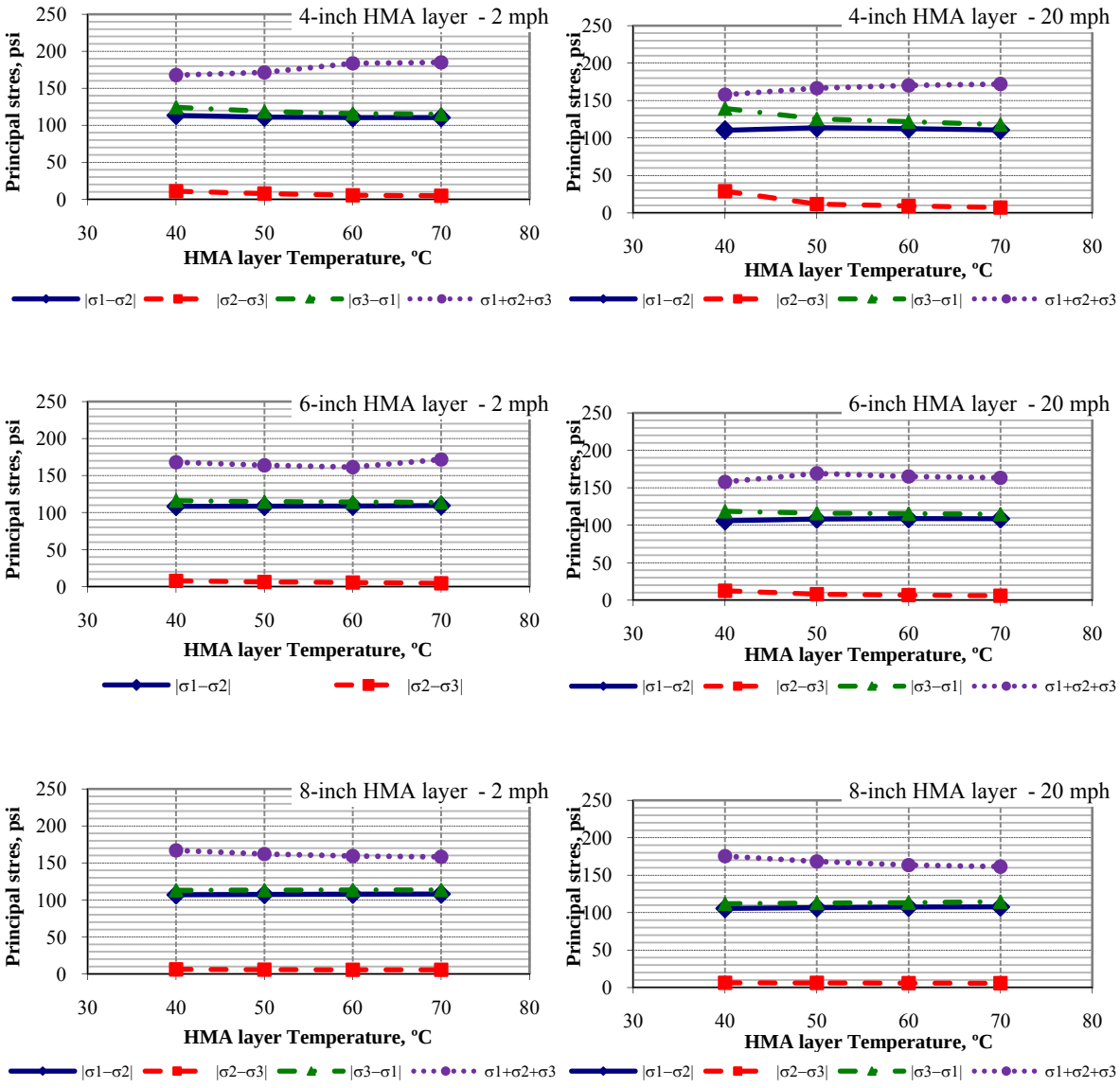

Figure A.14 Calculated principal stresses differences at 2 inch below the surface for the PG58-22 mix –Braking.

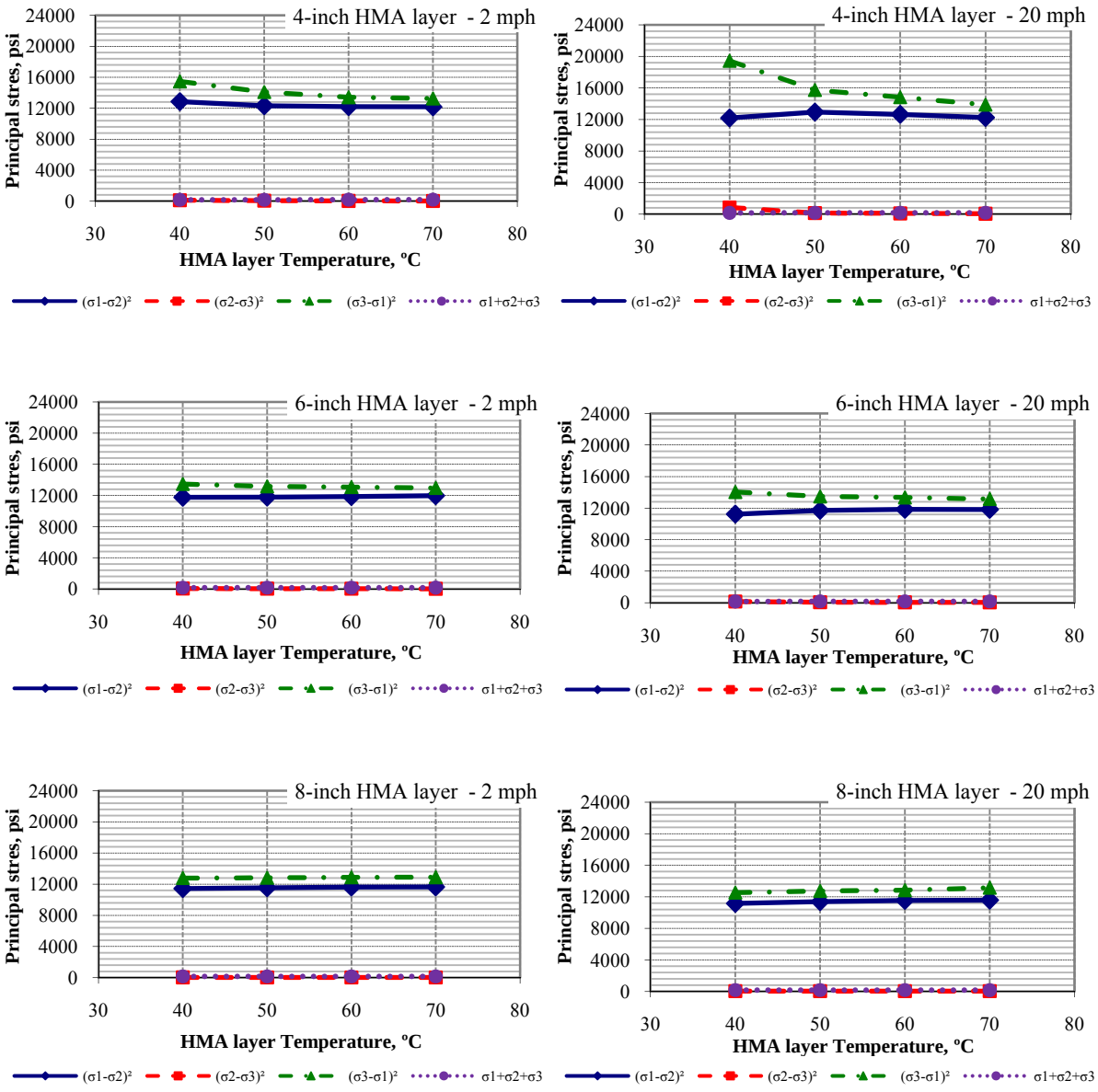

Figure A.15 Calculated principal stresses square differences at 2 inch below the surface for the PG58-22 mix –Braking.

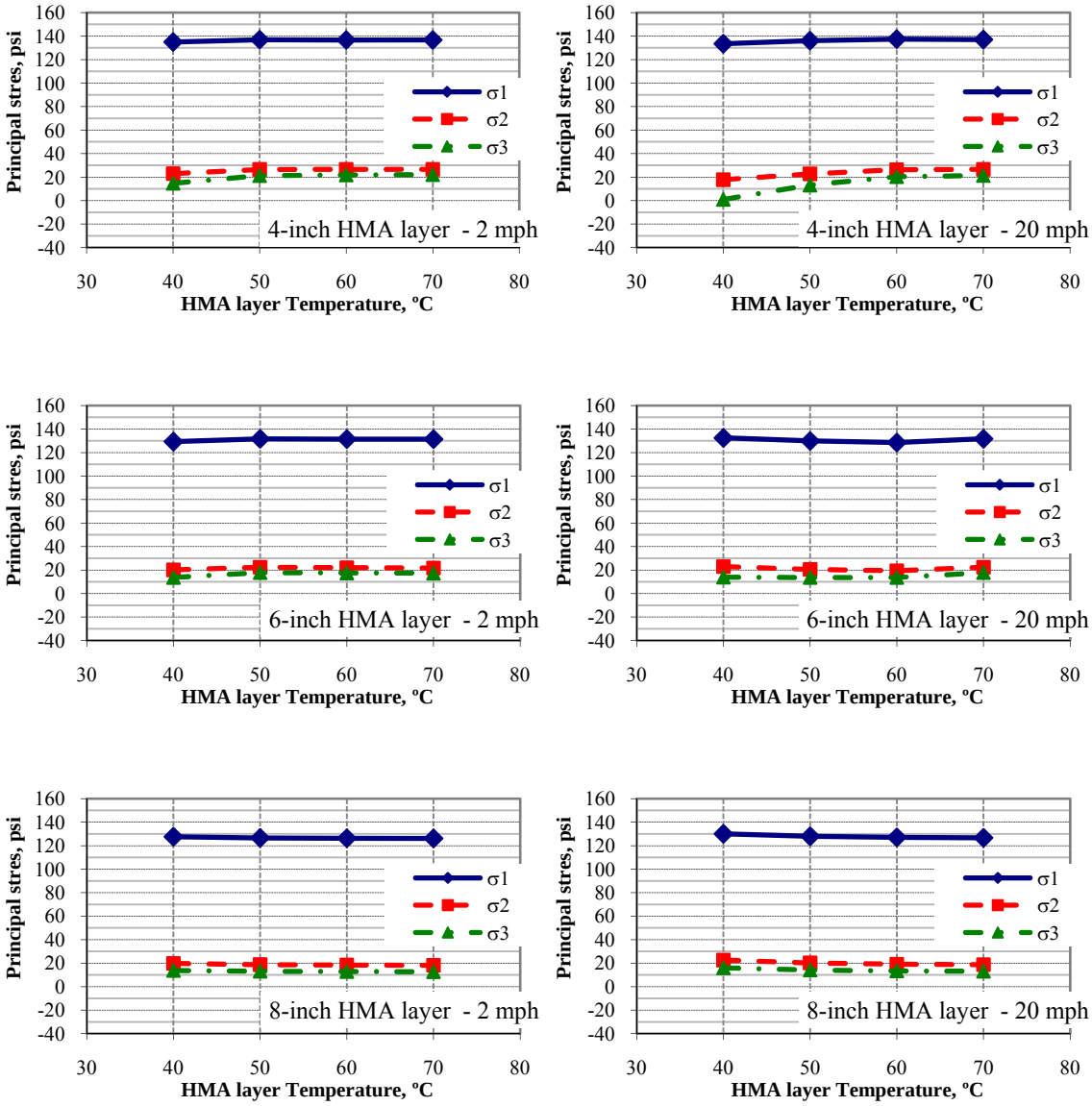

Figure A.16 Calculated principal stresses at 2 inch below the surface for the PG52-22 mix –Braking.

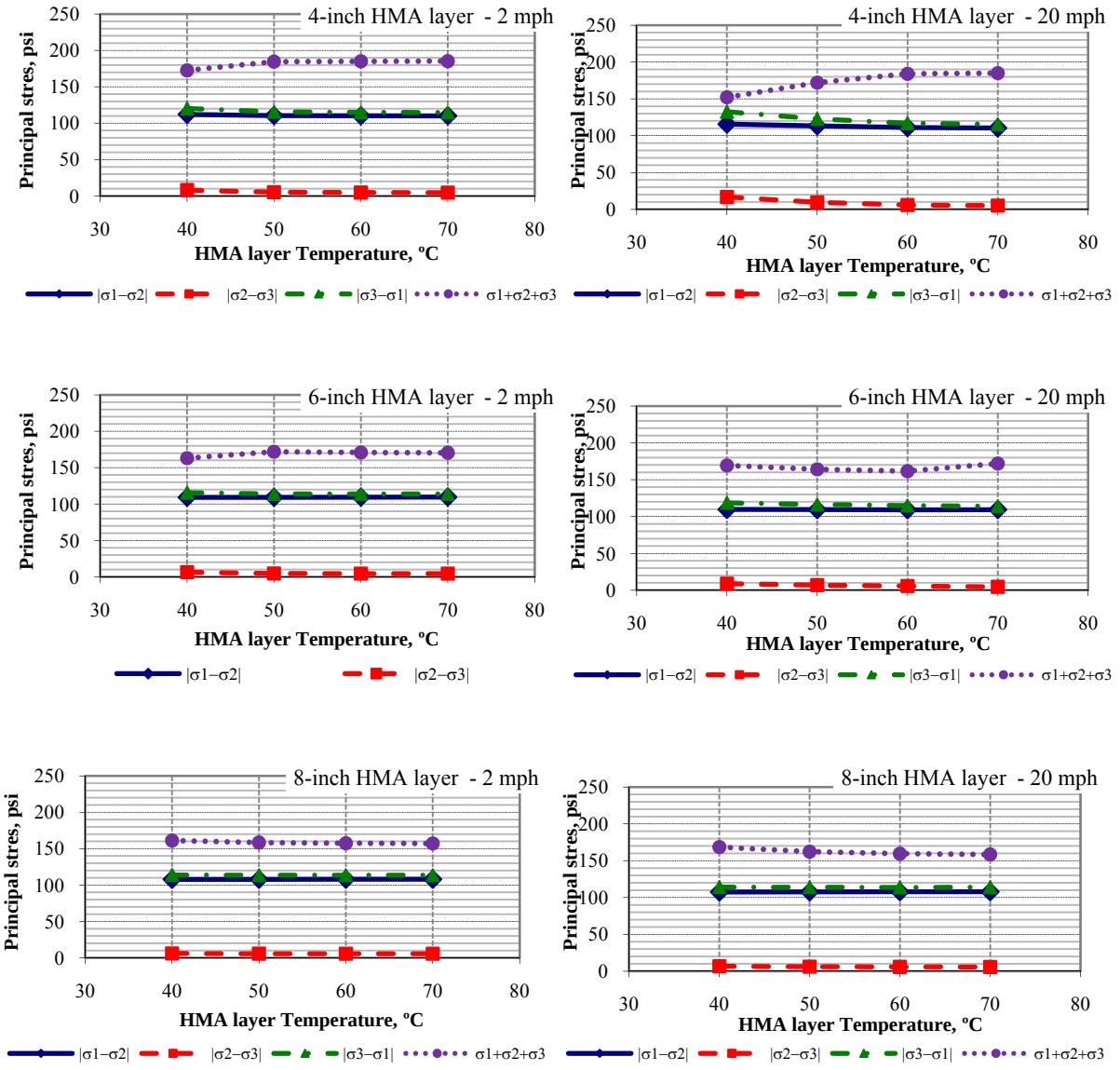

Figure A.17 Calculated principal stresses differences at 2 inch below the surface for the PG52-22 mix –Braking.

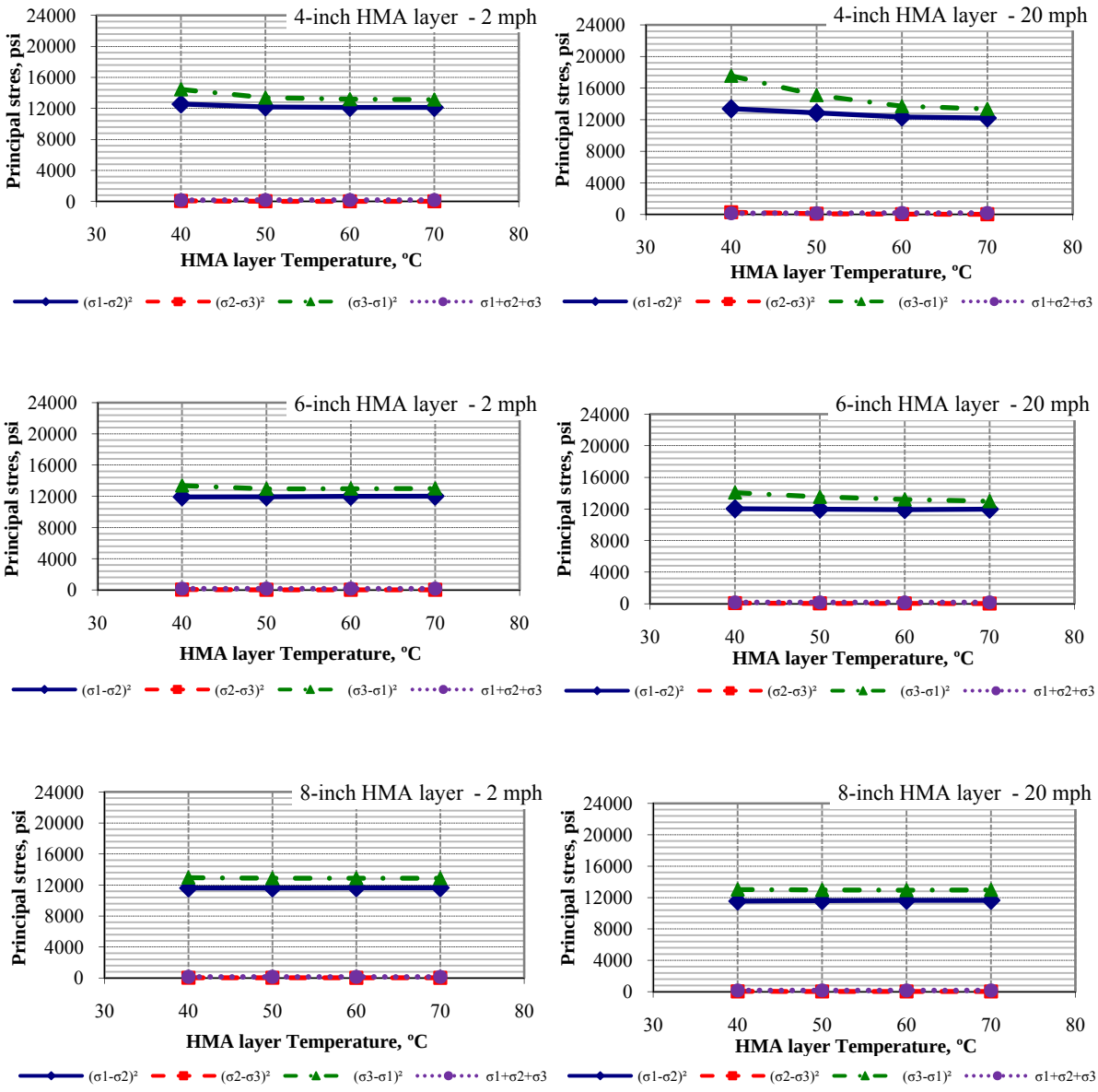

Figure A.18 Calculated principal stresses square differences at 2 inch below the surface for the PG52-22 mix –Braking.

APPENDIX B

1) Deviator stress pulse time– Non-braking

NAME	LABEL	NOBS	TYPE
ID		108	2
OBS		108	1
X1	HMA Thickness (in#)	108	1
X2	Temp (°C)	108	1
X3	Temp^2 (°C)	108	1
X4	Speed (mph)	108	1
X5	Speed^2	108	1
X6	log(H)	108	1
X7	log(T)	108	1
X8	log(T^2)	108	1
X9	log(S)	108	1
X10	log(S^2)	108	1
X11	Pulse Time (sec)	108	1
X12	log(Pulse Time)	108	1
_CI		108	1
_WT_		108	1

Number in Model	R-Square	Adjusted R-Square	C(p)	AIC	Root MSE	SBC	Variables in Model
1	0.9415	0.9410	298.5605	-659.0863	0.04686	-653.72205	X9
1	0.9415	0.9410	298.5605	-659.0863	0.04686	-653.72205	X10
2	0.9848	0.9845	2.8415	-802.3890	0.02403	-794.34263	X7 X9
2	0.9848	0.9845	2.8415	-802.3890	0.02403	-794.34263	X8 X9
3	0.9852	0.9848	1.9233	-803.4378	0.02381	-792.70924	X2 X7 X9
3	0.9852	0.9848	1.9233	-803.4378	0.02381	-792.70924	X2 X8 X9
4	0.9853	0.9847	3.2201	-802.1855	0.02384	-788.77481	X2 X6 X7 X9
4	0.9853	0.9847	3.2201	-802.1855	0.02384	-788.77481	X2 X6 X8 X9
5	0.9854	0.9847	4.2902	-801.1823	0.02385	-785.08950	X1 X2 X6 X7 X9
5	0.9854	0.9847	4.2902	-801.1823	0.02385	-785.08950	X1 X2 X6 X8 X9
6	0.9855	0.9846	6.0057	-799.4891	0.02393	-780.71421	X1 X2 X5 X6 X7 X9
6	0.9855	0.9846	6.0057	-799.4891	0.02393	-780.71421	X1 X2 X5 X6 X8 X9
7	0.9855	0.9845	8.0000	-797.4952	0.02405	-776.03818	X1 X2 X3 X5 X6 X7 X9
7	0.9855	0.9845	8.0000	-797.4952	0.02405	-776.03818	X1 X2 X3 X5 X6 X8 X9

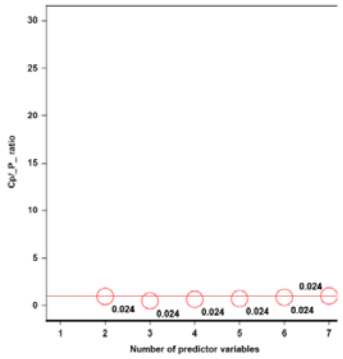

Root MSE	0.02489	R-Square	0.9838
Dependent Mean	-1.51575	Adj R-Sq	0.9833
Coeff Var	-1.64240		

Parameter Estimates										
Variable	Label	DF	Parameter Estimate	Standard Error	t Value	Pr > |t|	Type I SS	Standardized Estimate	Squared Partial Corr Type II	Variance Inflation
Intercept	Intercept	1	-0.66540	0.02159	-30.83	<.0001	248.13049	0	.	0
X2	Temp (°C)	1	-0.00353	0.00021426	-16.47	<.0001	0.16819	-0.20556	0.72295	1.00000
X4	Speed (mph)	1	-0.02360	0.00103	-22.98	<.0001	3.65632	-2.00742	0.83549	49.00000
X5	Speed^2	1	0.00015414	0.00001270	12.13	<.0001	0.09124	1.05984	0.58603	49.00000

Figure B.1 Statistical parameters to select the best model for deviator stress pulse time – 4-inch HMA layer – Non-braking – SAS output.

2) Deviator stress pulse time – Braking

NAME	LABEL	NOBS	TYPE
ID		72	2
OBS		72	1
X1	HMA Thickness (in#)	72	1
X2	Temp (°C)	72	1
X3	T^2	72	1
X4	S^2	72	1
X5	Speed (mph)	72	1
X6	H*T	72	1
X7	Pulse Time (sec)	72	1
X8	log(Pulse Time)	72	1
_CI		72	1
_WT_		72	1

Number in Model	R-Square	Adjusted R-Square	C(p)	AIC	Root MSE	SBC	Variables in Model
1	0.9993	0.9992	19.3098	-615.3833	0.01374	-610.83000	X4
1	0.9993	0.9992	19.3098	-615.3833	0.01374	-610.83000	X5
2	0.9993	0.9993	12.4210	-621.1140	0.01312	-614.28400	X2 X4
2	0.9993	0.9993	12.4210	-621.1140	0.01312	-614.28400	X2 X5
3	0.9994	0.9993	9.8532	-623.4349	0.01282	-614.32828	X2 X3 X4
3	0.9994	0.9993	9.8532	-623.4349	0.01282	-614.32828	X2 X3 X5
4	0.9994	0.9994	8.0758	-625.2151	0.01259	-613.83177	X2 X3 X4 X6
4	0.9994	0.9994	8.0758	-625.2151	0.01259	-613.83177	X2 X3 X5 X6
5	0.9994	0.9994	6.0000	-627.5295	0.01231	-613.86950	X1 X2 X3 X4 X6
5	0.9994	0.9994	6.0000	-627.5295	0.01231	-613.86950	X1 X2 X3 X5 X6

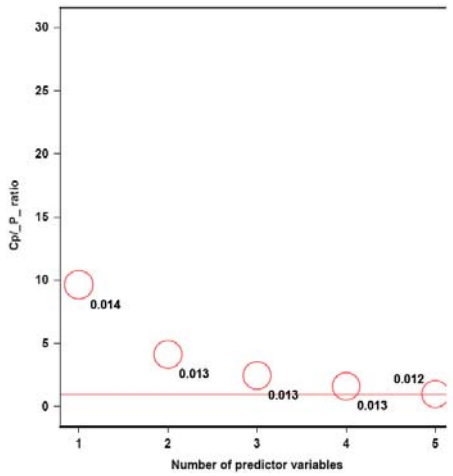

Root MSE	0.01312	R-Square	0.9993
Dependent Mean	-0.86577	Adj R-Sq	0.9993
Coeff Var	-1.51533		

Parameter Estimates										
Variable	Label	DF	Parameter Estimate	Standard Error	t Value	Pr > |t|	Type I SS	Standardized Estimate	Squared Partial Corr Type II	Variance Inflation
Intercept	Intercept	1	-0.23603	0.00799	-29.55	<.0001	53.96762	0	.	0
X2	Temp (°C)	1	-0.00038674	0.00013829	-2.80	0.0067	0.00135	-0.00868	0.10181	1.00000
X5	Speed (mph)	1	-0.05531	0.00017179	-321.99	<.0001	17.84444	-0.99963	0.99933	1.00000

Figure B.2 Statistical parameters to select the best model for deviator stress pulse time – 4-inch HMA layer – Braking – SAS output.

3) Deviator stress – 4-inch HMA layer – Non-braking

NAME	LABEL	NOBS	TYPE
ID		36	2
OBS		36	1
X1	speed (mph)	36	1
X2	Temperature, ºC	36	1
X3	E*, ksi	36	1
X4	sd (psi)	36	1
_CI		36	1
_WT_		36	1

Number in Model	R-Square	Adjusted R-Square	C(p)	AIC	Root MSE	SBC	Variables in Model
1	0.9522	0.9508	5.8527	30.0738	1.47804	33.24082	X3
1	0.7409	0.7332	173.4105	90.9609	3.44309	94.12790	X2
2	0.9584	0.9558	3.0000	27.1348	1.40080	31.88531	X2 X3

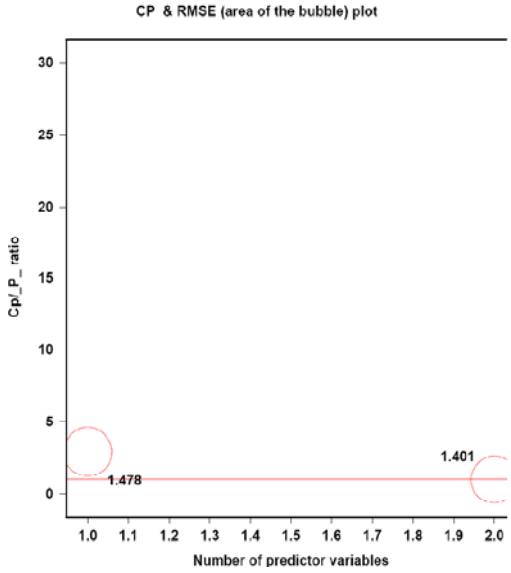

Root MSE	1.40080	R-Square	0.9584
Dependent Mean	85.82149	Adj R-Sq	0.9558
Coeff Var	1.63223		

Parameter Estimates										
Variable	Label	DF	Parameter Estimate	Standard Error	t Value	Pr > |t|	Type I SS	Standardized Estimate	Squared Partial Corr Type II	Variance Inflation
Intercept	Intercept	1	83.70762	2.56419	32.64	<.0001	265152	0	.	0
X2	Temperature, ºC	1	-0.08438	0.03831	-2.20	0.0347	1152.37843	-0.14353	0.12820	3.36500
X3	E*, ksi	1	0.06002	0.00457	13.13	<.0001	338.31124	0.85551	0.83935	3.36500

Figure B.3 Statistical parameters to select the best model for σ_d – 4-inch HMA layer – Non-braking – SAS output.

4) Confining stress – 4-inch HMA layer – Non-braking

NAME	LABEL	NOBS	TYPE
ID		36	2
OBS		36	1
X1	HMA layer thickness (in)	36	1
X2	speed (mph)	36	1
X3	Temperature, °C	36	1
X4	E*, ksi	36	1
X5	T^2	36	1
X6	E^2	36	1
X7	log(S)	36	1
X8	log(T)	36	1
X9	log(E)	36	1
X10	log(T^2)	36	1
X11	log(E^2)	36	1
X12	Max confining stress, sc (psi)	36	1
X13	log(Sc)	36	1
_CI		36	1
_WT_		36	1

Number in Model	R-Square	Adjusted R-Square	C(p)	AIC	Root MSE	SBC	Variables in Model
1	0.9709	0.9700	9.4683	-79.7973	0.32133	-76.63022	X4
1	0.7536	0.7463	318.6849	-2.9387	0.93446	0.22834	X3
2	0.9768	0.9754	3.0000	-86.0204	0.29096	-81.26984	X3 X4

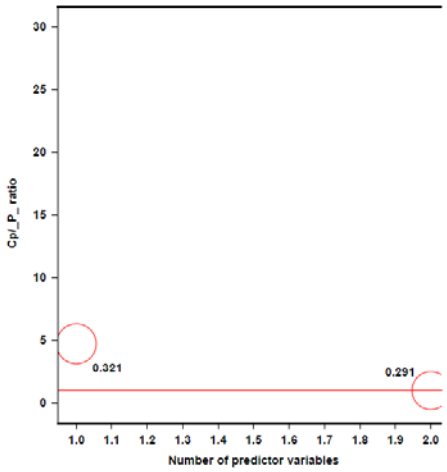

Root MSE	0.29096	R-Square	0.9768
Dependent Mean	31.86424	Adj R-Sq	0.9754
Coeff Var	0.91314		

Parameter Estimates										
Variable	Label	DF	Parameter Estimate	Standard Error	t Value	Pr > |t|	Type I SS	Standardized Estimate	Squared Partial Corr Type II	Variance Inflation
Intercept	Intercept	1	32.49536	0.53261	61.01	<.0001	36552	0	.	0
X3	Temperature, °C	1	0.02315	0.00796	2.91	0.0064	90.79443	0.14150	0.20421	3.36500
X4	E*, ksi	1	-0.01692	0.00094940	-17.82	<.0001	26.89524	-0.86669	0.90590	3.36500

Figure B.4 Statistical parameters to select the best model for σ_c – 4-inch HMA layer – Non-braking – SAS output.

5) Deviator stress – 4-inch HMA layer –Braking

NAME	LABEL	NOBS	TYPE
ID		24	2
OBS		24	1
X1	HMA layer thickness (in)	24	1
X2	Speed (mph)	24	1
X3	Temperature, °C	24	1
X4	E*, ksi	24	1
X5	S^2	24	1
X6	T^2	24	1
X7	E^2	24	1
X8	S*E	24	1
X9	T*E	24	1
X10	Max deviator stress, sd (psi)	24	1
X11	log(sd)	24	1
_CI		24	1
_WT_		24	1

Number in Model	R-Square	Adjusted R-Square	C(p)	AIC	Root MSE	SBC	Variables in Model
1	0.9610	0.9593	20.6093	-264.7553	0.00387	-262.39915	X4
1	0.7981	0.7889	190.4530	-225.2689	0.00880	-222.91281	X7
2	0.9761	0.9739	6.8813	-274.5124	0.00310	-270.97825	X4 X7
2	0.9747	0.9723	8.3351	-273.1495	0.00319	-269.61537	X3 X4
3	0.9808	0.9779	4.0000	-277.7536	0.00285	-273.04142	X3 X4 X7

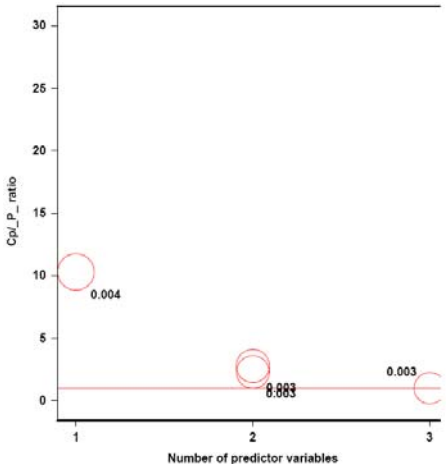

Root MSE	0.00285	R-Square	0.9808
Dependent Mean	2.06876	Adj R-Sq	0.9779
Coeff Var	0.13754		

Parameter Estimates										
Variable	Label	DF	Parameter Estimate	Standard Error	t Value	Pr > |t|	Type I SS	Standardized Estimate	Squared Partial Corr Type II	Variance Inflation
Intercept	Intercept	1	2.05992	0.00559	368.62	<.0001	102.71399	0	.	0
X3	Temperature, °C	1	-0.00017931	0.00008116	-2.21	0.0390	0.00494	-0.10691	0.19618	2.44054
X4	E*, ksi	1	0.00031924	0.00003510	9.09	<.0001	0.00329	1.17366	0.80528	17.35679
X7	E^2	1	-2.89819E-7	1.15146E-7	-2.52	0.0205	0.00005129	-0.28156	0.24056	13.04142

Figure B.5 Statistical parameters to select the best model for σ_d – 4-inch HMA layer – Braking – SAS output.

6) Confining stress – 4-inch HMA layer –Braking

NAME	LABEL	NOBS	TYPE
ID		24	2
OBS		24	1
X1	HMA layer thickness (in)	24	1
X2	Speed (mph)	24	1
X3	Temperature, °C	24	1
X4	E*, ksi	24	1
X5	S^2	24	1
X6	T^2	24	1
X7	E^2	24	1
X8	H*S	24	1
X9	exp(H)	24	1
X10	exp(S)	24	1
X11	exp(T)	24	1
X12	exp(E)	24	1
X13	exp(H*s)	24	1
X14	Max deviator stress, sc (psi)	24	1
X15	exp(Sc)	24	1
X16	log(Sc)	24	1
X17	S*E	24	1
X18	T*E	24	1
X19	S*T	24	1
_CI		24	1
_WT_		24	1

Number in Model	R-Square	Adjusted R-Square	C(p)	AIC	Root MSE	SBC	Variables in Model
1	0.9636	0.9620	5.4859	-42.6422	0.39526	-40.28613	X4
1	0.7778	0.7677	135.5789	0.7744	0.97658	3.13054	X17
2	0.9700	0.9672	3.0000	-45.2887	0.36724	-41.75454	X4 X17

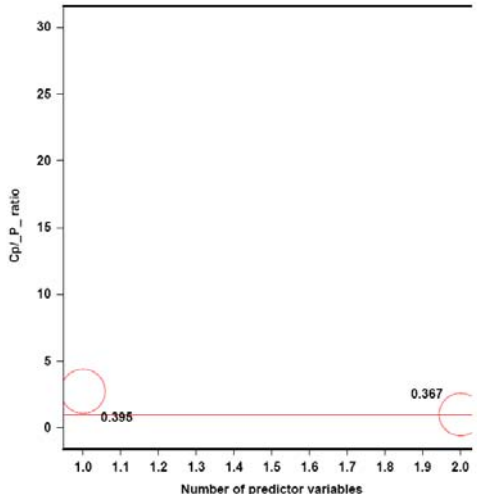

Root MSE	0.36724	R-Square	0.9700
Dependent Mean	35.51878	Adj R-Sq	0.9672
Coeff Var	1.03392		

Parameter Estimates										
Variable	Label	DF	Parameter Estimate	Standard Error	t Value	Pr > |t|	Type I SS	Standardized Estimate	Squared Partial Corr Type II	Variance Inflation
Intercept	Intercept	1	37.50492	0.11367	329.95	<.0001	30278	0	.	0
X4	E*, ksi	1	-0.03402	0.00293	-11.60	<.0001	91.00585	-1.18206	0.86502	7.27071
X17	S*E	1	0.00028991	0.00013688	2.12	0.0463	0.60498	0.21581	0.17601	7.27071

Figure B.6 Statistical parameters to select the best model for σ_c – 4-inch HMA layer – Braking – SAS output.

7) Deviator stress – 6-inch HMA layer –non-braking

NAME	LABEL	NOBS	TYPE
ID		36	2
OBS		36	1
X1	HMA layer thickness (in)	36	1
X2	Speed (mph)	36	1
X3	Temperature, °C	36	1
X4	S*T	36	1
X5	T*E	36	1
X6	E*, ksi	36	1
X7	log(E*)	36	1
X8	T^2	36	1
X9	S^2	36	1
X10	log(T*E)	36	1
X11	log(T^2)	36	1
X12	log(S^2)	36	1
X13	Max deviator stress, sd (psi)	36	1
X14	LOG(Sd)	36	1
_CI		36	1
_WT_		36	1

Number in Model	R-Square	Adjusted R-Square	C(p)	AIC	Root MSE	SBC	Variables in Model
1	0.6632	0.6533	107.3567	-3.1487	0.93173	0.01834	X7
1	0.4125	0.3952	211.0897	16.8815	1.23058	20.04852	X8
2	0.7109	0.6933	89.6320	-6.6429	0.87626	-1.89233	X3 X7
2	0.6859	0.6669	99.9404	-3.6673	0.91324	1.08329	X7 X8
3	0.8617	0.8487	29.2308	-31.1867	0.61547	-24.85260	X3 X7 X8
3	0.7474	0.7237	76.5286	-9.5014	0.83178	-3.16734	X2 X3 X7
4	0.9159	0.9050	8.8132	-47.0821	0.48771	-39.16453	X2 X3 X7 X8
4	0.9026	0.8900	14.3187	-41.7966	0.52486	-33.87905	X3 X4 X7 X8
5	0.9275	0.9154	6.0000	-50.4389	0.46022	-40.93779	X2 X3 X4 X7 X8

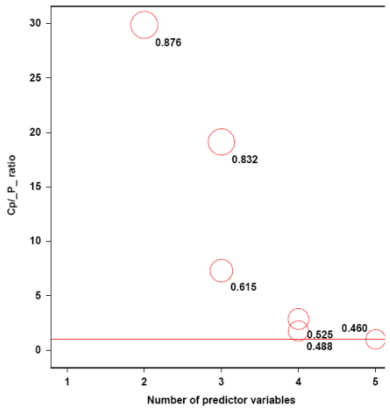

Root MSE	0.46022	R-Square	0.9275
Dependent Mean	78.42221	Adj R-Sq	0.9154
Coeff Var	0.58685		

Parameter Estimates										
Variable	Label	DF	Parameter Estimate	Standard Error	t Value	Pr > |t|	Type I SS	Standardized Estimate	Squared Partial Corr Type II	Variance Inflation
Intercept	Intercept	1	114.36645	3.32006	34.45	<.0001	221402	0	.	0
X2	Speed (mph)	1	0.07603	0.02367	3.21	0.0031	0.95381	0.79573	0.25593	25.38827
X3	Temperature, °C	1	-0.80398	0.09287	-8.66	<.0001	33.90712	-5.76127	0.71412	183.25362
X4	S*T	1	-0.00092200	0.00042026	-2.19	0.0361	1.35905	-0.60265	0.13826	31.21969
X7	log(E*)	1	-7.04504	0.52284	-13.47	<.0001	30.33455	-1.67555	0.85820	6.39769
X8	T^2	1	0.00655	0.00078523	8.34	<.0001	14.72393	5.17770	0.69854	159.55679

Figure B.7 Statistical parameters to select the best model for σ_d – 6-inch HMA layer – Non-braking – SAS output.

8) Confining stress – 6-inch HMA layer –non-braking

NAME	LABEL	NOBS	TYPE
ID		36	2
OBS		36	1
X1	speed (mph)	36	1
X2	HMA layer thickness (in)	36	1
X3	Temperature, °C	36	1
X4	E*, ksi	36	1
X5	T^2	36	1
X6	E^2	36	1
X7	T*E	36	1
X8	S*T	36	1
X9	log(H)	36	1
X10	log(T)	36	1
X11	log(E)	36	1
X12	log(T^2)	36	1
X13	log(E^2)	36	1
X14	log(T*E)	36	1
X15	log(S*T)	36	1
X16	log(S^2)	36	1
X17	Max confining stress, sc (psi)	36	1
X18	log(Sc)	36	1
_CI		36	1
_WT_		36	1

Number in Model	R-Square	Adjusted R-Square	C(p)	AIC	Root MSE	SBC	Variables in Model
1	0.9773	0.9766	43.9893	-17.1545	0.76703	-13.98744	X7
1	0.9595	0.9583	103.6856	3.7165	1.02495	6.88349	X4
2	0.9849	0.9839	20.6641	-29.7480	0.63572	-24.99741	X5 X7
2	0.9842	0.9833	22.8182	-28.2490	0.64910	-23.49845	X3 X7
3	0.9865	0.9852	17.1371	-31.9065	0.60935	-25.57239	X1 X5 X7
3	0.9858	0.9845	19.4447	-30.1115	0.62473	-23.77739	X1 X3 X7
4	0.9902	0.9890	6.7148	-41.4940	0.52707	-33.57644	X1 X5 X7 X8
4	0.9887	0.9873	11.7362	-36.3535	0.56607	-28.43592	X1 X3 X7 X8
5	0.9916	0.9902	4.1832	-44.8617	0.49729	-35.36056	X1 X3 X5 X7 X8
5	0.9910	0.9895	6.0836	-42.5125	0.51378	-33.01138	X1 X4 X5 X7 X8
6	0.9916	0.9898	6.1510	-42.9029	0.50550	-31.81823	X1 X3 X4 X5 X7 X8
6	0.9916	0.9898	6.1828	-42.8622	0.50579	-31.77759	X1 X3 X5 X6 X7 X8
7	0.9916	0.9895	8.0000	-41.0965	0.51307	-28.42830	X1 X3 X4 X5 X6 X7 X8

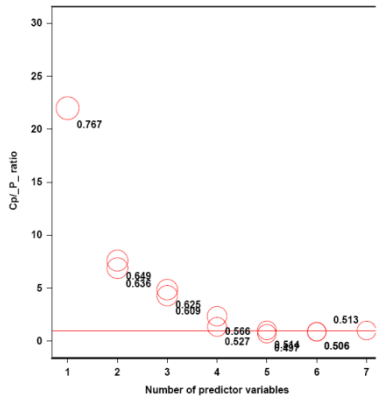

Root MSE	0.52707	R-Square	0.9902
Dependent Mean	34.97538	Adj R-Sq	0.9890
Coeff Var	1.50696		

Parameter Estimates

Variable	Label	DF	Parameter Estimate	Standard Error	t Value	Pr > |t|	Type I SS	Standardized Estimate	Squared Partial Corr Type II	Variance Inflation
Intercept	Intercept	1	31.40476	0.69741	45.03	<.0001	44038	0	.	0
X1	speed (mph)	1	-0.11069	0.02891	-3.83	0.0006	33.73860	-0.36541	0.32110	28.87657
X5	T^2	1	-0.00096723	0.00019114	-5.06	<.0001	611.46497	-0.24127	0.45237	7.20799
X7	T*E	1	0.00139	0.00004957	27.98	<.0001	223.78481	0.94586	0.96191	3.62412
X8	S*T	1	0.00171	0.00049842	3.43	0.0017	3.27002	0.35254	0.27521	33.48019

Figure B.8 Statistical parameters to select the best model for σ_c – 6-inch HMA layer – Non-braking – SAS output.

9) Deviator stress – 6-inch HMA layer –Braking

NAME	LABEL	NOBS	TYPE
ID		24	2
OBS		24	1
X1	HMA layer thickness (in)	24	1
X2	Speed (mph)	24	1
X3	Temperature, °C	24	1
X4	E*, ksi	24	1
X5	S^2	24	1
X6	T^2	24	1
X7	E^2	24	1
X8	H*S	24	1
X9	exp(H)	24	1
X10	exp(S)	24	1
X11	exp(T)	24	1
X12	exp(E)	24	1
X13	exp(H*s)	24	1
X14	Max deviator stress, sd (psi)	24	1
X15	exp(Sd)	24	1
X16	log(Sd)	24	1
X17	S*E	24	1
X18	T*E	24	1
_CI		24	1
_WT_		24	1

Number in Model	R-Square	Adjusted R-Square	C(p)	AIC	Root MSE	SBC	Variables in Model
1	0.3211	0.2902	41.1351	-297.2206	0.00197	-294.86447	X4
1	0.3170	0.2860	41.4974	-297.0788	0.00197	-294.72264	X17
2	0.4434	0.3904	32.1166	-299.9902	0.00182	-296.45603	X4 X7
2	0.3743	0.3148	38.3374	-297.1820	0.00193	-293.64787	X7 X17
3	0.5147	0.4419	27.6955	-301.2808	0.00174	-296.56855	X4 X7 X18
3	0.4990	0.4239	29.1089	-300.5167	0.00177	-295.80452	X4 X7 X17
4	0.7890	0.7446	5.0000	-319.2681	0.00118	-313.37783	X4 X7 X17 X18

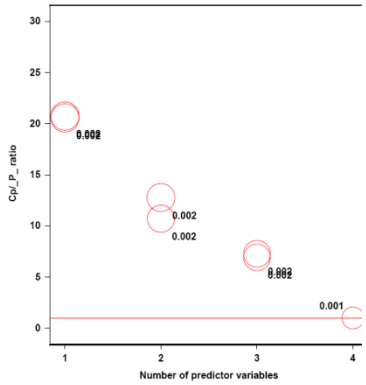

Root MSE	0.00118	R-Square	0.7890
Dependent Mean	2.04990	Adj R-Sq	0.7446
Coeff Var	0.05752		

Parameter Estimates										
Variable	Label	DF	Parameter Estimate	Standard Error	t Value	Pr > |t|	Type I SS	Standardized Estimate	Squared Partial Corr Type II	Variance Inflation
Intercept	Intercept	1	2.04942	0.00056959	3598.04	<.0001	100.85005	0	.	0
X4	E*, ksi	1	0.00020436	0.00003426	5.96	<.0001	0.00004020	6.35973	0.65187	102.36739
X7	E^2	1	-3.21345E-7	5.234542E-8	-6.14	<.0001	0.00001532	-2.73008	0.66482	17.80843
X17	S*E	1	0.00000298	6.006018E-7	4.97	<.0001	0.00000696	1.98196	0.56517	14.32290
X18	T*E	1	-0.00000419	8.19893E-7	-5.11	<.0001	0.00003630	-5.09737	0.57880	89.61141

Figure B.9 Statistical parameters to select the best model for σ_d – 6-inch HMA layer – Braking – SAS output.

10) Confining stress – 6-inch HMA layer –Braking

NAME	LABEL	NOBS	TYPE
ID		24	2
OBS		24	1
X1	HMA layer thickness (in)	24	1
X2	Speed (mph)	24	1
X3	Temperature, °C	24	1
X4	E*, ksi	24	1
X5	S^2	24	1
X6	T^2	24	1
X7	E^2	24	1
X8	H^5	24	1
X9	exp(H)	24	1
X10	exp(S)	24	1
X11	exp(T)	24	1
X12	exp(E)	24	1
X13	exp(H*s)	24	1
X14	Max deviator stress, sc (psi)	24	1
X15	exp(Sc)	24	1
X16	log(Sc)	24	1
X17	S*E	24	1
X18	T*E	24	1
X19	S*T	24	1
_C1		24	1
_WT_		24	1

Number in Model	R-Square	Adjusted R-Square	C(p)	AIC	Root MSE	SBC	Variables in Model
1	0.9467	0.9443	116.0628	3.3999	1.03149	5.75597	X4
1	0.9415	0.9388	129.5949	5.6754	1.08157	8.03150	X18
2	0.9777	0.9756	38.8944	-15.5262	0.68270	-11.99207	X17 X18
2	0.9753	0.9730	45.0268	-13.0695	0.71855	-9.53535	X6 X18
3	0.9903	0.9888	8.8124	-33.4427	0.46198	-28.73050	X6 X17 X18
3	0.9897	0.9882	10.2016	-32.1352	0.47474	-27.42300	X3 X17 X18
4	0.9908	0.9889	9.4800	-32.7674	0.46108	-26.87713	X4 X6 X17 X18
4	0.9906	0.9886	10.1346	-32.1074	0.46747	-26.21712	X3 X6 X17 X18
5	0.9930	0.9910	6.0000	-37.1460	0.41477	-30.07770	X3 X4 X6 X17 X18

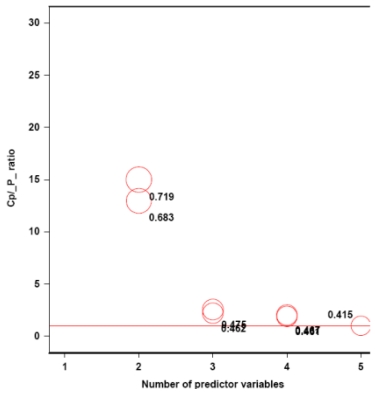

Root MSE	0.41477	R-Square	0.9930
Dependent Mean	35.21634	Adj R-Sq	0.9910
Coeff Var	1.17777		

Parameter Estimates										
Variable	Label	DF	Parameter Estimate	Standard Error	t Value	Pr > |t|	Type I SS	Standardized Estimate	Squared Partial Corr Type II	Variance Inflation
Intercept	Intercept	1	22.11707	4.17979	5.29	<.0001	29765	0	.	0
X3	Temperature, °C	1	0.33548	0.14331	2.34	0.0309	253.79530	0.87644	0.23339	358.15990
X4	E*, ksi	1	0.03343	0.01350	2.48	0.0234	168.98130	0.55516	0.25418	128.36949
X6	T^2	1	-0.00330	0.00121	-2.73	0.0136	2.46437	-0.95026	0.29348	308.57393
X17	S*E	1	-0.00140	0.00020850	-6.70	<.0001	7.60950	-0.49521	0.71389	13.95175
X18	T*E	1	0.00132	0.00028880	4.58	0.0002	3.61591	0.85979	0.53868	89.86360

Figure B.10 Statistical parameters to select the best model for σ_c – 6-inch HMA layer – Braking – SAS output.

11) Deviator stress – 8-inch HMA layer – Non-braking

NAME	LABEL	NOBS	TYPE
ID		36	2
OBS		36	1
X1	HMA layer thickness (in)	36	1
X2	speed (mph)	36	1
X3	Temperature, ºC	36	1
X4	E*, ksi	36	1
X5	T^2	36	1
X6	T*E	36	1
X7	S^2	36	1
X8	Max deviator stress, sd (psi)	36	1
_CI		36	1
_WT_		36	1

Number in Model	R-Square	Adjusted R-Square	C(p)	AIC	Root MSE	SBC	Variables in Model
1	0.9365	0.9347	78.1502	-13.2394	0.80989	-10.07233	X6
1	0.8931	0.8899	153.6069	5.5449	1.05131	8.71197	X4
2	0.9486	0.9455	59.1824	-18.8412	0.73970	-14.09063	X5 X6
2	0.9462	0.9430	63.3326	-17.2037	0.75672	-12.45313	X6 X7
3	0.9689	0.9660	25.9774	-34.9175	0.58439	-28.58337	X4 X5 X6
3	0.9663	0.9632	30.4538	-32.0493	0.60814	-25.71520	X4 X6 X7
4	0.9821	0.9798	5.0000	-52.8822	0.44996	-44.96465	X4 X5 X6 X7

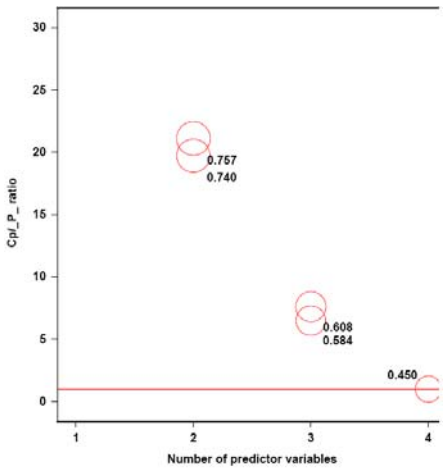

Root MSE	0.44996	R-Square	0.9821
Dependent Mean	76.08811	Adj R-Sq	0.9798
Coeff Var	0.59137		

Parameter Estimates

Variable	Label	DF	Parameter Estimate	Standard Error	t Value	Pr > |t|	Type I SS	Standardized Estimate	Squared Partial Corr Type II	Variance Inflation
Intercept	Intercept	1	79.01249	0.48926	161.49	<.0001	208418	0	.	0
X4	E*, ksi	1	0.04629	0.00649	7.14	<.0001	313.82960	1.36765	0.62163	63.74252
X5	T^2	1	0.00057577	0.00010989	5.24	<.0001	3.97941	0.22739	0.46967	3.26899
X6	T*E	1	-0.00199	0.00017123	-11.62	<.0001	22.67073	-2.17624	0.81315	60.92997
X7	S^2	1	0.00031601	0.00006592	4.79	<.0001	4.65207	0.13350	0.42569	1.34633

Figure B.11 Statistical parameters to select the best model for σ_d – 8-inch HMA layer – Non-braking – SAS output.

12) Confining stress – 8-inch HMA layer – Non-braking

NAME	LABEL	NOBS	TYPE
ID		36	2
OBS		36	1
X1	speed (mph)	36	1
X2	HMA layer thickness (in)	36	1
X3	Temperature, °C	36	1
X4	E*, ksi	36	1
X5	T^2	36	1
X6	E^2	36	1
X7	T*E	36	1
X8	S*T	36	1
X9	log(H)	36	1
X10	log(T)	36	1
X11	log(E)	36	1
X12	log(T^2)	36	1
X13	log(E^2)	36	1
X14	log(T*E)	36	1
X15	log(S*T)	36	1
X16	log(S^2)	36	1
X17	Max confining stress, sc (psi)	36	1
X18	log(Sc)	36	1

Number in Model	R-Square	Adjusted R-Square	C(p)	AIC	Root MSE	SBC	Variables in Model
1	0.9780	0.9773	37.7685	-19.2933	0.74458	-16.12622	X7
1	0.9628	0.9617	85.8058	-0.4345	0.96753	2.73257	X4
2	0.9836	0.9826	21.8075	-28.0085	0.65127	-23.25799	X1 X7
2	0.9832	0.9822	23.1369	-27.0965	0.65957	-22.34590	X5 X7
3	0.9860	0.9847	16.1917	-31.7325	0.61082	-25.39840	X1 X5 X7
3	0.9856	0.9843	17.5825	-30.6170	0.62036	-24.28289	X1 X3 X7
4	0.9897	0.9884	6.5898	-40.6958	0.53294	-32.77825	X1 X5 X7 X8
4	0.9886	0.9871	10.2455	-36.8685	0.56204	-28.95088	X1 X3 X7 X8
5	0.9908	0.9893	5.1267	-42.7403	0.51216	-33.23917	X1 X3 X5 X7 X8
5	0.9900	0.9883	7.7932	-39.5867	0.53509	-30.08557	X1 X4 X5 X7 X8
6	0.9912	0.9893	6.0001	-42.1603	0.51074	-31.07565	X1 X3 X4 X5 X7 X8
6	0.9911	0.9893	6.1539	-41.9631	0.51214	-30.87849	X1 X3 X5 X6 X7 X8
7	0.9912	0.9889	8.0000	-40.1605	0.51978	-27.49231	X1 X3 X4 X5 X6 X7 X8

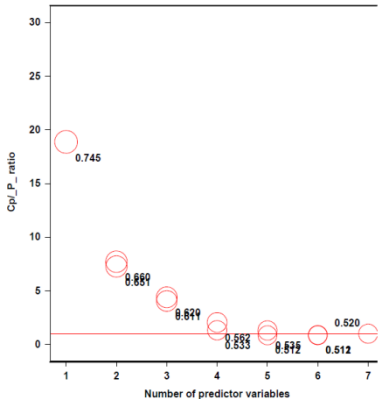

Root MSE	0.53294	R-Square	0.9897
Dependent Mean	34.18183	Adj R-Sq	0.9884
Coeff Var	1.55914		

Parameter Estimates										
Variable	Label	DF	Parameter Estimate	Standard Error	t Value	Pr > |t|	Type I SS	Standardized Estimate	Squared Partial Corr Type II	Variance Inflation
Intercept	Intercept	1	30.26259	0.70403	42.98	<.0001	42062	0	.	0
X1	speed (mph)	1	-0.11284	0.02930	-3.85	0.0006	30.51967	-0.37799	0.32360	29.01669
X5	T^2	1	-0.00082550	0.00019314	-4.27	0.0002	582.95454	-0.20895	0.37079	7.19850
X7	T*E	1	0.00139	0.00004968	27.98	<.0001	230.08833	0.97487	0.96192	3.65563
X8	S*T	1	0.00168	0.00050497	3.32	0.0023	3.13451	0.35094	0.26254	33.61365

Figure B.12 Statistical parameters to select the best model for σ_c – 8-inch HMA layer – Non-braking – SAS output.

13) Deviator stress – 8-inch HMA layer –Braking

NAME	LABEL	NOBS	TYPE
ID		24	2
OBS		24	1
X1	HMA layer thickness (in)	24	1
X2	Speed (mph)	24	1
X3	Temperature, °C	24	1
X4	E*, ksi	24	1
X5	S^2	24	1
X6	T^2	24	1
X7	E^2	24	1
X8	H*S	24	1
X9	exp(H)	24	1
X10	exp(S)	24	1
X11	exp(T)	24	1
X12	exp(E)	24	1
X13	exp(H*s)	24	1
X14	Max deviator stress, sd (psi)	24	1
X15	exp(Sd)	24	1
X16	log(Sd)	24	1
X17	S*E	24	1
X18	T*E	24	1
X19	S*T	24	1

Number in Model	R-Square	Adjusted R-Square	C(p)	AIC	Root MSE	SBC	Variables in Model
1	0.8225	0.8145	65.3477	-313.4718	0.00140	-311.11568	X7
1	0.8133	0.8048	69.7842	-312.2556	0.00144	-309.89949	X4
2	0.8679	0.8553	45.5248	-318.5591	0.00124	-315.02490	X8 X18
2	0.8478	0.8333	55.1979	-315.1574	0.00133	-311.62323	X7 X18
3	0.9196	0.9075	22.6761	-328.4681	0.00098922	-323.75584	X8 X18 X19
3	0.9175	0.9051	23.6814	-327.8522	0.00100	-323.14000	X7 X17 X18
4	0.9587	0.9500	5.8529	-342.4731	0.00072715	-336.58279	X4 X7 X17 X18
4	0.9325	0.9182	18.4818	-330.6571	0.00093010	-324.76682	X7 X8 X18 X19
5	0.9644	0.9546	5.1019	-344.0528	0.00069338	-336.98448	X4 X7 X17 X18 X19
5	0.9639	0.9539	5.3369	-343.7253	0.00069813	-336.65697	X4 X7 X8 X17 X18
6	0.9659	0.9538	6.4174	-343.0332	0.00069906	-334.78686	X3 X4 X6 X7 X17 X18
6	0.9656	0.9534	6.5498	-342.8404	0.00070188	-334.59399	X4 X6 X7 X17 X18 X19
7	0.9682	0.9544	7.2710	-342.7704	0.00069496	-333.34598	X3 X4 X6 X7 X8 X17 X18
7	0.9679	0.9539	7.4235	-342.5320	0.00069842	-333.10758	X3 X4 X6 X7 X17 X18 X19
8	0.9688	0.9522	9.0000	-341.2002	0.00071136	-330.59771	X3 X4 X6 X7 X8 X17 X18 X19

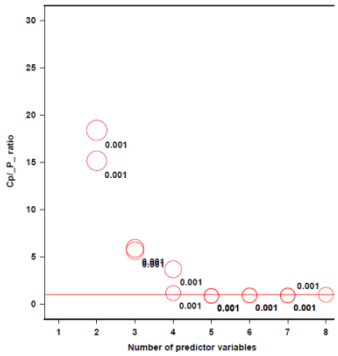

Root MSE	0.00072715	R-Square	0.9587
Dependent Mean	2.04290	Adj R-Sq	0.9500
Coeff Var	0.03559		

Parameter Estimates										
Variable	Label	DF	Parameter Estimate	Standard Error	t Value	Pr > |t|	Type I SS	Standardized Estimate	Squared Partial Corr Type II	Variance Inflation
Intercept	Intercept	1	2.04634	0.00035209	5811.92	<.0001	100.16279	0	.	0
X4	E*, ksi	1	0.00009169	0.00002105	4.36	0.0003	0.00019791	2.06090	0.49969	103.00696
X7	E^2	1	-2.32077E-7	3.143657E-8	-7.38	<.0001	0.00000626	-1.44291	0.74149	17.58174
X17	S*E	1	0.00000261	3.710575E-7	7.04	<.0001	0.00000839	1.25277	0.72309	14.55799
X18	T*E	1	-0.00000317	5.067413E-7	-6.26	<.0001	0.00002074	-2.78823	0.67372	91.19753

Figure B.13 Statistical parameters to select the best model for σ_d – 8-inch HMA layer – Braking – SAS output.

14) Confining stress – 8-inch HMA layer –Braking

NAME	LABEL	NOBS	TYPE
ID		24	2
OBS		24	1
X1	HMA layer thickness (in)	24	1
X2	Speed (mph)	24	1
X3	Temperature, °C	24	1
X4	E*, ksi	24	1
X5	S^2	24	1
X6	T^2	24	1
X7	E^2	24	1
X8	H*S	24	1
X9	exp(H)	24	1
X10	exp(S)	24	1
X11	exp(T)	24	1
X12	exp(E)	24	1
X13	exp(H*s)	24	1
X14	Max confining stress, sc (psi)	24	1
X15	exp(Sc)	24	1
X16	log(Sc)	24	1
X17	S*E	24	1
X18	T*E	24	1
X19	S*T	24	1
_CI		24	1
_WT_		24	1

Number in Model	R-Square	Adjusted R-Square	C(p)	AIC	Root MSE	SBC	Variables in Model
1	0.9518	0.9496	80.7560	1.6926	0.99545	4.04873	X4
1	0.9440	0.9414	97.0197	5.2840	1.07278	7.64012	X18
2	0.9779	0.9758	28.2395	-15.0002	0.69022	-11.46603	X17 X18
2	0.9747	0.9723	34.8512	-11.7927	0.73792	-8.25849	X3 X18
3	0.9886	0.9869	7.7351	-29.0053	0.50673	-24.29304	X6 X17 X18
3	0.9885	0.9868	8.0175	-28.7214	0.50973	-24.00918	X3 X17 X18
4	0.9900	0.9879	6.8180	-30.1525	0.48690	-24.26227	X4 X6 X17 X18
4	0.9898	0.9877	7.2504	-29.6592	0.49193	-23.76897	X6 X7 X17 X18
5	0.9918	0.9895	5.2059	-32.7262	0.45477	-25.65787	X5 X7 X17 X18 X19
5	0.9918	0.9895	5.2059	-32.7262	0.45477	-25.65787	X2 X7 X17 X18 X19
6	0.9925	0.9898	5.6942	-32.9332	0.44693	-24.68678	X5 X6 X7 X17 X18 X19
6	0.9925	0.9898	5.6942	-32.9332	0.44693	-24.68678	X2 X6 X7 X17 X18 X19
7	0.9927	0.9895	7.2183	-31.6723	0.45365	-22.24783	X2 X3 X6 X7 X17 X18 X19
7	0.9927	0.9895	7.2183	-31.6723	0.45365	-22.24783	X3 X6 X7 X8 X17 X18 X19
8	0.9928	0.9890	9.0000	-30.0190	0.46515	-19.41652	X3 X4 X5 X6 X7 X17 X18 X19
8	0.9928	0.9890	9.0000	-30.0190	0.46515	-19.41652	X2 X3 X4 X6 X7 X17 X18 X19

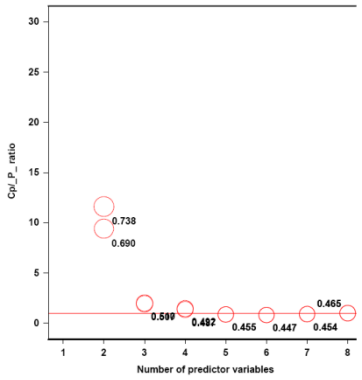

Root MSE	0.45477	R-Square	0.9918
Dependent Mean	34.78364	Adj R-Sq	0.9895
Coeff Var	1.30744		

Parameter Estimates

Variable	Label	DF	Parameter Estimate	Standard Error	t Value	Pr > |t|	Type I SS	Standardized Estimate	Squared Partial Corr Type II	Variance Inflation
Intercept	Intercept	1	30.11189	0.27119	111.04	<.0001	29038	0	.	0
X5	S^2	1	0.01961	0.00455	4.31	0.0004	63.64185	0.89469	0.50815	94.08216
X7	E^2	1	0.00005942	0.00002296	2.59	0.0185	291.08771	0.27106	0.27125	23.96923
X17	S*E	1	-0.00271	0.00042448	-6.39	<.0001	4.48792	-0.95413	0.69416	48.70589
X18	T*E	1	0.00214	0.00011501	18.63	<.0001	84.34525	1.38087	0.95069	12.00882
X19	S*T	1	-0.00641	0.00134	-4.80	0.0001	4.76723	-0.76832	0.56151	55.97652

Figure B.14 Statistical parameters to select the best model for σ_c – 8-inch HMA layer – Braking – SAS output.